DEPARTMENT OF ELECTRONIC & ELECTRICAL ENGINEERING

University of Strathclyde
Engineering

MICRO-ELECTROSTATIC PRECIPITATION FOR AIR TREATMENT

A thesis presented in fulfilment of the requirement for
the degree of

Doctor of Philosophy

Athanasios Mermigkas, MEng, MSc

2016

Department of Electronic and Electrical Engineering

University of Strathclyde

Glasgow, UK

Declaration of Authenticity and Author's Rights

‘This thesis is the result of the author’s original research. It has been composed by the author and has not been previously submitted for examination which has led to the award of a degree.’

'The copyright of this thesis belongs to the author under the terms of the United Kingdom Copyright Acts as qualified by University of Strathclyde Regulation 3.50. Due acknowledgement must always be made of the use of any material contained in, or derived from, this thesis.’

Signed:

Date:

ACKNOWLEDGEMENTS

I would like to wholeheartedly thank my supervisors, Dr Igor V. Timoshkin and Prof Scott J. MacGregor, for giving me the opportunity to undertake the particular PhD and for their excellent guidance, immense knowledge, continuous help, motivation and encouragement along with the patience they abundantly displayed throughout its course.

Furthermore, sincere thanks are due to all the members of the High Voltage Technologies group for their immeasurable support and advice. Special thanks to Dr Mark Peter Wilson who was always willing to answer my continuous queries regarding scientific and university matters, as well as providing invaluable help in the laboratory. Many thanks also to Dr Martin J. Given for his advice and insightful contribution on conference presentations and scientific publications. Moreover, i am greatly indebted to Michelle Maclean as the head of the ROLEST research group for providing me with the equipment (vacuum pump and air-compressor) without which I could not conduct any ESP experimental work, as well as for organising the ROLEST presentation events, that really sharpened my presentation skills, while additionally providing me with invaluable feedback regarding my research from fellow colleagues in the HVT group.

I would also like to express my gratitude to Joe McKechnie, David Griffin, Frank May, Andy Carlin and Sean Doak from the High Voltage Mechanical Workshop and Frank Cox from the Electronic Workshop for their assistance in producing complicated reactors and other topologies, in addition to machining and maintaining the apparatus.

A big thank you to Maureen Cooper for all her administrative assistance and patience regarding conference preparations, access card problems and office supply requirements. A thank.alot++ to Georgios Kyriakou for his incredible help on programming matters.

At this point I would like to acknowledge the assistance and constant support of some incredible colleagues through these years. Life is so much more fulfilling having such dear friends and exceptional scientists around. Thank you all, Mark and Michelle, Michael and Karen, Xiao, Dan, Caron, Sotiria, Rachael, Sian, Jonah, Laura, Tracey, Guangming, Yiming, Rong, Sirui, Burhan, Yingjia, Weijia, Yihan, Yi and David. Hope you are all always well, wherever you may be, and all the best for a bright and fruitful future!

Moreover, I would like to express my appreciation to my family for their unconditional love, support, encouragement and understanding throughout all those demanding and creative years.

I would like also to thank late Dr Simon Wolff and his charitable foundation for bestowing me their prestigious young scientist travel grant towards attending PPPS 2013 in San Francisco CA, in 2013. Many thanks also to the IEEE committee organising the aforementioned conference for providing me an IEEE student travel grant, which included student conference registration and two nights at the conference hotel. Additional support was granted by the University of Strathclyde, the Faculty of Engineering and the Department of EEE (University of Strathclyde), for which I am grateful.

This work has been part-funded by EPSRC, under Grant EP/H049428/1 “Impulsive Micro-Electrostatic Precipitation Systems” awarded in 2010 and EPSRC Pathway to Impact Grant Awarded in 2012. This work was supported by the Faculty of Engineering and the Department of Electronic and Electrical Engineering, University of Strathclyde.

ABSTRACT

Particulate matter suspended in the atmosphere is a major contaminant and is prevalent in urban environs, reducing the quality of air in the places that the majority of humans reside. Medical research has labelled PM2.5 as a potential risk to human health. To combat this issue, new legislation regarding PM2.5 has been passed. Electrostatic precipitators exhibit a drop in efficiency at ~(0.1-1) µm PM diameter. Therefore, the present work is focused on an investigation of microelectrostatic precipitation technology, for improvement of indoor air quality.

Initial work included investigation of impulsive positive energisation, in a specially designed single stage, coaxial reactor, utilizing 250 ns impulses superimposed on dc voltage. Precipitation efficiency for coarse and fine powders has been investigated for various levels of superimposed impulsive and dc energisation in order to identify optimal energisation conditions.

Further steps were taken to decouple charging from collection stages in order to optimize the air cleaning process to a greater extent. Precipitation experiments were conducted using ambient air and cigarette smoke. Maximum precipitation efficiency was achieved when both stages were energised, under impulsive and dc energisation in each stage respectively. Analytical work regarding PM charging has also been conducted.

Lastly, the coaxial precipitator reactor was scaled-up for possible indoor air cleaning applications. Similarly, impulsive energisation combined with dc voltage at the different stages has been used and proved to increase precipitation efficiency. Test fluids used were beeswax candle fumes and ambient air. Simulations have also been conducted to optimize the ESP process.

In conclusion, it has been shown that impulsive energisation of ESPs is highly efficient, 100% for particles greater than 250 nm, for PM2.5 in concentrations found in indoor environments. This could potentially help in increasing indoor air quality, with all the corresponding health, working efficiency and ultimately state economic benefits it could achieve.

Contents

1. INTRODUCTION

The problem of suspended particles in the air is of utmost importance, especially nowadays since a great proportion of the world's population resides in urbanized environments, thus billions of people are subject to it. This is augmented by the fact that in modern society people spend 60%-90% of their time indoors (Jantunen et al., 2011). Research has pointed out that airborne particulate matter with diameter less than 2.5 µm, called PM2.5, is a cause of higher mortality rates (Laxen et al., 2010). To make this matter worse, PM2.5 particulate matter which is generated by road traffic contains carbon soot from diesel combustion and other toxic chemicals. In addition to the above, constant movement of people and vehicles and the use of various machinery result in production of coarser airborne particles which are also present in the atmosphere and indoor environment. Industrial processes such as coal fired power plants, shipping and agricultural processes can also be a source of precursor gases (e.g. SO_3) released into the atmosphere that can form secondary particulates. This can make the air quality in cities quite poor. Therefore, people in modern society are constantly exposed to a significant amount of artificially generated airborne particles including PM produced by road traffic and industrial processes, independent of whether people are in an open or enclosed environment (Morabia et al., 2009). Although nowadays smoking is banned in indoor public environments in many countries, including most of the EU member states (Europa.eu, 2013b), cigarette smoke can be an additional source of indoor air pollution that needs to be tackled, as it contains a significant amount of different chemical species, some of them being carcinogenic. Lastly, pollen can be present in air (Lohmann and Mensah, 2013) at the blooming season, and airborne viruses and bacteria can also play an adverse role for sensitive population groups. Therefore, multiple governmental bodies, including the UK government and the EU, have introduced the air quality index (AQI) that reflects the air quality in terms of concentrations of different chemical species such as O_3, NO_2, SO_3 and airborne particular matter, PM2.5 and PM10. This index is intended to be used for warning the populace of any possible adverse effects expected when spending time in the open (AQI, 2014, CITEAIR, 2014, DEFRA, 2013).

Combining all the above sources of airborne particles in a poorly ventilated place could result in a significant increase in the concentration of airborne PM. Currently, PM2.5

concentration of 70 μg/m^3 is considered as the critical level above which a health warning can be issued (Kagoshima Prefectural Advisors, 2013). High concentrations of airborne particles can cause irritation to the respiratory system and to the eyes, and can, in some cases, lead to headaches, dizziness, and tiredness. In the past, these symptoms were attributed to a condition known as sick building syndrome. All of these aspects are important in increasing indoor air quality, which is directly connected to adverse health effects not only to vulnerable population groups, but can also cause reduced productivity in work environments and schools. Thus, there is a need for increased indoor air quality.

There are various methods for cleaning of air flows, most of them being used on an industrial scale. The most prevalent methods in different industrial applications are settling chambers, cyclones, wet scrubbers, fabric filters and electrostatic precipitators (ESPs). Each of these methods could have various modifications or additional stages, and several of these methods can also be used in a modular air cleaning system in order to combine the advantages of each one.

Despite their relatively simple design and low construction cost, settling chambers and cyclones cannot effectively deal with the PM2.5 problem, being efficient for particles with diameters > 5 μm. Wet scrubbers can remove part of the PM2.5 spectrum (these scrubbers are efficient for PM with diameter above 1 μm), however their main drawback is the necessary use of water for the collection of airborne contaminants. Therefore, wet scrubbers generate water having absorbed particles removed from the air and potentially polluted with toxic chemicals and this liquid byproduct might not be safe to be released into the environment without further processing. This leaves only two approaches to removal of PM2.5 from the air in a safe and efficient manner, namely the use of fabric filters and ESPs. Fabric filters, especially HEPA filters, can have a very high collection efficiency, even higher than ESPs, however they have a higher operational and maintenance cost compared to ESPs and are not designed to deal with liquid particulates, that could easily be found in the forms of unburned fuel or oil, or tar droplets from tobacco smoke. In addition, high PM2.5 concentration in the air could interfere with the filters operation, causing blockage and reduced efficiency. Thus, ESPs could be considered as an optimal solution for tackling the PM2.5 problem efficiently.

Existing ESPs have some limitations, however. Despite the fact that they are successfully used on an industrial scale for removal of PM10 particulate matter, these systems cannot simply be scaled down for indoor applications in terms of improved efficiency for removal of PM2.5 particles and reduction of ozone and NO_x production. Ozone and NO_x are produced by corona discharges during the ESP operation and their levels should be kept to a minimum, as they are classified as toxic for human beings. For example, the State of California in USA has recently introduced stringent regulations regarding the production of ozone by indoor air cleaning apparatus (ca.gov, 2008).

Other factors that affect the precipitation efficiency of ESPs are the nature of the suspended particles present in the air. It has been shown theoretically that the electrical characteristics of the particles, namely their permittivity and electrical conductivity, are among the factors which play a major role in the precipitation process. Therefore, for improvement of the precipitation efficiency and development of advanced ESPs, further investigation is required in this area. In addition, high dust loading detrimentally affects precipitation efficiency, and the operation of electrostatic precipitators at different loading conditions also requires further study.

ESPs are usually energised with dc high voltage, which can be inefficient for small-scale indoor applications as particle loading is much reduced compared to larger scale industrial applications, and having a steady state dc current in the precipitator's chamber is not required, as in this case airborne PM acquires its saturation charge relatively quickly. Therefore, to minimise the energy consumption and production of toxic by-products, and to maximise the precipitation efficiency, it is suggested in the present work to use impulsive energisation. Impulsive energisation of the electrostatic precipitator will potentially reduce energy consumption as the electrode(s) will be energised only intermittently, and smaller airborne particles can be charged more effectively, as higher voltage levels can be used in an impulsive energisation regime without spark breakdown as compared with dc and ac energisation regimes. Impulsive energisation with HV impulses with duration a few µs and 100 µs superimposed on dc voltage below corona ignition level have been investigated previously (Parker and Institution of Electrical Engineers, 2003), however, to the authors best knowledge, there were no attempts to use shorter, ns HV impulses in the precipitation process. These impulses potentially will provide an advantage in terms of higher field magnitude achievable in the precipitator without spark breakdown, which could potentially result in a reduction of the energy consumption and generation of ozone and NO_x during the precipitation process, and in an increase in the charging and precipitation of fine and extra fine air-borne particles, which are problematic for traditionally energized electrostatic precipitators. Moreover, impulsive energisation has been shown to increase the collection efficiency of high resistivity particles (like fly ash from burning of tobacco products), compared to dc energisation (White, 1963), high resistivity meaning > 10^{11} Ω·cm (McKenna et al., 2008). In addition, while negative energisation is used predominantly in industrial scale ESPs, due to the better overall characteristics and higher PM collection efficiency afforded by the higher breakdown voltage strength (Parker, 1997), it produces high concentrations of ozone and NO_x gases (Asbach et al., 2004).

In this study, experimental and analytical work has been conducted in order to investigate and improve the efficiency of micro-ESP (denoting both the use of sub-micro- and micro- second energisation impulses as well as the miniature scale of precipitators, designed in scale to either be connected to the ventilation system or as stand-alone devices in rooms) by using impulsive voltage energisation of short duration and low frequency and at the same time keeping energy consumption at very low levels.

Since this technology is intended for small, indoor, applications, the present research is focused on development of an electrostatic precipitator with a compact design in order to develop smaller scale ESP system which can be easily installed with minimum footprint in an urban indoor environment. The selected design is based on a wire-cylinder topology which allows development of a compact, easy to clean precipitation system. It has also been proven that such a topology can successfully be used in industrial air cleaning operations, even for removal of liquid and corrosive droplets (McKenna et al., 2008, White, 1963). Impulsive energisation and combined impulsive and dc stresses were used in the present work to maximize the precipitation efficiency of fine and extra fine particles, and to minimize ozone and potentially nitrogen oxides produced during the electrostatic precipitation process. Positive polarity of the HV stress (impulsive and dc) was used in the present study to achieve minimum ozone concentration in the exhaust air, while the use of an MnO_2 filter reduces the ozone level in the off-gas to that of background levels.

Two different energization regimes were proposed and investigated in the present work. HV impulses were either applied directly to the main HV electrode of the ESP system or were superimposed on dc voltage. HV impulses produce current impulses in the precipitation system which represent a transient, non-thermal plasma that is responsible for charging the airborne particles. During the course of this work, single stage and double stage precipitation reactors were designed, constructed and tested. It was found that the double stage reactor required less energy as compared with the single stage reactor to achieve a comparable precipitation efficacy. By using a suitable combination of energization parameters in each stage of the double stage reactor, the precipitation efficiency was maximised, while keeping the energy consumption at low levels.

Various powders and fumes have been used in the precipitation experiments to simulate airborne particles that could be found in an indoor environment. Two different methods were used for establishment of the precipitation efficiency for larger and smaller particles (powders and smokes): for larger particles, a direct weighting of the collected particles was used; in the case of finer airborne particles, a laser particle spectrometer was employed. For theoretical analysis and simulation of particle charging and particle dynamics in the precipitation reactor, the software package MATLAB was used to solve particle's equations of motion, which provided particle position and migration velocities in the ESP reactor; these parameters can be utilised to obtain the precipitation efficiency of the developed ESP reactors.

The topologies of the ESP reactors and advanced energization methods proposed and developed in the current work could be of utmost importance for improving the efficiency of removal of fine and ultra-fine airborne particles, while keeping the energy consumption of these continuously operating systems at very low levels. The proposed ESP precipitation methods could potentially improve the living conditions at homes or in work areas, and would be of particular importance to vulnerable population groups like asthma sufferers, and the very young and very old. A brief outline of the content of each chapter of this thesis is provided below.

Chapter 2 provides a comprehensive literature review, which discusses the phenomenon of airborne PM and their prevalence in the earth's atmosphere. This chapter also discusses and characterizes different types of particles present in atmospheric air in urban and industrial environments. Current methods of removing natural and man-made particulate matter from air are explained. Specific emphasis is given to the ESP method, as this is the main focus of the thesis. A brief history of the ESP technology is presented. ESP operation conditions, energisation options, precipitator design, particle charging and collection mechanisms, re-entrainment problems, and means of cleaning of the collection electrodes of the ESP precipitators are discussed. Particular attention has been paid to corona discharge, which is the method used in ESP systems for charging of airborne particles. Empirical equations which are used to obtain the efficiency of the ESP systems have been presented, and methods of agglomerating PM to increase the precipitation efficiency have also been described.

Chapter 3 constitutes the first experimental chapter of this thesis, this chapter describes the design and development of a single stage precipitation reactor and a combined dc/impulsive enegisation system. This chapter also presents the obtained experimental results on analysis of steady-state and transient corona discharges in the single stage ESP reactor. Current-voltage curves were obtained and plotted and desirable energisation levels were identified. Precipitation experiments were conducted using a Blumlein impulse generator, producing 250 ns impulses which were superimposed on dc voltage. Precipitation tests using different energisation regimes: dc only; impulsive only; and a combined dc/impulsive regime; were conducted using coarse and fine power particles (baking flour and dolomite respectively) and the efficiency of precipitation for each of these energization regimes was obtained. Positive polarity of energization was selected and used in the precipitation tests conducted in this chapter and in all precipitation tests described in this thesis.

Chapter 4 presents the next step taken in the development of an advanced precipitation system. Based on literature data on industrial scale electrostatic precipitators, the single stage reactor was expanded to a double stage ESP system. Thus, the two main mechanisms of the electrostatic precipitation process, particle charging and particle removal from air flow, are separated, which improves the efficiency of the whole ESP system. In this double stage ESP system, the particle charging takes place in the first stage where corona discharges are produced by an intensive impulsive electric field, while the lower dc field of the second stage provides particle drift and precipitation on the collection electrode(s). Precipitation tests were conducted with ambient laboratory air, while for heavier loading of air, cigarette smoke was used. Mathematical analysis of particle dynamics was conducted, and an analytical expression for the electric field between the electrodes in the presence of space charge was obtained. Using this space-charge limited electric field, the charge acquired by the particles as a function of time was also derived. This mathematical analysis is used for prediction of the precipitation of particles with different dimensions and different electrical characteristics (permittivity and electrical conductivity). Only conduction and polarisation charging processes were used in this analysis, diffusion charging was not taken into account; thus, a worst case charging scenario was established, as any charge acquired by diffusion would only increase the total charge. Investigations taking into account diffusion charge have been conducted recently, further information could be found at (Zhang et al., 2011, Liu et al., 2013, Liu et al., 2014).

Chapter 5 presents development of a scaled up 2-stage ESP system. This electrostatic precipitation system was used for analysis of the efficiency of 2-stage impulsively energized reactors which can be used in larger scale practical indoor air-cleaning operations. The obtained results demonstrate that high precipitation efficiency can be obtained using the developed ESP system. Empirical equations were also used to provide particle migration velocities inside the ESP by utilising the experimental precipitation efficiency data. Particles used in the precipitation tests described in this chapter were particles which were present in the ambient laboratory air at the time of the precipitation tests. For analysis of the precipitation efficiency in the case of higher concentrations of PM in air, beeswax candle fumes were injected into the ESP system. Using different numbers of candles, different particle loading levels were achieved in the ESP tests. An analytical model was used to obtain the particle's dynamics in the larger scale precipitation system. Ozone concentration in the exhaust air was measured, and the use of additional MnO_2 filter helped to reduce O_3 concentration to the natural background level.

Chapter 6 provides a summary of the conducted work, in addition to possible directions and ideas for future work. This chapter emphasises that it is established that the micro electrostatic precipitation technology (µ-ESP) developed in this thesis provides low footprint, low energy consumption and high precipitation efficiency for various types of airborne particles, and can be successfully used as an alternative method together with traditional dc or ac energised ESP systems.

Chapter 7 contains the references used in order to support this work, while Chapter 8 contains references of the 3 journal papers which are based on the work conducted for this thesis and published in the IEEE Transactions on Plasma Science. In addition, it contains references for conference publications and presentations also based on work presented in this thesis. Appendix A contains additional information on fabric filter materials used in air filtration systems and ways they can be cleaned, in case it is of interest to the reader. Appendix B and Appendix C present briefly the human respiratory system, discuss the health and environmental problems attributed to airborne PM, and describe the steps taken by governments worldwide to mitigate these effects. Agglomeration of PM is discussed in Appendix D, together with the recent advances in this area. Appendix E contains a step-by-step methodology for experimenting with fine PM, as this proved to be the most challenging aspect of this study, for anyone wishing to reproduce the results, while Appendix F contains software code developed and used in the thesis.

2. LITERATURE REVIEW

2.1. PARTICULATE MATTER

2.1.1. SOURCES OF PARTICULATE MATTER

Airborne particles are present in the atmosphere at all times. Their origin can be traced to various phenomena both natural and man-made (also called anthropogenic sources) (Lohmann and Mensah, 2013, White, 1963). Due to the plethora of sources, it comes as no surprise that they are present in the atmosphere in a wide range of sizes and distributions. Airborne particles can be liquid or solid. Liquid particles have the macroscopic form of mist, fog or spray (Hinds, 1982), and they are typically spherical in shape, while solid particles can be of various shapes, depending not only on their composition, but also on their source.

Natural sources of particulate matter include volcanoes, sea salt, wildfires, eroded soil particles, polymerized particles (from terpene vapors) emitted from trees, as well as various naturally made gases converted to particles. Volcano output and soil particles are fairly large particles that usually do not travel far from their sources (depending on wind), however particles produced by fires and particles converted from gases can be in the sub-micrometer range and thus they can stay airborne for a long period of time (Hinds, 1982).

Anthropogenic sources of particulate matter are various. From direct emissions, the most important are different industrial processes, power stations, road transport, residential sources (like wood burning for domestic heating) and shipping (Karvosenoja et al., 2008), (EPA, 2004), (Laxen et al., 2010). Others (non-directly emitted) include particles produced by conversion of man-made gases (SO_2 converted to SO_3 and NO_x converted to nitrate (Hinds, 1982)) and other photochemical reactions.

Comparison between natural and anthropogenic particulate production is difficult, as it includes large uncertainties and also depends on the particular location. While it seems that on a global scale anthropogenic sources contribute less to airborne particulate matter compared to particles produce by natural sources, according to (Hinds, 1982), (SMIC, 1971), man-made sources are highly concentrated in urban and industrialized areas, while particles from natural sources are produced in large areas (i.e. sand blown from deserts, salt particles in areas close to the seashore, etc.). Thus, in areas of high human activity, it is likely that the number of anthropogenic airborne particles exceeds that of particles of natural origin, which are more detrimental to human health, as explained in Appendix B. In terms of particular source, the majority of particles come from gases that reacted in the atmosphere and produced low volatility compounds that condensed, thus forming particles. The source of these gases can be natural or man-made. The formed particles are called secondary particles, as they were originally released as gases in the atmosphere. The most important examples of gases that can be the seed of secondary particle generation are NO_x, SO_2, NH_3 and Volatile organic compounds (VOCs) (Laxen et al., 2010). The rest of the particles are called primary particles, as they are released directly into the air (Hinds, 1982). VOCs can be defined as organic molecules, either man-made or naturally found, that can perform photochemical reaction with nitrogen oxides (under sunlight), and produce oxidants, one of the most important among them being ozone (European Parliament and Council of the European Union, 2008), (Ayres, 2009).

In terms of atmospheric distribution of airborne particulate matter (aerosol), the largest fractions are found in the first few km from the ground. For heights above ~5 km, there is little influence from surface emissions. In terms of horizontal distribution, it is strongly dependent upon the proximity from particulate sources and the weather conditions (Hinds, 1982). However, because secondary particles have the characteristic of being created very slowly, they are well dispersed from their production spots, having fewer concentration differences in urban and rural environments, and even crossing international borders, making it difficult to pinpoint their source (Laxen et al., 2010).

2.1.2. TYPES OF PARTICLES

Particles are named based on the type of suspended particle, and the suspended medium present, as shown in Table 2-1:

Table 2-1: Definitions of particulate suspensions (Hinds, 1982).

Medium\suspended PM	Gas	Liquid	Solid
Gas	-	Fog, mist, spray	Fume, dust
Liquid	Foam	Emulsion	Suspension, slurry
Solid	Sponge	Gel	Alloy

Dusts are tiny fragments of solid materials, such as minerals and rocks, which are generated due to wind erosion or fracturing by any means. Because of the way they are created, they tend to be irregularly shaped and have a wide size range, containing a substantial amount of larger particles. In practice, however, they tend to be from 1 µm up to 200 µm, with the larger particles settling too fast in calm atmospheres to be found in appreciable quantities. As in any case in which fine particles are produced by a starting mass, their size distribution is log-normal, as described by (Kolmogorov, 1941) (White, 1963). Examples of dusts are, among others, pulverized rocks (due to wind erosion or mechanical means), flour, icing sugar, cocoa and even fly ash. Fly ash particles usually form cenospheres (hollow spheres, Figure 2-1) which tend to harbour inside them or attach on their surfaces other smaller particles, frequently containing heavy metals (Kabata-Pendias, 2011, Llorens et al., 2001) due to the pulverized coal production process (White, 1963), (Ondov and Wexler, 1998). As a special subcategory, fibers could be included, in which case their length exceeds their other dimensions by a wide margin (Crown, 2011), like asbestos fibers. A more strict definition of a fiber is “any particle longer than 5 µm with an aspect ratio of 3 to 1” (Hinds, 1982). Fibers, when inhaled, have detrimental health effects, as discussed in Appendix B.

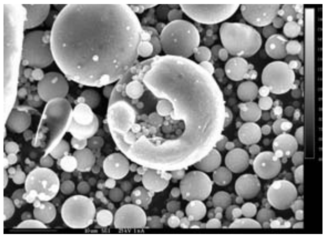

Figure 2-1: Fly ash cenospheres (Resources, 2014).

Fumes are generally formed by combustion at high temperatures and subsequent condensation (Crown, 2011), among other processes. Fume particles tend to be of very small, sub-micrometer, sizes of 0.1 µm up to 1 µm. One of their major production sources are smelter facilities, with the metallic fumes produced having extremely elongated shapes, like needles, stars or plates, while they may even coagulate to form particle chains. An example is lead oxide fumes produced by the oxidation of lead vapors (White, 1963) and also solder, welding and rubber fumes (Crown, 2011).

Fog (also known as mist if visibility is hindered to a lesser extend) is produced by condensing liquid vapors, thus creating a suspension of droplets, and by atomization of liquids (e.g. by ultrasounds (Rajan and Pandit, 2001)). They tend to be in the wide size range of 5 µm up to 100 µm, however there could be even in the sub-micrometer range (as in the case of sulphuric acid particulates). Their shape is spherical and they also have the physical characteristic of reducing visibility when suspended in the atmosphere (White, 1963). Examples are the most important aerosol on earth, water clouds (Hinds, 1982) and also paint sprays (Crown, 2011).

Smoke consists of airborne particles that are neither dusts nor mists (White, 1963), usually derived from incomplete combustion (Hinds, 1982). Their source could be, among others, volatilization and various chemical and photochemical reactions. The particles produced are extremely small, in the range of 0.01 µm up to 1 µm, meaning very high settling time and exhibiting strong Brownian motion. Their shape varies depending on the state in which they are found. For example, tobacco smoke contains a lot of liquid and tarry droplets of spherical shape, while soot or carbon black are found in irregular solid state. Another important example is the conversion of SO_2 to SO_3 by photochemical means (White, 1963).

Smog is the combination in the atmosphere of smoke and fog. It exists as naturally produced suspended liquid droplets (mists) and anthropogenic smoke from industrial or domestic applications are mixed (White, 1963). A natural type of smog can be found by the photochemical reaction of terpene vapor produced by trees (Hinds, 1982).

Finally, especially important if one considers health implications, are viable particles. These include a wide range of organisms, from nanoscale viruses, to sub-micrometer bacteria and algae, up to 10s of µm pollen particles. Their concentrations fluctuate widely, depending on the time of year (as blooming season exhibits a huge increase in the concentration of pollen) and the particular location (urban, rural) among other factors. Viruses are normally 120 nm long, while the largest of the species, prehistoric viruses from Siberian permafrost, can be as big as 600 nm long (Legendre et al., 2014), however still in the sub-µm range. Bacteria can also be in this size range, with many types being classified in the PM2.5 and PM10 ranges. Table 2-2 summarises the size and concentration of viable PM that could be present in an indoor environment, while Figure 2-2 defines the size range in which a great number of particles are usually found.

Table 2-2: Viable PM size and concentrations (Hinds, 1982).

Particle Type	Size (µm)	Concentration (counts/m^3)
Viruses	0.015-0.45	-
Bacteria	0.3-15	0.5-100
Fungi	3-100	100-10,000
Algae	0.5	10-1,000
Spores	6-60	0-100,000
Pollen	10-100	0-1,000

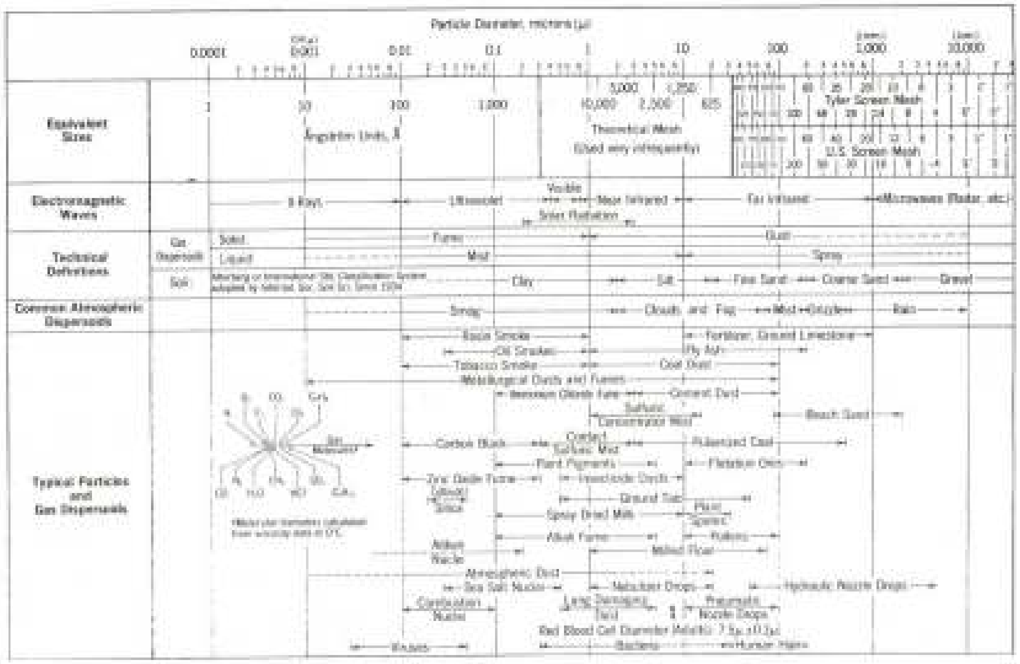

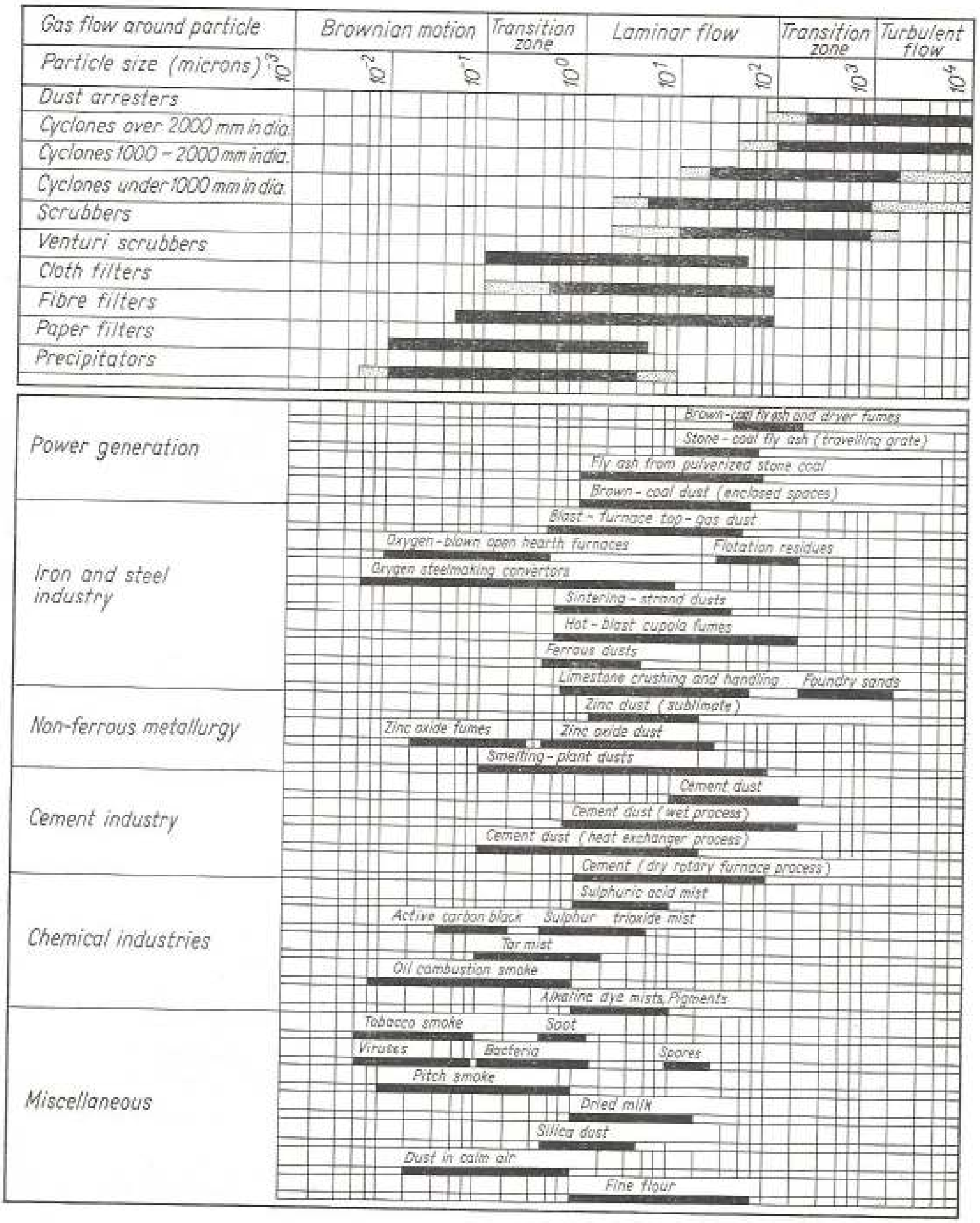

Figure 2-2: Size range of a wide range of PM. Top, (Hinds, 1982); bottom, (Böhm, 1982).

2.2. CATEGORISATION OF PM

2.2.1. CATEGORIES OF PARTICLES BASED ON THEIR AERODYNAMIC DIAMETER

It was made clear in the previous subchapter that it is difficult, if not impossible, to categorise airborne particles in terms of their chemical content (White, 1963). Not only are particles mixed by the effects of wind and Brownian motion, but they also can form agglomerates with one another despite the fact that they are from different sources and have different chemical composition. Thus, the properties that are of the greatest importance are the particle size and settling time (White, 1963). This is because even the physical laws that govern the particles behavior are different depending on the particle size (Hinds, 1982). When the main concern is the health and safety, however, then the source and chemical composition of the particulates are important (Laxen et al., 2010),(Grahame and Schlesinger, 2007, Grahame and Schlesinger, 2010, Beelen et al., 2008, Brunekreef et al., 2009).

Particles of the same diameter share the same aerodynamic characteristics and thus exhibit similar aerodynamic behavior. However, since solid particles come in a variety of shapes, there exists many ways of trying to categorize them. Thus the concept of the equivalent diameter is defined, which implies that a particular irregular particle shares the physical characteristics of a spherical particle with the same diameter (Hinds, 1982). There can be two ways of defining the equivalent diameter, one based on the geometrical properties of the particle and the other having to do with its physical properties. Examples of equivalent diameters based on geometrical properties is if the diameter of a sphere is calculated having equal surface or volume as a non-spherical particle (White, 1963). An example of an equivalent diameter based on physical properties of the particles is the Stokes' diameter (2.1) in which an equivalent diameter is based on the settling rate and density of the irregular particle within a fluid, according to the Stokes law (White, 1963).

$$\boldsymbol{d} = \sqrt{\frac{\mathbf{18}\cdot \boldsymbol{v}\cdot \boldsymbol{\eta}}{(\boldsymbol{\rho_p}-\boldsymbol{\rho_f})\cdot \boldsymbol{g}}} \tag{2.1}$$

where *d* is the Stokes' diameter, *v* is the particle's terminal velocity, η is the fluids' viscosity, ρ_p and ρ_f are the particle's and the fluids densities respectively, and *g* is the gravitational acceleration.

A subcategory important for definitions to be discussed later is the aerodynamic diameter, which is similar to the Stoke's diameter, with the difference of defining the sphere density as $\rho_p = 1\ \mathrm{g/cm^3}$. Of great importance in air-cleaning applications are the Stokes and aerodynamic diameters. They are extremely helpful for ESP design as the particulate matters' aerodynamic behavior inside reactors is of interest, in order to facilitate collection (White, 1963). An example showing how different the various diameters could be is shown in Figure 2-3 below:

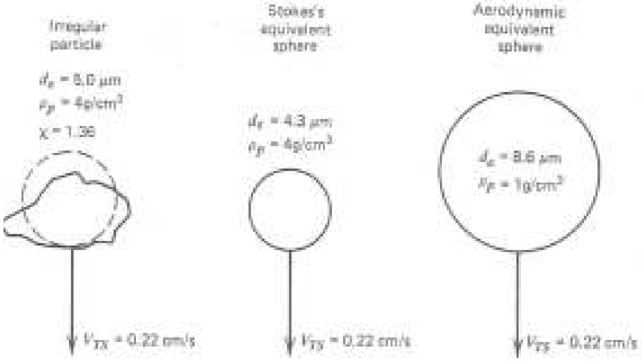

Figure 2-3: Stokes' and Aerodynamic equivalent diameter of an irregularly shaped particle (Hinds, 1982).

According to the 2008/50/EC Directive on ambient air quality and cleaner air for Europe (CAFE Directive), Article 2 (Definitions) clauses 18 & 19, PM10 and PM2.5 are defined as particulate matter that passes through a size selective inlet (as described in BS EN 12341 and BS EN 14907 respectively) with a 50% efficiency cut off at 10 µm and 2.5 µm aerodynamic diameter respectively (European Parliament and Council of the European Union, 2008). PM2.5 are called fine particles, while those between PM2.5 and PM10 are called coarse particles (PM2.5-10 or PMcoarse (Laxen et al., 2010)). PM0.1 or particulate matter less than 100 nm is called ultrafine particles (Laxen et al., 2010). This is because in the size separation process some particles with larges aerodynamic diameter might pass through while others with smaller diameter might not be collected. Thus the median aerodynamic diameter of the particles that manage to pass through defines their size, meaning that PM2.5 is defined as these particles that manage to pass through the 2.5 μm size selective inlet at 50% efficiency.

2.2.2. CHARACTERISTICS OF PM

Small sized airborne PM has extremely complex physical characteristics compared to ordinary matter (larger size particles). When collected in large quantities (for example from the hoppers of an industrial electrostatic precipitator) they exhibit characteristics of both gases, in that they are compressible, and liquids, in that waves can propagate through them and they can be pumped (White, 1963), (Martin, 1928). Another important characteristic is that they can absorb electrical charges on their surfaces, which is augmented by the fact that they inherently have large specific surface areas, e.g. fine carbon black can have a specific surface area of 100 m^2/g (White, 1963). The electrostatic precipitation technology owes its success exactly to this exhibited behavior. There are, of course, associated drawbacks, as such large surface areas can lead to accelerated chemical reactions leading to dust ignitions even with 'innocent' dusts like flour, sugar and cocoa, provided an adequate concentration is present (White, 1963). Also in terms of density, while dusts and mists have the same density as their parent material, smokes, fumes and most notably fly ash might have much lower density compared to their chemical composition. This is because of their highly sparse structure, which tends to be highly agglomerated (Hinds, 1982). A prime example is the hollow sphere structure of fly ash, shown in Figure 2-4.

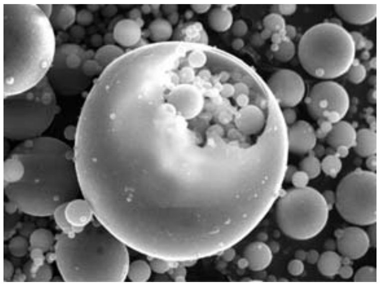

Figure 2-4: Electronic microscope picture of fly ash particles (Resources, 2014).

When suspended in the air, and depending upon their diameter, particulate matter can have very distinct characteristics. Usually three modes are recognized (Whitby, 1978), each one having its own way of creation, chemical composition, settling time and corresponding maximum travel distance. The first is the nucleation mode, which consists of newly created particles usually by combustion or atmospheric photochemical reactions. Sometimes this range is sub-divided into the nucleation (few nm) and the Aitken mode, up to 50 nm (Stier et al., 2005) or up to 100 nm (Lohmann and Mensah, 2013, Seinfeld and Pandis, 1998). Particles in this mode exhibit strong Brownian motion and tend to grow fast by coagulation and vapor condensation, having lifetimes of the order of seconds to hours (Laxen et al., 2010), thus forming larger particles. While their numbers are large, they constitute a small proportion of the overall suspended PM mass (Laxen et al., 2010). Since their atmospheric lifetime is so short, they can travel up to some tens of km from their creation sites (Laxen et al., 2010). Once ~0.1 µm diameter is reached, deposition to surfaces by diffusion becomes negligible (Hinds, 1982) and the particles enter the accumulation mode. In this mode, they agglomerate slowly and are also too small for rapid gravitational settling until they reach (1-3) µm, depending upon humidity (Laxen et al., 2010), when deposition by impaction and sedimentation become more prevalent. They typically reside in the atmosphere from a week up to a month, although weather conditions, like rain or snow, could shorted their lifetimes considerably (Laxen et al., 2010). Since they stay airborne for so long, they can travel worldwide distances (1000s of km depending upon weather conditions) before they settle. Particles created from gases tend to be found in this mode too (Laxen et al., 2010). The coarse particle mode is composed of particles which are generated by mechanical means, like re-suspension of dust by wind or even road traffic, or the production of salt particulates by sea waves. Coarse particles tend to stay less in the atmosphere compared to smaller ones, and they are easily carried away (or removed from the atmosphere) by rainfall and snow drops, a process called washout (Hinds, 1982). As an example, particles larger than 20 µm in diameter tend to stay in the atmosphere in a timeframe of hours (Hinds, 1982), thus not travelling more than a few tens of km at best. An exception is during sandstorms when such particles could travel thousands of km (NASA, 2012, Stier et al., 2005). A typical pattern is shown in Figure 2-5. Particles in the coarse mode represent a large proportion of the PM mass distribution. The whole process is summarised in Figure 2-6.

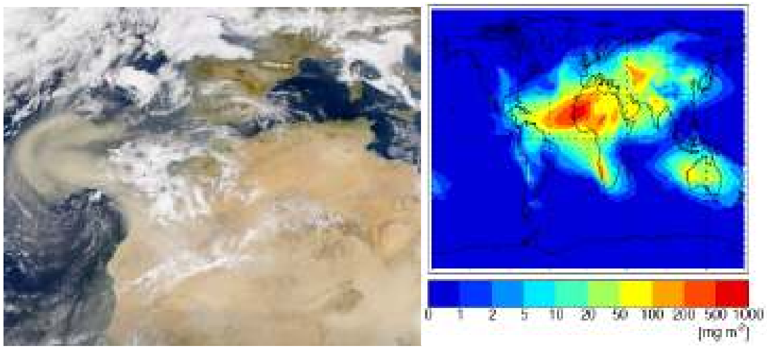

Figure 2-5: Dust migration due to sandstorms, on the left satellite picture (NASA, 2012), on the right quantified data from (Stier et al., 2005).

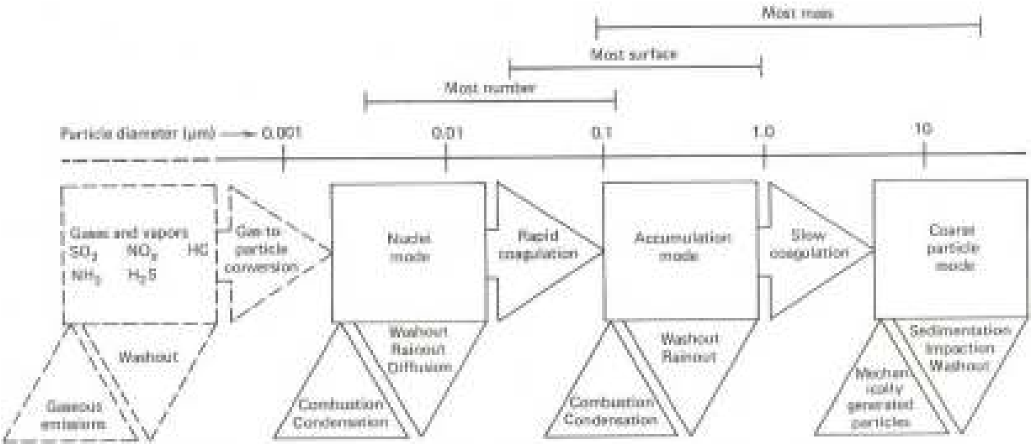

Figure 2-6: Atmospheric PM, its sources and sinks and agglomeration process (Hinds, 1982).

2.2.3. CHEMICAL COMPOSITION OF PM

The different origin of particles can also be identified by their different chemical composition. Fine particles tend to have more carbon (C), sulphur (S) and lead (Pb) which identifies them as having combustion origin, while the larger particles tend to have more aluminium (Al), silica (Si), calcium (Ca), and iron (Fe), which are elements predominately found in the soil (Hinds, 1982), and also salt (NaCl), especially in areas close to the sea (Laxen et al., 2010). In terms of C, fine particles have both elemental carbon (from diesel automobiles) and organic carbon (from oxidized VOCs or industrial applications) (Laxen et al., 2010). PM2.5 can harbor trace metals like Pb, cadmium (Cd), mercury (Hg), nickel (Ni), chromium (Cr), zinc (Zn) and manganese (Mn) derived from metallurgical processes or fuel combustion, because of the trace amounts of these elements found in fossil fuels (Biswas and Wu, 1998) (Laxen et al., 2010). The main sources of these PM2.5 with high metallic content are high temperature combustion sources like oil- and coal-fired power plants, cement kilns, motor vehicles, smelters and incinerators, among others (Ondov and Wexler, 1998). Organic compounds usually account for a significant part of the total particle mass and they are usually in the form of a great many different molecules (Laxen et al., 2010). Some of the most noxious substances found are aromatic hydrocarbons (part of the chemicals called VOCs). This, together with the heavy metals to be found, not only makes PM2.5 of great concern compared to the coarser fraction, but also constitutes the particulate source of great importance in terms of toxicity.

2.3. REMOVAL METHODS OF PARTICULATE MATTER

As it has been explained, particulate matter, depending on its size, has a variable resident time in the atmosphere. While for larger particles sedimentation, inertial impaction and electrostatic attraction are major methods of removal, for smaller particles, coagulation and diffusion play a major role. To these ends, various ways for PM removal have been developed, which take advantage of the particular PM behavior. Prior to discussion of extraction methods, it would be interesting to observe how these particles are removed from the air naturally, as these processes were also a source of inspiration for engineered solutions.

2.3.1. NATURAL WAYS OF REMOVAL OF AIRBORNE PARTICLES

Trees have the ability to remove particles from the contaminated air passing around them, (Beckett et al., 1998) and even to remove fog (Hori, 1953). This is because trees have a very large ratio of leaf area compared to the area covered by each individual tree, acting as natural filters (Beckett et al., 1998). Apart from direct impaction and electrostatic attraction, the inertia of large particles prevents them from following the air flow passing around leaves, forcing them to settle on them (Hinds, 1982). Smaller particles, on the other hand, can be deposited on leaves due to their vivid Brownian motion (Räsänen et al., 2012). Additionally, they can diffuse quickly towards areas of less concentration, thus they are attracted inside the leaves substomatal cavity (Thompson et al., 1984). To quantify this natural ability of trees in terms of air cleaning capability, it is estimated that 9.2 million US dollars are annually saved from the City of Chicago itself due to the urban trees present (McPherson et al., 1994). Reduction in particulate matter was also found in indoor spaces in the presence of plants (Lohr and Pearson-mims, 1996), however indoor plants also contribute to increased humidity, which is mostly unwelcome in terms of health effects (National Research Council, 2004). Trees were also shown to help in reducing SO_2, NO_2, CO, and even O_3 from the atmosphere (Nowak et al., 2006).

The major method of removal of airborne particles from the troposphere is by far precipitation scavenging. Also named wet deposition or washout, it involves weather conditions, like rain or snow, which carry away the particles from the air flow. It has been estimated that ~80% of the particulate matter (by mass) is removed by washout (Graedel and Franey, 1975, SMIC, 1971, Lohmann and Mensah, 2013). Dry deposition accounts for ~20% of the remaining particles, being the major sink for coarse PM (Lohmann and Mensah, 2013), as its main deposition mode is impaction and gravity settling. Apart from PM, rain and snow are also effective in removing gaseous pollutants (Vinther and Nielsen, 1984). In comparable terms, snow is 28-50 times more efficient than rain droplets of the same mass because of the far greater ratio of surface area of ice crystals compared to their volume (Radke et al., 1980). There is, however, a minimum observed in wet deposition efficiency for particles between (0.1-1) µm, which is often referred to as the Greenfield gap. This is due to the low collision efficiency of such particles with the snowflakes / rain droplets. In contrast, larger particles collide easily due to their larger inertia, while smaller particles have an increased Brownian motion which maximizes their chances of collision (Tinsley et al., 2000). To quantify, it is virtually impossible for a 5 µm particle to avoid collision with an incoming raindrop, while for particles in the Greenfield gap, ~0.5 µm (Greenfield, 1957, Shaw, 1986), only 1 in ~10,000 manage to collide with the drop (Lohmann and Mensah, 2013). There is a special case of in-cloud scavenging in which particles form the nucleus of droplets, or get attached to raindrops or ice flakes, and precipitate to earth (Vinther and Nielsen, 1984). This is the major removal mechanism for aerosols in the Greenfield gap range (Lohmann and Mensah, 2013).

Charged particles can also deposit electrostatically upon surfaces. The acquisition of charge can be, in the case of dusts, due to the weathering of solid materials. This can be explained by the frictional charging phenomenon, namely as particles lying close together on a single surface might have a contact potential difference, when the particles get removed from the surface due to erosion, they might retain this charge, making it easier for them to adhere on surfaces electrostatically (White, 1963).

2.3.2. INDUSTRIAL METHODS OF REMOVAL OF AIRBORNE PARTICLES

Based on the natural phenomena described in Section 2.3.1, various industrial methods of air cleaning have been developed. Depending upon their size and other characteristics, various methods are being utilized to remove particles, electrostatic precipitation being the most widely used for PM2.5.

Settling chambers are based on gravitational settling, these reactors are simple to construct, however are of very low efficiency, particularly for PM2.5. This is because the particles are left to settle by themselves, meaning it is effective for very large particles, > 100 µm (Vesilind et al., 1988), and depending upon the resident time and the internal turbulence, on some coarse fraction of the PM. The major advantage is that they require no power.

Cyclones are similar to settling chambers, though conical in design. The particle laden air is inserted tangential to the conical chamber, allowing the centrifugal force to act on the particles and detach them from the air flow, as shown in Figure 2-7. Cyclones are based on inertial impaction, meaning that coarse particles cannot follow the stream lines of air as it moves around the cone, and are thus ejected to the container walls. This, of course, is efficient for the larger fraction of particles (coarse) and is not used for PM2.5. It is, however, implemented as a first stage, before further treatment of the particle laden gas. Its operation is, like the settling chamber, extremely economical.

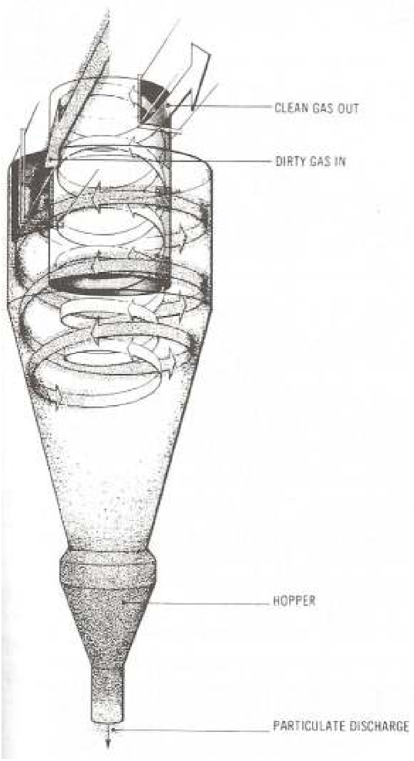

Figure 2-7: Cyclone design (Vesilind et al., 1988).

Bag filters base their operation in the same principle as the vacuum cleaner found nowadays in most homes. The particle laden air passes through a fabric bag having very small aperture holes, and at first, the largest particles get intercepted. Then as more of these coarse particles get attached, more and more of the fabric pores get blocked, and smaller particles manage to get collected too, thus increasing collection efficiency with time. However, in the meantime the air speed through the remaining holes increases substantially and there will be a point at which the free pores will be too few and the air speed so high that the filter would have reached its maximum efficiency. This method is particularly effective against PM2.5, however it introduces a large pressure drop, especially in the later stages of operation (or as the bag gets full of particles).

The accumulation of a filter cake plays a major role in increasing the efficiency of the bag filter; however it does so by considerably impeding the flow of the gas. This leads to a pressure drop and thus to increased energy requirements. Bag filters are classified by the way in which they are cleaned, which is a direct link to the bag material used. Further information on the cleaning processes and the bag materials can be found in Appendix A.

In terms of efficiency of removal of particles from air, there is no set of equations that can calculate such efficiency, and more importantly, unlike the other gas cleaning methods, the efficiency is always changing. This is dependent upon the cleaning cycle. As the fabric is cleaned, the efficiency is reduced until the collected PM cake thickens again, which increases efficiency. This process is repeated with the cleaning cycles. In terms of particle numbers, overall efficiency higher than 99% can be achieved, provided they are operated appropriately, are designed for the specific dust, and are well maintained. As can be inferred from above, fabric filters have a constant outlet concentration, not a constant efficiency.

Fabric filters have been shown to be readily adaptable for various gas cleaning applications, as there is a plethora of different fabric materials, types and cleaning methods. However, they have major drawbacks too, compared to the other cleaning methods. First of all are the properties of the dusts that are targeted for collection. While the variety of materials gives many choices, bag filters are not recommended for flammable or explosive dusts. Furthermore, they are not recommended for sticky particles, like oil fumes, as it will be very difficult, if not impossible, to remove the collected cake from them. Humid gas flows can also be problematic, as the operating temperature would need to be above the dew point to avoid the condensation of vapors. Another negative characteristic is high temperatures. While there are special fibers that can withstand hundreds of °C (Nextel fibers withstand 500°C), there are very expensive, and thus other methods are preferred for cleaning very high temperature gas streams (above 260°C there is a very limited selection of proper materials) (McKenna et al., 2008).

In terms of energy demands, most energy is spent on fans and the rest on the cleaning process and for possible air compression, as explained in Appendix A.

The actual process of filtration, as it had been discussed above, allows only one out of 1,000 – 10,000 particles to escape. Interestingly enough, it is not only the smallest fraction of PM that escapes, but the change from the inlet size distribution changes only slightly at the outlet. This is because of the filtration process occurring in bag filters. To explain further, as the first particles impact on the filter, they can become attached to the fibers at the edges of the filter pores, due to electrostatic forces. As more and more particles arrive, they tend to attach and form chains that inevitably block some of the pores. However, as this phenomenon continues, the few pores that remain unblocked receive the bulk of the air flow, thus the air speed in them is increased to great proportions. Therefore, the particles that enter these pores have adhesive forces lesser than the aerodynamic flow that pushes them away, and thus they manage to pass through the cake and the bag filter. It has been suggested that, in order for a pore to be bridged, the length needs to be less than the equivalent of 10 particle diameters. Being longer than that will force the chain to break due to aerodynamic forces (Billing and Wilde, 1970). This explains both the rising efficiency - pores gets blocked and the cake gets thicker - and the fact that the outlet PM distribution is, to a great extent similar to the inlet distribution, as not only fine but also larger particles manage to pass through.

Wet collectors are based on the washout principle, which is very effective in cleaning most PM, however is not ideal for the PM2.5 fraction, for the reasons explained in Section 2.3.1. Wet collectors have also the great disadvantage of producing a slurry residual, instead of solid as in the other mechanisms, meaning further processing might be needed before the sludge water is released into the environment and effectively transforming a problem of air-pollution to water-pollution (McKenna et al., 2008). Wet Scrubbers are ideal in the collection of mists, and also flammable PM. They can also remove gaseous pollutants, e.g. SO_2 (Srivastava et al., 2001) from the air flow and, because of the way they work, they can cool the gas stream inserted in them. However, they have the drawback of being susceptible to corrosion due to the wet environment they are constantly subject to, and also because the slurry they produce is a source of water pollution (McKenna et al., 2008).

Wet collectors' main particle removal mechanism is inertial impaction on the liquid droplets for large particles, while for smaller, ultrafine ones, is diffusion and Brownian motion. A particle moving across the fluid flow lines of a gas stream can be subjected to 2 forces when closing on an obstacle. The first is the fluid drag that tries to move the particle in the same direction as the fluid flow lines, and the other is the particle inertia, that resists any change of its speed. If inertia dominates, as in the case of larger particles, the particle will deviate from the fluid flow lines and impaction will occur. If not, the particle will bypass the obstacle, or in the wet collectors' case, the droplet. To put it into context, inertial impaction is significant for particles larger than 10 μm, because of their greater mass. For ultrafine particles, their very lively Brownian motion and strong diffusion play a major role in the collection of the particles by the droplets. Gravitational settling of the particles plays only a minor role, since the residence time of particles in the scrubber is particularly low and the velocities achieved inside it can be particularly high. This leads to a minimum collection mechanism for the scrubber design for particles of ~0.1 μm in diameter. Direct interception, of course, plays a role for all particle sizes.

The main principle of the wet scrubber, independently of the particular design, is the insertion of water, or other liquid, droplets into the gas stream, so as to promote mixing and contact of PM and the droplets. There are differentiations to this rule, as in some cases the gas stream is forced to impact liquid surfaces so as to impinge its particles there, or forced through a water layer at elevated velocities which produces jet streams, or in a recent development, water steam is used in supersaturated conditions, which promote condensation of the excess water on the PM, in a similar manner to how atmospheric clouds are formed. The basic design of a wet scrubber is shown in Figure 2-8.

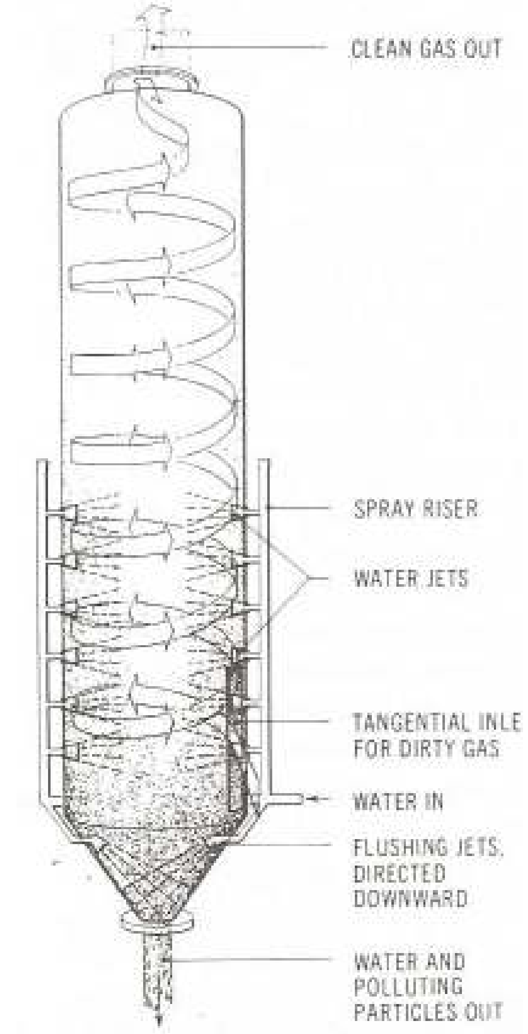

Figure 2-8: Wet scrubber design (Vesilind et al., 1988).

In terms of collection efficiencies, these can be variable, depending upon the design. Usually collection efficiency can be high for particles down to 1 µm in diameter, and for gases and small ultrafine PM, however wet scrubbers are not effective for fine PM. Exceptions to the above are scrubbers based on condensation or on charging of PM and / or droplets, which have higher efficiency for fine PM, approaching that of ESPs. Efficiency by itself is a function of the inlet PM size distribution, PM concentration and energy spent. As this method relies heavily on inertial impaction for large particles, it is imperative that the relative speed between particles and water droplets should be increased. This, however, leads to an increase of the velocity of the air flow, which in turn results in a pressure drop, leading to increased energy consumption and running costs for the scrubber. Also, since the average time that particles spend in the scrubber chamber is very short (of the order of a few seconds), it is expectable to have low efficiency for the particles less than 1 µm in diameter, as their Brownian motion is much more limited compared to the ultrafine fraction of the particles. As far as the efficiency is concerned, it has been proven that it is directly proportional to the inlet particulate concentration (Lerner, 1995), while the particulate concentration of the outlet is a constant, i.e. it is independent of the inlet dust concentration.

Wet scrubbers can be used in a wide variety of industrial processes, with the only exception being very large plants, as the flow rate should not exceed 250,000 acfm (425,000 $m^3/h \approx 7080 m^3/min$). They can be used in a variety of roles, like to collect gases, PM, or both. They are ideal for mist capture and also in collecting explosive or sticky PM. The major drawbacks are that they have low collection efficiency for PM2.5 and that the collected material is in liquid form. This means that they can be a source of water pollution, as trying to separate the water from the dry dust can be expensive; this fact makes them unsuitable if valuable dust should be reclaimed from the slurry. Corrosion is also a major concern, due to the continuous use of water.

A special case of wet scrubber that can have high efficiency on the fine PM fraction is the Venturi or gas-atomized spray, Figure 2-9. Its differentiation from mainstream scrubbers is that there is a narrowing on the design of the duct. This causes the particle laden air flow to accelerate at the narrowing before expanding after leaving it, with turbulence increasing too. At the same time, the scrubbing liquid is injected into the air flow just before it enters the narrowing venture throat. This acceleration atomizes the droplets while the turbulence enhances the liquid-particle contact, both effects increasing the collection efficiency significantly.

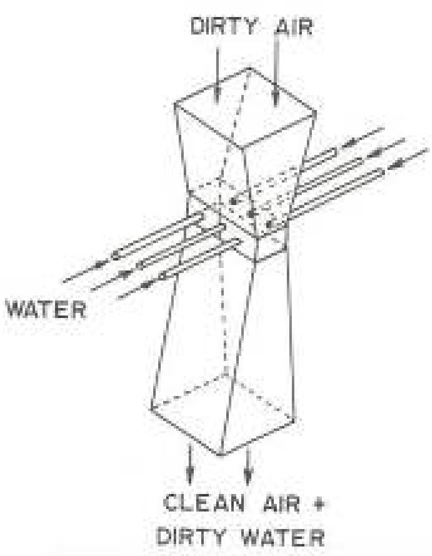

Figure 2-9: Venturi scrubber (Vesilind et al., 1988).

Overall, Venturi scrubbers have simple designs, requiring low maintenance and being easily installed. Their efficiency is a function of the air flow rate that can be achieved in the narrowing section of the chamber. They are one of the few types of scrubbers that manage to achieve high collection efficiency for small particles. However, they have the disadvantage that in order to increase efficiency, the pressure drop is increased too, which leads to a corresponding increased energy consumption.

2.4. ELECTROSTATIC PRECIPITATION

2.4.1. BRIEF HISTORY

Electrostatic attraction was known to the ancient Greeks very early in human history (Thomson, 1922), however it was not until the end of the 18th century that its forces were quantified and the inverse square law was discovered by Coulomb (Coulomb, 1785b)

(Coulomb, 1785a), even though it took a few decades of disputes before it was finally accepted (Heering, 1992).

While there are records on the interaction of electricity and smoke as early as the 17th (Gilbert, 1900) and 18th century (Beccaria, 1776), the first truly electrostatic precipitation tests were recorded in 1824, when Hohlfeld tried to clear mist using an electrified point (Hohlfeld, 1824). This test was repeated much later in a slightly different configuration and by using tobacco smoke instead (Guitard, 1850). These tests did not steer any particular interest in the scientific community at that time, however towards the end of the 19th century and with the rapid growth of the industrial sector, air pollution started to transform from a nuisance to a problem, and electrostatic precipitation was reinvented, this time to solve a problem, rather than out of scientific curiosity. First was Nahrwold, who noticed in a point-cylinder discharge experiment that there was an increased settling of atmospheric dust (Nahrwold, 1878). Walker and Huchings then tried to make the first commercial electrostatic precipitator, without success though, based on the work of Sir Oliver Lodge (Lodge, 1886). The reasons for their failure were the embryonic state of electrical science at that point, and the fact that the PM that they tried to precipitate, Pb fumes, is highly resistive and very small in size (White, 1963). Similar attempts were made in Germany (Möller, 1884), which was at that point a highly industrialized country too.

Pioneering practical work in the US was done by Cottrell (Cottrell, 1911), who had plenty of opportunities in the industrialized and rural California of the beginning of the 20th century. Cottrell used Tesla's recently developed ac energisation (Tesla, 1888) together with synchronous switch rectifiers that were available at that time, and observed that by utilising negative polarity voltage, better operational results were achieved (White, 1963), leading to some successful commercial installations. In 1912, one of Cottrell's former students at the University of California named W. A. Schmidt made 2 important discoveries that revolutionized the field. The first was the fine-wire corona electrode and the other the 2-stage precipitator (White, 1963) (Schmidt and Anderson, 1938). At the same time it was discovered that the resistivity of particles can be reduced by the use of SO_3 or even moisture (Howard, 1914). From then on there was an exponential increase in the applications used, the discoveries made, and the patents filed. Fractional electrostatic precipitation was used as early as 1913, while it took many years for the low ozone air cleaning precipitator to be successfully developed by Penney in 1935 (Penney, 1937). In terms of theoretical studies, the exponential efficiency law of an ESP was first discovered by

Anderson (Anderson, 1925) in 1919 and then derived theoretically by Deutsch in 1922 (Deutsch, 1922). In terms of theoretical work about charging, early attempts were made by Rohmann (Rohmann, 1923), before further attempts were made by M. Pauthenier and M. Moreau-Hanot (Pauthenier and Moreau-Hanot, 1932) and later by H J White (White, 1951). Furthermore, while even from the early work of Cottrell there seemed to be an advantage in impulsive electrostatic precipitation (White, 1963), it took many decades before the semiconductor industry made its wider application more reliable and affordable. Lastly, it took many decades for precipitator engineers to combine empirical data with theoretical analysis of the various phenomena and implement it into their studies of precipitator installations. This was because of the early scarcity of data, as well as the unpredictability of most results, as the corona discharge used is heavily dependent upon many parameters like temperature, humidity and gas flow loading, and by the fact that theory developed slowly (White, 1963). This then led to empirical approaches that neither advanced the field significantly nor provided their customers with adequate solutions. It was not until the 1950s that the combination of theory and practice started to occur (White, 1963), and continues today with the help of computer software programs (USEPA, 2013a).

Today's implementations of electrostatic precipitators span a wide range of applications, the most important being air-pollution mitigation, recovery of valuable dusts, high efficiency air cleaning for schools, offices, and hospitals. It is noteworthy from recent statistics (McKenna et al., 2008) that, in the US, 80% of installed ESPs are for air-cleaning applications in the electric utility industry (cleaning the exhaust fumes of pulverized coal combustion) while the remaining 20% are installed in pulp & paper, cement, steel, non-ferrous metals and other industries. While they can handle and clean the air flow for many different cases, once they are designed and operational, any change in the temperature or air flow condition will degrade the efficiency (McKenna et al., 2008).

2.4.2. PRINCIPLE OF OPERATION OF ELECTROSTATIC PRECIPITATORS

Electrostatic precipitation takes advantage of the fact that electrostatic forces are much greater compared to gravitational or inertial forces in order to separate the charged particles from the air flow (White, 1977). In the case of wet ESPs (to be discussed later), they also imitate the natural way of particle adhesion to a wet surface, which is usually water (McKenna et al., 2008). ESPs consists of an outside tank that fits the unit, HV sources (usually many), the energisation and collection electrodes in close proximity with one another, and the rapping systems together with hoppers at the bottom if it is a dry cleaning system, which is the most prevalent (McKenna et al., 2008).

In short, the particle laden air flow passes through a high field region, which also contains ionic carriers produced from corona discharge. This region is usually between a highly non-uniform arrangement of wires acting as high voltage electrodes, and earthed plates. As the particles are inside an electric field and in an area where charged carriers exist, they can be charged by both field and diffusion charging, and can then subsequently be deflected by the electric field towards the collection plates. The collection plates then get cleaned in a continuous or intermittent way, and the gas flow out of the unit is therefore cleaned, having to achieve specific legislation target levels. Thus, it is clear that ESP is the end result of several steps and different phenomena/procedures, in some cases happening at the same time, which will be explained in the subsections that follow.

2.4.2.1. Electric field

The electric field is of great importance in the electrostatic precipitation process, as it is the cause of a series of critical phenomena. First and foremost, this field is responsible for the generation of corona discharges in the vicinity of the high voltage electrode. To this end, the HV electrodes should be sharp or pointed, and the overall configuration (high voltage and collection electrodes) should be highly asymmetrical. This ensures that corona discharges are initiated at much lower voltages compared to more symmetrical topologies. Corona discharges are responsible for the production of ions that charge the PM. Secondly, since the ions produced are inside the electric field, Coulomb forces are exerted on them, and since their mobility is high, they will impact and attach to the PM. When the PM is charged, the electric field exerts a force on these charged particles, deflecting them and resulting in precipitation on the collecting electrode(s) of the precipitator.

The electric field created between the electrodes governs the effectiveness of an ESP (McKenna et al., 2008). The stronger the field is, the higher drift velocity acquired by the ions, the higher the saturation charge that the particles can achieve, and the stronger the force that drives the charged PM to the collection plates. The result is higher terminal velocities for the particles, which is an indicator of precipitation efficiency. However, this Laplacian field is also affected by the field due to the charged carriers produced by the corona, and of course by the space charge produced by the much more slowly moving charged PM (McKenna et al., 2008). The field is not uniform across the entire length of the precipitator, as the concentration of charged particles is obviously higher at the inlet, compared to the outlet of the ESP, and this concentration is time variable depending upon the particulate concentration in the gas stream. This makes any theoretical investigation of the precipitation phenomenon difficult to say the least justifying the length of time taken for development of a theoretical basis, as early investigators – at the beginning of the 20th century – did not have computers. However, it can be generalized that the more power delivered to the precipitator, the more efficient the precipitation efficiency is (McKenna et al., 2008).

As concluded from the proceeding discussion, the higher the electric field, the higher the precipitation efficiency. In practice, this is manifested in that ESPs are energised by such high voltages that are close to sparking voltage. Sparking is detrimental to the normal operation of an ESP, however it has been proven to be beneficial to have a high electric field with occasional sparking, e.g. once a minute (White, 1963), rather than to have slightly lower field and no sparking at all. After all, the parabolic waveform of the *I(V)* curve of a corona discharge clearly shows that a small increase in the applied voltage can greatly increase the corona current, and thus also increase the precipitation efficiency (White, 1963) and the power consumption. Thus, in practice, instead of operating at voltages well below the sparking voltage, it is desirable to find a regime where the occasional sparking does not adversely affect the efficiency obtained by the increased voltage (White, 1963). For this regime to be realized, mechanical alignment of the discharge-collection electrodes, despite the rapping process, is of great importance (McKenna et al., 2008).

It is also common practice for precipitators not to have just one section, but to have different sections that can be charged with different voltage levels. This not only mitigates the problem of the undesirable effects of sparking, as it is highly unlikely that sparking will occur in 2 sections at the same time, but also means that different voltages can be applied to each section. This is helpful as the gas loading is different at different stages of the ESP and, thus, different energisation regimes may be more efficient for different gas conditions and compositions. It is also true that collection efficiency is increased the more sections a particular ESP has, provided that they are independently energised (White, 1963). Different modes of energisation can be used, and some of the most important are discussed in the subsections that follow.

2.4.2.1.1. AC energisation

In principle, ac energisation should offer some operational advantages, mainly in terms of energisation, as the power sources would have been much simpler than for the dc energisation (Böhm, 1982). It would also have solved some of the problems arising from dust buildup on the collection plates (Böhm, 1982). However, it has failed to prove particularly fruitful on any particular application. One of the main reasons is, of course, the fact that the voltage changes polarity slowly enough for particles to be charged, but fast enough that they cannot reach the collection plates. This causes the particles to change polarity before they are collected. There are a few applications where ac energisation is used like agglomerators (Hautanen et al., 1995), that if used in modular configuration, can increase precipitation of fine and ultrafine PM. More information regarding agglomeration can be found in Appendix D.

2.4.2.1.2. Full and have wave rectified voltage

Using rectified voltage was one of the early methods of precipitation, which was even used by Cottrell (White, 1963). The energizing voltage is somewhat similar to DC voltage with superimposed impulses on it, Figure 2-10. This has the advantage of producing an increased electric field for the duration of the impulse for the efficient charging of PM, while for the rest of the cycle the voltage is not reversed, and there is a high enough electric field to force the charged PM onto the plates efficiently. Moreover, if a sparking occurs during the impulse phase, there is a period of lower electric field for the rest of the cycle that is long enough to extinguish the spark before the next impulse commences.

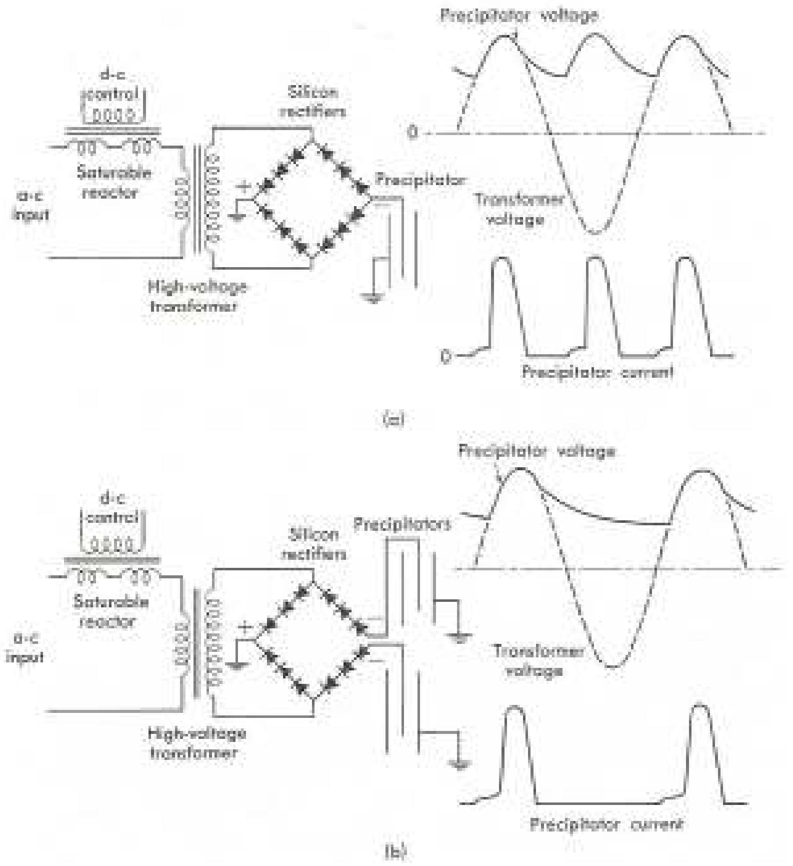

Figure 2-10: Full (a) and half- wave (b) rectified voltages for the energisation of ESPs (White, 1963).

The disadvantage of this method is the duration of the HV impulse. Since the impulse is a few ms long, a significant overvoltage (compared to the dc breakdown level) cannot be achieved. Thus, in order to increase the precipitation efficiency, the overall voltage should be increased, as for most of the cycle there is a dc voltage component which is much lower in magnitude compared to the dc breakdown level defined by the peak voltage. Thus, the most straightforward way to increase the efficiency of precipitation is to make the energisation waveform smoother. Another way, not possible for many decades in the beginning of the ESP development, is to reduce the duration of the impulse. By doing so, the overvoltage level can be increased further than the dc breakdown level since short high voltage impulses can be applied without breakdown occurring (Chowdhuri et al., 1997). This approach was implemented in the current research, and is discussed later in Section 2.4.2.1.4.

2.4.2.1.3. DC energisation

The most common way to energise an ESP is to use dc voltage. It has the advantage of charging the PM with one type of charge, in contrast to ac and it also has the same dc field for charging and collecting the PM. dc energisation is the preferred method of energisation for high conductivity PM, since the efficiency of precipitation is high (White, 1963). dc energisation is used in 2-stage precipitators, as they operate at lower voltage levels than single stage systems, and they also avoid sparking (White, 1963).

2.4.2.1.4. Impulsive energisation

As discussed in Section 2.4.1, it was established by Cottrell at the beginning of the 20th century that impulsive voltages resulted in superior precipitator performance compared to dc energisation (White, 1963). White also pointed out in 1963 that, in practice, steady state full and half wave rectified voltages at 60 pps (pulses per second) were mostly used. However, White also stated that pulsed voltages, once they became more economically accessible (and fast and reliable switching components were developed), were expected to take over in future ESP applications (White, 1963). Based on this knowledge from pioneers in the ESP field, it was decided to investigate energisation using impulses and to find optimal precipitation conditions, for removal of fine and ultrafine particles such as PM2.5.

World War II brought the development of impulse generators that were used for radar systems. These systems were able to produce 100 µs duration current impulses at a rate of up to 100s of pps. If used to energise an ESP, these impulse generators would have an advantage of having much sharper impulses, which if developed into a sparkover, had virtually the full cycle to be extinguished (White, 1963). This fact made it possible for a few kV higher energisation, which corresponded to 25–35% higher average current compared to half and full wave rectified voltage, while losses were reduced by 50-60% (White, 1963).

In terms of optimal frequency, attempts were made to use low pulse repetition rate (25 pps), however the waveshape was approaching that of dc energisation. On the other hand, higher frequencies did not allow sufficient time for possible sparks to be extinguished. Therefore, the optimal frequency found from practice was ~60 pps, although in other publications frequency of 120 pps was indicated as more favorable (White, 1963). Based on this experimental knowledge, a similar approach was tested in this work, mainly using frequencies of 50 and 100 pps, but also with other pulse repetition frequencies (prf) from as low as 10 pps to a maximum of 125 pps. Attempts to combine low pulse repetition frequencies using multiple impulses (bursts) had also been investigated (Dietz and Peters, 1986).

Approaching the core of the problem, it was discovered that the precipitation efficiency depends upon both the successful charging of the particles, and the efficient collection of the already charged particles. Thus, it is beneficial to have both, high peak voltage, in order to achieve a higher saturation charge on the particles (Hinds, 1982, Kanazawa et al., 1993), and a higher average voltage, in order to collect the charged PM more efficiently. The former is achieved with narrower and therefore higher amplitude pulses (without breakdown occurring as compared with wider impulses), while the latter requires high average voltage, and corresponding average current, without sparking occurring (White, 1963). However, the optimum waveshape of the impulse is not universal, as it depends upon the particles to be collected. For example, for very conductive particles, it was found that dc voltage is most favorable, while for particles of high resistivity, a ratio of 0.5 of the average voltage compared to the peak voltage was most effective (White, 1963).

In more recent applications, apart from impulses with 100 µs duration, impulses with a few µs duration have also been used (Parker and Institution of Electrical Engineers, 2003). This allows for considerable overvoltage to be achieved without the occurrence of complete spark breakdown. In some cases, 50 kV dc energisation and 100 kV impulses were used in ESP systems (McKenna et al., 2008). Another advantageous characteristic of impulses is their current distribution, which is more uniform than that of dc energisation (McKenna et al., 2008). While it is obvious that HV impulses are advantageous towards a higher ESP collection efficiency, the technique still continues to be developed (McKenna et al., 2008). In the course of this PhD, a novel approach was taken. While using, in most cases, the pulse repetition rate that has proven empirically, even from the early decades of ESP development, to be most advantageous, the duration of the voltage impulses was shorter than (sub-microseconds) and longer than (~400-500 µs FWHM) of the durations mostly used in practice today. The latter, wider, impulses were used without superimposing them on dc voltage and at lower prf compared to what is prevalently used in industry (Parker and Institution of Electrical Engineers, 2003).

2.4.2.2. Corona discharge

The all-important corona discharge is the source of the charge carriers (predominantly ions) which are needed to charge the PM. Generation of corona discharges requires high enough voltage to be applied across the discharge electrodes, and the electric field produced to be sufficiently high enough to accelerate a free electron at such a level so as to ionize a molecule and cause a consequent avalanche. The initial seed electrons can be generated by various sources, like from natural radioactivity, photoionization, or cosmic rays, which produce about 10 free electrons per cubic cm per second (Hinds, 1982).

The limitations on the electrical field achievable in practice, especially in the early stages of ESP development, a period when the equipment available had severe power restrictions, has led to extremely non-symmetrical electrode designs. Even in the first ESP systems developed by Sir Oliver Lodge, barbed electrodes were used so as to easily have corona inception voltages at the sharp points, while Cottrell used his own “Pubescent” electrode design. However, these designs were quickly abandoned once HV rectifier parts developed sufficiently (White, 1963). Another important discovery, as it has been discussed, came from W. A. Schmidt with his fine wire corona electrode that, together with the progress in the rectifier circuits, simplified corona electrode designs significantly. Barbs and other protruding electrodes are still used today, especially for heavy dust loading and for sticky particles (White, 1963). Another important invention, useful for gas cleaning applications, is the fact that tungsten high voltage electrodes have the ability to produce much lower quantities of ozone, compared to other materials (White, 1963).

There are two types of corona discharge, produced by corresponding voltage polarities: positive and negative. Apart from different I-V characteristics, they also have different visual appearance. Positive corona forms a uniform glow, while negative corona has visible active “beads” or “tufts” upon the discharge electrode that fluctuate in number if the voltage fluctuates. The negative corona has electrical characteristics that are favorable to the operation of an ESP, as it can exist under a higher electric field without breakdown occurring and has 2 potential ionic carriers, the highly mobile electrons and the more slow electronegative oxygen molecules. Negative corona has been shown to enhance collection efficiency (McKenna et al., 2008) and is used for most industrial applications. Positive corona, however, is used mostly for air cleaning applications, as it has been shown to produce much less O_3 and NO_x compared to negative corona (White, 1963, Asbach et al., 2005a). Further information regarding corona discharges and their formation mechanisms can be found in the Subchapters 2.4.2.2.1 to 2.4.2.2.9.

2.4.2.2.1. Townsend discharge

While there are many different types of gas discharge, most of them start in the form of an electron avalanche. One of the simplest forms of discharge occurs between two parallel plates, inside a homogeneous electric field, $E = V/d$, where V is the applied dc voltage and d is the inter-electrode distance. At first, some seed electrons must exist from an external source, in order to be accelerated and form successful avalanches that travel towards the anode. At this point, the first Townsend coefficient or ionisation coefficient, α, can be defined as the rate of ionisation per unit length, as the avalanche progresses. Thus, each electron can generate $e^{\alpha d} – 1$ positive ions as it progresses towards the anode. As these ions drift away and ultimately impact the cathode, they have the capability to release secondary electrons from the cathode, based on the third Townsend coefficient γ. This coefficient, also known as the secondary emission coefficient, is dependent upon many factors, mainly the work function of the cathode material, the gas, and the electric field present. According to Townsend, the total current at the cathode is $I_c = I_1 + \gamma I_c(e^{\alpha d} – 1)$ where I_1 is caused by external sources like photoionization, α and γ are the first and third Townsend coefficients respectively, I_c is the current at the cathode and d is the inter-electrode gap. Thus, $I_1 = I_c [1 - \gamma(e^{\alpha d} – 1)]$ (Fridman et al., 2005). However, the current at the anode is $I_i = I_c e^{\alpha d}$, thus the current caused by electron avalanches at the anode is (Timoshkin, 2010b):

$$\boldsymbol{I_i = \frac{I_1 \cdot e^{ad}}{1-\gamma\left(e^{ad}-1\right)}} \tag{2.2}$$

If $1 - \gamma\left(e^{ad} - 1\right) = 0$, then the discharge becomes self-sustaining, meaning there is discharge current without the need of external ionisation sources ($I_1 = 0$) (Timoshkin, 2010b). This means that the positive ions that reach the cathode will release at least one electron that will start another successful avalanche, thus eliminating the need of external seed electrons for avalanches to develop. The time needed for this process (ions to traverse the gap and release an electron) is called the formative time lag (Howatson, 1976). The other important time parameter in this type of discharge is the statistical time lag, which is the time needed for the first seed electron to appear (Timoshkin, 2010a, Howatson, 1976), in order to start the avalanche process.

2.4.2.2.2. Formation of corona discharge

In the case of non-uniform topologies, partial breakdown can occur at the most sharp electrode, once the electric field reaches the 28-30 kV threshold, at sufficiently high *pd* (1 atm and gap of a few cm). This correspond to the conditions at which the attachment and ionization coefficients equalise, thus there are electrons remaining that start successful avalanches, without being attached to electronegative gas molecules. An electronegative gas is a type of gas in which the molecules (atoms in the molecules according to (Pauling, 1932)) have an ability to attract electrons and to form negative ions. For short gaps, there is no corona formation as the gap is more uniform. This self-sustaining discharge cannot develop into a successful avalanche that will bridge the inter-electrode gap, as the electric field drops exponentially away from the active electrode. Such discharges were termed corona, because they appeared floating on top of conductors or in the form of "St Elmo's fire" on top of ships masts, resembling a crown (Chang et al., 1991, Fridman et al., 2005). Corona discharges are mostly accompanied by visual and audible phenomena (Kuffel et al., 2000). There are many different types of corona discharge, the most important being the positive, negative, impulsive and ac corona discharges. This nomenclature is derived from the type of voltage that the protruding electrode is charged with, and for the course of this PhD there was extended use of impulsive and positive corona, with limited use of negative corona and no interest in ac. Close to the protruding electrode, there is an area of extreme ionisation, called the active zone (Timoshkin, 2010a), while away from it and covering most of the inter-electrode area is the ion transport zone (Timoshkin, 2010a), where the charge carriers drift towards the other electrode. The boundary can be defined as the point where $\alpha = \beta$, as discussed above, or the point that $E \leq 26$ kV/cm for atmospheric air (Timoshkin, 2010a). The active zone depends upon the applied voltage and the topology. If the topology is cylindrical, like the topologies used in the course of this work, then the critical electric field for corona ignition was found by Peek to be (Peek, 1915, Fridman et al., 2005):

$$\boldsymbol{E_{cr}\left(\frac{\mathrm{kV}}{\mathrm{cm}}\right) = 31\delta\left(\frac{0.308}{\sqrt{\delta r(\mathrm{cm})}}\right)} \tag{2.3}$$

where r is the wire radius and δ is the ratio of the air density over its standard value, while the radius of the active zone is (Fridman et al., 2005):

$$\boldsymbol{r_{act}} = \frac{\boldsymbol{V}}{\boldsymbol{E_{break}} \ln(\boldsymbol{R}/\boldsymbol{r})} \tag{2.4}$$

where *R* is the radius of the external cylinder, *V* the applied voltage and E_{break} ≈ 25 kV/cm. In the case of a point to plane topology, this formula becomes (Fridman et al., 2005):

$$\boldsymbol{r_{act}} \approx \sqrt{\frac{\boldsymbol{rV}}{\boldsymbol{E_{break}}}} \tag{2.5}$$

Their ratio (r_{act} of wire over r_{act} of point) is usually found to be ~3 (Fridman et al., 2005), meaning that the corona created around a wire creates a much higher volume of non-thermal plasma, which makes it more efficient for use in various applications, including the air cleaning application that this work is focused upon.

In terms of current generation and power consumption for the wire-cylinder topology, the following equations can be extracted:

$$\boldsymbol{I} = \frac{4\pi\varepsilon_0\mu V(V-V_{cr})}{R^2\, ln(R/r)} \tag{2.6}$$

where V_{cr} is the corona inception voltage, *R* is the internal radius of the cylinder, *r* is the radius of the wire, ε_0 is the dielectric permittivity of free space and μ is the mobility of the charged carriers (Fridman et al., 2005). The corresponding power released is (Timoshkin, 2010a, Fridman et al., 2005):

$$\boldsymbol{P} = \frac{4\pi\varepsilon_0 L\mu V^2(V-V_{cr})}{R^2\, ln(R/r)} \tag{2.7}$$

where L is the length of the cylinder.

The power delivered in a corona discharge cannot rise to high levels (even in the conditions close to breakdown), thus in most non-thermal plasma applications impulsive corona is used (Fridman et al., 2005).

2.4.2.2.3. Negative corona discharges

Negative corona discharges have many similarities to the Townsend discharge, with successful avalanches developing near the protruding electrode (Figure 2-11, top). However, the avalanches cannot progress much further, as the non-uniformity of the topology causes a steep decrease of the electric field into the ion transport zone. Additionally, the electrons can get attached to electronegative molecules present in air, forming slow moving negative ions (in the form of space charge, Figure 2-11, middle) that hinder further ionisation and giving rise to the impulsive nature of corona current, reaching up to 1 MHz (Howatson, 1976, Kuffel et al., 2000, Fridman et al., 2005). When the positive ions bombard the cathode, further electrons are liberated, based on the third Townsend coefficient, γ (Fridman et al., 2005), which guarantee the continuity of the electric current in the circuit (Fridman et al., 2005). However, the electric field for the ignition of negative corona is independent of the material of the anode in contrast to the Townsend breakdown mechanism (Lowke and D'Alessandro, 2003). The ignition condition for negative glow corona in electronegative gases satisfies the following equation (Fridman et al., 2005):

$$\int_{0}^{x_{max}} [\alpha(x) - \beta(x)]dx = \ln\left(1 + \frac{1}{\gamma}\right) \tag{2.8}$$

where x_{max} is the distance from the cathode where $\alpha(x_{max}) = \beta(x_{max})$ (corresponding to the breakdown electric field), and in essence defines the end of the glow or active zone of the corona (Fridman et al., 2005), where β is the attachment coefficient and represents the electrons attached to electronegative gas molecules per unit length, thus acting opposite to α. The current is impulsive in nature (Fridman et al., 2005), and if the electric field is high enough, then streamers will start to propagate towards the cathode (Figure 2-11, bottom) (Howatson, 1976), until the applied voltage increases to the point that breakdown occurs. Negative corona is composed of reddish-purple distinct beads (Kuffel et al., 2000), which can grow in number once the voltage increases. Lastly, the space charge effect in electronegative gases means that the negative breakdown voltage is higher than the positive breakdown voltage, unless at much reduced pressures (Kuffel et al., 2000) because without significant concentration of gas molecules, the space charge phenomenon is limited, and with the higher electric field at the cathode, γ plays a major role in the breakdown of the negative polarity thus, happening at lower voltages (Kuffel et al., 2000). This is despite the fact that positive corona ignition voltage is higher than negative.

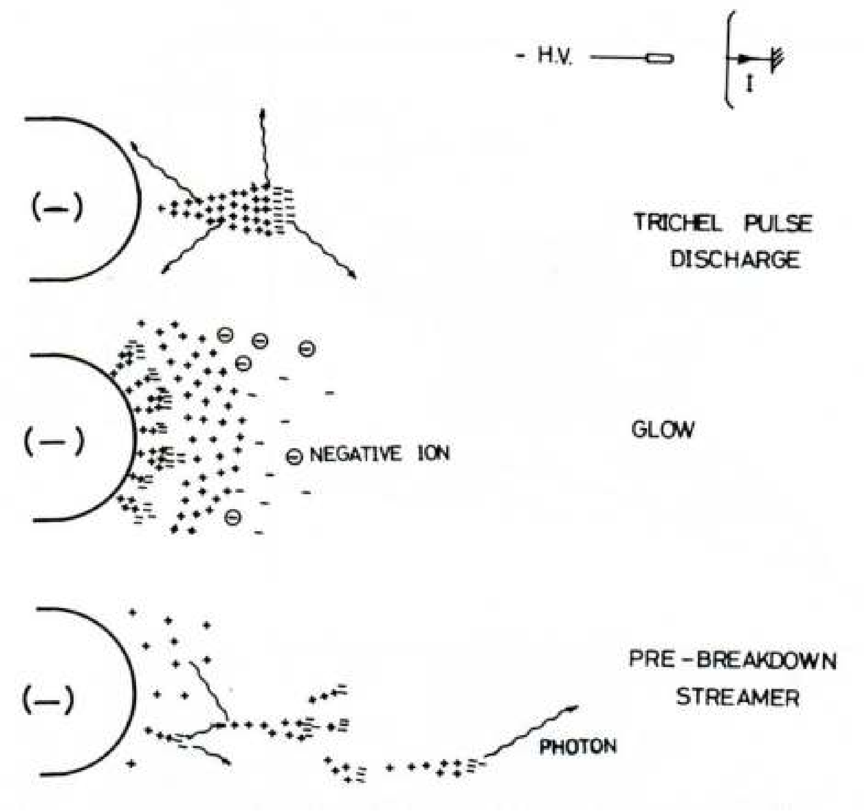

Figure 2-11: Negative corona at non-uniform topology (Khalifa, 1990).

2.4.2.2.4. Trichel impulses

The process of negative corona discharge in electronegative gases begins with the appearance of seed electron(s) in the high electric field zone (Kuffel et al., 2000, Trichel, 1938). Seed electrons can be produced in many ways, including photoionization or cosmic irradiation (Allen, 2004, Denat, 2006). The seed electron(s) are accelerated in the electric field (repulsed from the cathode), and if they gain sufficient energy for ionisation (collisions becoming ionizing ones), an avalanche starts to develop (Townsend mechanism). However, a portion of the electrons generated get attached to the electronegative gas molecules, creating a negative space charge that quenches the avalanche process due to the steep reduction in the electric field. In the case of atmospheric air, the electronegative gas present is O_2, while N_2 is electropositive. As the negative ions have much lower mobility compared with the free electrons, these ions stay in the inter-electrode gap for a longer time, while the electrons travel towards the anode, generating a short current impulse, Figure 2-12. The negative space charge takes some time to clear sufficiently for new successful avalanches to develop. This gives rise to the impulsive nature of corona current, these impulses were named after their discoverer, Trichel impulses, caused by the intermittent arrival of electrons at the anode resembling short bursts (Trichel, 1938). Therefore, further voltage increase is needed to overcome this process, which makes the negative breakdown voltage higher compared to the positive one (Kuffel et al., 2000), excluding conditions of very low pressures, as discussed in subchapter 2.4.2.2.3. In addition, for very high pressures (above some critical value in air, ~7 atm for positive polarity and much higher for negative polarity (Kuffel et al., 2000)) breakdown occurs without any corona discharge (MacGregor et al., 1996). Trichel pulses are very short (~100 ns) and can carry very high corona currents, in the range of 10s of mA (Fridman et al., 2005). The way of their creation implies that they cannot occur inside purely electropositive gases (Fridman et al., 2005), while their appearance rate is on the order of (10s-100s) kHz, increasing as the applied voltage increases and decreasing with a decrease in pressure (Kuffel et al., 2000).

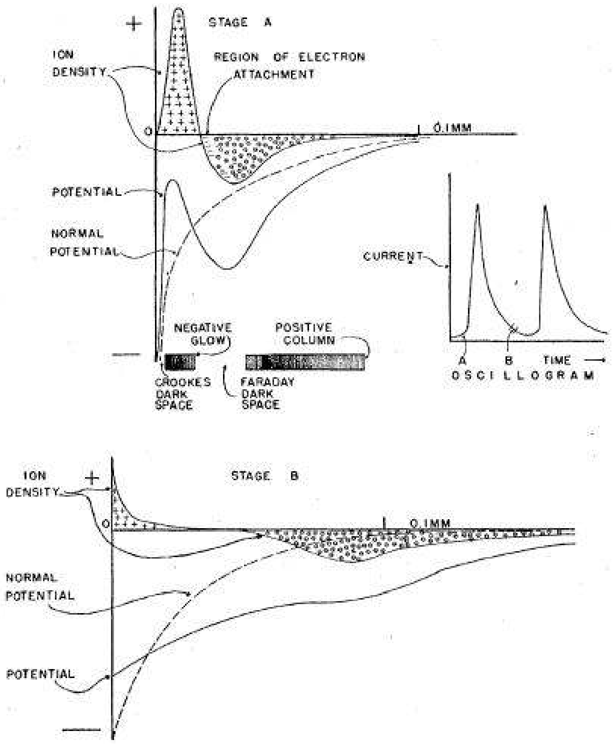

Figure 2-12: Formation of Trichel impulses, picture from the original work by (Trichel, 1938).

2.4.2.2.5. *Positive corona discharges*

Positive corona discharges are developed in a different way. The first avalanches are created by photoionization, or other external means (Howatson, 1976), and they start propagating towards the anode (which is the protruding electrode) as cathode directed streamers (Fridman et al., 2005), (Figure 2-13 first from top), and are named onset streamers or burst pulses (Kuffel et al., 2000). Thus, their formation can be derived from Meek's criterion as (Fridman et al., 2005):

$$\int_{0}^{x_{max}} [\boldsymbol{\alpha}(\boldsymbol{x}) - \boldsymbol{\beta}(\boldsymbol{x})] \boldsymbol{dx} = \mathbf{18-20} \qquad (2.9)$$

If the current is higher than ~100 nA then the current becomes impulsive with ~1 kHz frequency (Howatson, 1976), without falling to zero (Fridman et al., 2005), (Figure 2-13 second from top and (a)). If the current increases further, then the whole process becomes self-sustaining, meaning that each avalanche creates, by photoionization, at least another electron that, in turn, creates another successful avalanche, and so forth (Howatson, 1976). By this time, the current is of the order of μA (Howatson, 1976), fluctuating up to 10 kHz (Fridman et al., 2005) but continuous (Kuffel et al., 2000), and an external view shows a glow, (Figure 2-13 third from top and (b)). Furthermore, there is no secondary electron emission, as the electric field at the cathode is very low (Timoshkin, 2010a, Howatson, 1976, Fridman et al., 2005). The fluctuating current can be explained by the fact that the positive ions take time to cross the gap, thus ionisation is suppressed, much like in the Trichel pulses case. However, at elevated voltages, the electric field in the ion transport zone is high enough to clear the positive space charge quicker, thus there is an increase in the pulse frequency until this flashing corona stops (Fridman et al., 2005). With further increase in voltage, pre-breakdown streamers appear, much larger compared to the burst pulses that appeared at first, until breakdown occurs (Kuffel et al., 2000), (Figure 2-13 fourth from top and (c)). In comparison with negative corona, their ignition electric fields are almost identical, despite the different breakdown mechanisms involved (Fridman et al., 2005). Positive (glow) corona is usually observed as a uniform blue-white hue above the conductor (Kuffel et al., 2000), and in the gaps that it is present, the sparking potential is increased (Kuffel et al., 2000).

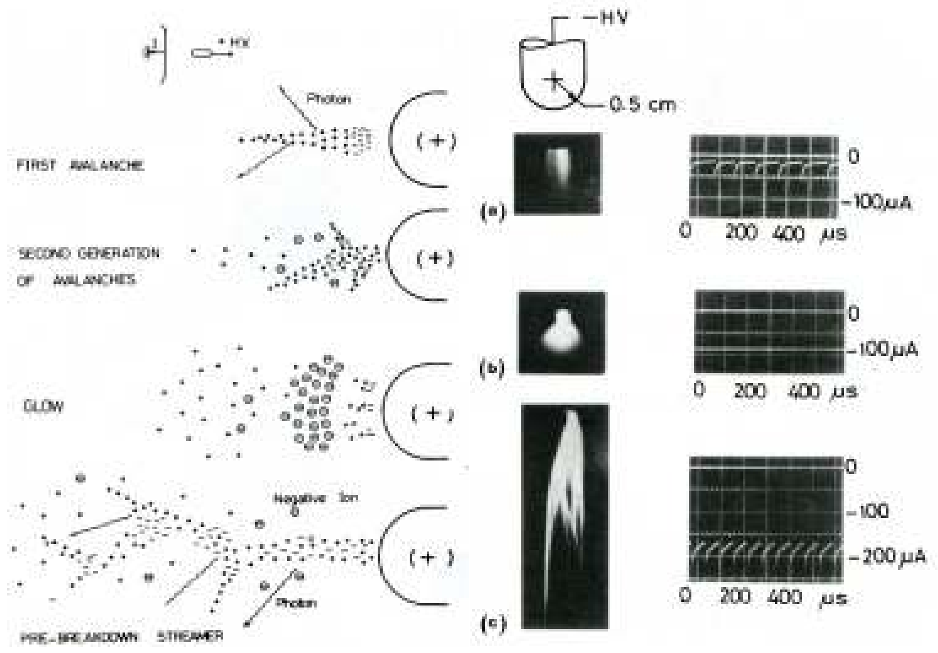

Figure 2-13: Positive corona discharge in non-uniform electric fields (Khalifa, 1990).

2.4.2.2.6. Limitations of the Townsend theory

As the gap increases, larger avalanches can be developed. As a consequence, they disturb more the uniform electric field around them and are therefore less dependent on secondary emissions from the cathode. This explains the reduction of the electric field needed for breakdown, as the gap increases, under constant pressure (Kuffel et al., 2000). This drop is, however, reduced in the presence of electronegative gases, as they have an affinity to attach free electrons and hinder the ionisation process. This is why the breakdown voltage is higher when electronegative gases are present, compared to when they are absent (Fridman et al., 2005). Thus, for gaps longer than 5 cm at 1 atm, the larger avalanches developed cause a significant change in the background uniform electric field, which leads to another breakdown mechanism, the spark discharge (Fridman et al., 2005).

Despite the fact that Townsend theory can explain the breakdown mechanism for atmospheric pressures and gaps less than ~50 mm (Fridman, 2008), it cannot explain breakdown for larger *pd*. This is because it has been shown that for large pd, the time for ions to cross the gap (formative time lag) is much longer than that of electrons (Timoshkin, 2010c), due to their lower mobility of the ions (Timoshkin, 2010d). Thus, in the time needed for electrons to cross the gap and breakdown to occur, ions have barely moved, thus no cathode emission of electrons is expected (Timoshkin, 2010c). At high pressures, therefore, the breakdown voltage is not influenced by the cathode material (Howatson, 1976), and the logarithm of the current versus distance curve is linear (Howatson, 1976) (secondary emissions would deform the linearity of the plot). This is the major difference between the Townsend and spark breakdown mechanisms, as well as their spatial difference, namely that a spark develops across a narrow channel, while avalanches are wider, due to diffusion (Fridman et al., 2005).

2.4.2.2.7. Streamer theory

Based on the evidence described in Section 2.4.2.2.6, Raether, Loeb, Meek and Craggs developed a new theory (Timoshkin, 2010c, Raether, 1964, Loeb, 1955, Meek and Craggs, 1954, Fridman et al., 2005), the streamer theory, to explain this discrepancy. The first step is, like the Townsend theory, an avalanche that travels toward the anode. After a very short time, the avalanche would have a drop-like shape, with many electrons residing in the avalanche head, and an almost equal number of positive ions being left behind (Fridman, 2008), Figure 2-14.

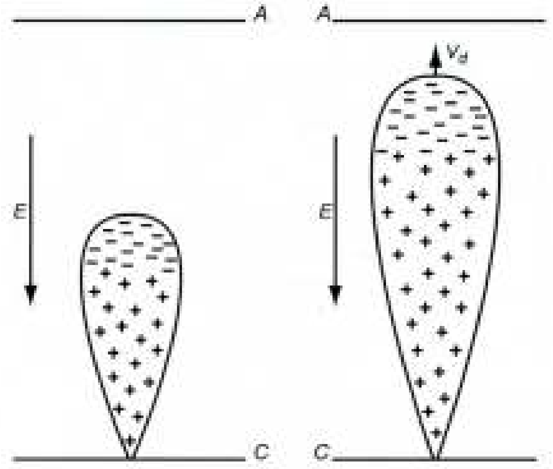

Figure 2-14: Anode directed avalanche (Fridman, 2008).

This drop is essentially a dipole that has its own electric field E_a, which acts in a summative manner with the external field E_0 and the resultant electric field accelerates the ionisation process (Fridman, 2008, Fridman et al., 2005) close to the head and tail of the dipole (Fridman et al., 2005), Figure 2-15.

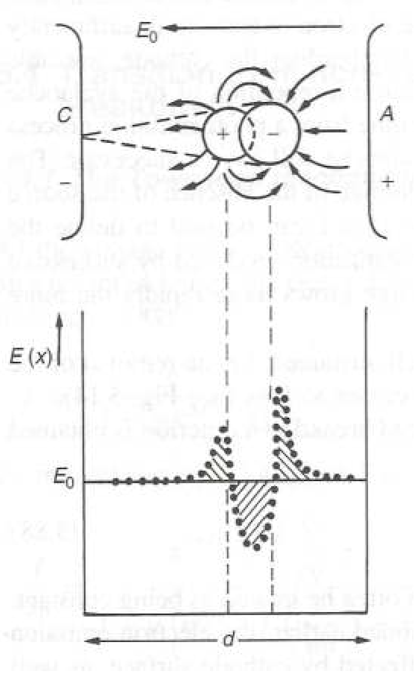

Figure 2-15: Electric field, in and around the avalanche (Kuffel et al., 2000).

A side effect of this high electric field is that further photoionization occurs near the avalanche head, and the corresponding avalanches are attracted into the positive tail of the dipole (Howatson, 1976). The number of electrons present at the avalanche head can even reach levels of 10^{13} /cm^3 (Fridman et al., 2005). At some point the avalanche will reach the anode (in small gaps (Fridman et al., 2005)), and the electrons will quickly be absorbed into it, leaving the slow moving, positive ions behind (Fridman, 2008), Figure 2-16.

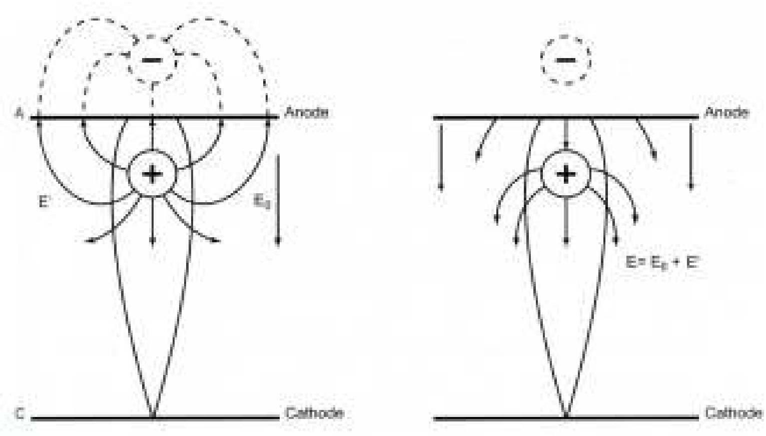

Figure 2-16: Avalanche reaching the anode (Fridman, 2008).

The electric field associated with this space charge will have a maximum at $1/\alpha$ away from the anode (~1 mm, which corresponds to the radius of the avalanche head (Fridman et al., 2005)). If this field $E_a \approx E_0$, then a streamer (positive or cathode directed streamer (Fridman et al., 2005)) is formed (Timoshkin, 2010c, Meek and Craggs, 1954). This field requires a space charge of $N_e = e^{\alpha x} \approx 10^8$ or $\alpha x_c = \alpha d \geq$ 18-20 (Timoshkin, 2010c), which is Meek's breakdown criterion (Fridman, 2008, Fridman et al., 2005), where x_c is the critical avalanche length in order to create a streamer.

The streamer consists of a needle shaped (Fridman et al., 2005) ionized channel that is created from the tail of the avalanche that successfully reached the anode (Howatson, 1976), on the condition that $E_\alpha = E_0$ is fulfilled and also has a great number of positive ions. The head of the streamer has a high electric field (26-30 kV/cm) and is glowing, while the streamer body, which is called the passive region, is dark and weakly conductive. Due to the high electric field of the streamer head and the corresponding ionisation that occurs, secondary avalanches are produced near the streamer head that feed it with electrons (Timoshkin, 2010c, Fridman, 2008), keeping the electric field high, and ensuring the streamer's further propagation, Figure 2-17.

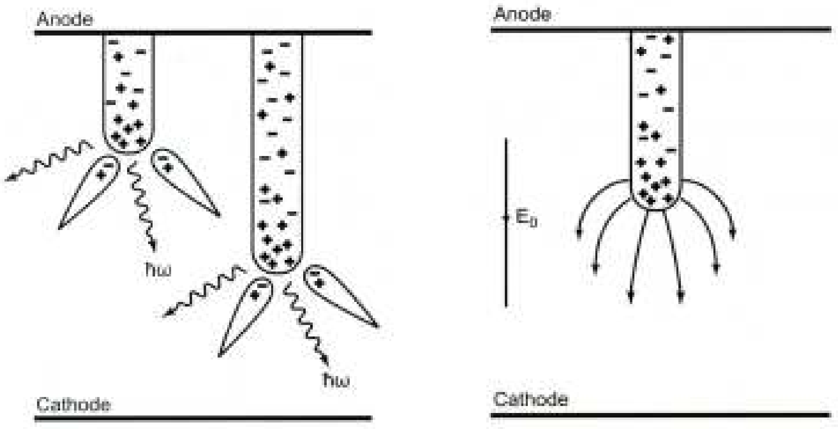

Figure 2-17: Cathode-directed streamer (Fridman, 2008).

On the whole (active and passive region), streamers are near to ambient temperature (raised only by ~10°C), short lived, carrying currents of 10s of A, and are fast propagating at ~2 km/s (Fridman, 2008, Timoshkin, 2010c) and up to 100s km/s (Cooray, 2014). When, however, they reach the cathode, the situation changes, as a huge number of electrons are released and race towards the anode (Timoshkin, 2010c). This happens at much higher speeds of 10,000 km/s, which causes significant heating of the channel, and increases its conductivity (Timoshkin, 2010c). Thus, a spark channel carrying very high currents is formed (Timoshkin, 2010c), and breakdown occurs (Howatson, 1976), (see Figure 2-18).

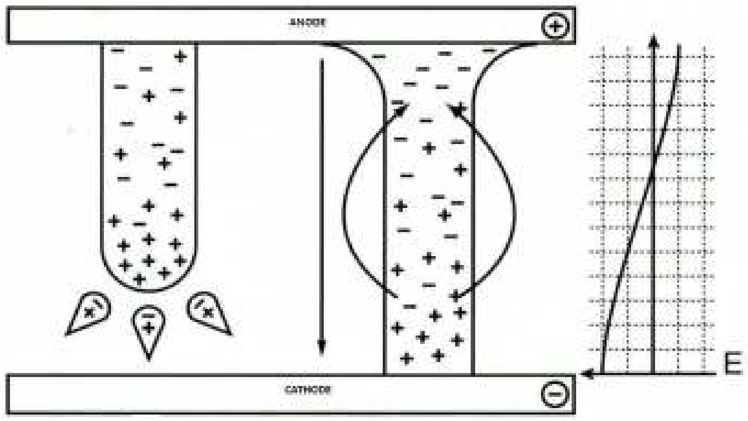

Figure 2-18: Streamer reaching the cathode (Fridman, 2008).

A special case occurs when a streamer fulfills the streamer formation criterion, $E_\alpha = E_0$ (Howatson, 1976), without having reached the anode, as illustrated in Figure 2-19.

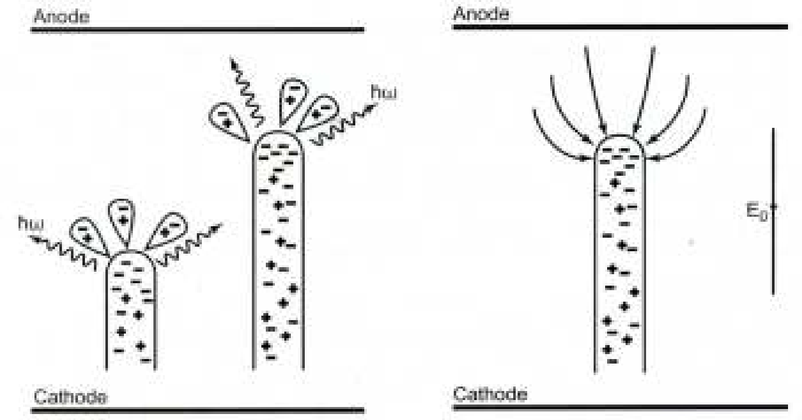

Figure 2-19: Anode-directed streamer (Fridman, 2008).

In such a case 2 streamers are formed, each progressing in the opposite direction, named anode and cathode directed streamers (Fridman, 2008, Fridman et al., 2005). The anode-directed (also known as negative (Fridman et al., 2005)) streamer neutralises the ions in the bodies of the secondary avalanches, which are created by photoionization as well as preceding electrons (Fridman, 2008, Fridman et al., 2005). This usually occurs in long, overvolted gaps (Fridman et al., 2005).

2.4.2.2.8. *Special cases – non-uniformity in electric field*

Another special case is for non-uniform topologies. In this case, the streamer formation equation becomes:

$$\int_0^{x_c}[\alpha(x)-\beta(x)]dx \geq 18 \tag{2.10}$$

and x_c is the distance at which $E \geq 26$ kV/cm (Timoshkin, 2010c), Figure 2-20.

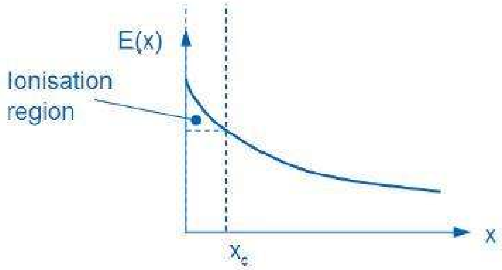

Figure 2-20: Electric field as a function of space, for a non-uniform electrode topolory. x = 0 corresponds to the protruding electrode (Fridman, 2008).

In the case of an electronegative gas, the minimum electric field needed for streamer transition is $\alpha(E_0/p) = \beta(E_0/p)$, independent of the gap length (Fridman et al., 2005). In a uniform field, the same restriction on streamer propagation applies as in the non-uniform field, namely the presence of (4-6) kV/cm for positive polarity and (10-20) kV/cm for negative polarity (Timoshkin, 2010c, Cooray, 2014). The voltage required for breakdown obviously decreases in non-uniform gaps (Fridman et al., 2005). Streamer propagation in positive and negative polarity is shown in Figure 2-21.

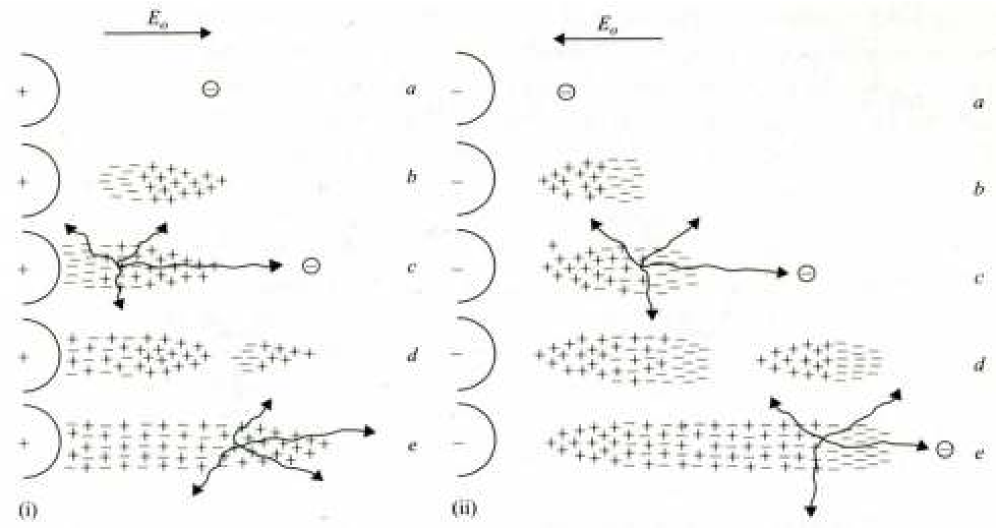

Figure 2-21: Streamer propagation under positive and negative polarity in non-uniform topologies (Allen, 2004).

In Figure 2-22 the behavior of a non-uniform electric field is shown, as a function of inter-electrode distance. For very small, almost uniform gaps, there is no corona, while as the non-uniformity increases, with increasing distance, corona glow, onset streamers and pre-breakdown streamers start to appear.

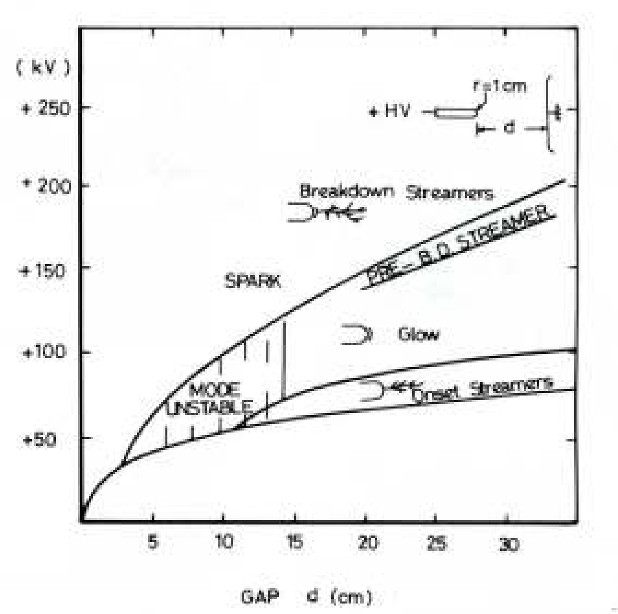

Figure 2-22: Breakdown behaviour of non-uniform electrode topology, as distance between the electrodes (and thus non-uniformity) increases (Timoshkin, 2010c) (Kuffel et al., 2000).

2.4.2.2.9. Impulsive corona discharges

Impulsive corona has been shown to be a very effective method of non-thermal plasma production for technological applications. Very short pulses can not only increase the applied electric field significantly, since breakdown occurs at higher levels (Fridman et al., 2005, Kuffel et al., 2000), but also are able to have streamers present without breakdown occurring, thus increasing considerably the power output, compared to dc corona (Fridman et al., 2005). This is because for gaps of a few cm long, the time for the first seed electron to appear, a successful avalanche to develop, fulfillment of Meek's criterion, and the streamer propagation can take between ~(100-300) ns. Thus, if particularly short impulses are used, there will be no time for spark breakdown transition, while there will be an effective non-thermal plasma generation by the repetitive streamers.

As far as corona polarity is concerned, positive corona is much more desirable, because of its very stable ignition delay, ~100 ns, while, as previously discussed, the negative ignition delays are dependent upon the cathode material and its general condition (Fridman et al., 2005). A cylindrical topology is typically chosen, as this guarantees maximization of the active corona discharge volume (Fridman et al., 2005). In addition to the above, positive corona is filamentary in nature, with increasing length and branches as the voltage increases (Kuffel et al., 2000). The associated velocity, however, decreases in an exponential manner away from the protruding electrode due to the much reduced electric field, still being in the order of ~1,000 km/s (Kuffel et al., 2000).

2.4.2.3. Particle charging

The corona discharge divides the inter-electrode space into 2 zones: the active zone, where there is enough energy for electrons to ionize neutral molecules by impaction; and the ion transport zone. The boundary between the 2 zones can broadly be defined as the edge of the corona glow. In the active zone, ionic carriers of both polarities exist, as new ions are being created by impaction of high energy electrons and some of them are also recombined, emitting the extra energy as light, making the corona discharge visible. This zone is very small, usually no more than a few mm around the corona wire. In this zone, plasma charging of particles takes place (Goree, 1994), however this type of charging is not the focus of this thesis. Instead, the charging phenomena occurring in the much larger ion-transport zone will be analysed.

The ion-transport zone, which spans from the edge of the ionisation zone all the way to the surface of the collected material on the discharge electrode, is the volume that ions transverse drifting from the ionisation electrode to the particle collection electrode, due to electrostatic forces. In this area, the particle laden air flow passes in a perpendicular direction compared to the electric field. As the electric charges, being either ions or electrons, get close to the uncharged particle, they induce a dipole moment on the particle. This is called polarisation charge and is produced by the separation of charges inside the particle, as the dipoles inside the particle get oriented relative to the charge, while any free charges move towards or away from the inducing charge, depending upon their polarity. Polarisation charge is also induced by the electric field in the ESP reactor.

Since the permittivity of the particles is different compared to that of the medium (gas), the field lines get distorted around the particle, and since the field lines are the paths that ions or electrons travel upon, they collide and attach to the particles. However, the more charge a particle acquires, the more the field lines are distorted, until they no longer intercept the particle. At this point, the particle has acquired its saturation charge and no more charging of this type occurs. This charging process is called field charging, because it occurs in the presence of the field, and stops if the field disappears or particles move away from this field. It has also been prove theoretically that there is a limit to the amount of charge that the particles can acquire from this method (Hinds, 1982), which is usually on a faster timescale compared to the resident times of an ESP (Hinds, 1982). This is the main charging method for particles larger than 0.5 μm (McKenna et al., 2008) or 1 μm (Hinds, 1982).

Another mechanism of particle charging is with the random thermal (Brownian) motion of particles and charge carriers, being more vivid for smaller particles, well below the sub-micrometer range (Hinds, 1982). The electric field is not required for this type of charging, however it can be enhanced by its presence as the ion movement is strongly dependent upon the field. This charging mechanism requires mixing of airborne particles and ions. Since the ions have random thermal motion, they diffuse and impinge on some of the airborne particles. As the particles become charged, they repel extra charges, however they will still be charged by higher and higher energy ions that manage to penetrate the electric field around them. The charging rate is thus greatly reduced as more and more ions at the tail of the Boltzmann distribution will contribute towards charging. Thus, in theory, diffusion charge does not stop (Hinds, 1982, McKenna et al., 2008), however there is an upper limit to the charge that a particle can sustain (limited by the breakdown field of the gas around the particle). Particles smaller than 0.2 μm (McKenna et al., 2008) or 0.1 μm (Hinds, 1982) have diffusion charging as their main charging mechanism.

Particles between 0.1 and 1 μm (Hinds, 1982) constitute a transitional region where there is no prevalent charging mechanism, however both are present. This size range was found to be the weakest point for an ESP, showing the lowest fractional efficiency (Parker and Institution of Electrical Engineers, 2003). This was chosen also to be the main focus of this research, to increase the precipitation efficiency for this size range, which constitutes the major numerical fraction of PM2.5 particles. In addition, since diffusion charge lacks a clear theoretical equilibrium state (reaches a steady state only after infinite time has elapsed), in the theoretical analysis conducted, only the charge acquired by field charging was taking into account for the efficiency calculation, as its saturation charge can be defined precisely (Böhm, 1982). Any charge acquired by diffusion will only add to the total charge and the present analysis, therefore, will constitute a worst case scenario.

2.4.2.4. Particle collection

Particle collection on a precipitator's electrodes is a process comprising several distinct phases. The first phase is the process of charged particle migration towards the collection plates. When the particles impact upon the plates, they should be successfully and firmly attached, despite the gas flow rate, the impaction of other particles, or their loss of charge to the plates, and be easily removed by rapping or any other cleaning process.

The motion of a charged particle towards the collection electrode is governed by electrostatic forces in the direction of the collection plate, and by inertial and viscous forces impeding its transit towards the plates (White, 1963). For the PM that is typically found in ESPs, viscous forces are governed by the Stokes law, while the inertial forces are negligible (White, 1963). The equilibrium between these forces makes the particle move at almost constant speed, termed the migration velocity, towards the plates (White, 1963). For larger particles (> 10 μm), their movement can be governed by the migration velocity and the gas velocity, reaching the collection plates with a parabolic trajectory. However, smaller particles can have a more complicated path towards the collection plate as any turbulence can have a much greater effect on them compared to larger particles (McKenna et al., 2008). In industrial scale ESPs, migration velocities can be ~0.1 ft/min (0.51 mm/s) for 500 nm particles, while a 30 μm particle can reach up to 4 ft/min (~20 mm/s) (White, 1963). More recent literature (Böhm, 1982), also points to migration velocities of ~10 mm/s.

When the particles impact on the collection plates, they are expected to remain there until the cleaning process commences. Particularly problematic particulates are those with high conductivity, as they can release their charge easily upon impaction and bounce off (Hughes, 1997), or adhere loosely upon the plates and cause serious reentrainment during the cleaning process (McKenna et al., 2008). At the other end of the spectrum, particles with high resistivities do not lose their charge easily, leading to back corona problems and difficulties from removing them from the collection electrode (McKenna et al., 2008). If this issue is addressed just by increasing the rapping intensity, this can also lead to severe reentrainment and, thus, to reduced efficiency (McKenna et al., 2008). In general the resistivity ranges for normal precipitation operation are between $5 \cdot 10^{3}$-$2 \cdot 10^{10}$ Ωcm, while for resistivities > 10^{11} Ωcm, precipitation can become problematic (McKenna et al., 2008). This, however, is not a hindrance for wet ESPs (McKenna et al., 2008).

Modern precipitators can reach efficiencies of more than 99% in all PM size fractions. However, of critical importance to reach those efficiencies are the dust resistivity, the gas temperature, the chemical composition of the collected PM, and its size distribution (McKenna et al., 2008). Chemical composition affects both the resistivity and permittivity of the particles, while temperature affects their resistivity. All of these factors affect the sparking potential of the precipitator, and thus limit the voltage applied to the discharge electrodes, meaning that a reduced electric field will be present, the result of which is reduced efficiency (McKenna et al., 2008). Collection electrodes can have various shapes, like flat plates, or pipes with cylindrical, square or hexagonal shape (McKenna et al., 2008).

2.4.3. LIMITATIONS OF ELECTROSTATIC PRECIPITATORS

Despite the very high efficiencies that ESPs manage to achieve, there are some particles that still manage to avoid collection: This can be due to design flows, high particle resistivity, high gas flow rate, or some other reasons. The most important reasons which allow particles to escape from electrostatic precipitators will be described in the subchapters that follow.

2.4.3.1. Reverse ionisation (Back Corona)

Reverse ionisation, also widely known as back corona, is the phenomenon where corona of the opposite polarity to that of the discharge electrode is formed on the dust layer of the collection plates, and is driven towards the discharge electrode (Hughes, 1997) (McKenna et al., 2008). This reverse flow of opposite charged ions or electrons causes part of the charge collected by the PM to be neutralized, thus reducing the Coulomb force acting on them and subsequently reducing the efficiency (McKenna et al., 2008). It has also been suggested that the disruption of the space charge near the collection plates reduces the efficiency even further, as in practice the electric field near the collection plates due to the space charge present contributes ~50% of the total electric field (McKenna et al., 2008).

2.4.3.2. Dust reentrainment

Dust reeintrainment in general is the accidental release of already collected dusts. This can happen for various reasons such as during the rapping process, by high gas speed inside the ESP, or even due to electrical reasons.

Heavy dust reentrainment can happen right after the collection electrode rapping in a dry ESP. After the rapping, the dust layer may start breaking up in mid-air, before reaching the hoppers, thus the air flow might pick up some of the dust and reinsert it into the ESP.

Moreover, when the dislodged dust cake falls into the hopper, it will raise some of the dust by impaction and the air flow will pick it up. Even without rapping, the collected particles can be reinserted back into the air flow if there is an air leakage into the hopper (McKenna et al., 2008).

Another way for particles to be released from the collection electrodes is to be eroded by high gas velocities in the ESP. This should be taken into consideration even from the design stage of the ESP, as the cross-section of the ESP must be chosen in such a way as to keep the gas velocity at low levels (McKenna et al., 2008). To avoid this direct erosion case, it has been found that gas velocities should not exceed 10 ft/s (fps). That is why in most ESPs the air speed is less than 8 fps (~2.44 m/s), while for newer designs it is lower still, at a maximum of 4 fps (~1.22 m/s). For fly ash ESPs, air flow speeds have been found to be even lower, at 5 fps (~1.52 m/s) for plate-wire ESP and 3 fps (~0.91 m/s) for flat plate ESPs. The worst case scenario seems to be the direct erosion of particles that do not adhere well to the collection plates, such as low resistivity particles, in which case the air flow speed is chosen to be less than 3 fps (McKenna et al., 2008). Another way of releasing already captured particles into the airflow is by having a particle colliding with the collection plates with such force as to release other particles. In the course of this PhD, air speeds were less than 0.5 m/s, corresponding to about 1.5 fps. However, because of the low concentration of particles in ambient air, which results in very slow buildup of PM on the plates, it was considered that air speed would not constitute a major hindrance on particle collection.

2.4.3.3. Electrical factors

Usually particles with low resistivity are difficult to adhere to the collection electrodes, as they can release their acquired charge easily and thus be released easily from the plates. This is why gas speeds lower than 3 fps are used for such particles. Another way for particles to be released due to electrical reasons is when sparkover occurs, as this disrupts the dust cake formed on the collection electrode (McKenna et al., 2008) (Hughes, 1997). In the tests conducted for this research, it was decided to avoid the spark regime at all costs, not only because of particle reeintrainment, but also because of the corresponding energy losses and ozone production, among others.

A practical problem than can appear, drastically affecting the corona current and thus the efficiency of the ESP, is when heavy particle loading is present. At the first stages of the ESP, the space charge produced by the large number of charged particles, together with the thick particle layer that builds up on the collection plates, suppresses the corona current, and thus the first stages of the ESP are underutilised. To make matters worse, if all parts of an ESP are energised by the same source, most of the current will be drawn from the energizing units near the outlet, which treat cleaner gas and have much cleaner collection plates, depriving even more current from the first stages and thus augmenting the low performance problem (White, 1963). This problem has been tackled in practice by different voltage sources for sectionalizing various stages of the ESP; this however, increases the installation cost. The use of multiple voltage sources, however, has the advantage of being able to apply different voltages for the different sections, that seem appropriate due to the loading present. Having different energisation sections along the face of an ESP is less important, as the dust loading is not expected to fluctuate significantly. Practically, this sectonalisation problem was solved in the past by having half wave rectified voltage at the first stage, and full wave rectified voltage at the last stages (White, 1963). This practical idea is fundamental in the development of the 2-stage design that is used in this thesis, in which the first stage is used, mainly, for charging, while the second for collection purposes.

2.4.3.4. Dust sneakage

This is a design problem of ESPs, rather than a problem that arises due to their everyday operation. Since not all parts are electrified in an ESP, there are areas that are outside the collection field, especially on the top and on the bottom of an ESP (like the plate and electrode support systems, area close to the hoppers etc.). The gas flow that inevitably passes though those areas, will not have its PM charged or even subject to the collection field, thus these particles can sneak out easily and escape. These losses usually place an upper limit on the collection efficiency that can be achieved for a particular ESP design (McKenna et al., 2008). In the present study, the tubular design guarantees that all air should pass through the active treatment zone and exit at the other end, thus it is not possible to have dust sneakage of this type.

2.4.4. DESIGNS OF ESPS

There are many different types of ESPs, which can be categorized based on their constructional design, their cleaning mechanism, or the number of distinct stages they have. In the following subchapters, the different types of ESP will be presented, together with their advantages and disadvantages depending on the application in which they are used.

2.4.4.1. Collection plate design

2.4.4.1.1. Flat plate design

ESPs of this type are composed of a number of chambers, called ducts, which are in essence 2 flat plates acting as collection electrodes. The discharge electrodes, usually wires, lie equidistant between the plates, without exceeding a 5% misalignment from either side (Böhm, 1982). Ducts lie parallel to one another, and are arranged in sections, meaning other set of ducts lie further on in the ESP in a serial arrangement (Böhm, 1982). Each section has its own HV power, and usually is of different type than other sections, however all sections are housed in a common casing (Böhm, 1982).

One of the most common EPS designs found today is the wire-plate topology (McKenna et al., 2008). In this design, the wires are suspended from the top of the installation with weights attached to their other ends to keep them straight (McKenna et al., 2008). These act as energisation electrodes, while in between them are parallel plates which act as collection electrodes (McKenna et al., 2008), and there are usually many ducts in parallel with the air flow (McKenna et al., 2008). The cleaning mechanism can be either wet or dry, with wet cleaning being prevalent among smaller, mobile units, while dry cleaning is common for large, fixed installations (McKenna et al., 2008).

A variant of the above design is the rigid frame ESP, where the energisation electrodes are firmly fixed upon a frame, rather than being simply hang. This eliminates the use of weights to keep them straight. Compared to wire-plate systems, rigid-frame ESPs have a more robust design; however, this comes at a higher capital cost (McKenna et al., 2008). This design is commonly found in the paper industry (McKenna et al., 2008). Other variations of this design can have rigid cylindrical electrodes on a frame, instead of wires. In some cases, even barbed wires or needles are used at regular intervals, as they help in establishing a uniform electric field (McKenna et al., 2008). In some cases, even plates can be used as HV electrodes, or wire mesh plates used as collection electrodes (McKenna et al., 2008).

In practice, 2 arrangements of flat plate ESPs are found depending upon the direction of the air flow, namely horizontal and vertical air flow units (Böhm, 1982). Horizontal units are much more common, however they have the disadvantage of taking up a huge amount of space (Böhm, 1982). Thus, vertical air flow systems were developed in cases of lack of space, or for special applications (Böhm, 1982). However, this arrangement is usually composed of a single section and with the air flow rising (Böhm, 1982). In terms of the discharge electrodes, horizontal air flow units have vertical electrodes, while vertical units have a horizontal electrode arrangement (Böhm, 1982). If used in highly corrosive environments, the electrodes are usually made from stainless steel coated with Pb, or resistant Ni-Cr alloys (Böhm, 1982).

In general, parallel plate design is used for larger air flows, and is mostly used in dry collection processes (Böhm, 1982, White, 1963). They can also be arranged to have either horizontal or vertical air flow (McKenna et al., 2008). Wide electrode spacing is usually preferable, as it creates higher electric field strength due to the increased amount of space charge present. Thus, higher migration velocities can be achieved, increasing the overall efficiency. This also means that less plate area is needed for a particular efficiency level, thus reducing the initial capital costs. Wide electrode spacing has been shown to allow for more variation in the energisation electrode design, and to allow for more uniform current densities (McKenna et al., 2008). In comparison to tubular designs however, the parallel plate design is considered less efficient and more antiquated (Kumar and Mansour, 2002, McKenna et al., 2008), despite the fact that plate type precipitators were developed later compared to tubular ones (Böhm, 1982), possibly to allow for treatment of larger air flows. Therefore, in the course of this PhD, a tubular design was used, as will be discussed in the next subchapter.

2.4.4.1.2. Tubular design

The tubular design consists mostly of a single wire acting as a discharge electrode, which is placed coaxially inside a cylinder that acts as a collection electrode. There could be other approaches like hexagonal (honeycomb as in (Seppälä and Skroch, 2011)) or square collection electrodes that grow in popularity as they can be clustered closer together in the case of parallel ESP modules (McKenna et al., 2008, Böhm, 1982), making the most of the limited industrial space available. However, in such cases, extra care must be taken in choosing the right discharge electrode, as it might cause asymmetrical power distribution that would result in reduced efficiency (McKenna et al., 2008). In addition, in such an arrangement, there must be many HV supply sources in parallel so as to mitigate the detrimental effects of a sparkover, and extra care should be taken to avoid a misalignment of more than 5% between the energisation and collection electrode (Böhm, 1982).

Tubular design is usually applied in small scale, stand-alone applications (McKenna et al., 2008). It is very effective at small gas flows, and for collecting liquid droplets (McKenna et al., 2008, White, 1963), even tar (Böhm, 1982). Thus, it is usually wet cleaned, though dry type ones can also be found (McKenna et al., 2008). In case of wet cleaned and many parallel tubes, the cleaning system should supply uniform water quantities in each tube (Böhm, 1982), as if the water film is not uniform or runs dry, a reduction in efficiency is expected. Air flow can also be up or down the collection electrode alignment (McKenna et al., 2008), however, in the case of the air flowing down, severe reentrainment problems can occur in case of dry cleaning ESPs (Böhm, 1982). Therefore, tubular design is used mainly with wet cleaning arrangements, that require no rapping of the electrodes (Böhm, 1982), or in case it has to be dry cleaned, the gas flow in that section of the ESP that is rapped is shut off (Böhm, 1982). Another disadvantage of such a design is that it is hard to achieve a uniform distribution of the air flow across the cross section of the tube (Böhm, 1982).

2.4.4.2. Number of stages

2.4.4.2.1. Single stage

As the name implies, charging and collection of the PM happens in the same location in a single stage design (McKenna et al., 2008). Also named the “Cottrell type” ESP, it is usually energised by full or half wave rectified voltages, or impulsive voltages (White, 1963). These ESPs are usually energised with voltages ranging from (30 – 100) kV (White, 1963). In the single stage design there is corona current over the full length of the precipitator, thus corona power is much higher compared to double stage designs (White, 1963). Another practical aspect that has been discovered in industry is that a small, single stage tubular design can perform better than larger commercial ESPs, proportionally to their size of course (White, 1963). Thus, it is not a good idea to try to increase the precipitation efficiency by just increasing its length in a single stage design. This has been observed from the early years of ESP development, that by increasing the length of precipitator does not increase precipitation performance, due to the unwanted effects produced by long HV energized sections. Indicative effects, the terminal velocity which characterizes precipitation efficiency as a function of HV electrode length published by (Anderson, 1925), are shown in Figure 2-23. Magnitude of those effects could vary according to ESP design and conditions (White, 1963).

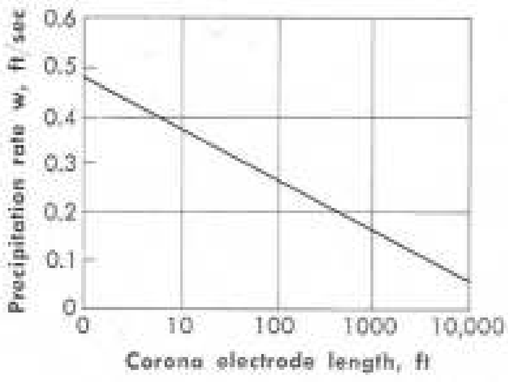

Figure 2-23: Fall in PM terminal velocity inside an ESP, as a function of increased length of energisation electrode, adopted from (Anderson, 1925).

2.4.4.2.2. Double-stage

A double stage precipitator is composed of 2 stages, each playing a completely different role. The first stage is the charging stage, where corona current exists, while the second stage is the collection stage which is energised by a dc voltage below that of corona inception and of lower amplitude compared to the first stage (Böhm, 1982). In contrast with the single stage design, usually dc voltage is used at much lower levels, of the order of (10–15) kV (White, 1963), approaching the theoretical low energy needs for electrostatic precipitation (White, 1963). The second stage is usually narrow (even 8 mm wide), meaning that large fibers can be a cause of sparks (Böhm, 1982). Thus, filters are used to filter fibers or very large particles that might cause sparkover (Böhm, 1982). Double stage precipitators are the preferred choice for low PM loading and PM2.5 particle collection, and are mainly found in air cleaning applications (McKenna et al., 2008, Böhm, 1982), where there is an imperative need for low O_3 production (White, 1963). For positive energisation, O_3 levels as low as 0.005 ppm can be achieved (Böhm, 1982). Thus, this design was used in the course of this work, both in a small and in a scaled-up form, as its purpose was air cleaning. Additionally, in order to reduce power consumption and enhance precipitation efficiency, impulsive voltage was used instead of dc voltage, while for heavy loading, a fine mesh filter was also used. Another positive characteristic of double stage ESPs is that, if specially designed, they have been proven to maintain high levels of efficiency at elevated gas velocities (White and Cole, 1960). However, this is not the norm, as double stage precipitators have higher reeintrainment losses compared to single stage versions (White, 1963). This drawback can be corrected by using wet type cleaning of the collection electrodes, or by coating the collection electrode with an adhesive substance, like oil (White, 1963) which is extensively used for air cleaning applications (White, 1963). This is possible as the particle concentration in ambient air is low, and cleaning intervals can be long, weeks rather than minutes (Böhm, 1982, White, 1963).

2.4.4.3. Classification by means of cleaning

2.4.4.3.1. Dry cleaning

In this cleaning process, dust is removed from the collection electrode by means of rapping the electrodes, either impacting it with specially designed hammers or by vibrating it (McKenna et al., 2008). This is thus done in an intermittent and not continuous fashion. Sonic energy has also been applied for augmenting the removal process (McKenna et al., 2008). Rapping intensity and rapping frequency play an important role in the final ESP efficiency (McKenna et al., 2008), as too much PM might be re-entrained into the airflow if high rapping intensity is applied (Böhm, 1982) (White, 1963), or a large PM cake might create conditions for back corona. A cleaning cycle is usually implemented, where all collection electrodes are rapped once during the cycle and boundary electrodes are never rapped in a row allowing the PM that has been reintroduced into a duct to be recollected successfully (Böhm, 1982). An important problem with solid waste ESP is the waste disposal of collected dusts, which can be tons per day in large pulverized coal fired units (White, 1963, McKenna et al., 2008). Vibration rapping is used for cleaning the energisation electrodes (White, 1963).

2.4.4.3.2. Wet cleaning

In the wet cleaning of ESPs, a liquid is used to keep the collection plates clean (McKenna et al., 2008). It can be used intermittently, the liquid being sprayed upon the electrodes at regular intervals or continuously by having a thin liquid layer covering the collection electrodes at all times (McKenna et al., 2008). The most widely used liquid is water (McKenna et al., 2008), although some other liquids, or even gels ((Nahrwold, 1878) used glycerin) can be used. Thus, there are no hammers, vibrators or hoppers and in their place a drainage system is installed, which transforms the waste disposal problem of dry ESPs into a water pollution one (McKenna et al., 2008).

This cleaning method can be found widely in nature, in humans and other mammals, in the form of the mucociliary film found in most parts of the pulmonary system, as discussed in Appendix B.1. Despite that fact, and the fact that ESP technology has been applied for more than 100 years, wet cleaning still holds many secrets (McKenna et al., 2008, Doonan and Reynolds, 2007) and has not been developed to its full potential. Wet ESPs have been employed mainly for sub-micrometer particulate pollution and even for condensable gases like SO_2 (McKenna et al., 2008). In many cases, the last stage of a wet ESP is a mist eliminator device in order to reduce liquid droplets at the outlet.

One major advantage of the wet ESP is the very low level of particle penetration, as back corona, dust reentrainment or direct erosion do not occur, since there is no rapping or no buildup of particles on the collection electrodes (McKenna et al., 2008). A direct consequence of this is that there is no reduction of the inter-electrode electric field due to collected PM. Another positive characteristic is that PM resistivity does not affect operation, as humidity has the effect of lowering resistivity of PM, in addition to their ability to collect efficiently sticky or explosive PM (McKenna et al., 2008), that constitute a problem and a hazard, respectively, for dry ESPs. Furthermore, the low maintenance costs and high reliability constitute wet ESPs prime candidates as the final stage of gas cleaning in many industrial applications (McKenna et al., 2008). Moreover, wet ESPs can achieve efficiencies of ~99.99% for both PM2.5 and some aerosols, like SO_3, thus they are often found in pulverized coal fired plants, as they can reduce PM output to environmentally acceptable levels, and simultaneously make the output gas flow less opaque (McKenna et al., 2008). Important design considerations to avoid reduced efficiency are also the uniform liquid circulation of the collection electrodes, despite high gas velocities, as any asymmetry or even dryness might cause sparking, increased power consumption and, of course, higher particulate penetration, thus much lower gas flows compared to dry ESPs can be achieved (McKenna et al., 2008). However, the most serious problem for wet ESPs is the significantly higher power needed, compared to dry ESPs (McKenna et al., 2008). It would have been beneficial to use a wet ESP design in the present study, however, due to low particle loading and the fact that a practical application scheme is not imminent, the cleaning system was not taken into account in this research project. In strict terms of minimizing power consumption, a dry ESP would be preferable.

2.4.5. CALCULATION OF ESP EFFICIENCY

2.4.5.1. Deutsch-Anderson equation

The Deutsch-Anderson equation was used for sizing of ESPs from the 1920s until ~1960s (McKenna et al., 2008). The equation was determined both theoretically by Deutsch (Deutsch, 1922) and experimentally by Anderson (Anderson, 1925), independently, and has the form shown in Equation (2.11):

$$\boldsymbol{\eta_p = 1 - e^{-\left(\frac{A \cdot u_d}{Q}\right)}} \tag{2.11}$$

where η_p is the precipitation efficiency, Q is the gas flow rate, u_d is the migration velocity achieved inside the reactor and A is the reactor's collection area. In practice, higher migration velocities correspond to higher precipitation efficiency (White, 1963). How this takes place in pure mathematical form is shown in Figure 2-24. The problem with this approach is that different particles have different migration velocities, thus the Deutsch-Anderson equation can only be applied to narrow size distributions, where the migration speed of all particles can be approximated to be the same, and not for the full size distribution spectrum, unless the PM is mono-dispersed. However, collection efficiency nowadays is not always used in practice, as the EU directives and governmental codes are usually stated in terms of emissions at the outlet, usually in µg/m^3 (Mastropietro, 1997) (European Parliament and Council of the European Union, 2008).

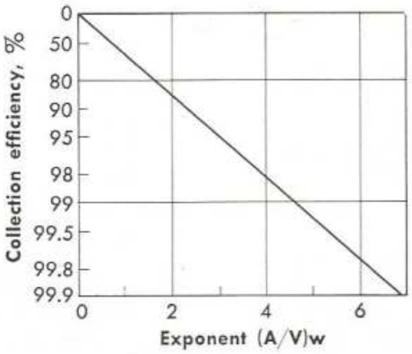

Figure 2-24: Change in efficiency for the Deutsch-Anderson equation, as a function of the exponent term (White, 1963).

The Deutsch-Anderson equation is based on the theoretical assumptions of constant air flow, constant particle concentration across any cross section of the ESP perpendicular to the air flow, and uniform concentration of charge carries. It also presupposes that all particles have the same migration velocity, and that no particles are re-inserted into the airflow after being collected (Lin et al., 2012). Therefore, since theoretical assumptions can vary greatly compared to practical operational conditions, underrating of the actual efficiency has been observed (Yoo et al., 1997) (Kim and Lee, 1999) (Park and Chun, 2002). Thus, the Deutsch-Anderson equation was supplemented with a correction factor by Matts and Öhnfeldt in order to make more accurate predictions (Matts and Öhnfeldt, 1964), as it was pointed out that calculated migration velocity was consistently lower compared to experimental data (Riehle and Löffler, 1993), and therefore the equation could not be used to accurately calculate PM migration velocity.

2.4.5.2. Modified Deutsch-Anderson equation or Matts-Öhnfeldt equation

Based on the Weibull distribution (Bäck, 2013), Matts and Öhnfeldt introduced a modification factor k to the Deutsch-Anderson equation (Matts and Öhnfeldt, 1964). This formula was the backbone of empirical ESP sizing for the last half century. Depending on the particular application, k can range from 0.4 (Lin et al., 2012) up to 0.8 (McKenna et al., 2008).

It was claimed that by using this formula to calculate the migration velocity, and then making a plot of resident time vs emission output estimation, is one of the best ways of sizing ESPs (Mastropietro, 1997). However, many scientists, including Anderson himself, have abandoned the concept of using treatment time, and decades later scientists were of the opinion that there is little proof, either theoretical or experimental, of treatment time to significantly correlate with efficiency (White, 1963), as the vast majority of particles acquire their saturation charge pretty fast (in the range of few 100s µs as shown in 4.5). The theoretical proof is that treatment time is in essence the ratio of the total volume of the precipitator over the gas flow rate (White, 1963). The migration velocity, on the other hand, has been found to be directly proportional to the corona power injected into the system (White, 1963): $W = k1(Pc/A)$, where Pc is the corona power, A is the collection area of the ESP, $k1$ is a constant and w is the migration velocity. The energisation voltage is the most important factor affecting efficiency (White, 1963).

2.4.5.3. Specific collection area method

One modern method for ESP efficiency estimations is the specific collection area (SCA) method. The SCA is actually the ratio of the negative Napierian logarithm (or natural) of the fractional penetration ($1–\eta$) over the PM migration velocity (McKenna et al., 2008). It can be shown that it is proportional to the ratio of the total area of the collection plates over the gas flow rate (McKenna et al., 2008). The SCA is composed of 15 distinct complicated calculation steps and, if found, gives a close approximation of the size of the unit needed, thus the ESPs' initial capital, maintenance and annual costs can be effectively calculated (McKenna et al., 2008). However, this procedure is used for large (industrial) scale, wire or flat plate ESPs (McKenna et al., 2008). Thus, it is of no use for the smaller, two-stage tubular ESPs that were used in the current research, and it will not be analysed any further. Additional information, as well as the whole SCA calculation procedure can be found in (McKenna et al., 2008).

Another point of note regarding this approach is that newer ESPs with lower SCA can have higher efficiencies compared to older ESPs with higher SCA because of the use of optimized topologies corresponding to higher electric field and corona current (McKenna et al., 2008), or perhaps with the addition of wet cleaning technology. Thus, it is not safe to draw conclusions simply by comparing the SCA of ESPs.

2.4.6. ENERGY CONSIDERATIONS

There are different ways to calculate the energy consumption of ESPs. One of the ways used extensively from the past is by calculating the ratio of power per volume of treated air (White, 1963). A similar approach is sometimes taken, by calculating the specific energy needed to clean a particular volume of air, expressed in J/m^3 (Kim et al., 2010, Bologa et al., 2007, Liqian et al., 1996). Both ways have been used in the current research.

Another approach to expressing the power consumption of an ESP is by calculating the ratio of the corona power over the area of the collection plates. However, this can be affected by properties of the PM to be collected, especially their resistivity, and by electrical factors like the sparking rate (White, 1963).

In general, current density for tubular precipitators is many times higher compared to parallel plate precipitators with the same interelectrode distance (White, 1963). This higher power injected in the tubular design is expected to aid in the precipitation of the difficult to capture PM2.5. The reasons for higher current densities in a particular design compared to normal operation might be low particulate loading of the air flow, very low resistivity PM, low gas temperatures or short interelectrode distances (White, 1963). In terms of power losses, it is not acceptable in practice to have more than 2% of the supplied power lost to back corona or sparking (White, 1963).

2.4.7. PARTICULATE MATTER

The amount and size distribution of PM in the air flow is of prime importance in trying to estimate the efficiency of an ESP. One of the most important characteristics is the particle loading of the air flow, which if increased, can decrease the ESP efficiency considerably (McKenna et al., 2008). This happens due to the space charge quenching phenomenon, where despite the high voltage present, the current remains low, causing insufficient charging of PM and thus reduced efficiency (McKenna et al., 2008). This is especially prevalent if, in addition to the heavy loading, large amounts of PM2.5 are also present (McKenna et al., 2008). In addition, the size distribution of the suspended particulate plays an important role in the final ESP efficiency, as it depends upon the size of the PM (McKenna et al., 2008). The size distribution of PM, as discussed in Section 2.1.2, follows a log normal distribution, its main parameters being the mass median diameter and the standard deviation (McKenna et al., 2008). As its name implies, the mass median diameter represents the particle size that has half of the particles smaller than it, while the other half are larger (McKenna et al., 2008).

The properties of the particulate matter can influence the efficiency of ESPs. Despite the fact that sticky particles and fog droplets can be easily collected, they cannot be easily detached from the collection plates, unless a wet ESP is used (McKenna et al., 2008). As it had been analysed, highly resistive PM can lead to reduced efficiency and severe effects, like back corona and excessive sparking (McKenna et al., 2008). In practice, maximum value of particle resistivity should be $2 \cdot 10^{10}$ Ωcm for the normal operation of an ESP (White, 1963). This is explained by the fact that particles with high resistivity cannot release their charge easily to the collection plates, thus the charge acquired impedes the flow of charged PM and ions (White, 1963). This causes a reduction of corona current and electric field, reducing the precipitation efficiency (White, 1963). On the other hand, if the PM is of high conductivity, such as carbon particles, they may exhibit a strange effect, called the pith-ball effect, where instead of being attracted to the collection electrodes, they become attached to the charging electrodes instead (White, 1963). The physics behind this phenomenon will be explained in Sections 4 and 5, as it depends on the combination of the dielectric constant and electrical conductivity of particle and medium. However, even if the low resistivity PM gets to the collection electrodes, they can release their charge easily, thus they get reentrained in the case of a dry ESP. Dry ESPs are also prone to explosions if flammable or explosive PM is being collected (McKenna et al., 2008).

Gas properties also affect efficiency, as they can affect the PM that is to be collected. For example, higher temperatures affect viscosity and thus the drag force of the airborne particles and also the resistivity of PM. In special cases, if the gas flow is acidic and humid, H_2SO_4 is absorbed by the PM (McKenna et al., 2008). As in earlier subchapters, the gas flow volume is of prime importance in calculating the SCA, and thus making an estimate of the collection area required (McKenna et al., 2008).

2.4.8. ADVANTAGES AND DISADVANTAGES OF ESPS

Electrostatic precipitation has numerous and crucial advantages compared to other air cleaning methods, it is therefore no wonder that it is used for so many applications, especially when pollution consisting of fine and ultrafine particles needs to be combated. Additionally, the collection efficiency of ESPs is high compared to other methods not only for the smaller fraction of PM, but the whole PM size spectrum (McKenna et al., 2008). A comparison with other cleaning methods regarding the level of efficiency over a wide spectrum of particle size ranges can be seen in Figure 2-25.

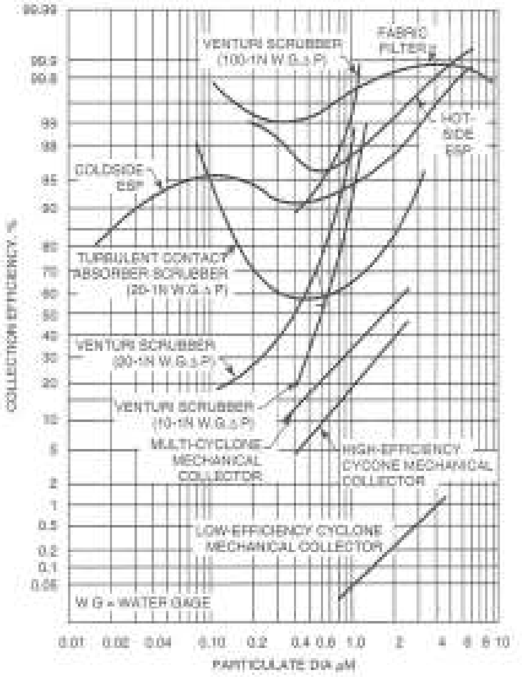

Figure 2-25: Collection efficiencies for various air cleaning methods as a function of PM size (McKenna et al., 2008).

Additionally, ESPs exhibit desirable operational characteristics like low pressure drops; treatment of air flows with a wide variety of temperatures and laden with a wide variety of PM like mists, dusts or fumes; and low operational costs (McKenna et al., 2008). Low operational costs and pressure drop can be attributed to the fact that the collection forces are exerted only on PM and not to the whole air flow as in the case of other cleaning methods (McKenna et al., 2008, White, 1963). For example in cyclones, the energy is used to accelerate the whole air flow, and a small proportion of it is utilized by the centrifugal forces to separate PM successfully (White, 1963). Lastly, there has been an extensive use of precipitation in the last century, thus a lot of theoretical and engineering solutions have been found for various cases (McKenna et al., 2008).

Disadvantages in using ESPs include the fact that they require huge volumes, as higher efficiencies are achieved with lower air speeds, and significant capital investments. Moreover, despite the fact that they can handle different types of particles and operating conditions, any change of the particulate laden gas properties that it was designed for will degrade performance. Thus, industries that have shifting emissions are not best suited for utilizing ESPs. In addition, for dry ESPs that are used more commonly, there is a problem with collecting particles of high resistivity as well as handling and disposal of the huge amounts of collected dusts. Even in the case of wet ESPs, the solid waste problem is transformed to a water pollution one (McKenna et al., 2008). A comparison list of various air-cleaning methods is summarised in Table 2-3.

Table 2-3: Comparisons of various air-cleaning methods (Bologa et al., 2007).

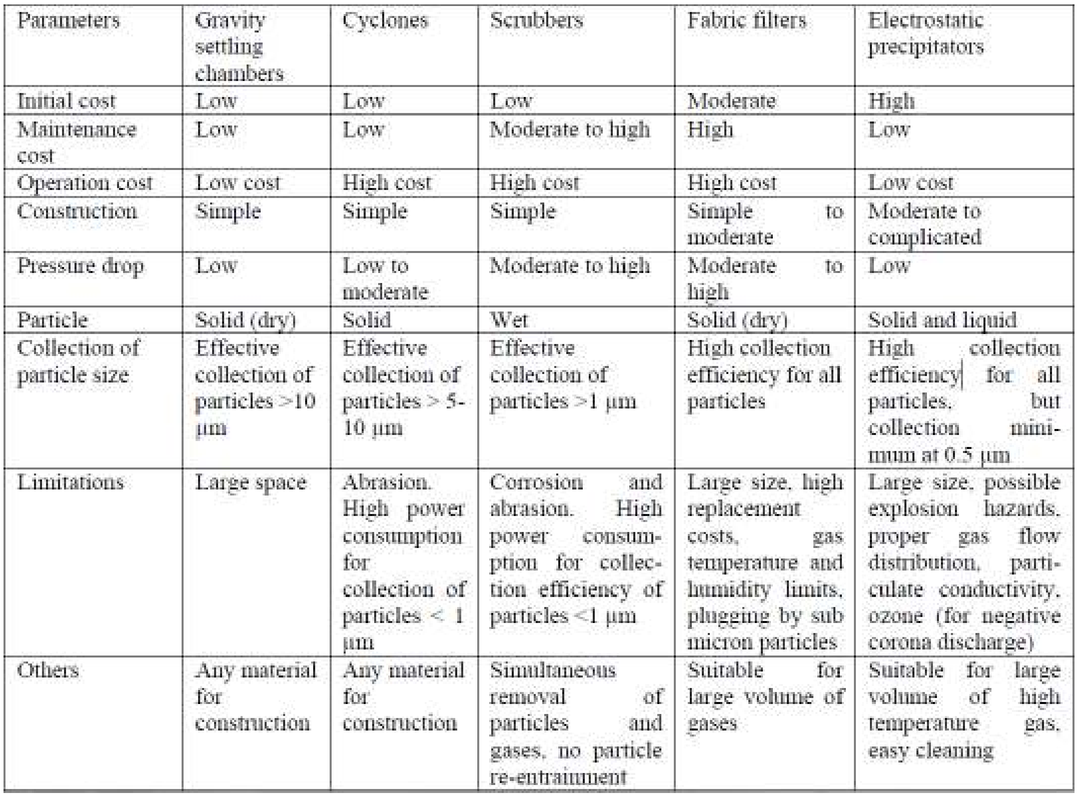

Parameters	Gravity settling chambers	Cyclones	Scrubbers	Fabric filters	Electrostatic precipitators
Initial cost	Low	Low	Low	Moderate	High
Maintenance cost	Low	Low	Moderate to high	High	Low
Operation cost	Low cost	High cost	High cost	High cost	Low cost
Construction	Simple	Simple	Simple	Simple to moderate	Moderate to complicated
Pressure drop	Low	Low to moderate	Moderate to high	Moderate to high	Low
Particle	Solid (dry)	Solid	Wet	Solid (dry)	Solid and liquid
Collection of particle size	Effective collection of particles >10 µm	Effective collection of particles > 5-10 µm	Effective collection of particles >1 µm	High collection efficiency for all particles	High collection efficiency for all particles, but collection minimum at 0.5 µm
Limitations	Large space	Abrasion. High power consumption for collection of particles < 1 µm	Corrosion and abrasion. High power consumption for collection efficiency of particles <1 µm	Large size, high replacement costs, gas temperature and humidity limits, plugging by sub micron particles	Large size, possible explosion hazards, proper gas flow distribution, particulate conductivity, ozone (for negative corona discharge)
Others	Any material for construction	Any material for construction	Simultaneous removal of particles and gases, no particle re-entrainment	Suitable for large volume of gases	Suitable for large volume of high temperature gas, easy cleaning

It has been shown that fabric filters have the highest available efficiency for PM2.5 (McKenna et al., 2008), in addition to the lower initial costs associated in comparison with an ESP (McKenna et al., 2008). It also simultaneously tackles the problem of airborne particulates and acidic gases (McKenna et al., 2008). However, they have high maintenance, operational and replacement costs compared to ESPs. In addition, disposal of the collected material would require manual intervention, in contrast to ESPs, where this can be done automatically.

2.5. CONCLUSIONS

In this literature review, types of particles and their suspensions were defined, in order to give the standard nomenclature used in the literature. Fundamental aspects of natural removal of PM from the atmosphere were presented, as these represent a source of inspiration for the development of ways to clean air flows. A review of the methods of removal of PM from atmospheric air was conducted, giving special consideration to ESP. The main aspects of the breakdown mechanisms of gaseous dielectrics were discussed, and special attention was paid to corona discharge, as this is the main charging mechanism inside an ESP, and thus of prime importance to ESP operation. Particle charging and collection in ESPs has been presented together with limitations of the ESP air cleaning method. A plethora of ESPs have been also presented, based on their design, number of stages and cleaning mechanisms used. Moreover, methods of calculating the collection efficiency proposed in the literature have been presented and discussed. Lastly, energy considerations have been discussed as they are of particular importance for modern energy efficient systems and the chapter closed with a summary of the advantages and disadvantages of the ESP method.

This thesis presents a new approach to the energisation of an ESP, namely using short impulses to charge the airborne PM, thus accomplishing it in an efficient manner, while the design is one used extensively and proven for its many advantages for air-cleaning applications. In the following chapters, this thesis discusses the experiments conducted using 2 different configurations, single and double stage, and a scaled-up version of the double stage precipitatior.

3. SINGLE STAGE PRECIPITATION REACTOR

The first phase of this research project was focused on the development of a precipitation system and efficient energisation method for removal of coarse particles from air flows (PM of a few micrometers and larger in diameter). Although modern commercial electrostatic precipitators can provide a relatively high efficiency of precipitation of coarse particles, it is important to increase the energy efficiency of this precipitation process and to optimise the topology of the precipitation system. The present work is focused on the development of small scale precipitation reactor to remove particles in the range from 100 nm to 2.5 µm. A novel energisation method has been proposed in this research project in order to minimise the energy consumption of the precipitation process. This method is based on the superposition of impulsive charging and dc stresses, in order to provide more efficient charge transfer to airborne particles during the action of short (sub-µs duration), high voltage impulses, with the subsequent removal of these charged particles by a lower magnitude dc electric field. Short impulses allow the application of higher voltages to the ionisation electrodes of a precipitation system without the initiation of electrical breakdown. These higher levels of electric field generate higher ionic concentrations, resulting in more efficient charging of the airborne particles, which helps to improve precipitation efficiency.

A precipitation system consisting of HV and grounded electrodes in a coaxial topology was developed. In order to energise this coaxial precipitation reactor with a superposition of short high field impulses and steady state dc electric field, a novel pulsed and dc power driving system was designed and developed. The present work is focused on analysis of the behaviour of positive impulsive corona discharges in a coaxial reactor designed for precipitation studies. Chapter 3 presents the results of an investigation into the efficiency of precipitation of coarse and fine PM suspended in the air flow. In order to optimise the energisation parameters of the coaxial reactor, and thus to optimise its precipitation performance, breakdown voltage, corona ignition voltage, and the parameters of the impulsive corona discharges were obtained under different energisation regimes. It has been established experimentally that the positive or negative charging regimes play an important role in the precipitation efficiency. *I(V)* curves were obtained for both positive and negative polarities, in order to establish safe energisation voltage levels. Analytical studies for the electric field distribution have been conducted by using the ELECTRO electrostatic software package in order to investigate the suitability of various HV electrodes. The efficiency of precipitation of coarse and fine (PM2.5) particles has been investigated by applying different dc and impulse voltage levels, in order to establish optimal energisation modes.

3.1. DESIGN OF THE SINGLE STAGE REACTOR

The precipitation reactor designed in this study has a coaxial topology. In this single stage topology, charging of airborne particles by impulsive corona discharges and their transportation in the electric field toward the collection (grounded) electrode take place in the same cylindrical volume. This topology has been selected as it is known that it provides high precipitation efficiency in conventional small scale, stand-alone ESP systems (McKenna et al., 2008). Coaxial topology also allows the electric field to be calculated, which will be necessary for further optimisation of the energisation of the system, and for analysis of the kinetic behaviour of solid particles in the reactor. In addition to the above, the coaxial design combined with the inlet/outlet configurations can guarantee a minimum amount of PM sneakage (PM that pass through the reactor without being subject to its electric field, see section 2.4.3.4).

The µ-ESP energisation circuit used in the present study is shown in Figure 3-1. In the centre of the reactor, an M3 stainless steel threaded rod, acting as a plasma-generation high voltage electrode, is placed coaxially and is connected to the HV power supply. At one end, the rod is attached to the top part of the reactor, while the other end has a 5 mm diameter brass sphere attached, to decrease the non-uniformity of the topology and thus the electric field. The particle collection electrode is the internal surface of a 200 mm long stainless steel tube, with an internal diameter of 28 mm. Attached on each end are 2 PVC flanges, having an external diameter of 60 mm, that can be opened in order to have access to the internal surface of the grounded electrode, so that precipitated particles can be collected and the reactor cleaned. The right hand (inlet) flange on Figure 3-1 has four air inlet holes of 6 mm diameter, while the outlet flange (shown on the left of Figure 3-1) has a 12.7 mm internal diameter outlet, connected through flexible tubing straight to the exhaust, forcing the particle laden air to flow from the top to the bottom of the reactor (from right to left as viewed in Figure 3-1).

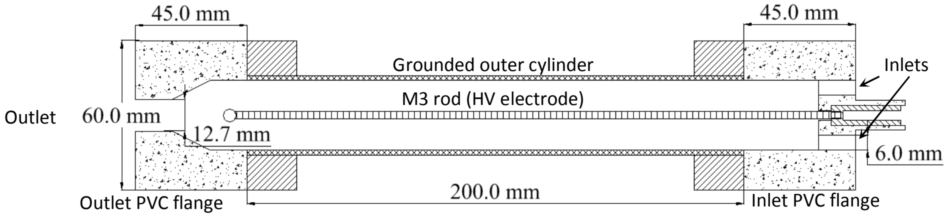

Figure 3-1: Cross section of the single stage precipitation reactor. The reactor was located vertically for testing, with the inlet side on the top.

The high voltage electrode of the reactor, that produced corona discharges, was charged with HV impulses superimposed on a dc voltage. This had the effect of decreasing the overvoltage duration so as to be able to increase overvoltage levels without breakdown occurring. The overvoltage above the breakdown levels of the gap is important, as it increases the charge that can be acquired by the PM, as discussed in Section 2.4.2.1.4.

The precipitation reactor is represented by the electrical circuit in Figure 3-2 as a capacitance in parallel with a resistance. The reactor has an intrinsic capacitance due to its cylindrical shape, while the resistance is that of the corona discharges formed between the electrodes.

The capacitance of the reactor was calculated theoretically, in order to calculate the relaxation time of the reactor and to model the whole energisation circuit. The capacitance of the coaxial reactor has been calculated using equation (3.1) (Buck and Hayt, 2001):

$$\boldsymbol{C = \frac{2\cdot\pi\varepsilon_0\varepsilon_r l}{ln\left(\frac{\beta}{a}\right)}} \tag{3.1}$$

where α is the diameter of the stainless steel threaded rod used as high voltage electrode ($\alpha = 3\cdot10^{-3}$ m), β is the internal diameter of the stainless steel tube that acts as collecting electrode ($\beta = 2.84\cdot10^{-2}$ m), ℓ is the length of the reactor (0.2 m), ε_0 is the permittivity of free space ($8.854\cdot10^{-12}$ F/m) and ε_r is the relative permittivity of air which equals 1. Substituting these values in (3.1) the value of C is 5 pF. Resistance R is that of the drifting ions produced by the impulse inside the reactor and is transient in nature.

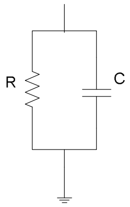

Figure 3-2: Electric equivalent of the single stage reactor.

3.2. ELECTROSTATIC ANALYSIS OF ELECTRIC FIELD IN THE REACTOR

As discussed in Section 2.4.2.3, in order for the airborne particles to be electrostatically precipitated, electrical charges should exist in the inter-electrode gap, the region that the particle laden air flow passes through. To this end, rod shape and voltage applied on the rod should be such that charged carriers are produced, without breakdown occurring, and without excessive power losses.

In order to determine the voltage levels required to yield an elevated electric field in the inter-electrode gap, capable of charging effectively the particles suspended in the air flow without reaching the breakdown levels of the inter-electrode gap (providing ignition of the corona discharge for production of ions during intensive charging), a theoretical investigation and electric field simulations have been conducted. In these analyses, various types of electrodes have been compared, in order to identify the most suitable electrode topology (in terms of corona inception voltage, breakdown voltage and ease of manufacturing and installation).

Electric field simulations inside the reactor have been conducted for the present topology using the “ELECTRO 2D/RS” electrostatic field simulation package by INTEGRATED Engineering Software Ltd. Simulation runs were conducted with various types of electrode configurations, based around the M3 threaded rod acting as the high voltage electrode. This was done as the thread introduces non-uniformity into the coaxial electric field, therefore, it was imperative to know the electric field enhancement compared to a smooth rod of equal diameter and other electrode variants, like a smooth rod with a single M3 thread; a rod with a similar thread, protruding 1 cm above the rod’s surface; a smooth

1.5 mm diameter rod; and a 125 μm diameter metal wire. Through these simulations, the choice of using an M3 threaded rod was justified, as it resulted in a higher electric field close to the rod compared with the smooth (3 mm or 1.5 mm) rods, it can sustain higher breakdown voltages compared to long and sharp protrusions (as inter-electrode distance is decreased in the latter case), it has higher electric field at most points along its length compared to a single thread on a smooth rod, and it is much easier to manufacture, install and maintain compared to a very thin metallic string. In addition, it can sustain higher electric field before breakdown occurs compared to the smooth rod with a single 1 cm protrusion. Finally, it has a higher electric field compared to all electrodes examined further away from the HV rod and close to the collection electrode, as seen in Figure 3-3, which shows the electric field as a function of distance between the high voltage electrode and the outer earthed cylinder. This is important in the transportation and collection of the charged PM. Figure 3-5 shows that a 3 mm diameter smooth rod does not produce fields above $3.35 \cdot 10^6$ V/m, however the electric field will be above $5.6 \cdot 10^6$ V/m in the case of M3 rod. These simulation results verify the selection of an M3 rod as an HV electrode. The energisation voltage applied during these simulations was set at an arbitrary value of +11 kV, which is less than the gap's breakdown voltage.

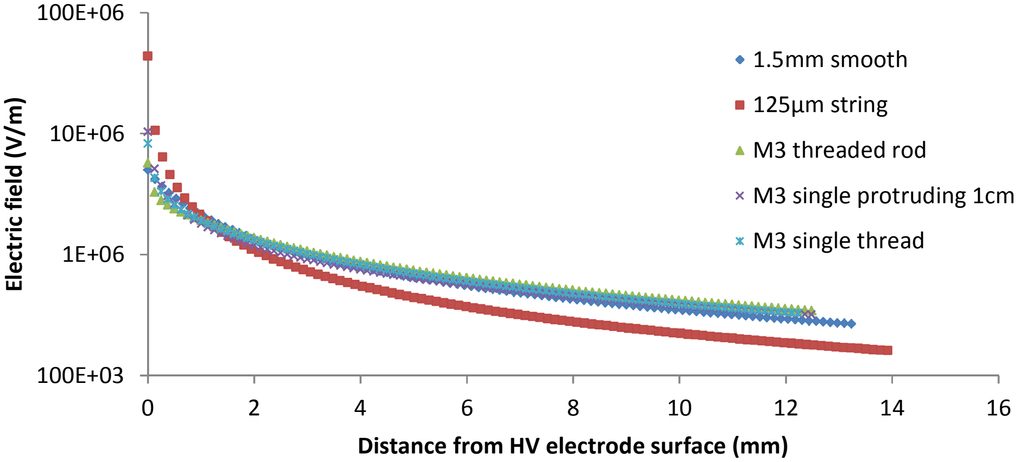

Figure 3-3: Maximum electric field as a function of distance from the electrode surface for various energisation electrodes (high voltage central rods). Energisation voltage had an arbitrary value of +11 kV.

In Figure 3-3 comparison of the electric field produced has been conducted at points at equal distance from the electrodes surface, and not at equal distance from the HV electrode center (which is the axis of symmetry of the reactor). This was conducted, in order to compare directly the electric field at the surface of various types of HV electrodes, as for equal distances from the electrodes centers of symmetry, points directly above the surface of thinner electrodes, might correspond to points inside wider electrodes. This is the reason behind having more datapoints for some electrodes, compared to others, as they all terminate on the internal surface of the collection electrode (earthed cylinder), whose diameter was fixed at 28 mm.

Simulations, therefore, continued with an M3 rod as the central HV electrode, and the results of these simulations are shown in Figure 3-3 and Figure 3-4. The magnitudes of the electric field parallel to the rod at various distances from the rod are shown in Figure 3-4, where X-axis represents the double the length of an M3 pitch (length from one thread to another, which is equal to 0.5 mm (British Standards, 1998)). In Figure 3-5, the *E*-field has been plotted starting from 0.01 mm from the rod and ending 0.01 mm from the earthed cylinder. The *E*-field for a 3 mm diameter smooth rod has also been plotted. It can be seen that the thread of the M3 rod significantly increases the electric field at distances up to 0.125 mm. From then onwards, the *E*-field is almost the same as with a smooth rod with the same diameter. In both plots, +11 kV energisation voltage was applied.

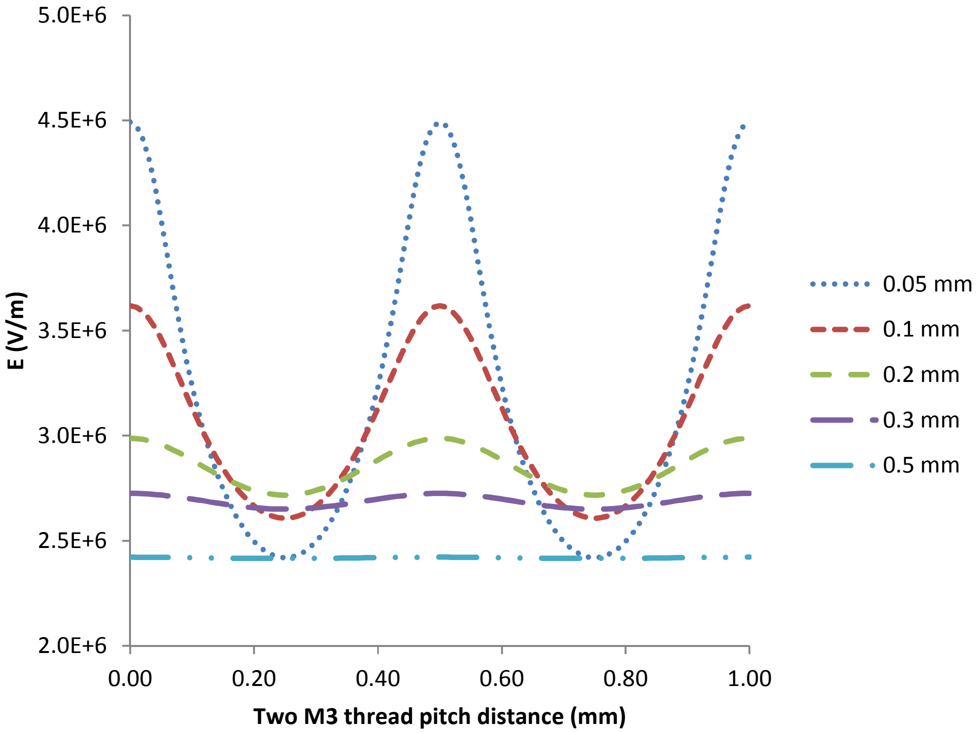

Figure 3-4: Electric field at distances of 0.05, 0.1, 0.2, 0.3, and 0.5 mm from the external part of the M3 threaded rod. Energisation voltage is +11 kV.

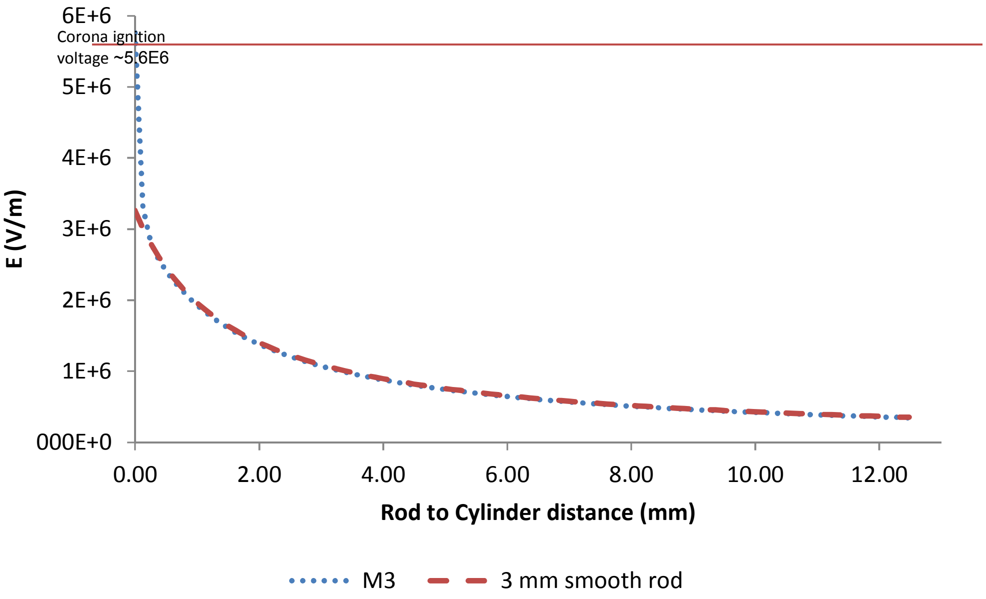

Figure 3-5: Electric field from 0.01 mm from the external part of the M3 threaded rod up to 0.01 mm from the internal surface of the cylinder. Energisation voltage is +11 kV.

In order for corona discharge to commence, the electric field near the protrusion should be sufficiently high, above ~30 kV/cm in atmospheric air, so that the number of new electrons produced by the avalanche mechanism is greater than the number that get recombined, meaning the ionisation coefficient α is higher than the attachment coefficient β. Due to the fact that positive and negative corona differ in their formation mechanisms (Raizer, 1991), in the topology used, negative corona had a ~10% lower inception voltage compared to the positive energisation case.

In order to calculate the electric field required for the coaxial topology used, Peek's phenomenological equation was used. (Raizer, 1991) and (Morrow, 1997) present Peek's equation for cylindrical topology in different forms, and by inserting the dimensions of the reactor used, ~56 kV/cm is calculated by Raizer's formula (Raizer, 1991), and ~64 kV/cm by using Morrow's formula (Morrow, 1997), the latter requiring first and the second Townsend coefficients for air. Despite the small divergence of the corona inception voltage based on (Raizer, 1991) and (Morrow, 1997), the solutions converge for distances greater than ~0.3 mm from the surface of the high voltage electrode.

From Figure 3-4 and Figure 3-5, +11 kV does not produce a high enough electric field for the corona to ignite, however, if the charging voltage is increased to +15 kV, then the corresponding field increase can be seen in Figure 3-6, which is high enough for corona inception according to the theoretical calculations performed.

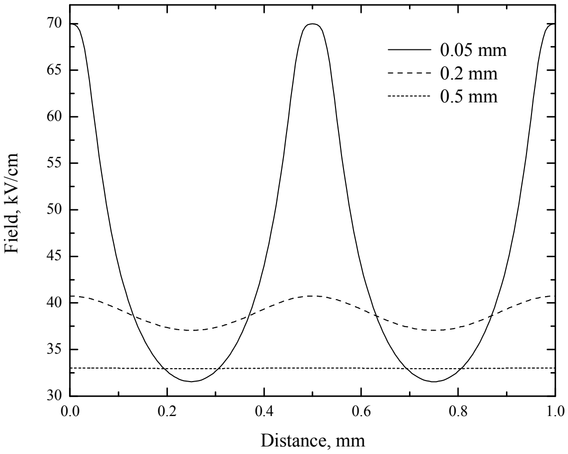

Figure 3-6: Electric field at distances of 0.05 mm, 0.2 mm, and 0.5 mm from the M3 threaded rod and parallel to it, drawn in ORIGIN 8.5. Energisation potential is +15 kV. The x-axis represents double the M3 pitch. Adapted from (Mermigkas et al., 2012).

As can be seen from Figure 3-6, the energisation voltage of +15 kV is enough to satisfy corona initiation requirements, *E* > 30 kV/cm. The ionisation zone (where generation of charges takes place) is very narrow, at only 0.23 cm around the edge of the high voltage electrode; however, the ions migrate towards the earthed electrode, through the ion transport zone, due to the electric field present, and thus charge the particulate matter as it passes through the reactor. Power consumption will be calculated and discussed in Section 4.9.

3.3. SUPERPOSITION ENERGISATION SYSTEM

For energisation of the coaxial reactor with the combination of HV impulses and dc voltage, an energisation system was designed and constructed. This system consists of a Blumlein pulse generator, dc charging circuit and the precipitation reactor. A circuit diagram of the precipitation energisation system together with the coaxial reactor is shown in Figure 3-7.

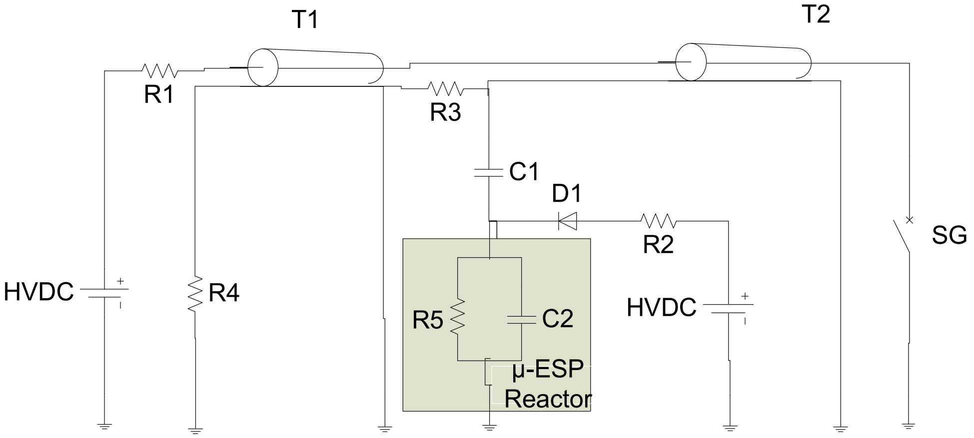

Figure 3-7: The circuit diagram of the HV energisation system used to generate HV impulses superimposed on dc voltage.

The Blumlein impulse generator is composed of 2 coaxial transmission lines, T1 and T2, each of them consisting of 25 m of URM67 coaxial cable, having characteristic impedance of 50 Ω, wrapped around a PVC cylinder (former) with an external diameter of 22 cm, for structural purposes. This length of cable was chosen so as to produce ~250 ns HV impulses. The impulse duration is equal to the 2-way transit time, the transit time along the URM67 cable can be obtained using the following equation (Wilson, 2011, Buck and Hayt, 2001):

$$\boldsymbol{u} = \frac{\boldsymbol{c}}{\sqrt{\boldsymbol{\mu_r} \cdot \boldsymbol{\varepsilon_r}}} \tag{3.2}$$

where c is the speed of light in vacuum, μ_r is the relative magnetic permeability and ε_r is the dielectric constant of the insulation of the coaxial cable (URM67 uses polyethylene, thus μ_r is 1 and ε_r is 2.2 respectively). This corresponds to a propagation time u inside the Blumlein of ~4.994 ns/m. Thus, the 2-way transit time is ~250 ns.

Two separate dc power supplies (Glassman High Voltage Inc., USA) were used to energise the Blumlein generator and to provide the dc energisation component to the plasma reactor. These dc supplies were connected to the circuit through current limiting charging (protection) resistors, R1 and R2 each having a nominal value of 1 MΩ and made of 100 Meggitt SBCHE 15 CGS 10k J CF HF individual ceramic resistors in series (TE Connectivity, Schaffhausen, Switzerland). The dc voltage source, V1, was used to charge the Blumlein generator through the charging resistor R1 (1 MΩ). By closing the air-filled plasma switch, SG, the Blumlein generator produces a HV impulse with polarity opposite to polarity of the dc charging unit, since the Blumlein generator has an inverting topology.

The magnitude of the HV impulses was adjusted by varying the dc charging voltage, V1, and the resistance of R3. It was found experimentally that in the case that R3 = 150 Ω, this circuit produces HV impulses with magnitude equal to the charging dc voltage, V1.

The pulse repetition rate of the Blumlein was controlled by the plasma closing switch (SG). Two different switches were used in the present work: a self-closing switch and a triggered switch (trigatron). In the case of self-closing configuration, the switch consisted of two electrodes separated by a gas gap, filled with atmospheric air at elevated pressures (up to 4 bar gauge). This switch was stressed with rising dc voltage until a breakdown event occurred and the switch closed. In this way, the pulse repetition rate was 10 pps. An air-filled trigatron switch was also used, in order to provide higher pulse repetition rate. The trigatron was triggered with an external trigger generator, and in this case a pulse repetition rate of 50 pps was used.

The outer conductors of the Blumlein generator where earthed, one directly and the other with a 50 Ω resistor (R4) for matching purposes, in order to avoid power losses and reflections.

The μ-ESP cylindrical reactor, which is represented in Figure 3-7 by capacitor C2 and resistor R5, was connected to the Blumlein generator through capacitor C1 and the dc charging part of the circuit. Thus, superposition of the dc voltage and HV sub-μs impulses was achieved.

The dc part of the energising circuit was decoupled from the impulsive part (Blumlein generator) by the use of two 1 nF capacitors (NWL Capacitors, USA, max voltage withstand 70 kV dc) connected in series and a HV diode, D1, (6HV50K, HVCA, USA). The capacitors were substituted with 13 ceramic ones (30 kV dc, 2700 pF, Morgan Electro Ceramics Ltd, UK). The total capacitance of the decoupling capacitor C1 was 500 nF, later changed to 212 pF. The capacitor C1 stops the dc voltage from leaking to the impulsive energisation circuit, while diode D1 stops the positive impulses from penetrating the dc energisation circuit. Each of the resistors had a resistance of 10 Ω and had a maximum power of 17 W.

Voltage measurements were conducted with a Tektronix P6015A HV probe (Tektronix, USA), having a 1000:1 voltage division ratio and 75 MHz bandwidth, or with a TES-TEC (max 40 kV dc, ~3 dB at 300 Hz, TESTEC Elektronik, Germany) dc probe, while for current measurements a Pearson 6585 current monitor (Pearson Electronics, Inc., Palo Alto, CA) with 250 MHz bandwidth and sensitivity of 0.5 V/A into a 50 Ω load was used. The peak measuring current of the Pearson 6585 must not exceed 500 A, while its rms current rating is 10 A. Both diagnostic devices were connected to a Tektronix TDS 3032 digital phosphor oscilloscope (Tektronix, USA), having bandwidth of 500 MHz and a sampling rate of 2.5 GS/s. Voltage probe was connected on top of the reactor, between capacitor C1 and diode D1, in order to record both dc and impulsive current, while current probe was connected between the μ-ESP reactor and the earth point.

3.4. DC ELECTRICAL CHARACTERISTICS OF THE REACTOR

In order to determine the dc voltage level to be used for precipitation experiments, *I(V)* curves in atmospheric air were obtained, in order to determine the corona onset voltages and power losses. Therefore, current-voltage measurements were conducted in order to obtain the *I(V)* curves for positive and negative dc polarity respectively (using atmospheric air at room temperature as test fluid). At least 6 independent experimental runs were undertaken for each polarity. Current was calculated by measuring the voltage drop across a 1 kΩ current viewing resistor connected between the reactor and earth. The *I(V)* curves were drawn in the same graph for each polarity and trend lines were fitted using Equation (3.3). The I_0 and V_0 coefficients for these analytical fitting lines were calculated. In the case of negative energisation, I_0 and V_0 corona coefficients were obtained for two cases: for low currents, close to the corona ignition current (few μA levels) and for higher currents. The results of investigation of the corona *I(V)* characteristics for both conditions are given in Sections 3.4.1 and 3.4.2.

3.4.1. POSITIVE ENERGISATION: I(V) CHARACTERISTICS

As described in Section 2.4.2.2.5, positive corona discharge has several distinctive phases. At first, just below the dc corona inception level, self-extinguishing streamers appeared even at +13 kV (with or without air flow), with corresponding current impulses. These initial steamers or burst pulses were small and did not manage to bridge the inter-electrode gap (with very few exceptions). As the voltage was increased (~17 kV), dc corona current appeared, entering the glow discharge phase and the current impulses started to get increasingly smaller. At higher voltages, the corona current wave form was much smoother, appearing almost sinusoidal in waveshape, and spark breakdowns occurred very rarely. It was only at much higher voltages (>18.5 kV) that breakdowns started to occur again. An explanation of this burse pulse phenomenon (1st stage of positive corona corresponding to Figure 3-9) in positive corona can be seen in the Figure 3-8. This can be seen clearly in the waveforms that follow (Figure 3-9 to Figure 3-11) where: the cyan trace is the current from the current viewing resistor; the magenta trace is the voltage from the TES-TEC probe and the green trace is the current from the Pearson current monitor.

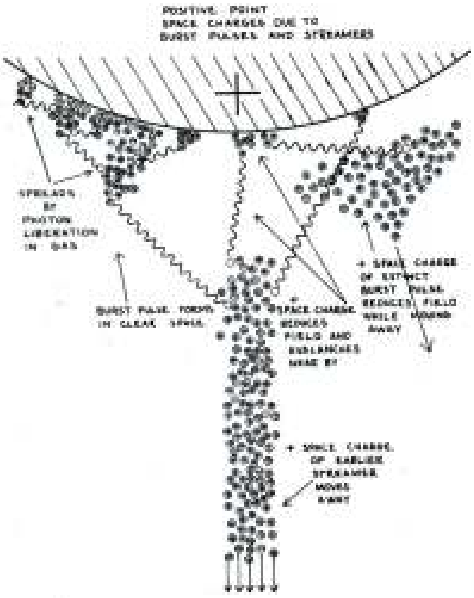

Figure 3-8: Self-extinguishing initial streamers as explained by (Loeb, 1965).

As the field increases, the first successful avalanches start to form around the high field electrode. Then, as they move away from the high field area, collisions stop being ionizing and are extinguished, leaving a trail of slow moving positive ions behind them. These ions hinder the formation of new avalanches as they reduce the electric field around them. Therefore, new avalanches can develop when this positive space charge moves away, or due to photoionization at areas close to the sharp electrode that have no space charge present. In Figure 3-9 to Figure 3-11 the following color legend applies: purple corresponds to voltage and blue corresponds to current by measuring the voltage drop across a 1 kΩ current viewing resistor.

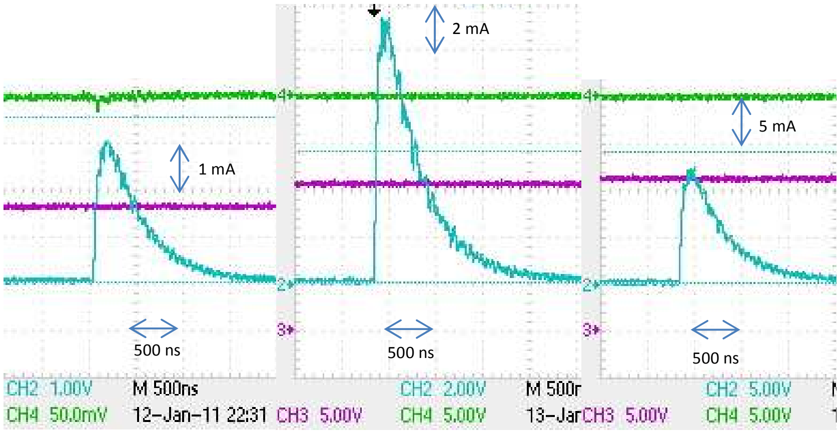

Figure 3-9: Current pulses before measurable corona inception (dc $I_{cor} < 1$ µA). From left to right: Current pulse at +13.68 kV, +16.03 kV and +16.68 kV. Horizontal axis: time in 500 ns/div; vertical axis for cyan trace: current at 1, 2 and 5 mA/div respectively, from left to right.

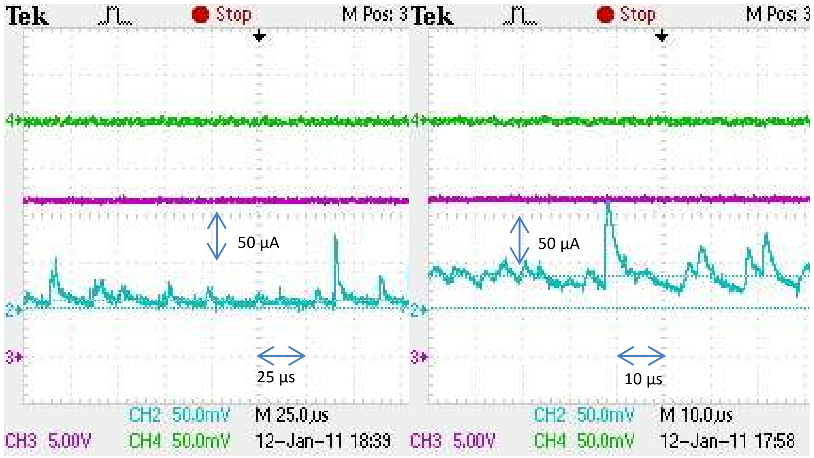

Figure 3-10: Corona current at +17.14 kV and +17.28 kV. dc corona current is 8 µA and 18 µA respectively. Horizontal axis: time in 25 µs/div and 10 µs/div respectively from left to right; vertical axis for cyan trace: current at 50 µA/div.

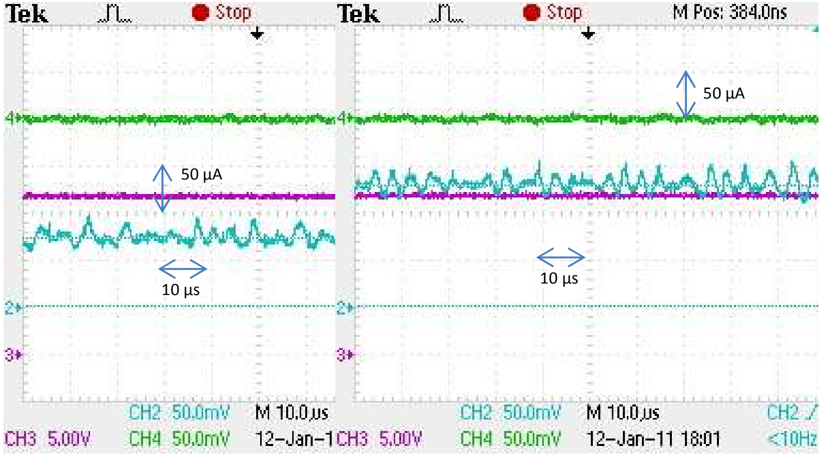

Figure 3-11: Corona current at +17.33 kV and +17.44 kV. dc corona current is 72 µA and 128 µA respectively. Horizontal axis: time in 10 µs/div; vertical axis for cyan trace: current at 50 µA/div.

In order to calculate the corona inception voltage of the precipitation reactor, the breakdown voltage, and the corona current levels at voltages between the corona inception and breakdown voltages, for positive polarity energisation, ten experimental runs were conducted and the results are combined in Figure 3-12.

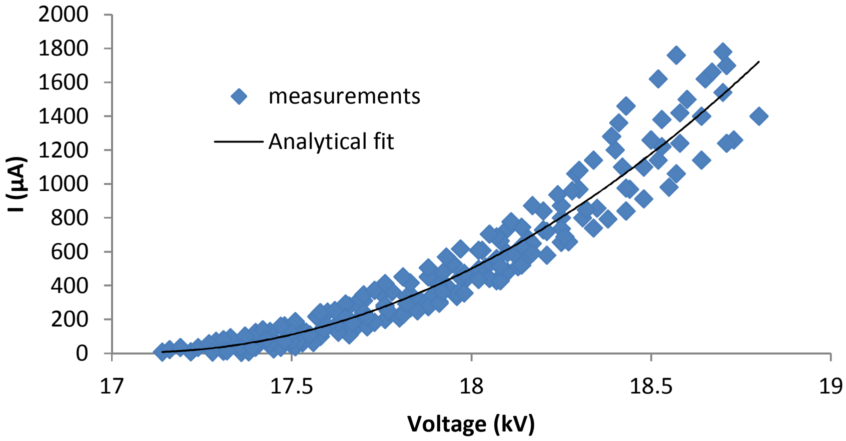

Figure 3-12: Combined point sets for the experimental runs for positive polarity energisation. Solid line, analytical fit, (3.3).

These runs had to be conducted in a timely manner, as the Joule heating effect after a long delay at one voltage level saw an increase in the current level, meaning there was higher current at higher voltage levels, compared to a test where there was only minimal delay in order to gather the data.

An analytical polynomial fitting line was added using the fitting procedure in Microsoft Excel software. A 2nd order polynomial fitting was selected in order to calculate I_0 and V_0 coefficients in the analytical Equation (3.3) shown below, where coefficients a, b and c are given below in Equation (3.5). This fitting also provides a relatively high ("goodness of fit" coefficient of determination), $R^2 = 0.93$.

$$\boldsymbol{I = a \cdot V^2 + b \cdot V + c = 575.98 \cdot V^2 + 19668 \cdot V + 167913} \tag{3.3}$$

where V is in kV and I in μA. For point plane topology, the corona current can be given by the formula found in (Given et al., 2011, Sigmond, 1982):

$$\boldsymbol{I = I_0 \cdot (V - V_0)^2} \tag{3.4}$$

In order to calculate the I_0 and V_0 coefficients, the equation (3.5) was used:

$$\boldsymbol{I = I_0 \cdot \left(V^2 - 2 \cdot V \cdot V_0 + V_0^2\right) = I_0 \cdot V^2 - 2 \cdot V_0 \cdot I_0 \cdot V + V_0^2 \cdot I_0} \tag{3.5}$$

Using equation (3.3) it can be seen that $\alpha = I_0$, $\beta = -2V_0I_0$ and $c = V_0^2I_0$. Therefore, I_0 can be calculated by α, then V_0 can be calculated from b, and c can be used for validation of the V_0 result. Also, the power of 2 refers to a space charge saturation regime of current being achieved. If this value is < 2, then the current is not saturated (fully governed by space charge).

For the positive polarity tested above, the coefficients from Figure 3-12 (that includes all the experimental runs in a single plot) have been calculated.

Table 3-1: Corona current coefficients for positive polarity.

Coefficients	Values calculated from trendline
α (A/V^2)	$5.76\cdot10^2$
b (A/V)	$-1.97\cdot10^4$
c (A)	$1.68\cdot10^5$
I_0 (A/V^2)	$5.76\cdot10^2$
V_0 (V)	17.07

3.4.2. POSITIVE ENERGISATION: CORONA DISCHARGE IN AIR FLOW LADEN WITH POWDER

In order to optimise the precipitation process, it is necessary to find a voltage level with dc energisation only at which current impulses would exist. In these tests, coarse particles (baking flour) were introduced into an air flow through the precipitation reactor. The particle size distribution for the flour samples is discussed in Section 3.6.1.

Corona current pulses appear at ~13 kV, with or without air flow. For the case with no air flow, corona current starts to appear at ~16.5 kV, and at ~18.5 kV there is a ~750 μA current without any breakdown, while even at ~21.5 kV there is still the same current ~750 μA. With air flow, measurable corona current starts to appear at ~19 kV and almost immediately after that, spark breakdowns start occurring at ~50 μA or even lower corona current. If tested with the particle laden air flow, there were many breakdowns even at ~17 kV during the initial phases (first minutes) of the bulk amount of the particulate delivered to the reactor. Thus, it was decided to conduct precipitation tests at a maximum of +16 kV dc charging voltage level.

In order to compare the corona characteristics in the reactor for air flow laden with coarse particles (flour) and finer particles, dolomite powder was used as a source of fine airborne particles. The particle size distribution for the dolomite samples is discussed in Section 3.6.2.

The corona current with particle laden air flow was deemed appropriate to be measured with finer particulate matter suspended in the air flow. Because there was a danger of breakdown, a spark gap was inserted at the coaxial cable connecting the 1 kΩ resistance and the oscilloscope. The spark gap would close at any overvoltage above 90 V, according to its datasheet. Three experiments were conducted and the results are displayed in Figure 3-13. The obtained corona onset voltage was ~17 kV, which is similar to the corona onset voltage measured for air flow laden with flour particles.

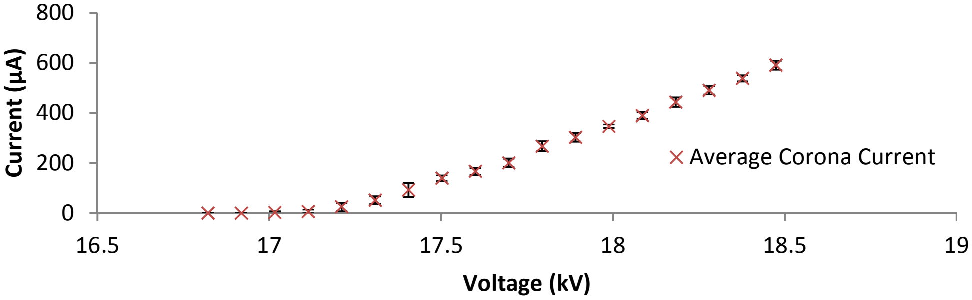

Figure 3-13: Average of 3 corona current tests conducted with positive energisation voltage and dolomite particles in the air flow.

Despite the fact that I(V) curve appears linear to the eye, it can be approximated very accurately ($R^2 = 0.99$) from $I = 154.5 \cdot I^2 – 5062.5 \cdot I + 41497$, having onset voltage ~17 kV.

3.4.3. NEGATIVE ENERGISATION: I(V) CHARACTERISTICS

Corona discharge characteristics in the cylindrical precipitation reactor were also obtained for negative energisation Corona discharge characteristics for both, negative and positive, polarizations were investigated, in order to identify the optimal energisation regime for practical air cleaning operations. Initially, corona current was obtained for ambient atmospheric air without artificially introduced particles. Initially, at the corona ignition voltage, Trichel impulses appeared, although no dc current was detected at this stage. Examples of Trichel current impulses are shown in Figure 3-14.

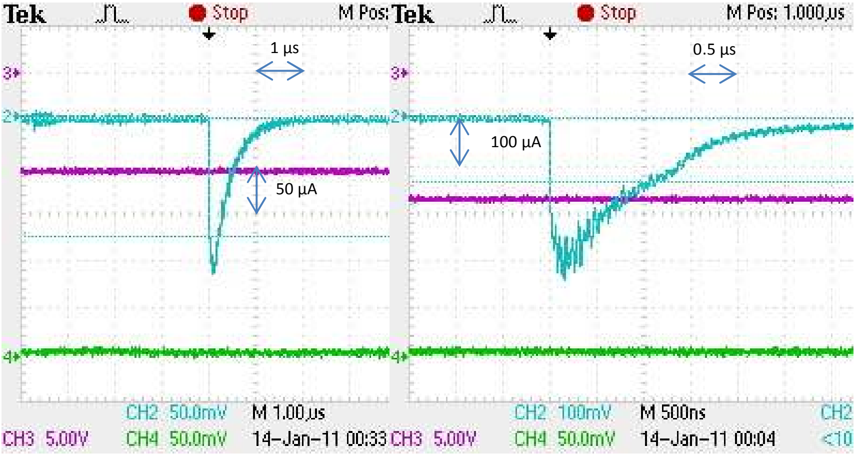

Figure 3-14: Trichel pulse at -10.61 kV and -13.73 kV (left to right). Corresponding corona current is ~160 µA and ~260 µA respectively. Horizontal axis: time in 1 µs/div and 0.5 µs/div respectively from left to right; vertical axis for cyan trace: current at 50 µA/div and 100 µA/div respectively from left to right.

With an increase in voltage, a dc component appears on the corona waveform, and Trichel impulses become superimposed on the dc current. With an increase in voltage, the magnitude of the current impulses also increases. Examples of the current waveforms under negative energisation in atmospheric air are shown in Figure 3-15.

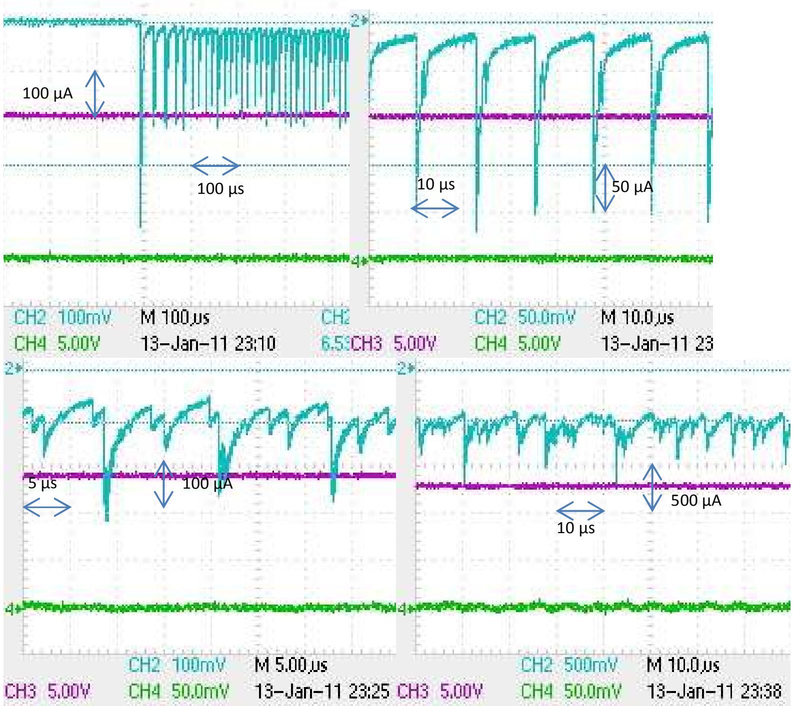

Figure 3-15: Corona current at -15.07 kV (inception), -15.25 kV, -16.44 kV and -17.60 kV. Sequence is from left to right and top to bottom. Horizontal axis: time in 100 µs/div, 10 µs/div, 5 µs/div and 10 µs/div respectively; vertical axis for cyan trace: current at 100 µA/div, 50 µA/div, 100 µA/div and 500 µA/div respectively.

For an additional *I(V)* test run for negative polarity, the frequency of the Trichel pulses as a function of voltage was measured. The results are given in Figure 3-16 for Trichel pulses which produced a corresponding current higher than 28 µA (recorded as 28 mV in the oscilloscope through a 1 kΩ current viewing resistor) only, pulses of lower current could not be counted easily.

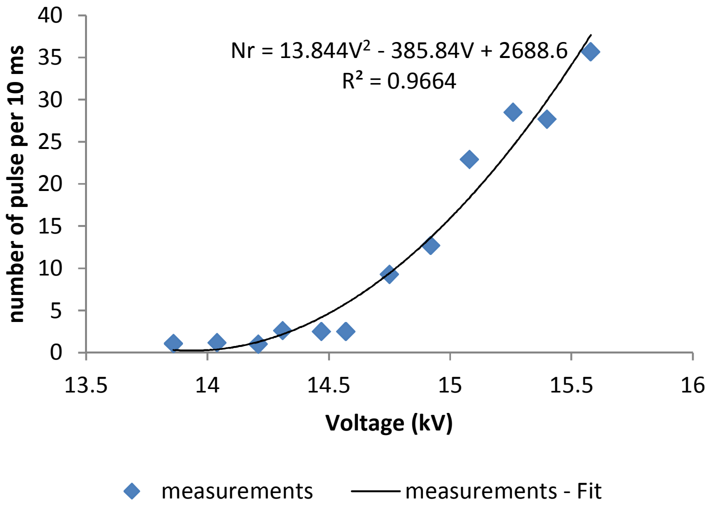

Figure 3-16: Number of Trichel impulses as a function of negative charging voltage.

It can be seen that the frequency of the negative corona pulses increased in a parabolic manner as the voltage was increased. This is in agreement with (Kuffel et al., 2000).

In the case of negative energisation, 2 trendlines were used, one for low dc corona currents and one for higher currents, as the voltage range with corona current was much wider compared to positive polarity. The results are shown in Figure 3-17 and Figure 3-18, for currents near to corona inception (up to 10 μA), and for higher currents respectively.

The experimental data points for low dc corona currents have been fitted with the parabolic function in Origin graphing software, the results of this fitting are shown in Figure 3-17. Equation (3.6) gives the analytical expression for the fitting line with numerical fitting parameters, the goodness of fit coefficient is $R^2 \approx 0.8$.

$$\boldsymbol{I = 0.69 \cdot V^2 - 17.71 \cdot V + 113.76} \tag{3.6}$$

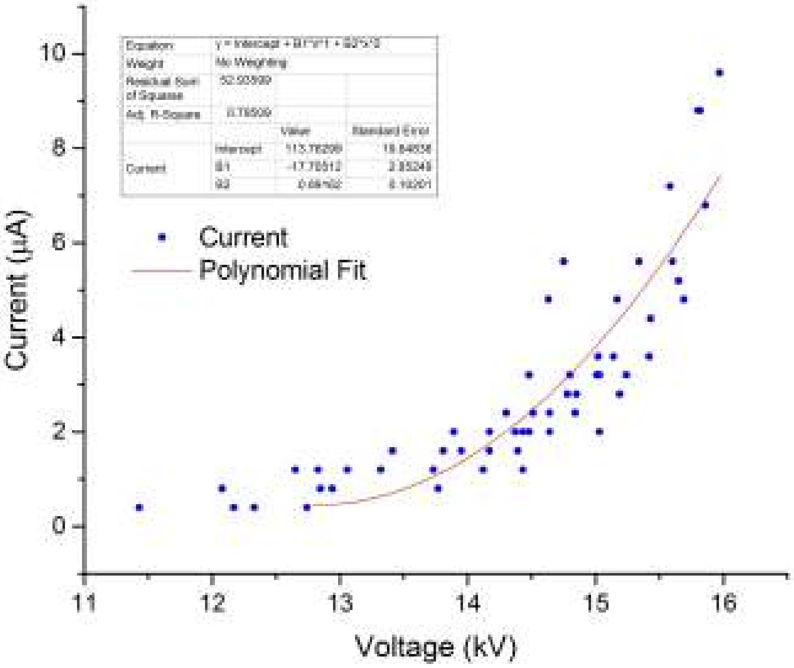

Equation	y = Intercept + B1*x^1 + B2*x^2		
Weight	No Weighting		
Residual Sum of Squares	52.93509		
Adj. R-Square	0.78509		
		Value	Standard Error
Current	Intercept	113.78209	18.84836
	B1	-17.70512	2.85249
	B2	0.69402	0.10201

Figure 3-17: I(V) curves with negative polarity energisation for small currents (less than 10 µA) drawn on the same graph.

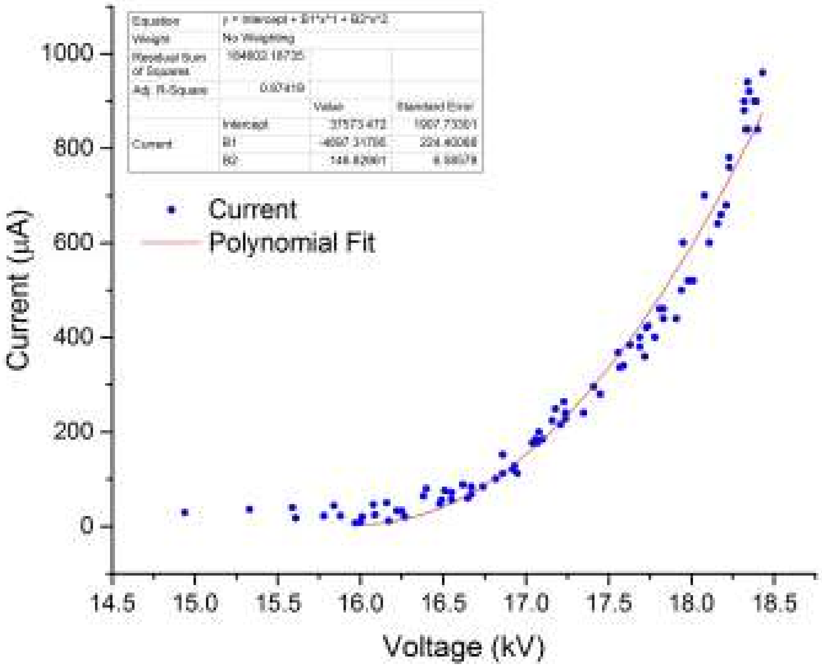

Figure 3-18: I(V) curves with negative polarity for experimental runs for large currents drawn on the same graph.

The experimental data points for higher corona currents shown in Figure 3-18 have been fit with the parabolic function in Origin graphing software. Equation (3.7) gives the analytical expression for the fitting line with numerical fitting parameters, the goodness of fit coefficient is $R^2 = 0.97$.

$$\mathbf{I = 37573.47 \cdot V^2 - 4697.32 \cdot V + 113.76} \tag{3.7}$$

In order to calculate the I_0 and V_0 coefficients, the following formula will be used (for both polarities, assuming that for negative polarity there is only a single current source in the rod):

$$\boldsymbol{I = I_0 \cdot (V - V_0)^2 = I_0 \cdot \left(V^2 - 2 \cdot V \cdot V_0 + V_0^2\right) = I_0 \cdot V^2 - 2 \cdot V_0 \cdot I_0 \cdot V + V_0^2 \cdot I_0} \tag{3.8}$$

where *Intercept* = I_0, $B1 = -2V_0I_0$ and $B2 = V_0^2I_0$. For negative energisation there will be two curves and only the data above ~10 µA will be used. This is because different trendlines can be fitted for the lower and higher corona currents respectively.

Table 3-2: Corona current coefficients for low currents and negative energisation.

Coefficients	Values calculated from trendline
α (A/V^2)	0.69
b (A/V)	-17.7
c (A)	$1.14\cdot10^2$
I_0 (A/V^2)	0.69
V_0 (V)	12.8

Since the dc energisation characteristics have been established for both positive and negative polarity, it is possible to establish the dc voltage levels for the precipitation experiments to follow.

Table 3-3: Corona current coefficients for low currents and negative energisation.

Coefficients	Values calculated from trendline
α (A/V^2)	$1.47\cdot10^2$
b (A/V)	$-4.7\cdot10^3$
c (A)	$3.76\cdot10^5$
I_0 (A/V^2)	$1.47\cdot10^2$
V_0 (V)	16

3.5. IMPULSIVE ENERGISATION OF THE PRECIPITATION REACTOR

Thus far in Section 3, the results of an investigation into the electrical characteristics of the precipitation reactor have been presented. In order to optimise the precipitation process, it is necessary to monitor and characterise the voltage wave-forms to be used in the novel energisation approach – a combination of the short HV impulses generated by the Blumlein pulsed power system and a steady state, dc electric field.

The voltage and current waveforms were observed in order to establish the charge injected into the system at various energisation voltage levels, an important parameter of precipitation efficiency. In addition, it was imperative to obtain the energy per impulse and thus to provide grounds for energy optimisation of the precipitation process. Lastly, the waveforms were used in order to monitor spark breakdown events, that should be avoided. The locations of the HV probe and current monitor in the test circuit are indicated in Figure 3-7. All the impulses were captured in a single shot mode operating regime. In all of the waveforms in Figure 3-19 to Figure 3-22 the colours correspond to the following values: purple: voltage waveform obtained by HV probe; green: current waveform obtained by Pearson monitor; cyan: current waveform obtained by a 29.6 V/kA current viewing resistor (voltage measured across the cvr).

Figure 3-19 shows voltage (250 ns wide impulses) and corresponding current waveforms for negative (left) and positive (right) polarity. It can be seen that while with negative polarity a current impulse was created, with positive polarity there is an insignificant one.

The 29.6 V/kA current viewing resistor to measure the current was used to capture dc current in addition to current impulses, and was connected to a -20 dB attenuator due to high signal amplitude. However, as can be seen, this is susceptible to high frequency noise.

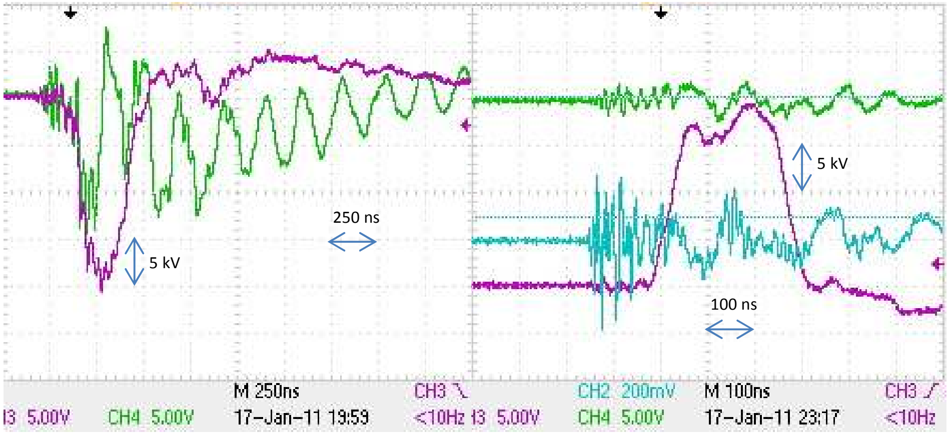

Figure 3-19: Current (green and cyan traces) and voltage (purple traces) wave forms in the case of Negative (a) and positive (b) energisation with 20 kV impulses. Green trace: 10 A/div.

HV impulses were then superimposed on dc voltages. As can be seen from Figure 3-20, there were cases with and without the appearance of current impulses. It was found that the current pulses start to appear in a statistical manner as the dc voltage was increased, without any clearly defined threshold.

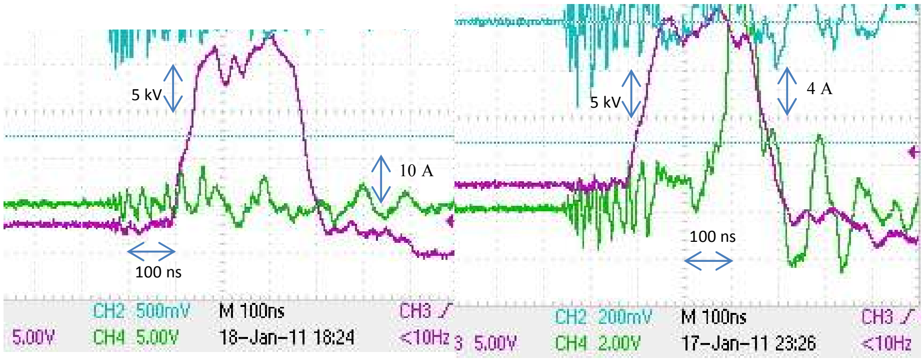

Figure 3-20: Current (green traces) and voltage (purple traces) wave forms in the case of +20 kV impulses superimposed on +3 kV dc charging voltage. Despite the same energisation levels, only the one on the left produced a current impulse.

As the voltage was increased, the appearance of current impulses became more consistent. However, the current impulses produced had variations in their time delay, amplitude, width and jitter, as seen in Figure 3-21. Moreover, as dc voltage charging levels increased, so did the corresponding amplitude of the current impulses, as can be seen on the far right of Figure 3-21. In the following energisation test the voltage impulse amplitude was kept constant at +20 kV, while the dc voltage was increased from +5 to +8 kV.

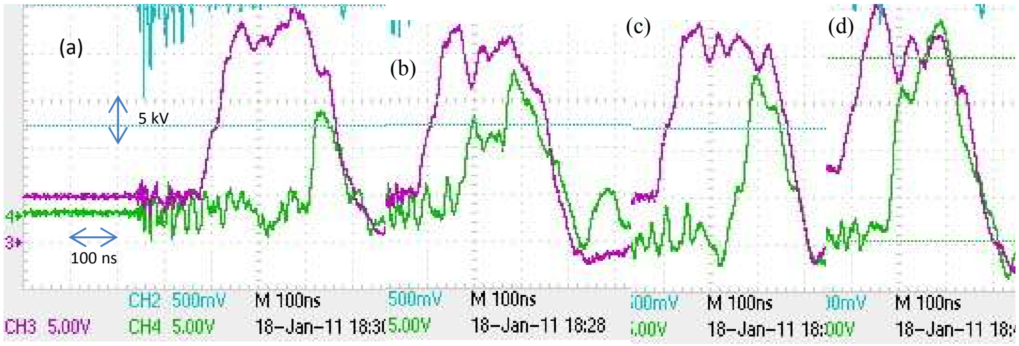

Figure 3-21: Waveforms a, b, c: Positive polarity dc +5 kV with superimposed +20 kV impulse charging; Waveform (d): Positive polarity dc +8 kV with superimposed +20 kV impulse charging. Green trace: 10 A/div.

From the waveforms in Figure 3-21, it can be observed that there is deviation from the expected peak voltage amplitude, for the vast majority of cases being lower compared to the expected amplitude. This deviation is higher for the higher dc voltages and superimposed impulse amplitudes. In addition to the above, the shape of the impulse was not square as expected from the theory (Kentech Instruments Ltd.), meaning that the average impulse amplitude was lower, compared to the peak one. Thus, it was decided to save 12 waveforms with +11 kV dc charging and +25 kV impulse charging, another 12 for +11 kV dc charging and +30 kV impulse charging, and another 12 with +16 kV dc charging and +31 kV impulse charging in order to calculate the average magnitude of the impulsive voltage, as shown in the Table 3-4. These values were chosen for consistently generating current impulses, and also for the fact that these dc voltage levels generate no corona discharges (+11 kV), or very low dc corona currents (for +16 kV, being < 1 μA), which is important in order to minimise power losses during the precipitation of particles.

Table 3-4: Average peak voltage for impulses superimposed on dc voltage for 12 impulses captured in each case.

Voltage dc/Impulse	+11 kV/+25 kV	+11 kV/+30 kV	+16 kV/+31 kV
Average peak magnitude (kV)	23.8	24.5	29.3
Standard deviation (kV)	0.58	1.03	1.56

Another important finding was that for the lower voltages, there were practically no current impulses observed (or they appeared very rarely), while as the impulsive voltage and dc voltage levels were increased, current impulses appeared more often and were also of much higher amplitude. Statistically, for +5 kV dc voltage with superimposed +20 kV impulses, only 3/16 voltage impulses were accompanied by a current impulse. This was raised to 10/14 for +6 kV dc, then to 10/11 for +7 kV dc, while for +9 kV dc all voltage impulses (10/10) were accompanied by a current impulse. These current impulses are substantial in their magnitude (10s A) compared to the impulses from dc corona only presented in Section 3.4 (maximum magnitude a few mA), and they constitute an important source of charged species into the inter-electrode gap, which help to charge and remove particulate matter.

Something that was thought to be detrimental to the precipitation efficiency was that after the appearance of the current impulses, the voltage dropped and even reached the opposite energisation polarity in a few cases, an example being seen in Figure 3-22. This polarity reversal will be analysed further in Section 3.5.3.

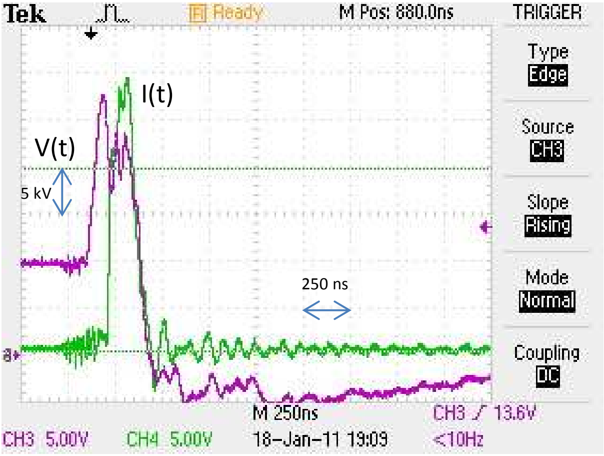

Figure 3-22: Positive polarity dc +10 kV with +20 kV impulse charging. Green trace: 10 A/div.

3.5.1. CURRENT IMPULSES DURING IMPULSIVE ENERGISATION OF THE REACTOR

It was found in Section 3.5 that above threshold dc and impulse voltage levels, the voltage pulse was followed by a current pulse. These energisation tests were conducted in atmospheric air without any air flow or particles in the reactor. In order to establish the magnitude of the charge injected into the reactor, which will result in charging of the particles to be precipitated it is necessary to investigate the parameters of the current impulses. Also, it is important to establish the energisation conditions that will not result in complete (spark) breakdown in the reactor, as this would reduce the precipitation efficiency significantly, and would perhaps result in the re-introduction of already precipitated particles into the air flow.

For investigation and optimisation of impulsive energisation it was necessary to measure: the delay time (t_d), which is the time required for the current pulse to develop after the voltage pulse has arrived; the rise time of the current pulse (t_r); *t pulse*, which is the pulse width; *I max* which is the maximum amplitude of the current pulse; and the pulse voltage at the moment of maximum current. From these data, the following were calculated: the resistance of the conducting current was calculated at the moment of maximum current; the rise and fall times of the voltage pulses; and the charge injected by the current pulse (by integrating the current waveform). The current amplitude is double that of the voltage amplitude shown on the oscilloscope, because a Pearson current probe was used and was terminated with a 50 Ω resistance (0.5 V/A, (Pearson Electronics Inc., 2012)). Finally, all measurements were conducted with positive polarity in order to avoid excessive O_3 production. Resistance was calculated at the point of maximum current, which corresponds to $dI/dt = 0$. This is not only easier, as the $dI/dt = 0$ is much cleaner than $dV/dt = 0$, which could occur multiple times in an oscillatory manner, but also preferable, because of the various parasitic effects that interfere with the system. These effects include parasitic inductance from the cables connecting the various parts of the electric circuitry and parasitic capacitance because of reactor design and adjacency of the system with the earthed HV cage. The former was in the order of μH while the later was 5 pF for the reactor in addition to 10s of fF due to adjacency. Inductance of reactor few 100s nH. Thus it was deemed prudent to have an estimation of resistance at the point where $L \cdot dI/dt = 0$.

The first experiments were conducted with +5 kV dc and +20 kV impulse voltages, however there were too few current pulses achieved (3/16 successful attempts before abandoning). Therefore, it was decided to continue with tests with constant impulsive voltage and variable dc voltage, starting from +6 kV, then +7 kV, +9 kV, +11 kV and +13 kV in order to see if a trend in the t_d or $I\ max$ was apparent, with dc voltage charging, as rising the voltage would statistically guarantee a high degree of probability that there will be current impulses. The Blumlein charging voltage was kept constant at +20 kV. The results are plotted in Figure 3-24 and Figure 3-25. Each data point represents the average of 10 tests, and the error bars indicate values of standard deviation.

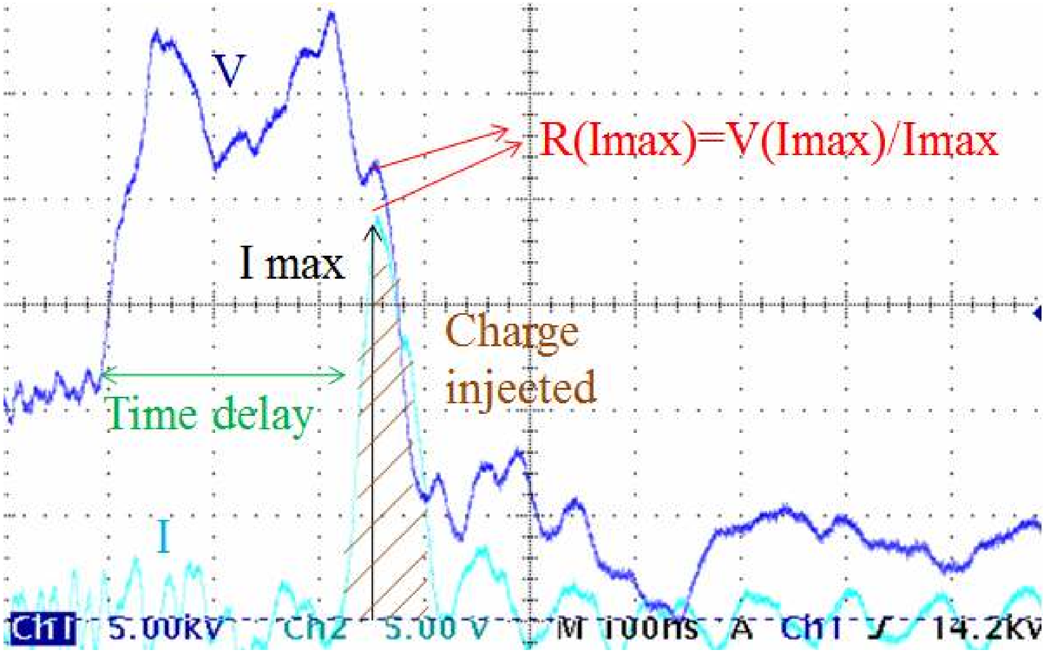

Figure 3-23: Voltage impulse accompanied by a current impulse. Time resolution is 100 ns/div, current is 10 A/div and voltage is 5 kV/div. The area below the current waveform is the charge injected into the inter-electrode space.

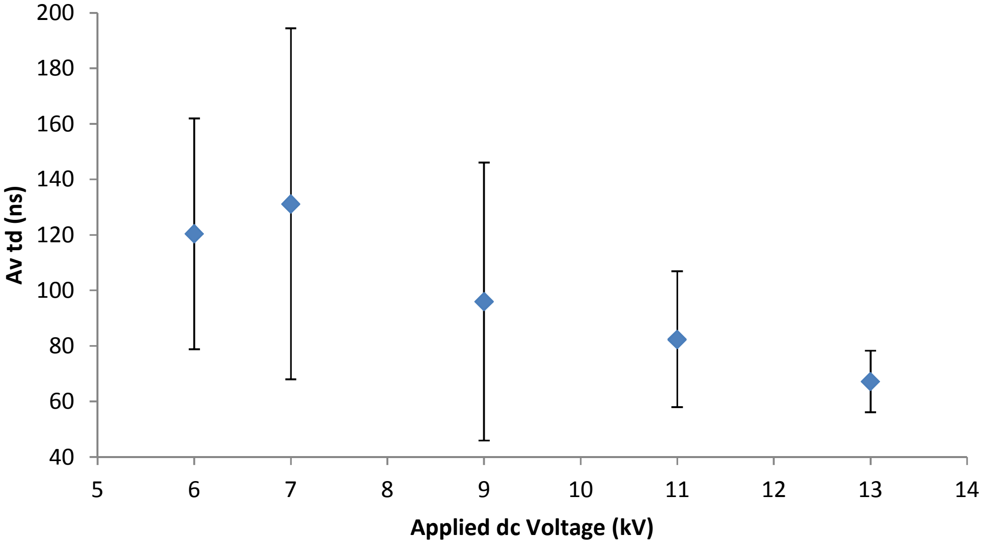

Figure 3-24: Average current pulses time delay as a function of applied charging voltage for +20 kV impulse voltage.

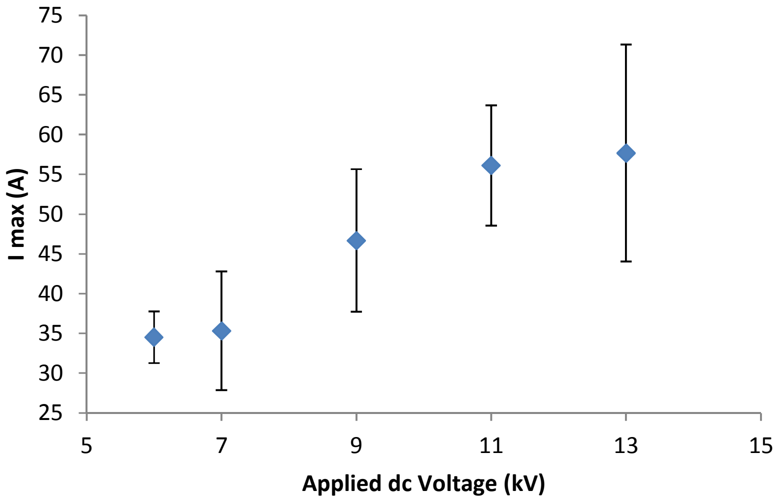

Figure 3-25: Average current pulses peak current amplitude as a function of applied charging voltage for +20 kV impulse voltage.

It was found not only that t_d decreases considerably as dc voltage increases, but also that its standard deviation decreases considerably too. In terms of maximum current, the opposite trend was observed, namely that it not only increases with dc voltage, but that its standard deviation increases too.

The next logical step was to keep the dc voltage constant and change the impulsive charging voltage. However, because of the results of the previous experiments with variable dc voltage, it was decided to perform 2 set of tests, with +7 kV dc voltage, and with +13 kV dc voltage, in order to analyse the behaviour for similar impulses superimposed on different dc voltage levels. The impulsive charging voltage was varied through +17 kV, +20 kV, +23 kV, and +25 kV. The results for +7 kV dc voltage are plotted in Figure 3-26 and Figure 3-27, while for +13 kV dc are in Figure 3-28 and Figure 3-29 respectively.

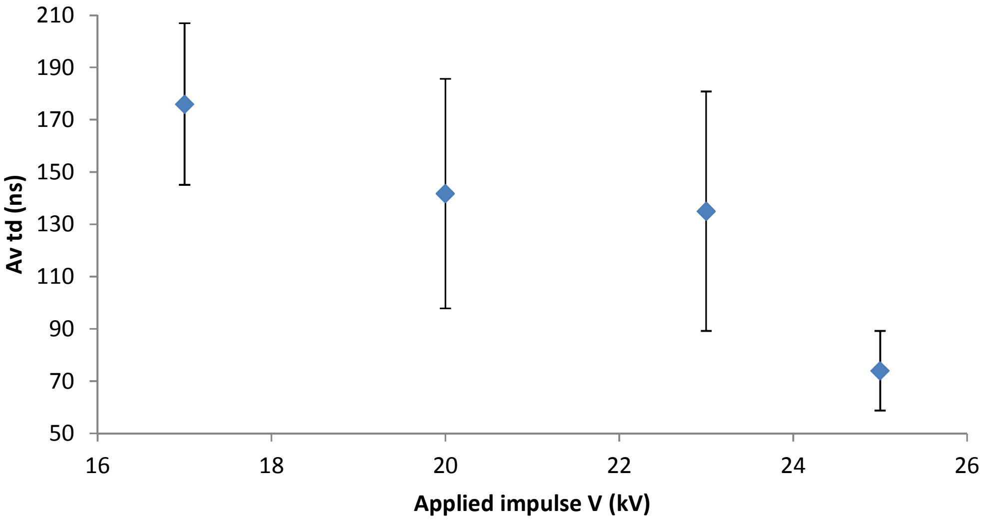

Figure 3-26: Time delay of current pulses as a function of magnitude of voltage impulses for +7 kV dc voltage.

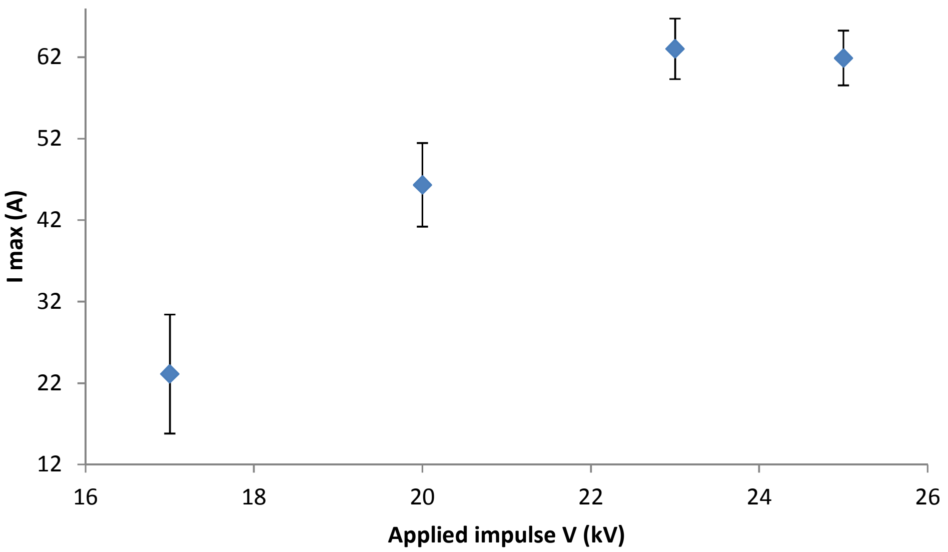

Figure 3-27: Average current pulses peak current amplitude as a function of impulsive voltage for +7 kV dc voltage.

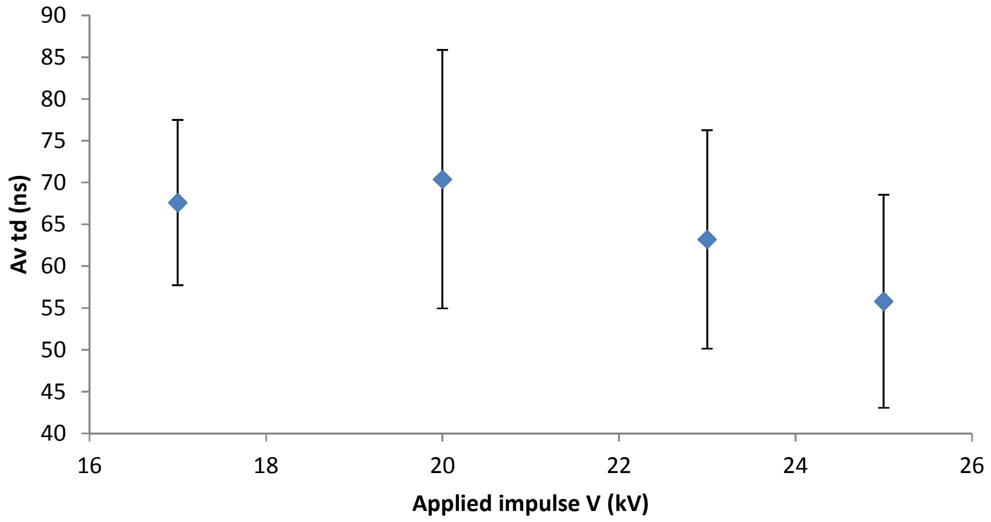

Figure 3-28: **Average current pulses time delay as a function of impulsive voltage for +13 kV dc voltage.**

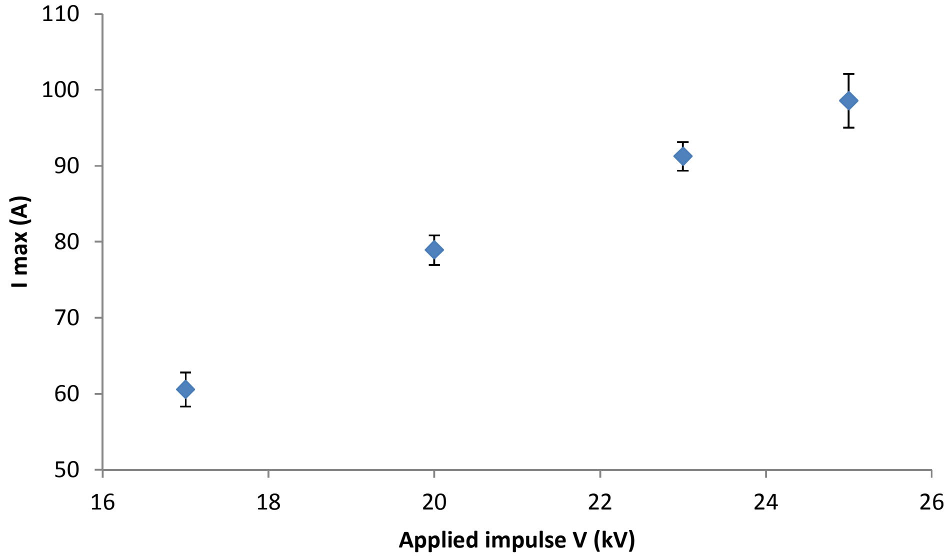

Figure 3-29: **Average current pulses peak current amplitude as a function of impulsive voltage for +13 kV dc voltage.**

The results of the tests with the constant, +7 kV dc voltage, bear similarities with the constant maximum amplitude impulsive voltage case. It has been established that time delay reduces as impulsive voltage increases, with the greatest reduction occurring for the +7 kV dc case compared to the +13 kV one. However, standard deviation (jitter) decreases only for the higher (+25 kV) voltage levels, and not as much compared to the constant dc voltage case. In terms of maximum current, it increases with increasing impulsive voltage, however it appears to become asymptotic at +23 kV, meaning that at +25 kV the magnitude is similar. A major difference from the constant dc voltage case is that the standard deviation (jitter) is decreasing slightly, instead of increasing.

The same also applies to the +13 kV dc voltage case, t_d deceases with an increase in impulsive voltage, however this time standard deviation (σ) remains high and does not decrease as impulsive voltage levels increase. In terms of I_{max}, again it increases with increasing impulsive voltage, however there is no asymptotic region reached, as was the case with the constant +7 kV dc voltage level. Also, σ remains low for all tests, and almost constant overall.

The charge injected per pulse into the inter-electrode space was obtained, as this charge would be transferred to the PM, either by collision or polarisation processes. Moreover, based on the maximum current of a pulse and the voltage amplitude at that point in time, a calculation of the resistance of the inter-electrode space at the peak of the pulse was made feasible. These two calculations are very important, because the former gives a definitive indication of the efficiency of the particle charging process, as current impulses provide charges for the effective charging of solid particles in the reactor, while the latter gives an estimate of the power losses, both of which are important and novel parts of this research project.

For each combination of dc and impulse voltage level, the current impulses were shown to have different t_d after the application of the voltage pulse, and have different peak magnitudes (I_{max}). Therefore, different amount of electric charge is injected into the reactor, and the plasma has different resistance values. The injected charge was obtained for 2 cases of constant dc voltage (+7 kV and +13 kV dc), while Blumlein charging voltage was through +17 kV, +20 kV, +23 kV, and +25 kV, as previously. The results of this analysis are shown in Figure 3-30 and Figure 3-31 for the constant +7 kV dc case, and in Figure 3-32 and Figure 3-33 for the constant +13 kV dc case.

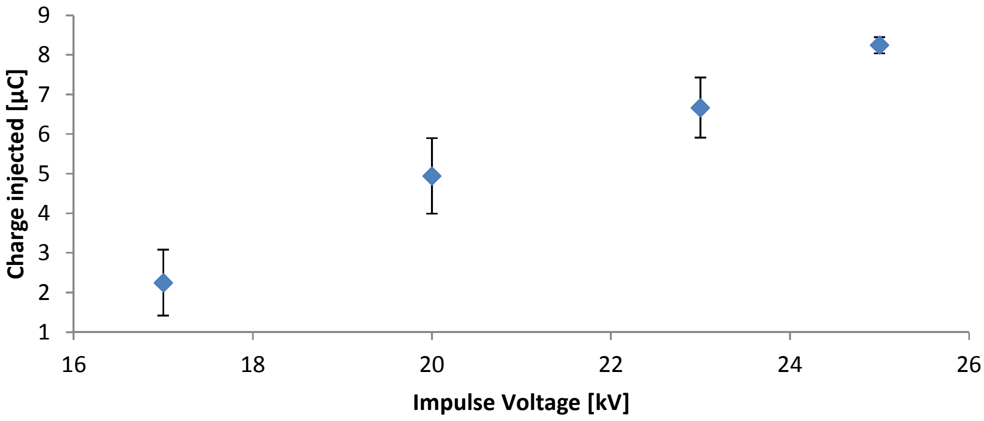

Figure 3-30: Average charge injected due to the current impulses as a function of impulse voltage for +7 kV dc charging.

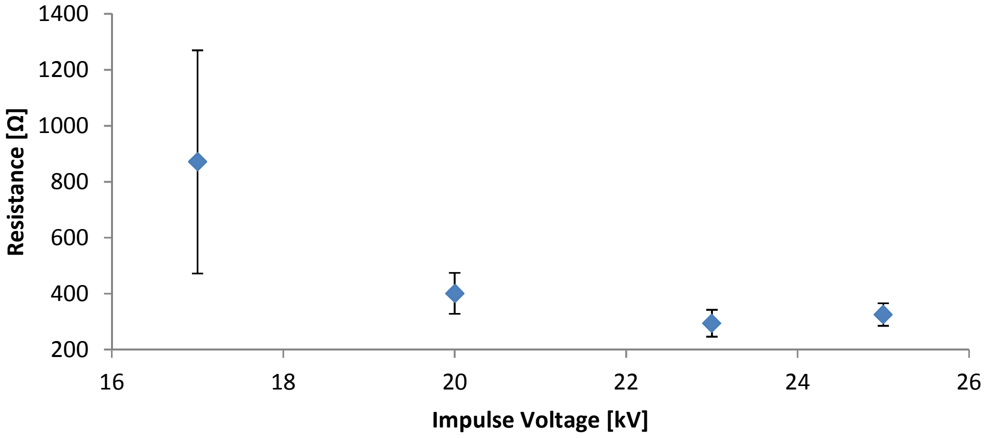

Figure 3-31: Average resistance at the peak current amplitude as a function of impulse voltage for +7 kV dc charging.

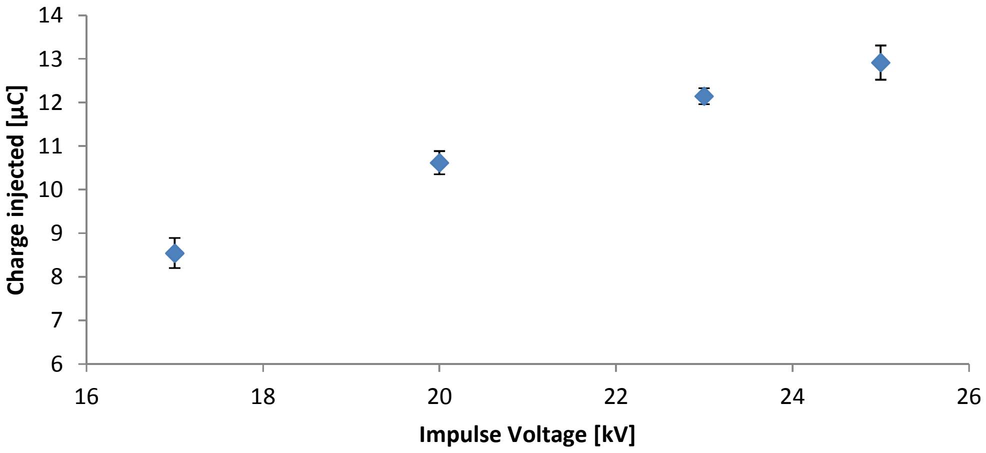

Figure 3-32: Average charge injected due to the current impulses as a function of impulse voltage for +13 kV dc charging.

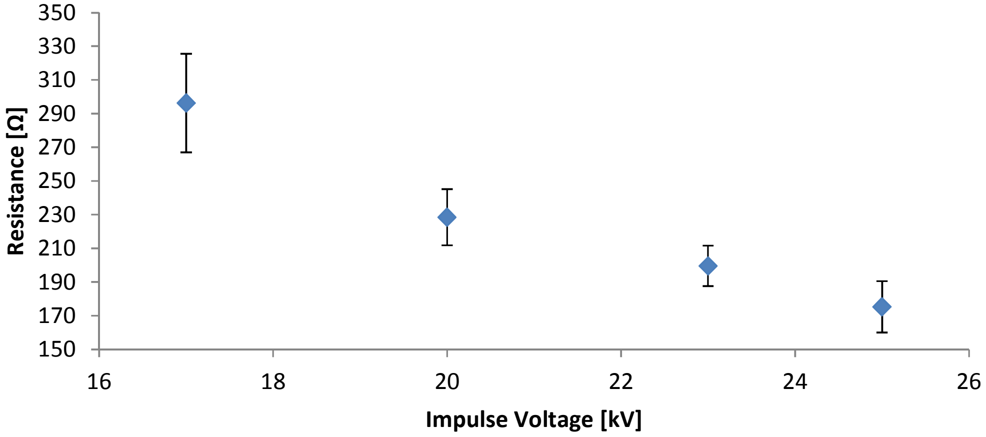

Figure 3-33: Average resistance at the peak current amplitude as a function of impulse voltage for +13 kV dc charging.

Charge injected shows an almost linear relationship with the impulsive voltage, with increased charge for higher voltage amplitude. On the contrary, there is an inverse relationship with resistance: as the voltage magnitude increases, the resistance decreases in a polynomial fashion. However, further tests are required to validate this polynomial trend.

Table 3-5: Charge fitting curves equations. Q in C, V in kV.

dc voltage level	Fitting equation
+7 kV	$Q = -0.0177 \cdot V^2 + 1.4723 \cdot V - 17.611$
+13 kV	$Q = -0.0282 \cdot V^2 + 1.7288 \cdot V - 12.695$

Table 3-6: Resistance fitting curves equations. R in Ω, V in kV.

dc voltage level	Fitting equation
+7 kV	$R = 16.48 \cdot V^2 - 758.26 \cdot V + 8992.7$
+13 kV	$R = 1.17 \cdot V^2 - 63.732 \cdot V + 1040.1$

For both the +7 kV and +13 kV dc cases, the results show an almost linear increase for the charge injected as a function of the impulsive voltage level. The standard deviation is much lower the higher the voltage, both dc and impulsive. In terms of the resistance of the plasma channel for the + 7 kV dc case, both its standard deviation and its amplitude decrease with increase in the impulsive voltage. An asymptotic point is reached at the +23 kV impulsive voltage level, being almost equal to the resistance of a +25 kV impulse at ~300 Ω. For the +13 kV case, a similar decreasing trend is observed, however its standard deviation decreases in a less pronounced way compared to the +7 kV dc case, and with no obvious saturation limit.

3.5.2. ENERGISATION REGIMES FOR PRECIPITATION TESTS

In Section 3.5.1, it was shown that the applied dc voltage defines the amount of electric charge released into the reactor (by integrating the current impulses): the total charge is ~2-3 times higher for +13 kV dc energisation as compared to +7 kV dc energisation, for the same level of impulsive voltage charging. Also, according to the theoretical analysis and simulation conducted in Section 3.2, dc corona is already present at +15 kV dc charging, however the current is too low to measure with the diagnostic devices available. Current pulses were also found to appear at ~+13 kV dc voltage levels.

Based on the results obtained and presented in Section 3.4, it was decided to use +15 kV and +16 kV dc energisation levels in practical precipitation tests (described in Section 3.7). This is because dc corona current exists at these voltage levels, meaning that charged particles will be present continuously to augment the charging process that the impulses achieve intermittently. In addition, higher energisation voltage also results in a higher electric field, thus the forces exerted on the charged particles would be higher, aiding in the collection process. However, at these levels of energisation, the corona current is still quite low, and thus would have a negligible effect on the system's power losses. Also, a lower voltage level, +11 kV, was chosen, in order to obtain precipitation levels without dc corona. At +11 kV, the current impulses would inject a larger amount of charge compared to the +7 kV dc voltage used in Section 3.5.1. In some precipitation tests, +14 kV was also used as a dc voltage level, since it is at the verge of dc corona onset, very close (sub-mm), to the M3 thread of the high voltage electrode.

It has been shown that higher voltage impulses result in higher levels of charge injection into the inter-electrode gap, thus it was decided to raise their levels too, without reaching breakdown levels (+22 kV to +32 kV peak impulse voltage, with a +2 kV increment).

Since the reactor was intended to be used in an impulsive regime (for +11 kV, +15 kV and +16 kV dc with superimposed impulses), electrical parameters including the amplitude of the current impulses, the charge released into the inter-electrode space, and the resistance of the corona discharges were obtained in a single shot impulse regime for those energisation levels. By using impulses of sufficient magnitude to exceed the corona inception threshold, corona current impulses are generated and advance into the inter-electrode space. The inception voltage of dc corona depends upon each particular topology and can be calculated by the Peek equation (Peek, 1915), as discussed in Section 3.2.

The current impulses are the source of the charges present in the inter-electrode space that play a crucial role in particle charging. Different combinations of dc and superimposed impulsive voltage levels generate impulses with different I_{max}, and at different instances in time after the voltage inception time (t_d). Thus, the charge released from each impulse is highly dependent upon the combination of the energisation voltages used (impulsive superimposed on dc voltage). Experiments were carried out with the following combinations: +22 kV, +24 kV, +26 kV peak voltage impulses, superimposed on +11 kV and +15 kV dc voltage; and +26 kV, +28 kV, +30 kV, +32 kV peak voltage impulses, superimposed on +16 kV dc voltage. The results of these tests, which include peak current, charge injected, resistance at peak current, and time delay of the current impulse, are summarized in Figure 3-34 to Figure 3-37. All data points are an average of at least 10 measurements.

The peak impulsive voltage levels applied were in the range of ±1.2% of the quoted nominal values.

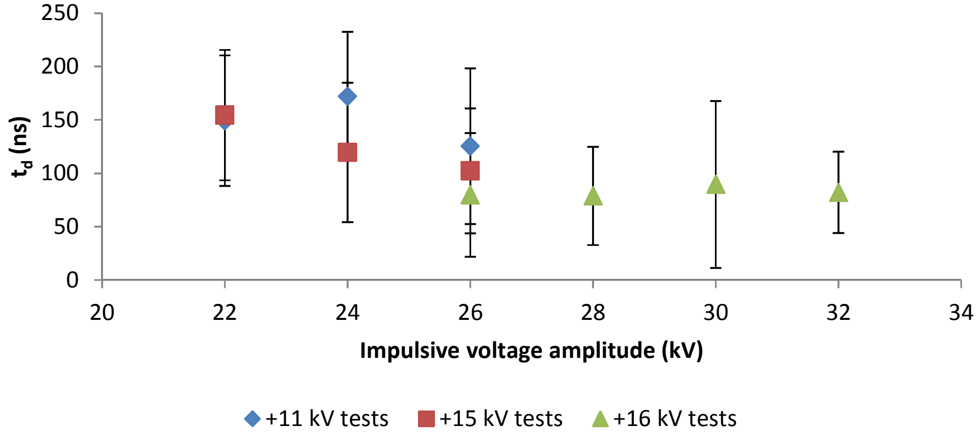

Figure 3-34: Average time delay as a function of impulse voltage superimposed on dc voltage. dc voltage levels were +11 kV, blue diamonds; +15 kV, red squares; and +16 kV, green triangles.

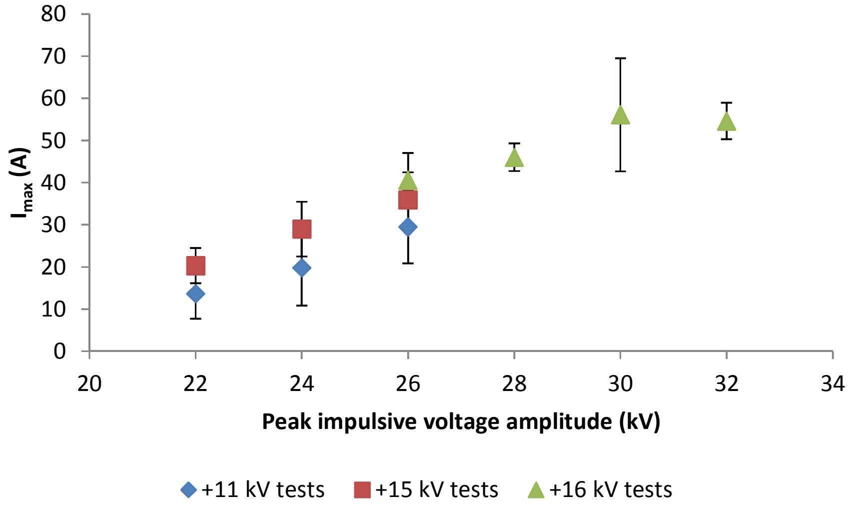

Figure 3-35: Average I_{max} as a function of impulse voltage superimposed on various dc voltages used. dc voltage levels were +11 kV, blue diamonds; +15 kV, red squares; and +16 kV, green triangles.

Figure 3-34 to Figure 3-37 show various impulse parameters, namely the t_d, I_{max}, electric charge released, and corona resistance at the point of I_{max}, as functions of impulsive and dc energisation voltage levels. Each data point in these figures corresponds to an average of at least 10 tests, and the error bars represent standard deviation. The trend observed from

Figure 3-34 and Figure 3-35, depicting t_d and I_{max} as functions of the peak impulsive voltage, is that maximum current and injected electric charge increase with higher levels of impulsive voltage: for the range tested an increase of up to six times has been observed.

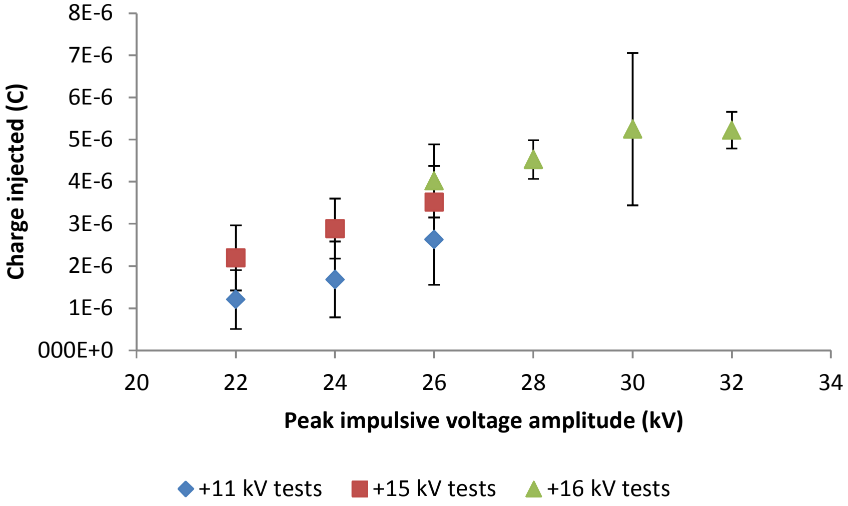

Figure 3-36: Average charge injected as a function of impulse voltage superimposed on dc voltage. dc voltage levels were +11 kV, blue diamonds; +15 kV, red squares; and +16 kV, green triangles.

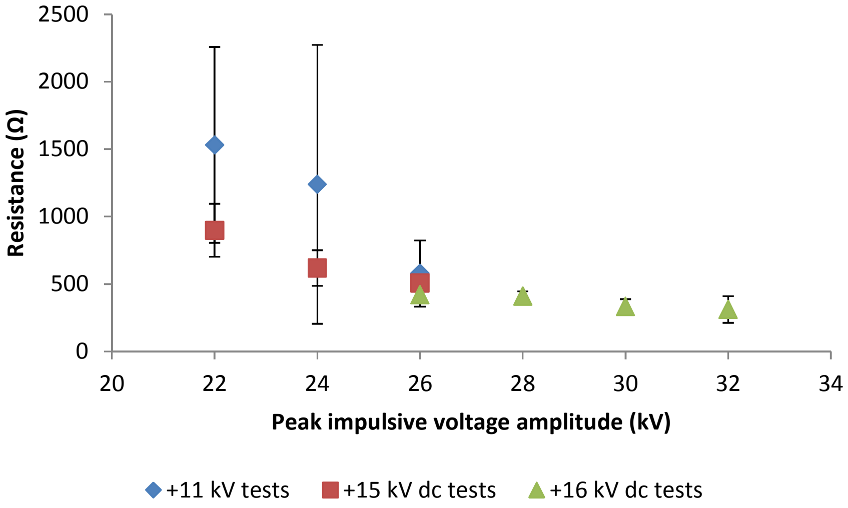

Figure 3-37: Resistance at I max as a function of impulse voltage superimposed on dc voltage. dc voltage levels were +11 kV, blue diamonds; +15 kV, red squares; and +16 kV, green triangles.

In Figure 3-36 and Figure 3-37, the opposite trend is observed. Time delay and the resistance of the corona discharges decrease as the amplitude of the impulsive voltage increases. The resistances were calculated at the point of the maximum current, meaning the ratio of the voltage level at the point in time at which I_{max} occurs, divided by that maximum current amplitude. The functional dependency of the voltage was as follows: the resistance decreases from ~1600 Ω to ~300 Ω as the impulsive voltage increases from +22 kV to +32 kV, (Figure 3-37). For constant voltage amplitude of +26 kV, a similar tendency was observed by increasing the dc voltage level from +11 kV to +15 kV and +16 kV dc, (see Figure 3-34 to Figure 3-37). Based on these results, the parameters for the precipitation energisation voltage levels were selected.

3.5.3. TIME CONSTANT OF THE PRECIPITATION SYSTEM

During the energisation of the coaxial precipitation reactor with HV impulses, a voltage drop was observed after impulses that produced a current impulse. This drop could, in some cases, last for a long time (even 100s of ms) and the voltage could be so depressed that the polarity could even be briefly reversed. The voltage recovery time after this drop is important, since after each impulse, the voltage across the electrodes of the reactor should be re-established. Any amount of time with depressed voltage means a weak electric field between the electrodes and thus reduced charging and collection capabilities of PM that corresponds to low precipitation efficiency. Thus, the recovery time should be characterised. In order to calculate the *RC* time constant of the precipitation energisation circuit, a series of experiments were conducted where voltage pulses were applied to the reactor and the time needed for the voltage to reach the dc level was obtained. The results are shown in Table 3-7, Table 3-8 and Table 3-9, and Figure 3-38. Table 3-7 shows the recovery time of the voltage to reach the original dc voltage level (+7 kV), from the time a voltage impulse was applied, and no corresponding current impulse was present. Table 3-8 is similar to Table 3-7, with the exception that it records the recovery time when current impulses were present after a voltage impulse. Table 3-9 states the recovery time of the system when impulses were superimposed on a +13 kV dc voltage level. At that level, even the lowest impulsive voltage used (at +17 kV) produced a current impulse after its application to the reactor.

Table 3-7: Time for voltage to reach pre-pulse level at +7 kV dc charging and without any current impulse present.

impulse (kV)	17	20	23	25
time (µs)	2.64	2.93		
	2.84	3.09		
	2.8			

Table 3-8: Time for voltage to reach pre-pulse level at +7 kV dc charging and with current impulses present.

impulse (kV)	17	20	23	25
time (ms)		2.82	241	279
		180	240	261
		185		

Table 3-9: Time for voltage to reach pre-pulse level at +13 kV dc charging and with current impulses present.

impulse (kV)	17	20	23	25
time (ms)	244	267	313	334
	263	258	267	294
	275		273	

An example waveform used to measure recovery time can be seen in Figure 3-38 (single pulse).

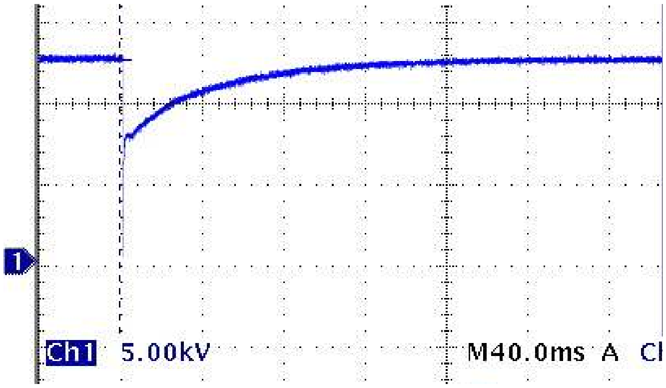

Figure 3-38: Recovery time for +20 kV impulse charging on top of +13 kV dc charging.

It can be seen from Table 3-7, Table 3-8 and Table 3-9 that if there is no current pulse associated with the voltage pulse, the time needed for the voltage to recover is ~2.5 µs, while if a current pulse is present, then the time needed ranges from 180-340 ms. The 2.5 µs value is expected from theory, as it almost equals 5 *RC*, as can be seen in Table 3-10. For that reason, the capacitor was changed in order to have a capacitance value that was more than halved, at 212 pF. This corresponded to a proportional decrease of the time constant, *RC*, shown in Table 3-10.

Table 3-10: RC of dc circuit used; left, before and right, after the new capacitors.

R (MΩ)	0.982	0.982
C (pF)	500	212
RC (µs)	**491**	**208**

The current waveforms shown in Figure 3-39 and Figure 3-40 were obtained for +16 kV dc and impulsive energisation in the case when the reactor was loaded with atmospheric air loaded with particles. The precipitation reactor was energised with HV impulses with frequency of 50 pps, however after ~12-15 impulses, the dc voltage drops considerably for about 5 cycles (100 ms). This happens in the first 1-2 min of the experiment, when the maximum amount of PM is injected into the reactor. This phenomenon stops after the first few minutes, as can be seen from Figure 3-41.

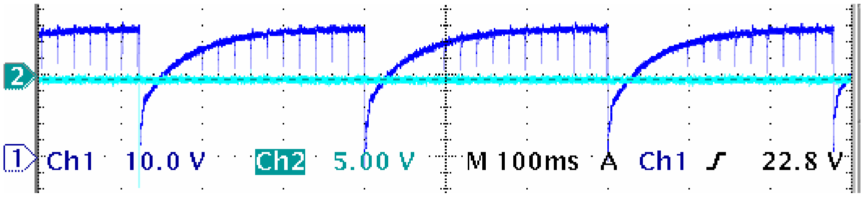

Figure 3-39: Current waveform for +16 kV dc with impulses energisation voltage with particle laden air flow. Frequency of voltage pulses is 50 pps. Voltage (blue) trace: 10 kV/div; current (cyan) trace 10 A/div.

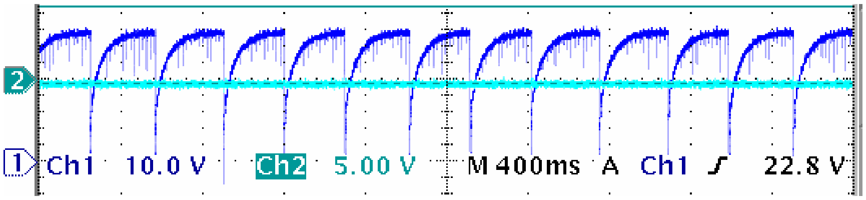

Figure 3-40: Current waveform for +16 kV dc with impulses energisation voltage with particle laden air flow. Frequency of voltage pulses is 50 pps. Voltage (blue) trace: 10 kV/div; current (cyan) trace 10 A/div.

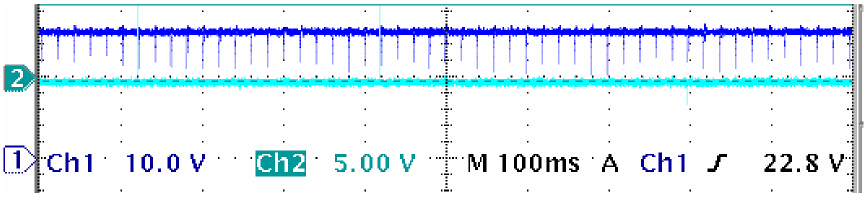

Figure 3-41: Current waveform for +16 kV dc with impulses energisation voltage with particle laden air flow. Frequency of voltage pulses is 50 pps. Voltage (blue) trace: 10 kV/div; current (cyan) trace 10 A/div.

From Figure 3-39, Figure 3-40 and Figure 3-41, it was found that an increase of PM concentration into the system can cause periodical voltage drops, and thus a reduction of the electric field inside the reactor, which corresponds to lower precipitation efficiency. The reason behind this phenomenon is the increased number of charged PM present, which reduces the resistance of the air gap between the electrodes. Therefore, a high voltage impulse could cause increased conduction and thus a voltage drop for an increased amount of time, until the charged particles migrate and the air flow carries new, uncharged, particles between the electrodes. The dc voltage then has time to recover to its original levels, and to charge an additional amount of particles, before this phenomenon repeats itself in a cycle. The cycle stops when the concentration of PM in the air flow lowers.

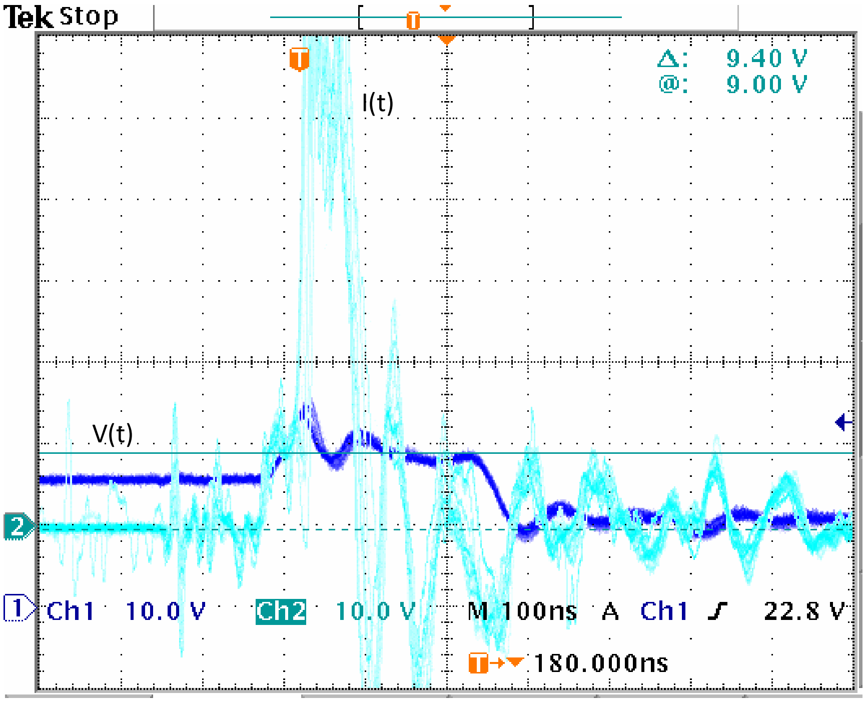

Figure 3-42: +16 kV impulse followed by current impulse with particle laden air flow. Frequency is 50 pps and an attenuator was used (ratio of 114). Peak at about 22.5 kV. Time resolution is 100 ns/div, voltage (blue) is 10 kV/div while current (cyan) is 20 A/div.

In Figure 3-42, it can be observed that by using +16 kV dc voltage, the current pulses corresponding to superimposed impulses can be very high. To be more specific, the voltage signal across the current viewing resistor correspond to ~120 A peak current. This is in agreement with measurements with the Pearson current monitor.

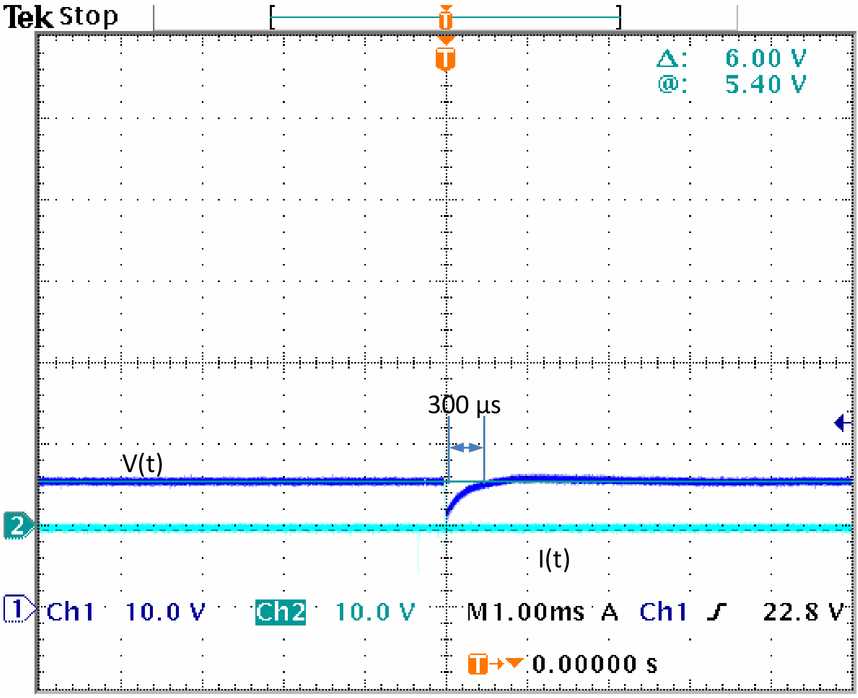

Figure 3-43: Recovery time after an impulse followed by a current impulse at +16 kV HV. Frequency is 50 pps. Time resolution is 1 ms/div and voltage is 10 kV/div.

The same energisation levels were used in Figure 3-43. This figure, however, is focused on the recovery time of the system, which is ~300 µs. Taking into account the 50 pps repetition rate used, this means that there is reduced voltage across the electrodes, for 0.3 out of 20 ms per cycle, or for 1.5% of the time, which would not affect the efficiency significantly, based on the reactor length and the air flow inside it.

3.5.4. ENERGISATION CHARACTERISTICS WITH AIR FLOW LADEN WITH PARTICLES

3.5.4.1. Transient waveforms: air flow laden with flour particles

In practical applications, the reactor will be filled with airborne particulates, therefore it is necessary to investigate the energisation parameters with PM laden air flow. Examples of the impulses captured with the particle laden air flow are shown in Figure 3-44 and Figure 3-45.

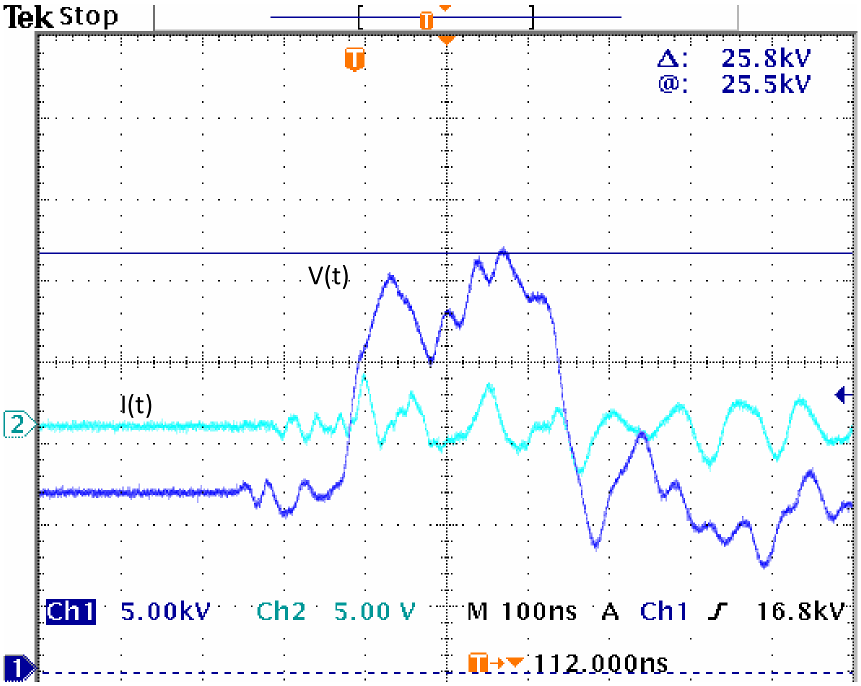

Figure 3-44: Current (cyan) and Voltage (blue) impulses captured with particle laden air flow with dc energisation of +11 kV and impulse voltage amplitude of +25.8 kV. Time resolution is 100 ns/div, voltage (blue) is 5 kV/div while current (cyan) is 10 A/div.

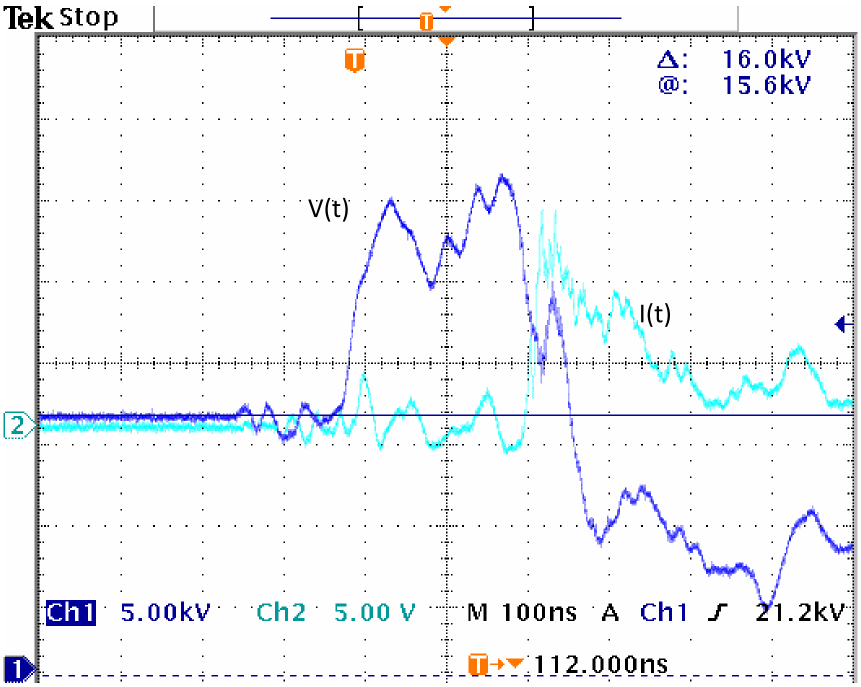

Figure 3-45: Current (cyan) and Voltage (blue) impulses captured with particle laden air flow with dc energisation of +16 kV and impulse voltage amplitude of +30 kV. Horizontal axis: time; vertical axis: amplitude. Time resolution is 100 ns/div, voltage (blue) is 5 kV/div while current (cyan) is 10 A/div.

Experiments were carried out for the evaluation of the impulse voltage level for the dc charging levels used (+11 kV, +14 kV and +16 kV dc) conducted with particle laden air flow, as these energisation levels were deemed appropriate for the precipitation experiments. There were cases where a current impulse appeared after the application of the voltage impulse, and cases where it did not, which should be investigated in terms of having an effect on precipitation efficiency. Additionally, the number of breakdown events at +16 kV dc with superimposed impulses was very low. One such example is shown in Figure 3-46.

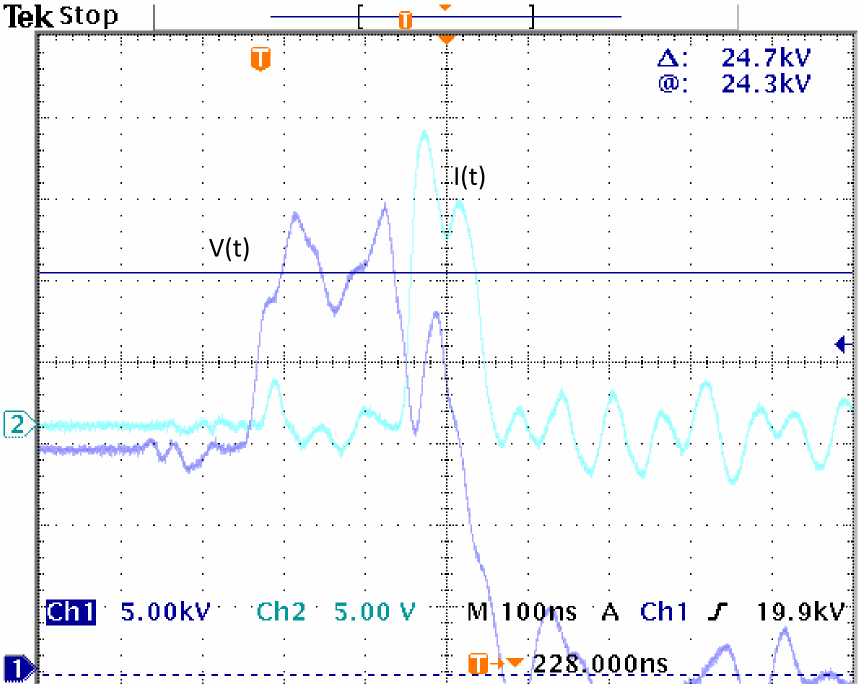

Figure 3-46: Current (cyan) and Voltage (blue) impulses captured with particle laden air flow with dc energisation of +14 kV. Horizontal axis: time; vertical axis: amplitude. Time resolution is 100 ns/div, voltage (blue) is 5 kV/div while current (cyan) is 10 A/div.

Figure 3-44 to Figure 3-46 show that, the energisation levels chosen are appropriate for the safe and efficient operation of the precipitation reactor. Moreover, the voltage levels chosen exhibit a wide range of corresponding current pulse behaviours, from occasional appearance, to those regimes described in Section 3.5.2. Thus, precipitation efficiency could be measured for various cases of energy consumption, and an optimised solution could be investigated.

3.5.4.2. Transient waveforms: Air flow laden with dolomite particles

In section 3.5.4.1, waveforms of air laden with coarse particles (flour) were studied. In this section, finer particles of dolomite were used, as they contain a greater fraction of particles in the PM2.5 range compared to flour. The Pearson current monitor was used in these tests, and this monitor has a bandwidth high enough to capture ns impulses and also to reject HF noise. However, it cannot be used for dc current measurements. According to its datasheet, it has a usable risetime of 1.5 ns, a high frequency ±3 dB at 250 MHz, and a low frequency 3 dB cutoff at 400 Hz. The Tektronix P6015A high voltage probe on the other hand has a risetime of ~5 ns, constituting the Pearson much more suitable than the probe. In addition, the 200/500 MHz oscilloscopes had a risetime of 3.75/1.5 ns. The risetimes are based on the datasheets and on the empirical formula in equation (3.9) (Mittermayer and Steininger, 1999):

$$\boldsymbol{RT = \frac{0.35}{BW}} \tag{3.9}$$

where *RT* is the risetime in s and *BW* is the bandwidth in Hz. Actual waveforms showing the voltage recovery after impulses are shown in Figure 3-47 to Figure 3-49.

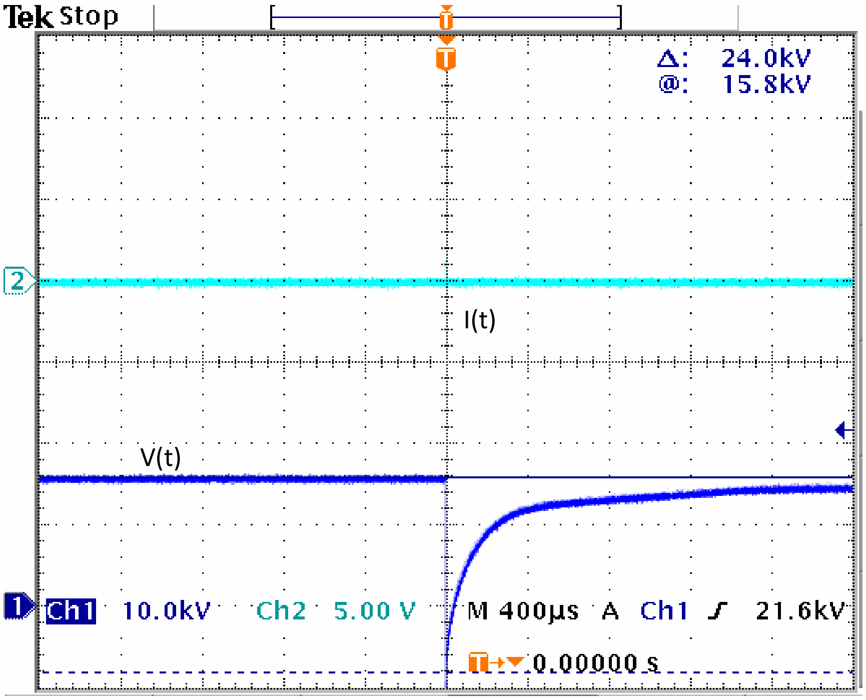

Figure 3-47: Recovery time after a +16 kV voltage impulse followed by a current impulse. Frequency is 50 pps. Horizontal axis: time; vertical axis: amplitude. Time resolution is 400 µs/div and voltage is 10 kV/div.

From Figure 3-47, it is observed that the recovery time of the voltage across the gap, after a voltage impulse superimposed on +16 kV dc voltage, that was accompanied by a current impulse, was greater than 2 ms. This is more than 10% of the time between the impulses, and such a long interval with reduced electric field might have serious effects on precipitation efficiency.

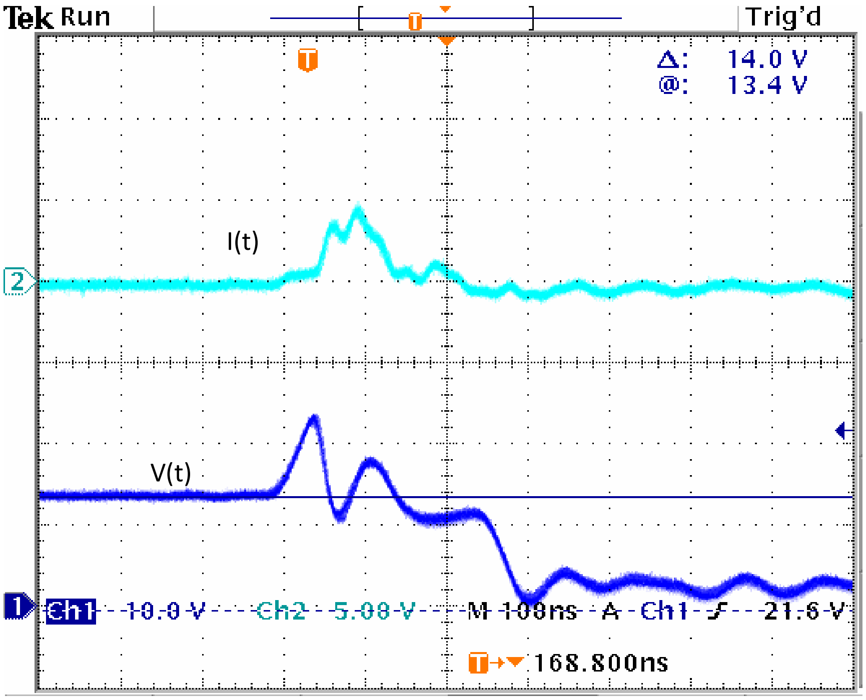

Figure 3-48: +14 kV impulse followed by current impulse with particle laden air flow. Frequency was 50 pps. Peak observed at about 22 kV. Horizontal axis: time; vertical axis: amplitude. Time resolution is 100 ns/div, voltage (blue) is 10 kV/div while current (cyan) is 10 A/div.

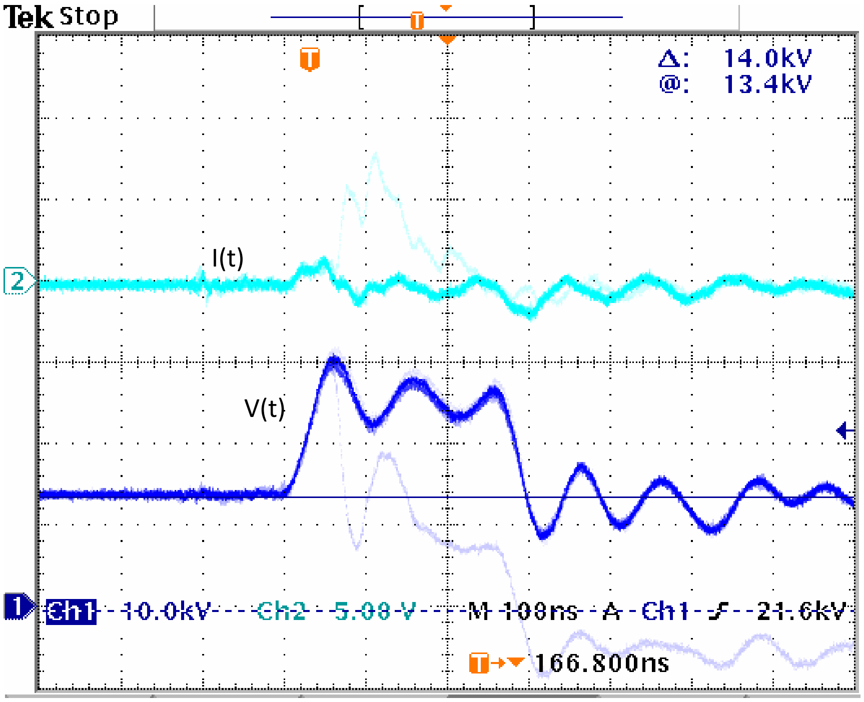

Figure 3-49: +14 kV impulse with particle laden air flow. Frequency was less than 50 pps. Peak observed at about 25.5 kV. Horizontal axis: time; vertical axis: amplitude. Time resolution is 100 ns/div and voltage is 10 kV/div while current (cyan) is 20 A/div.

In Figure 3-48 and Figure 3-49, the same energisation voltage was applied, and the difference in voltage drop and recovery time is clearly visible, based on the appearance or not of a current impulse.

As discussed in Section 3.5.3, the increase of PM concentration in the air flow can cause higher conduction in the inter-electrode space, and thus prolonged periods of low electric fields across the reactor electrodes. This is a cause of reduced precipitation efficiency.

3.6. PARTICLES USED IN THE PRECIPITATION EXPERIMENTS

This section is focused on an experimental study of the precipitation efficiency when the single stage precipitation reactor was energised by superposition of dc and impulsive voltages. Two types of precipitation experiments were conducted using the novel energisation method. In the first series of precipitation tests, coarser particles of flour were used, these particles being easier to remove from the particle laden air flow (Parker, 1997). In the second series of the precipitation tests, finer dolomite particles were used, these particles being constituted from a substantial part in the PM2.5 range and thus being more difficult to precipitate.

3.6.1. COARSE PARTICLES

For the precipitation tests with coarser particles, baking flour was selected. The flour particles range in size from 5 µm to 150 µm (Behall et al., 1999) (Irani and Fong, 1961). According to (Irani and Fong, 1961), 50% of the flour particles by weight are larger than 45 µm, while a negligible amount of particles under 2 µm should be present (0.4% by weight less than 5 µm), Figure 3-50. The mass particle distribution of flour particles is given in Table 3-11, while their size distribution is in Figure 3-50.

Table 3-11: Cumulative mass distribution of fine ground whole grain wheat flour particles (Behall et al., 1999).

100%	< 150 µg
90%	< 73 µg
53%	< 42 µg
45%	< 36 µg

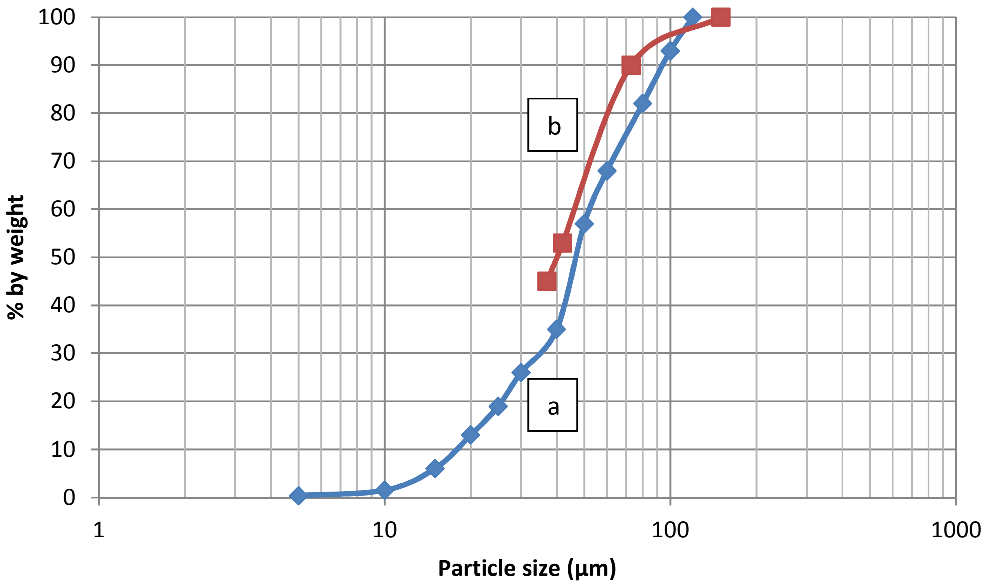

Figure 3-50: Cumulative flour particle size distribution, were line a is by (Irani and Fong, 1961) and line b is by (Behall et al., 1999).

3.6.2. FINE PARTICLES

Microdol H600 dolomite powder was used as the source of fine particles. The dolomite poweder has, by weight, 27% of is particles smaller than 2 µm (Figure 3-51), while only 0.01% are larger than 45 µm (Omya UK Ltd, 2005).

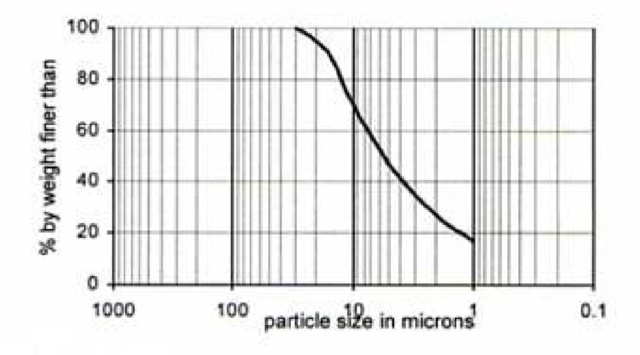

Figure 3-51: Particle size distribution of H600 dolomite powder, bought from Omya (Omya UK Ltd, 2005).

Dolomite powder is a clay type material containing, among other substances, CaO (30.3%), MgO (21.6%), Fe_2O_3 (0.08%) and also having HCl insoluble content (0.6%) (Omya UK Ltd, 2005). In addition, 50% are greater than 1 µm in size (by weight) while the mean particle size is 5.5 µm (Omya UK Ltd, 2005). Another major advantage of dolomite is that it is poly-disperse (GRIMM Aerosol Technik GmbH & Co. KG, 2010), meaning that its particles are within a broad range of sizes, thus they can be examined in the same tests with the particle analyzer used. It is also stable during storage and not hydroscopic (GRIMM Aerosol Technik GmbH & Co. KG, 2010). Dolomite powder also was used by GRIMM Ltd, the company which produced the particle analyser used in this research project, to calibrate this analyser (GRIMM Aerosol Technik GmbH & Co. KG, 2010). Thus, it was decided to use dolomite as the preferred source of PM2.5 material in the tests in which the Grimm 1.109 laser scattering particle analyser was used for measurements of precipitation efficiency.

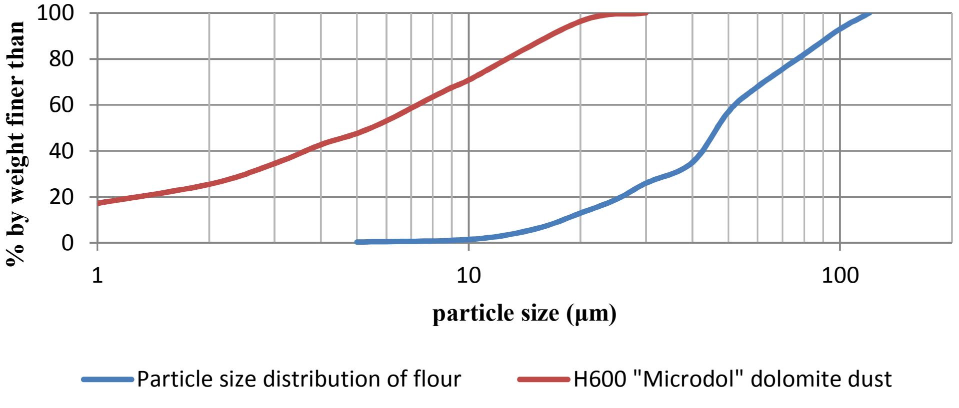

Figure 3-52: Comparison of size distribution of coarse and fine PM, based on (Irani and Fong, 1961) and (Omya UK Ltd, 2005).

3.7. PRECIPITATION EXPERIMENTS: RESULTS

3.7.1. SELECTION OF ENERGISATION POLARITY

Experiments were conducted with different polarity of energisation voltage in order to investigate its effect on the precipitation efficiency. The procedure for calculating the percentage of PM precipitated was as follows. The reactor consists of 3 main parts, an upper PVC flange, a grounded cylinder, and a lower PVC flange (Figure 3-53). For each experiment the flour particle laden air was passed through the energised reactor for 5 minutes. After each experiment the reactor was disassembled, and the flour particles attached to each part of the reactor were carefully collected in plastic containers and weighed using precision scales (Sartorius handy H51 digital scales with readability up to 0.1 mg and precision greater than ±0.2 mg, Sartorius GMBH Göttingen, Germany).

Percentage of PM precipitated was calculated by measuring the amount of flour particles at the lower part of the reactor compared with the amount of flour particles precipitated in the other parts of the reactor (upper flange and cylinder), as a percentage. Those particles that passed through the lower flange and left the reactor completely were not taken into account, therefore strict efficiency calculations could not be conducted. However, the percentage of PM that got attached at the lower part of the reactor, could act as an indicator of level of PM that manage to escape, and thus of efficiency, η, too. The percentage of PM precipitated, *PP*, is given by the equation (3.10):

$$\boldsymbol{PP = \frac{(M1)+(M2)}{(M1)+(M2)+(M3)} 100\%} \tag{3.10}$$

where *M1* is the mass of particles collected from the upper PVC flange part, *M2* is the mass of particles collected from the grounded cylinder, and *M3* is the mass of the particles collected from the lower PVC flange part of the reactor, respectively.

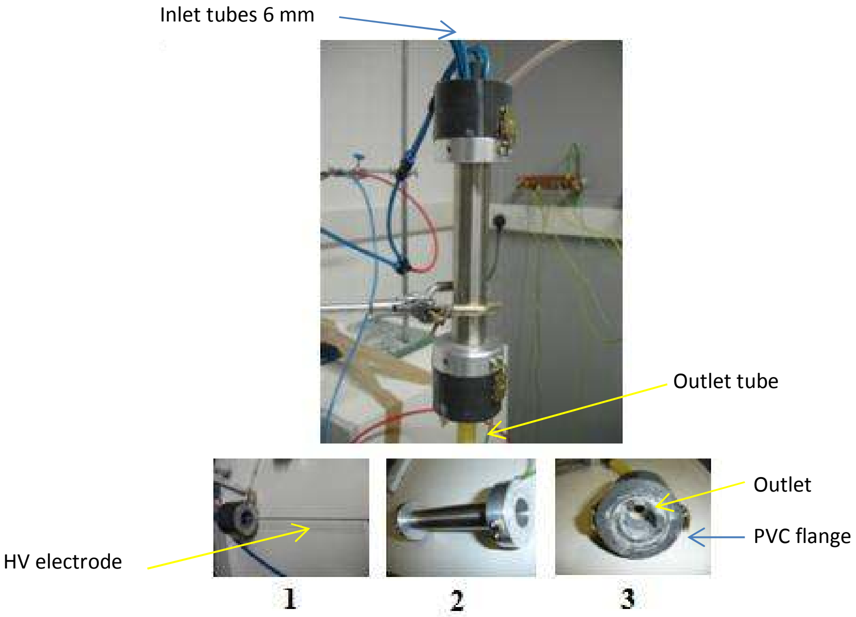

Figure 3-53: General view and the constituting components of the single stage reactor, 1-Upper PVC flange through which particles are being injected into the reactor; it also holds central HV electrode (M3 threaded rod), 2-Outer grounded cylinder which is a collection electrode, 3-Lower PVC flange of the reactor, contains the outlet tube.

The results of the precipitation tests using negative and positive charging regimes are shown in Figure 3-54 and Figure 3-55. Each bar represents the average of 3 individual tests.

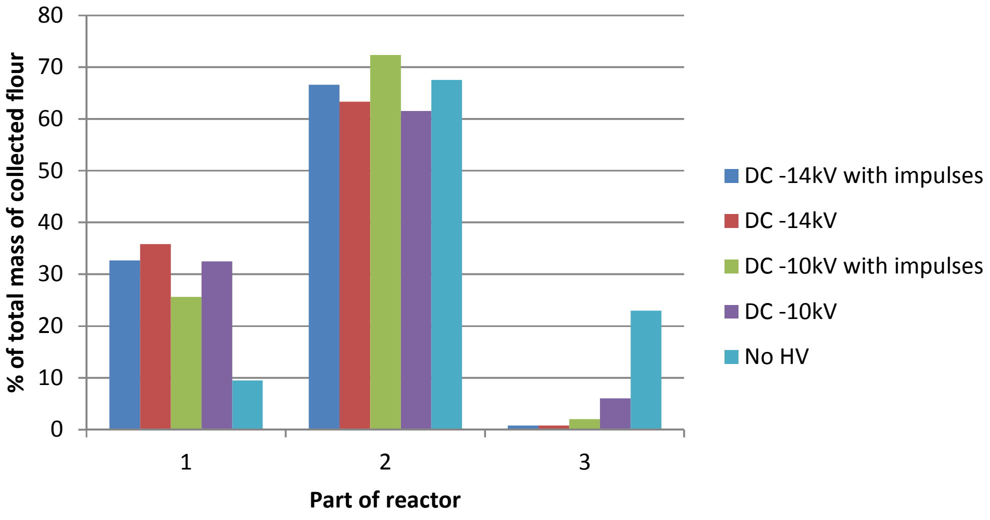

Figure 3-54: Negative dc energisation. 1-Upper PVC flange, 2-Outer grounded cylinder which is a collection electrode, 3-Lower PVC flange.

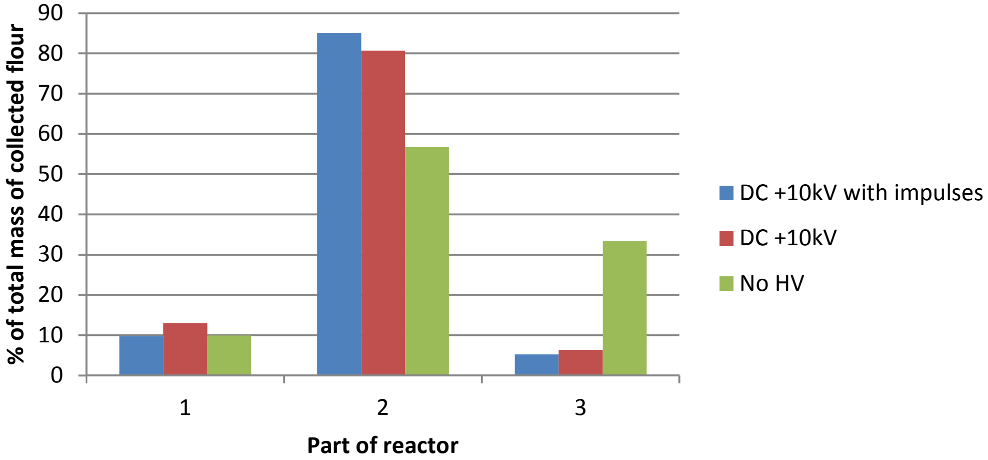

Figure 3-55: Positive dc energisation. 1-Upper PVC flange, 2-Outer grounded cylinder which is a collection electrode, 3-Lower PVC flange.

Combined results can be seen in the histogram in Figure 3-56. Again, each bar represents the average value of at least 3 individual tests. The impulsive voltage was ±25 kV for the ±10 kV dc case, while for the -14 kV dc an impulse of -28 kV (peak) was produced. The particles not precipitated, *PNP*, is *1-PP* (where *PP* is the percentage of PM that were precipitated) or:

$$\boldsymbol{PNP} = \mathbf{1} - \boldsymbol{PP} = \frac{(\boldsymbol{M3})}{(\boldsymbol{M1})+(\boldsymbol{M2})+(\boldsymbol{M3})}\mathbf{100}\% \tag{3.11}$$

PNP is indicative of the penetration rate (*1 - η*). Higher penetration rate corresponds to lower efficiency, and vice versa. Penetration rate is easier to calculate, and it is more intuitive when conducting experiments, as only a visual inspection of *M3* on a petri dish can reveal the level of precipitation.

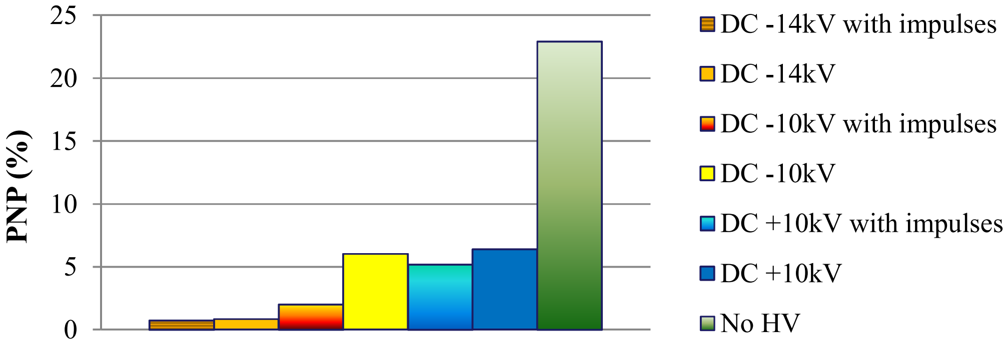

Figure 3-56: Penetration rate of the ESP reactor for different polarity of charging voltage and different energisation modes.

It was found that negative energisation results in a higher precipitation efficiency compared to the positive energisation case, which is in agreement with (Parker and Institution of Electrical Engineers, 2003). This is made clearer from the comparison of the -10 kV with impulses and the +10 kV with impulses experiments, shown in Figure 3-56, where in the case of negative energisation, the amount of particles that collected at the lower part of the reactor (end thus avoided collection) was almost 3 times lower for the -10 kV case as compared with the +10 kV case, as a percentage of the total PM collected. An important finding is that with positive polarity, the flour particles collected from the lower flange of the reactor are much finer, meaning that smaller particles tend to evade the reactor and escape. However, it was decided to use positive energisation in further tests in order to avoid excessive production of ozone and nitrogen oxides (Asbach et al., 2005a).

3.7.2. PRECIPITATION OF COARSE PARTICLES: METHODOLOGY

The experimental procedure was as follows: 20 g of flour particles were placed in the container, which had 1 inlet for the air from the air pump, and 4 outlets for delivering the particles to the reactor. However, the number of particles delivered was extremely small, thus it was decided to use a rotary shaker, this time with 4 different tubes emanating from a single outlet, for a more uniform particle delivery to the reactor. A picture of the shaker can be seen in Figure 3-57.

Figure 3-57: Particle container on top of the shaker.

The container's cap has 1 inlet for the air flow from the pump and 1 outlet to feed air with particles into the reactor. The use of the shaker provides an enhanced delivery of particles compared to tests performed without it. The outlet starts as a single tube, is then divided into two tubes, and each one is subsequently divided into another 2 tubes, giving a total of 4 tubes which are then attached to the top of the reactor. This is done in order to have an as uniform a delivery of particles into the cylindrical shaped reactor as possible. The velocity of the air flow inside the reactor was measured, using a Testo 405 Anemometer, and it was equal to ~0.5 m/s. After the reactor, the air flow was connected to a central exhaust.

Experiments were first conducted by turning on the shaker first and immediately after the air pump, and the system was run for 5 minutes. As the efficiency was calculated by mass, 5 minute intervals were thought to be sufficient for accumulation of measurable mass on all reactor parts. After a test, the shaker was to be turned off, the reactor had to be carefully disassembled so as to have the powder attached at its various parts (upper, cylinder, and lower) collected in Petri dishes. After preliminary tests, it was decided to measure the mass of the particles collected on the rod too, since this was not negligible as originally thought, especially for experiments where the reactor was not energised. A relaxation period of 20 mins, proven by early tests to circumvent issues with reduced numbers of precipitated particles in subsequent experiments, was observed between each experimental run.

Frequency was carefully monitored, so that tests were conducted at the same energisation conditions. The trigatron employed was tested to determine the maximum pulse repetition rate that could be achieved. The minimum time between impulses was 84 ms, limiting the pulse repetition rate to a maximum of ~12 pps.

In some experiments there were many breakdowns (especially in the dc only case) and this could have a negative impact on the particles collected since some craters were visible on the surface of the collected particles attached on the cylinder like in Figure 3-60.

Efficiency was calculated using (3.12):

$$\boldsymbol{\eta = \frac{Mcyl}{Mreactor} 100}\% \tag{3.12}$$

where *η* is the efficiency, *Mcyl* is the mass of the flour attached to the cylinder after the end of the experiment and *Mreactor* is the total amount of PM delivered to the reactor. *Mreactor* was calculated as:

$$\boldsymbol{Mreactor = Mr + Mt + Mcyl + Mb + Mesc = 20\ g - Mremaining} \tag{3.13}$$

where *Mr*, *Mt*, *Mb*, and *Mesc* are the amounts of flour particles collected from the HV electrode, upper PVC flange, the lower PVC flange and the particles that managed to escape from the reactor, after passing through it, respectively.

PM delivered can be calculated readily by subtracting the mass of the flour remaining in the container after the experiment from the initial 20 g flour sample. This is equal to the combined mass of the particles attached to the rod, upper part, cylinder and lower part of the reactor. If collection is defined not only as the particles attached to the cylinder (which is the collection electrode), but as the particles attached to all parts of the reactor, then efficiency can be re-written as:

$$\eta = \frac{Mr+Mt+Mcyl+Mb}{Mreactor}100\% \qquad (3.14)$$

It is expected that some inconsistencies with the results might arise because of the fact that the rod could not always be placed in the center of the cylinder, but could be displaced by a few mm. It is speculated also that with a longer cylinder, the efficiency may rise. The obtained efficiency has been plotted in two graphs, Figure 3-58 and Figure 3-59, one for the percentage of the particles that were attached to the cylinder compared to the delivered total, and one showing the percentage of the particles that were attached to any part of the reactor compared to delivered total.

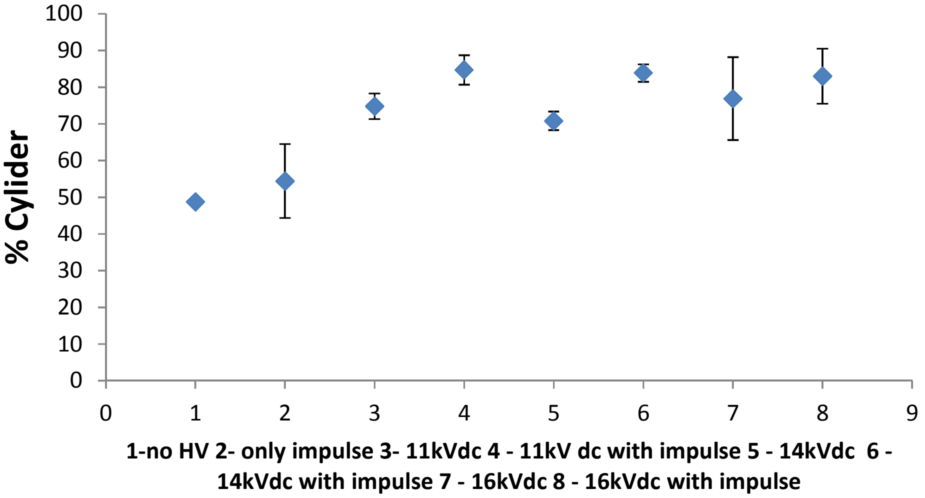

Figure 3-58: Efficiency (mass of particles on the cylinder compared to the mass of the delivered particles) for the various experiments conducted.

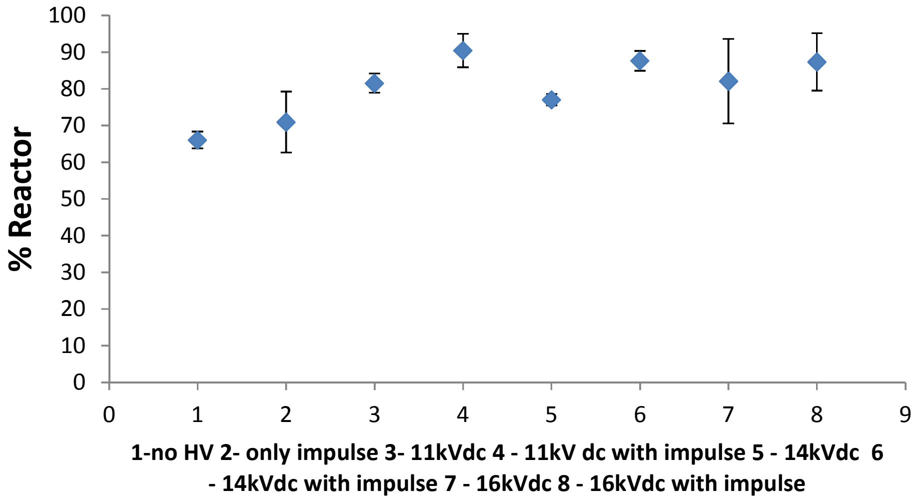

Figure 3-59: Efficiency (mass of particles on all reactor parts compared to the mass of the delivered particles) for the various experiments conducted.

It can be seen from Figure 3-58 and Figure 3-59 that the efficiency is much higher if it is calculated using the mass of all reactor parts over the particles delivered (equation (3.14)). The equation (3.12) for efficiency seems sounder, as it is the particles on the collection electrode that are efficiently collected. The particles on the HV electrode, upper PVC flange, the lower PVC flange part could easily escape towards the outlet, in case any automated cleaning mechanism was installed.

A photograph showing the craters (pits) on the powder layer surface attached to the cylinder due to the spark breakdowns that occasionally occurred is shown in Figure 3-60. As was analysed in the literature review, some spark breakdowns are acceptable (White, 1963), however the more frequently they occur, the greater the amount of PM that is re-introduced into the air flow, thus compromising precipitation efficiency.

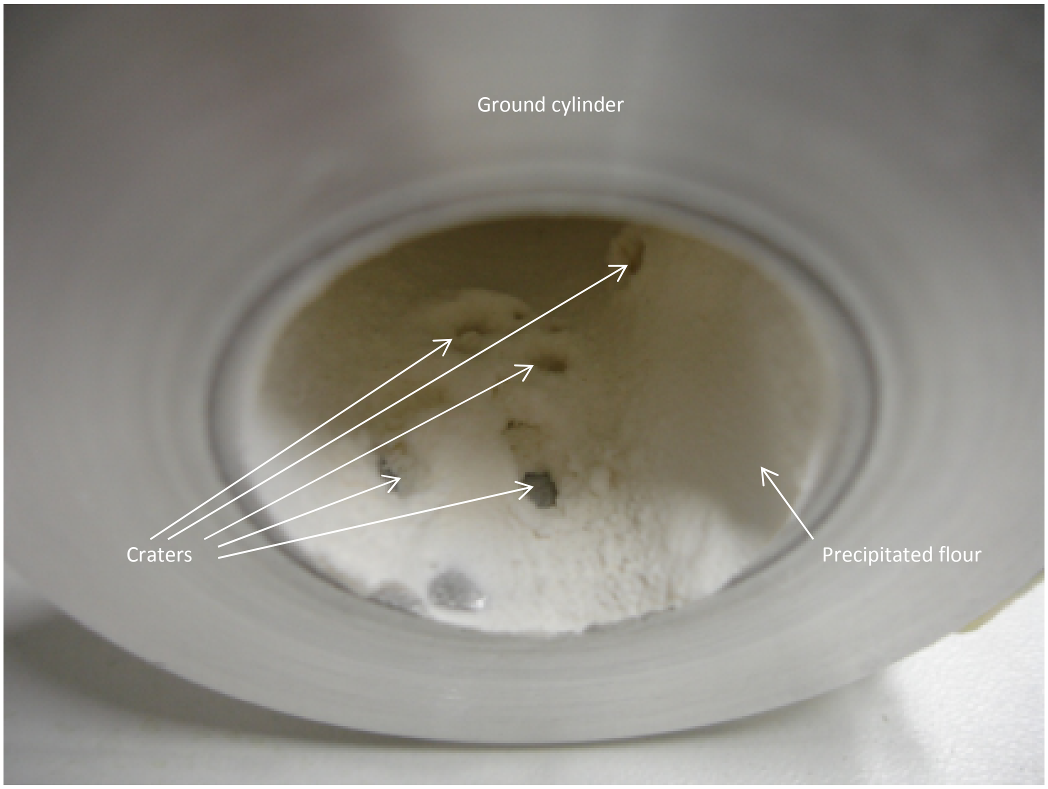

Figure 3-60: Photograph of the “craters” created on the flour layer on the inner surface of the cylinder due to spark breakdowns.

Based on the previous results, the standardised procedure used during the subsequent precipitation experiments is as follows. Firstly, 20 g of flour were measured using precision scales and put into a plastic container that was fixed on top of a microbiological centrifuge shaker. Then the container’s cap was fixed and the inlet on top of the cap was connected to an air pump that delivered 16 ℓ/min of air. From the outlet, four 6 mm diameter flexible plastic tubes delivered the flour particles blown by the air flow from the container to the top of the coaxial reactor, each delivering it to its own quadrant of the top part of the reactor for uniform spread of the PM. Air speeds in the reactor were ~0.5 m/s. When experiments commenced, both the shaker and air pump where turned on and the time of the experimental runs was fixed at 2 minutes. The precipitation time had to be reduced from 5 min to 2 min to avoid particle saturation on the collection electrode in these batch style precipitation tests. Energisation voltages were +11 kV, +14 kV and +16 kV dc, with superimposed impulses of +26 kV, +29.3 kV and +30.9 kV, respectively. It was also decided to test the precipitation efficiency with just impulses, at +15.9 kV level and without HV at all, in order to observe how much of the powder self-precipitates. The pulse repetition rate was set at 10 pps for all tests.

Efficiency was defined as the ratio of the mass of the PM precipitated on the collection electrode (internal cylinder surface), over the (calculated) mass of the particles delivered. This was straightforward to calculate as the initial mass was known, and the mass on each part of the reactor was measured by carefully disassembling it. Thus, the amount of flour that passed through the reactor could be calculated by simple subtraction of the initial amount of flour minus the PM collected on all parts of the reactor. Then the mass that escaped was added to the mass collected (on every part of the reactor), yielding the mass delivered. Mass measurements were conducted with an OHAUS Adventurer AR1530 digital scales with readability down to 0.001 g and precision ±0.002 g.

3.7.2.1. Results

The results of the first set of precipitation experiments using flour and only dc voltage for energisation are shown in Figure 3-61. Five experiments were conducted for each energisation level, and their average precipitation efficiency and standard deviation were calculated. In addition, 5 tests were also conducted without energising the HV electrode, and this was used as a control test. Each data point represents the average efficiency of precipitation (ratio of particles collected on the collection electrode only, over the delivered particles) and the error bars represent ±1 σ. It can be pointed out that precipitation efficiency is almost equal for all tested energisation levels, varying between ~71% and ~77%. At the +16 kV dc energisation level, there were occasional breakdowns that were later connected with craters found on the surface of the precipitated material, which was accumulated on the internal surface of the collection electrode. These breakdowns caused part of the precipitated material to reenter the air-flow, manifesting in the larger standard deviation (error bars) shown in Figure 3-61, case 4. In the case of no energisation voltage, ~50% of the particles were precipitated, possibly as a result of friction with the plastic delivery tubes or between themselves in the turbulent air flow.

Precipitation experiments were conducted with the HV electrode energised with impulses superimposed on dc voltage. The results of this set of tests are presented in Figure 3-62, again with each point representing the average of 5 individual tests and the error bars ±1 σ. Tests were conducted for energisation of +15.9 kV impulses only, for +26 kV impulses superimposed on +11 kV dc, for +29.3 kV impulses superimposed on +14 kV dc voltage, and for +30.9 kV impulses superimposed on +16 kV dc voltage. In addition, the test with no energisation voltage (control case) is included for comparison.

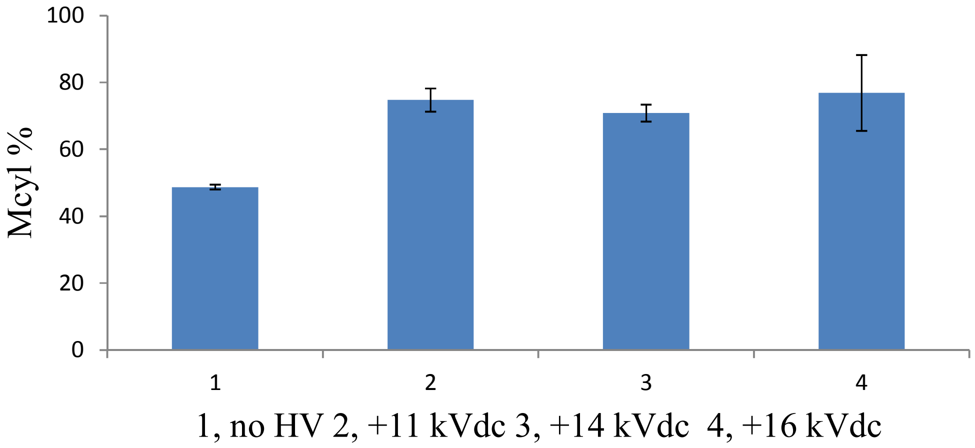

Figure 3-61: **Efficiency of precipitation, dc energisation only. 1) control (no HV); 2) +11 kV; 3) +14 kV; 4) +16 kV.**

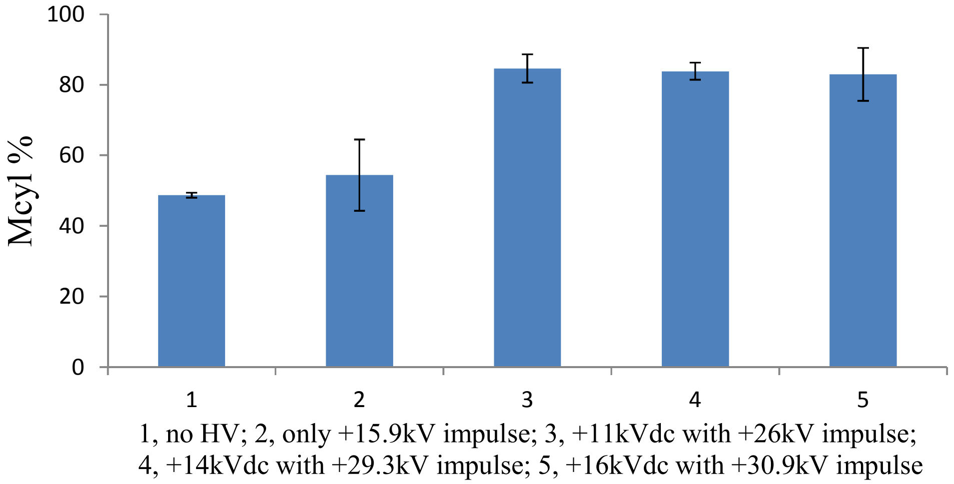

Figure 3-62: **Efficiency of precipitation, superposition of dc and impulses. 1) control (No HV); 2) +15.9 kV impulses only; 3) +11 kV dc with +26 kV impulses; 4) +14 kV dc with +29.3 kV impulses; 5) +16 kV dc with +30.9 kV impulses.**

From Figure 3-62, it can be pointed out that energisation with HV impulses only, displayed the lowest precipitation efficiency, at ~55% (Figure 3-62, case 2), only marginally higher than the control case (no HV). +26 kV impulses superimposed on +11 kV dc voltage (Figure 3-62, case 3) showed the highest precipitation efficiency at ~84%. However, for higher voltages (+14 kV dc with +29.3 kV impulses and +16 kV dc with +30.9 kV impulses), the efficiency was almost the same, at ~83% and ~82%, respectively. This is probably due to the fact that at lower voltage levels, the particle saturation charge has been reached, or additionally that the cylinder cannot sustain any more particles due to the corresponding increase in air-speed in the reactor because of the contraction of the air flow by the collected material. For this to happen, the air speed in the reactor should be at least 1 m/s according to (McKenna et al., 2008). This could happen in extreme cases that there is 5 mm of accumulated material on the collection electrode, constricting the internal diameter of the reactor to only 1.84 cm. It should be noted also that for the highest energisation voltage, (+16 kV dc with +30.9 kV impulses), the same increase in standard deviation is observed as in the previous (only dc energisation) test set. This is most probably due to the same reason, sporadic breakdowns and corresponding reeintrainment of captured particles.

As a last step, it was decided to perform additional experiments in order to see if the results could be reproduced accurately. Experiments conducted were with +14 kV dc charging voltage, with and without superimposed impulses. This voltage was chosen because it lies between the +11 kV dc charging cases, which were the first conducted with both dc and impulse charging, and the +16 kV dc cases, in which many breakdowns occurred. These additional experiments proved very close to the original 14 kV results, to within 1 standard deviation for efficiency.

3.7.3. PRECIPITATION OF FINE PARTICLES: METHODOLOGY

The particle analyser used in the tests with fine particles was the “Portable Laser Aerosol Spectrometer and Dust Monitor”, Model 1.109, produced by GRIMM Ltd. It has the capability to conduct measurements for particle concentration in particles per litre (counts/ℓ) or for mass concentration in particle mass per volume (μg/m^3). It can also display data in powder mass fractions according to EN 481 standards for occupational health (respirable, thoracic and alveolic) or in terms of emission (PM10, PM2.5 and PM1). The latter are for comparison purposes (for example with outdoor experiments), however they do not comply with EN 12341 or US EPA standards. Particles down to 250 nm in diameter can be detected, which can be classified in 31 different size ranges from 0.25 μm to > 32 μm. The width of these size channels is pre-set and cannot be changed. Data are collected in intervals from 6 s up to 60 min, however if a pc with a Grimm software package is connected to the laser monitor, its sampling time can go down to 1 s. Connection is provided through an RS-232 port.

Figure 3-63: Grimm 1.109 particle analyser.

Additional changes to the whole system had to be made because of the different particles to be used. Since the particle analyser is calibrated by the use of dolomite powder, it was decided to use the same material in precipitation tests. For these tests, a new sealed container to deliver these particles to the reactor was designed and developed, to avoid leakage of fine particles. The new PVC container for handling fine dolomite particles shown in Figure 3-64 was designed. There was no need to use the shaker, as there were enough particles delivered with only the air flow through the container with dolomite powder.

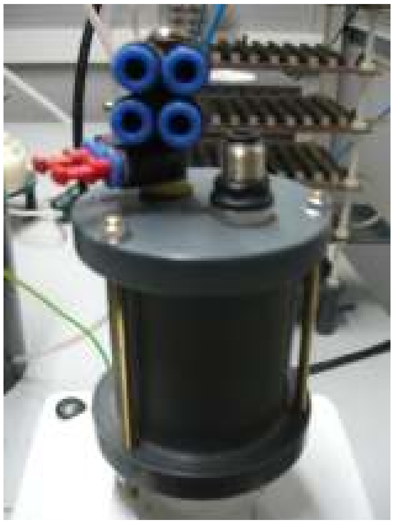

Figure 3-64: New PVC container used for fine particles.

A new gas distribution board was designed and developed and included a flow meter. The air flow rate measured with this flow meter was 16 ℓ/min. The particle analyser was attached at the outlet with a T-junction being used in order to provide a sample of the particles that passed through, as only a fraction of the air flow needs to pass through the particle analyser. The particle analyser uses a pump rated at 1.2 ℓ/min, therefore the air flow at the exhaust should be 14.8 ℓ/min. Both the pneumatic and energisation systems can be seen in Figure 3-65.

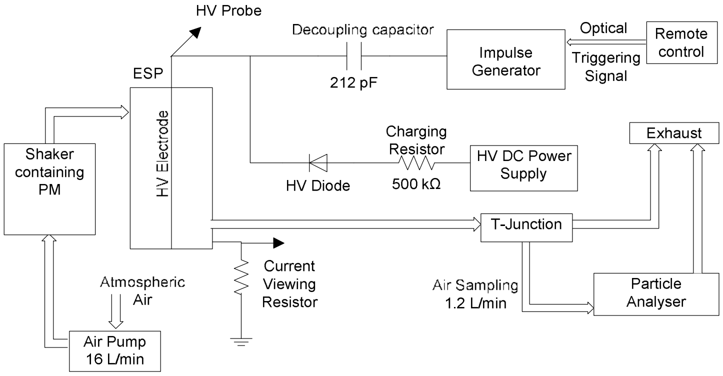

Figure 3-65: Pneumatic and electric circuitry of the single stage ESP system used.

Changes were made to the electrical circuit in order to improve its behavior (recovery of voltage) upon the presence of current pulses. In order to have shorter voltage recovery time, the dc charging voltage resistor was halved (from 0.982 MΩ down to 0.562 MΩ). RC is now down to 119 μs.

Moreover, a new trigatron with interchangeable electrodes was built, so that a wide range of frequencies could be achieved. In the experiments that follow, a pulse repetition rate of 50 pps was chosen, in order that there would be no particles passing through the reactor without experiencing at least one pulse (with flour particles, the pulse repetition rate was 10 pps, in self breakdown mode, which meant that a particle flying straight through the reactor (shortest path) would be subject to at least 4 impulses). As the reactor's length was 0.2 m and the measured speed was 0.5 m/s, thus a particle passing straight through the reactor (worst case scenario) would be remain in it for at least 400 ms.

The particle analyser was placed in a grounded, shielded, metallic container, in order to minimise electromagnetic noise, and also to provide room for a laptop computer connected to the analyser.

Experiments were conducted with different amounts of powder into the container, so as to establish optimal conditions for efficiency measurements, for the experiments to follow. For 4 g and 2 g of powder, there was an overflow of data, as the amount of particles was too high, in some cases even millions, overflowing the particle analyser. Therefore, further reduction was necessary in order to have particle concentrations which could be measured by the analyser. It was established that 1 g of dolomite powder in the container produced a sufficient number of particles in the air flow for registration. 0.5 g of dolomite were also used, however, in this case, the amount of powder delivered to the precipitator during tests was less stable, and the corresponding efficiencies calculated had higher standard deviations. Therefore, it was decided to continue with precipitation tests using 1 g of powder and 5 min run time. Due to the particle analyser used, the efficiency was calculated not by weight of the particles collected, but by calculating the percentage of the particles collected compared to a non-energised experiment. This constitutes a change in the precipitation efficiency definition: test with no high voltage now corresponds to 0% efficiency. Thus, experiments were initially conducted with no dolomite powder inserted to the system.

A problem arising was the fact that there were different levels of background (or ambient) particles on different days. This was perhaps due to variable weather (if it is dry and sunny, there tends to be higher levels of dust in the air), due to the ventilation in the laboratory, or perhaps due to the nearby technical activity during that day. This issue was resolved by conducting all precipitation experiments belonging to a set in a single day (without energisation, energised with dc, energised with dc and impulses), and by comparing different energisation level tests only within the same set, in order to calculate precipitation efficiency.

PM concentration levels (in counts/ℓ) were measured for each test every 6 s. Three tests were conducted for each set of experiments and an average concentration was found for each particular time interval. This was done because the pattern of particle delivery into the reactor had a uniform "impulsive" shape, meaning that as soon as particles started entering the reactor, their concentration rose sharply and stayed at that level for ~10 time intervals (≈ 1 min). The concentration levels then fell considerably, as the container became almost depleted of fine particles. For the efficiency calculations conducted, only measurements close to the peak were taken into account, meaning that a high concentration of particles was present in the reactor, which constitutes a worst case scenario for efficiency calculations according to (Zukeran et al., 1999). However, for these efficiency values at the peak of particle concentration, the maximum was chosen as the efficiency outcome, as this shows the true potential under adverse conditions that the reactor under test can achieve. To put it in mathematical formulation: Experimental results are presented as $E_n(t)$, where n is the experimental run number (1, 2 or 3), and t is the discrete time of concentration sampling by the particle analyser ($t = \tau, 2\tau, 3\tau$... where $\tau = 6$ s for the particular tests conducted). Then, the median for each test under the same conditions was calculated, for each particular time step separately:

$$\overline{E_{test}(t)} = \frac{E_1(t)+E_2(t)+E_3(t)}{3} \qquad (3.15)$$

The precipitation efficiency is calculated by dividing each the average of each experimental result by the average of the non-energised case as follows:

$$\eta(t) = 100\% - \frac{\overline{E_{test}(t)}}{\overline{E_{non-energised}(t)}} 100\% \qquad (3.16)$$

Finally, the precipitation efficiency is:

$$\boldsymbol{\eta} = \boldsymbol{max}(\boldsymbol{\eta}_{\boldsymbol{\tau}}, \boldsymbol{\eta}_{\boldsymbol{2\tau}}, \dots, \boldsymbol{\eta}_{\boldsymbol{x\tau}}) \tag{3.17}$$

where *x* is the point that PM delivery into the reactor reduces considerably.

It can be seen that precipitation efficiency is much higher for PM2.5 and at the same levels with coarse particles, if 0.5 g of dolomite powder is used. This most probably has to do with the fact that a portion of the dolomite powder gets attached to the internal part of the PVC container used to deliver the particles to the reactor, leaving a substantially smaller amount of powder delivered to the system compared to the use of 1 g of dolomite powder.

Furthermore, a change had to be made to the exhaust in order to prepare a sample point at which the particle analyser would be fed. This was done with the help of a T-junction, a Cu water tube of ~30 cm length and 4 mm dia flexible plastic tubing.

Since the precipitation reactor is intended for indoor use, where the air flow contains much lower concentrations of PM than those used in the coarse particle tests, it was decided to reduce the amount of particles injected into the reactor. However, this made the counting of particles by mass virtually impossible, as not only are the actual amounts much lower, but also the finer state of dolomite powder makes its collection much harder. Therefore, for the analysis of the precipitation efficiency of fine particles a portable particle spectrometer Grimm 1.109 (Grimm Aerosol Gmbh) was used. dc Corona ignition voltage was measured at +17.5 kV. In these tests, only 1 g of dolomite powder was placed in the container, to be delivered into the reactor with the same flow rate of 16 ℓ/min, as in the coarse particle experiments.

The energisation levels for precipitation tests with dolomite powder were +11 kV dc superimposed with +24 kV impulses, +15 kV dc superimposed with +26 kV impulses and +16 kV dc superimposed with +32 kV impulses. Precipitation tests were also conducted with dc energisation only (+11 kV dc, +15 kV dc and +16 kV dc), in order to compare precipitation efficiency for these two types of energisation.

Precipitation efficiency in the case of fine particles, was obtained by equation (3.17): the efficiency of precipitation was calculated as the ratio of the number of particles per litre in energised mode and the number of particles (known as counts) per litre for the case that no high voltage was applied on the energisation electrode. Despite the fact that the particle analyser had 31 channels, it was decided to use only 19 of them (from 0.25 μm up to 5 μm,

Figure 3-66, Figure 3-67 and Figure 3-68, for various energisation modes), as negligible amounts of particles were registered in the size ranges greater than 5 µm, making any statistical analysis futile. In order to calculate the efficiency data points in Figure 3-66, Figure 3-67 and Figure 3-68, at least three individual tests were conducted. The detailed steps of the precipitation experiments can be found in Appendix E.

3.7.3.1. Results

In Figure 3-66, Figure 3-67 and Figure 3-68, the experimental results of precipitation tests using dolomite powder as a source of airborne PM are shown. The red lines represent experiments with dc voltage only, while the blue lines denote impulsive energisation superimposed on dc voltage. For +11 kV dc energisation, either with superimposed impulses or not, the efficiency remained virtually the same. Efficiency increases as size increases for particles less than 0.4 µm. The efficiency is much lower for particles in the range 0.45 µm to 0.65 µm, however then increases with increasing size. The second part of behaviour is predominantly field charging, while the first is diffusive. The behaviour between these two regimes is complicated with an apparent peak in efficiency for 0.5-0.58 µm. It is not clear why this peak is occurring though it is consistently seen in Figure 3-66, Figure 3-67 and Figure 3-68. According to (European Parliament and Council of the European Union, 2008), it is expected to have a drop in efficiency in the range of transition between field charging and diffusion charging, and this trend is generally followed. Increasing the dc voltage to +15 kV boosted the precipitation efficiency up to ~81%-99.6% (depending upon the size range) for the combined impulsive (+26 kV) and dc energisation case. For the dc only case, the precipitation results were similar to those with +11 kV dc energisation. In Figure 3-68, it can be seen that further increase in the energisation voltage enhanced the precipitation efficiency even further, especially for particles > 2.5 µm, where the efficiency was ~100% for +32 kV impulses superimposed on +16 kV dc voltage. +16 kV dc only energisation demonstrated higher precipitation efficiency, ~75%-93.5% depending upon PM size, which is lower compared to the combined energisation case (+16 kV dc with superimposed +32 kV impulses). For both +15 kV and +16 kV dc levels (with and without superimposed impulses) there were fluctuations in the (0.4-0.65) µm size ranges, but not as pronounced as in the +11 kV dc case.

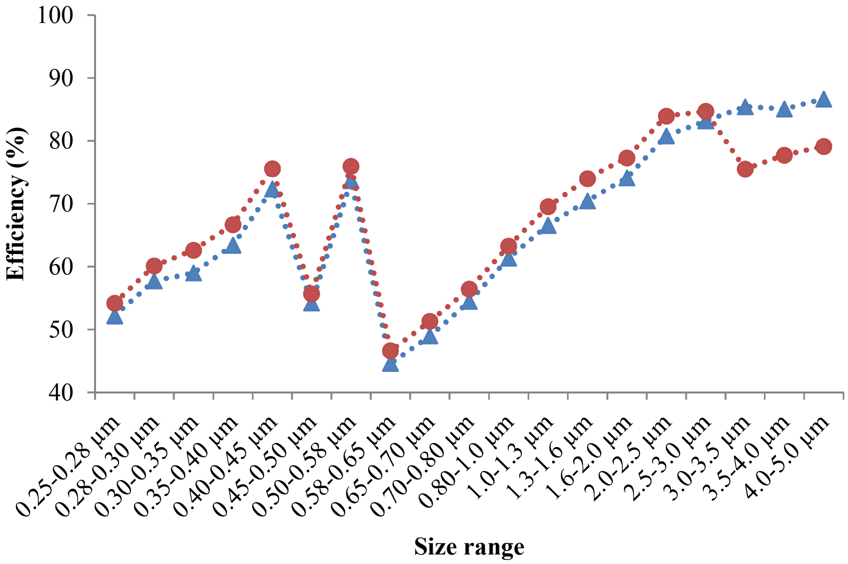

Figure 3-66: Precipitation efficiency at +11 kV dc with +24 kV impulse energisation. Circles, dc energisation only; triangles, superposition of dc and HV impulses.

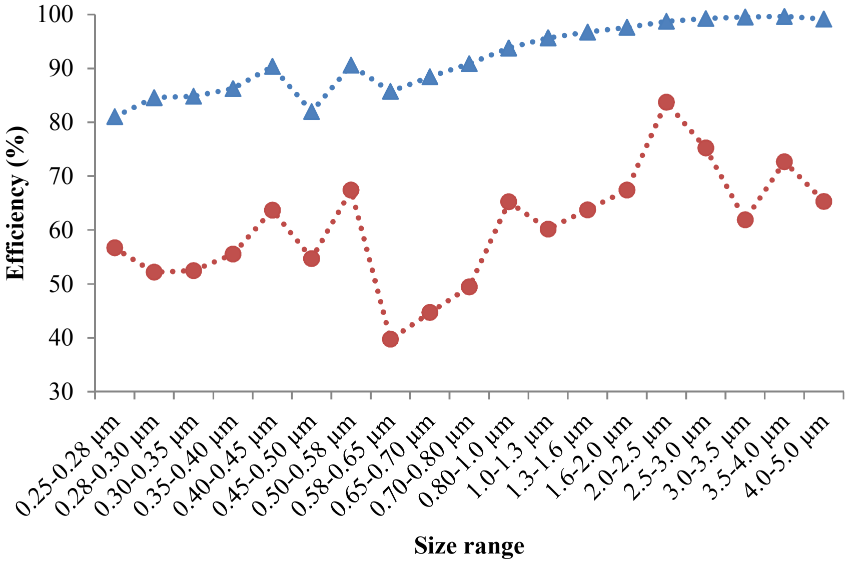

Figure 3-67: Precipitation efficiency at +15 kV dc and +26 kV impulse energisation. Circles, dc energisation only; triangles, superposition of dc and HV impulses.

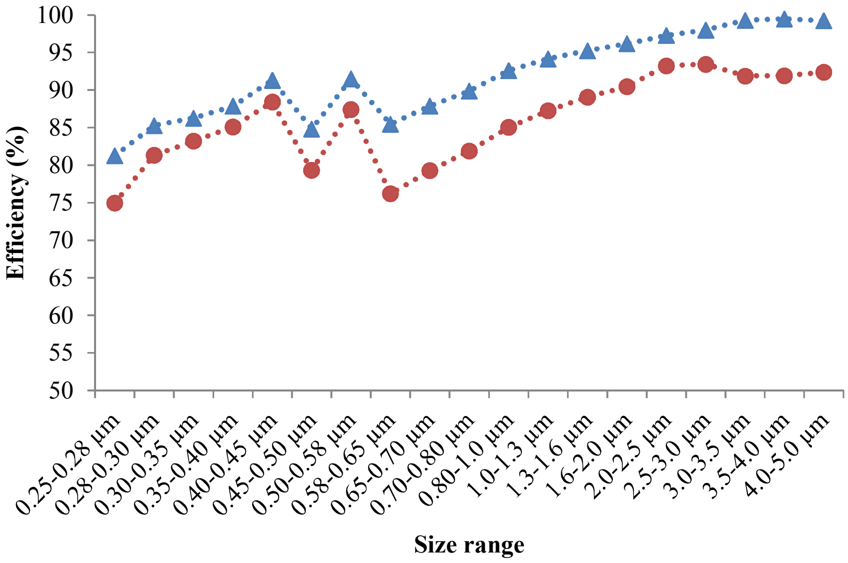

Figure 3-68: Precipitation efficiency at +16 kV dc with +32 kV impulse energisation. Circles, dc energisation only; triangles, superposition of dc and HV impulses.

3.8. CONCLUSIONS

A single-stage, coaxial, electrostatic precipitation reactor has been developed and tested. Its central electrode is composed of an M3 threaded steel rod, and is intended to charge and deflect PM. It was designed to be compact so that it could be used as a standalone device in small scale indoor air-cleaning applications, or to be easily incorporated into existing devices. A novel energisation method has been developed, using 250 ns duration impulses superimposed on dc voltage. The effect of impulses superimposed on dc energisation on precipitation efficiency has been investigated. Precipitation of coarse (flour) and fine (dolomite) particles has been studied, using different dc and impulsive voltage energisation combinations. The air flow rate of the suspended particles was 16 ℓ/min, while the temperature, pressure and humidity were that found in ambient laboratory air.

The electric field distribution in the reactor has been obtained and analysed; *I(V)* curves, breakdown voltage and corona inception voltage have been obtained for air and air loaded with powder, with and without particle laden air flow. This was necessary in order to establish the operational limits of energisation of the reactor and to optimize its design.

It was found that ~50% of coarse particles precipitate even without any applied voltage. HV Experiments with coarse particles showed that ~80% efficiency was reached. The efficiency could be increased further by superimposing impulsive voltage on the otherwise dc energised HV electrode. For a superposition of +26 kV impulses on +11 kV dc voltage, a precipitation level of ~85% was reached. By increasing the dc voltage higher than +11 kV, no corresponding increase in precipitation efficiency was achieved. This counter-intuitive fact could be explained if the charge on particles had reached its saturation level, even for lower energisation levels.

Precipitation experiments in which different energisation polarities were used showed that negative polarity has higher efficiency compared to positive, and especially in the superimposed mode tested (±10 kV dc with ±25 kV superimposed impulses), the efficiency of precipitation was almost 3 times higher for negative HV stress. However, negative polarity produces higher levels of O_3 and NO_x gases according to (Asbach et al., 2005a), and thus should be avoided for indoor, small-scale air cleaning applications that this μ-ESP technology is intended for.

Precipitation experiments with fine powder showed that impulses do not affect precipitation efficiency for low levels of dc voltage. It was found that +11 kV dc voltage only, and +24 kV impulses superimposed on +11 kV voltage, resulted in almost identical precipitation efficiencies, which varied from 45% to 90% depending upon the particle size range. When the impulses were combined with higher dc voltage (+15 kV and +16 kV dc), though, an increase in precipitation efficiency was obtained, from 81% to 99.6%, depending upon the particle size range. The particle size range of (0.4-0.65) μm showed a dip in the precipitation efficiencies, that could be expected from the gradual change of dominant charging mechanisms (from diffusion to field) in this size range (Parker and Institution of Electrical Engineers, 2003). In addition to the above, for particles > 4 μm, the combined energisation always produced increased precipitation efficiencies compared to the dc only energisation, on similar level. In terms of absolute numbers, ~100% efficiencies were achieved only for size ranges > 2.5 μm, however it is expected that in an improved double-stage precipitation design that has separate charging and deflection stages with different energisation levels, the precipitation efficiency of PM2.5 particles would be increased. The use of different lengths of Cu tube could affect the measurements. The fact that efficiency seems to be higher for the PM2.5 particles with a longer Cu tube could imply that by increasing the length of the collection electrode (cylinder), higher efficiency values could be achieved. In summary, it was successfully demonstrated that sub-μs impulses superimposed on dc voltage can increase precipitation efficiency.

4. DOUBLE STAGE PRECIPITATION REACTOR

4.1. INTRODUCTION

A two stage precipitator reactor was designed and developed, in order to improve the precipitation efficiency of fine particles and to reduce the energy consumption of the ESP process. In single stage designs, corona discharge is generated along the whole length of the precipitator, thus the corona discharge power is significantly higher compared to double stage designs (White, 1963). In contrast with single stage designs, the typical dc voltage levels needed for efficient particle charging in double-stage designs are much lower (White, 1963). Moreover, according to (McKenna et al., 2008, Böhm, 1982), double stage precipitators are usually implemented for low PM loading and PM2.5 particle collection, and are mainly found in air cleaning applications. Another advantage of double stage ESPs is their ability to maintain high precipitation efficiency levels at elevated gas flow velocities (White and Cole, 1960). Thus, a double stage precipitation design was designed, constructed and tested in the course of this research program. In order to reduce power consumption and to enhance precipitation efficiency, impulsive voltage was used instead of dc energisation.

The first stage of the ESP reactor is intended to be used as a particle charging stage, which is energised by HV impulses or superposition of impulses and dc voltage, while the second stage of the reactor is used for particle deflection and collection and thus energised with lower levels of dc voltage. To these ends, the first stage had a thin metallic wire acting as high voltage electrode in its centre, while the second stage had a larger diameter smooth rod as a HV electrode. Thus, high electric field is developed in the first stage of the ESP system, while in the second stage the field can be below or just above corona ignition - was found that such superposition worked well in the case of the single stage design when loaded with coarse PM (flour). However, when fine and ultrafine particles (dolomite) were passed through the single stage reactor, the precipitation efficiency achieved with shorter impulses (250 ns) was not sufficiently high (~81%-91%), for particles (250-500) nm in diameter, thus longer, microsecond impulses were used in this chapter. Experiments with shorter, 250 ns impulses were conducted only for comparison with the longer impulses used in the double-stage reactor. In both stages of the precipitation system, the outer metallic cylinders were earthed and acted as particle collection electrodes. In order to investigate precipitation efficiency of PM2.5 particles, cigarette smoke and particles present in ambient laboratory air were used as test particles. Analyses of the precipitation reactor, energisation system, particles used and experimental results are given in the subchapters that follow.

4.2. AIR FLOW AND ELECTRIC FIELD DISTRIBUTION

In order to select optimal dimensions of the new double stage reactor, the air flow and electric field distribution in coaxial topology was analysed. An important aspect that influences precipitation efficiency of an ESP is the air velocity of particles in the reactor, as this not only affects the number of impulses each particle would be subjected to, but also the process of reeintrainment of particles (washing away of already precipitated particles) due to the high air flow speed. Air velocity, *u*, was calculated using equation (4.1):

$$\boldsymbol{u} = \frac{\boldsymbol{Flow\ rate\ of\ air}}{\boldsymbol{Cross{-}sectioned\ area\ of\ reactor}} \tag{4.1}$$

Air velocity was calculated for the new reactor with a larger radius of 23.88 mm and for the single stage reactor, which had a 14 mm internal radius. The results are shown in Figure 4-1. The air-pump used in the tests was capable of delivery of up to 16 ℓ/min of air. It can be seen that, even with the narrower reactor vessel (14 mm) and the highest achievable air flow rate, the air speed is not near the reeintrainment air speed limit according to (McKenna et al., 2008), which is ~1 m/s. In practical applications, the air flow rate could be increased even beyond the maximum achievable air flow rate of the laboratory air-pump (16 ℓ/min), however with the smaller diameter of the reactor, the precipitation efficiency could be reduced, as the collected particles might start to be washed away and thus re-enter the air circulation due to the high air flow speed (Blejan et al., 2010). The air flow rate was, therefore, kept at its maximum value of 16 ℓ/min in all experiments. The internal diameter of the single stage reactor described in Section 3.1 was 28 mm while a new, wider double stage reactor has 47.8 mm diameter. Using these numbers, (4.1) gives the air speed based on the maximum air flow at 0.43 m/s for the single-stage reactor described in Section 3.1, and 0.149 m/s for the double stage reactor proposed in this section.

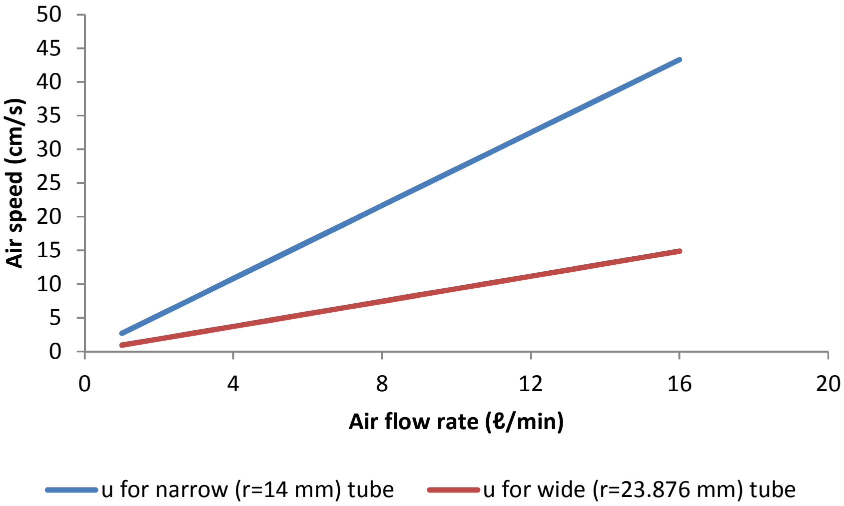

Figure 4-1: Air speed inside the reactor as a function of air flow rate for a narrow and a wide cylinder. Narrow cylinder has 14 mm internal radius, while the wide one has 23.876 mm (1.88 inch internal diameter).

In the precipitation tests presented and discussed in this chapter, the wider reactor with diameter of 47.8 mm was used. This diameter will allow for increasing the air flow rate without re-entraining collected PM, which can be needed for practical, air cleaning applications.

The newly developed reactor is a 2-stage one, therefore for optimisation of the topology of the reactor, the electric field was calculated for different topologies of energisation electrodes. In this analysis, the outer collection electrode was a cylinder with a 14 mm or 23.88 mm radius.

The amplitude of the electric field in the cylindrical reactor was calculated using (4.2) (Buck and Hayt, 2001) for a +10 kV energisation voltage. The electric field as a function of distance from the central HV electrode in the reactor for different radii of the central HV wire (α = 0.1 mm, 0.25 mm, 0.75 mm, 1.5 mm and 3 mm) is shown in Figure 4-2, for different radii of the external cylinder (β = 14 mm and 23.88 mm). Figure 4-2 shows the ideal (Laplacian) field distribution in the reactor obtained by (4.2).

$$\boldsymbol{E} = \frac{\boldsymbol{V}}{\boldsymbol{r}\boldsymbol{ln}\left(\frac{\boldsymbol{\beta}}{\boldsymbol{a}}\right)} \tag{4.2}$$

were *E* is the electric field, *V* is the charging voltage, *r* is the radial dimension in cylindrical coordinates, β is the internal radius of the cylinder and α is the radius of the coaxially positioned, HV electrode.

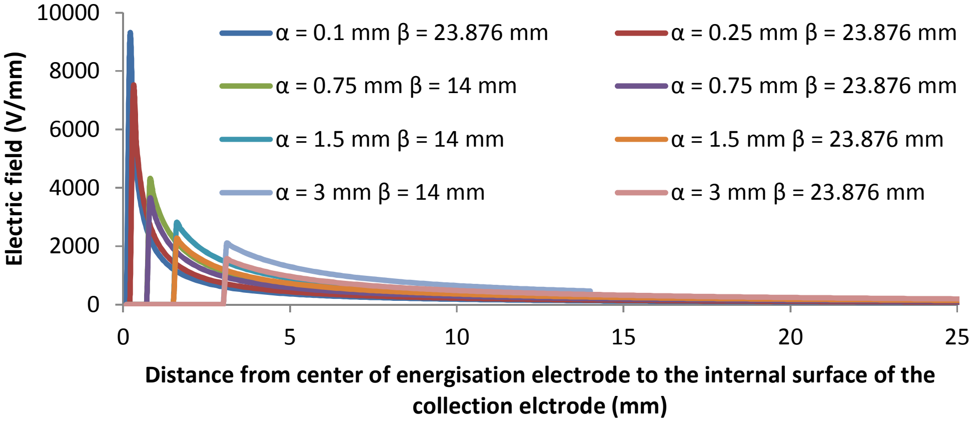

Figure 4-2: Electric field as a function of distance from the charging electrode for energisation rods with various radiuses.

The *E*-field is higher for the central electrode with smaller radius (β = 0.1 mm) and narrower outer tube (14 mm), however, the wider outer electrode of 47.8 mm diameter was selected for this double stage design, in order to enable higher flow rate of air should it be required for specific applications, while the electric field remains at a comparably high level. It is expected that the double stage design proposed in the present work will help to improve precipitation efficiency and to achieve desirable levels of precipitation of PM2.5 particles in practical applications.

4.3. DEVELOPMENT OF THE DOUBLE STAGE REACTOR

In this phase of the research project, a 2 stage reactor was designed and constructed, with both stages having coaxial topology. As discussed in Section 4.1, the first stage is intended for charging the PM suspended in the air flow, while the second stage is needed for deflection and collection purposes.

To these ends, and based on the simulation presented in the Section 4.2, a 0.1 mm radius wire was selected for the HV electrode for the charging stage, as this results in sufficiently high electric field close to the wire surface, resulting in the production of impulsive corona current. In practice, a 35-*gauge* wire with 0.2134 mm diameter was used. This is because despite the fact that thinner wires could be found, their mechanical strength was lower, which could be a potential problem for practical applications, especially if the need for regular cleaning is taken into account.

As the second stage of the reactor is intended for particle deflection and collection, a 3 mm diameter smooth rod, charged with dc voltage, was deemed appropriate for this purpose – to produce an electric field that will deflect the charged particles from the air flow. This rod was placed coaxially at the centre of the second stage. For both stages, the collection electrodes were composed of 47.75 mm internal diameter, earthed, stainless steel cylinders, surrounding their respective energisation electrodes. Each stage was 200 mm long.

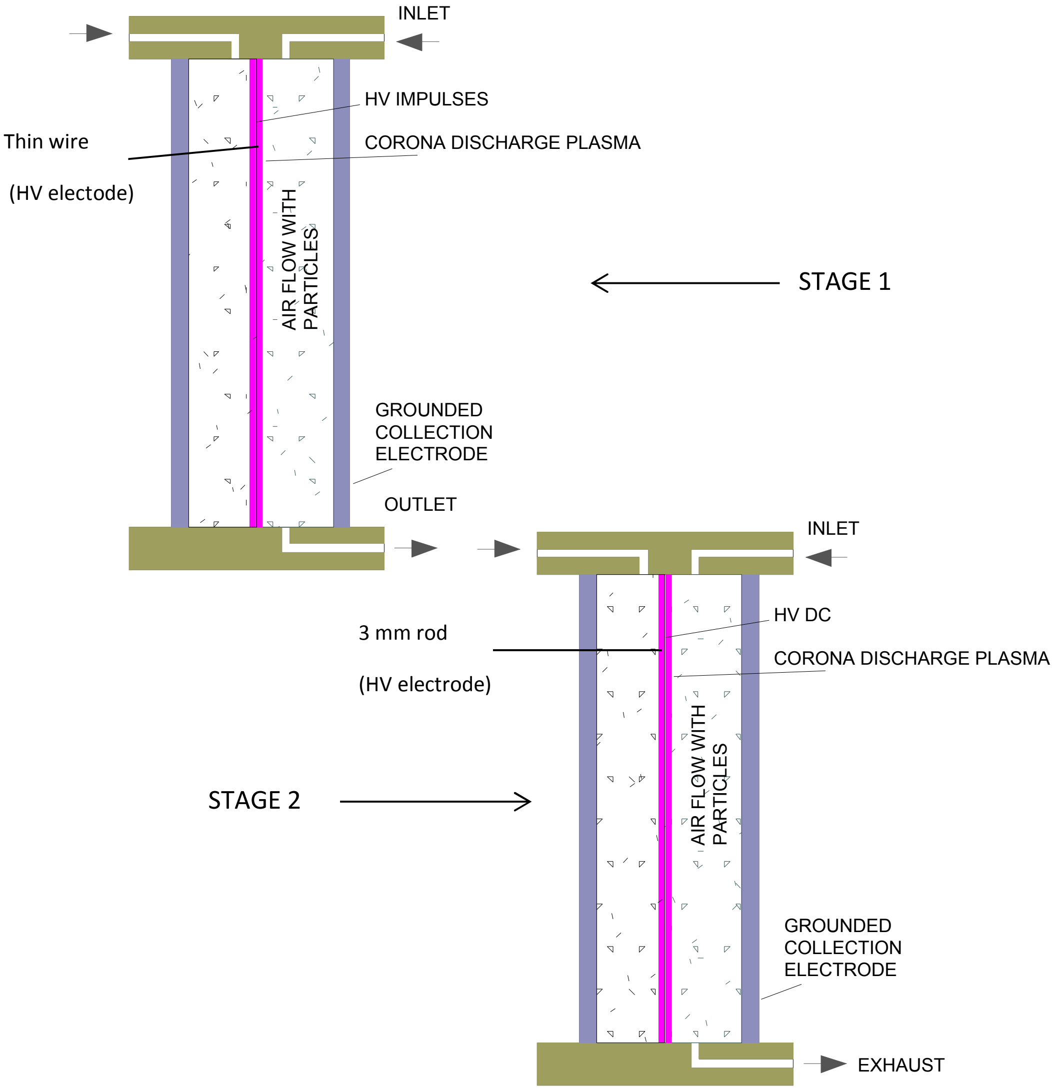

Figure 4-3: Schematic diagramme of the 2-stage precipitator.

A sealed container was built in order to contain smoke particles for precipitation tests with tobacco smoke. This type of smoke has almost all of its particles in the PM2.5 range. The unknown parameter is what concentration number can be injected in the reactor and measured. This has to be found via experimentation.

The 1320/1365 Nano Check and Adaptor instrument was used in these tests, providing the capability to monitor particles down to 25 nm. By using the 1.109 particle spectrometer, equipped with the Grimm 1320 Nanocheck module, ultra-fine particles can be monitored: this module is able to detect an average size of particles and their number in a single size range of (25-300) nm. The Nanocheck 1320 module is sensitive to the number of inlet particles, and in order to avoid saturation of this module, an input air flow was passed through a fine stainless-steel mesh filter, which was grounded and placed at the outlet of the second stage of the reactor. The filtration mesh is a woven mesh made of a 28 μm diameter stainless-steel thread, and has an aperture of 99 μm. This aperture was larger than the size of particles used in the tests, meaning that mechanical filtering was negligible. Each time interval with the Grimm 1320 Nanocheck module corresponds to a measuring step of 10 s, during which the particle analyser takes air samples. A complete diagram of the experimental set up is shown in Figure 4-8, together with the energisation modules which are discussed in Section 4.4.

4.4. ENERGISATION

During this stage of the research, longer μs impulses and dc voltage in the first and second stages of the precipitator were used in order to increase precipitation efficiency. These duration impulses provide an increase in the electric field inside the reactor beyond the levels of continuous dc voltage, without breakdown occurring (Chowdhuri et al., 1997). The amount of electric charge each particle can acquire is a function of the electric field (Hinds, 1982, Hughes, 1997, Timoshkin et al., 2012b). This means that an increase in the electric field amplitude would correspond to a higher amount of charge induced on the airborne particles. This, in turn, will lead to a higher precipitation efficiency as the charge induced is one of the defining factors in ESP operation. Moreover, the very low duty cycle (ratio of energised to non-energised duration of the HV electrode) means that the energy consumption is expected to be low (Dinelli et al., 1991).

The μs impulses applied to energise the first stage of the reactor were produced by an impulse generator, which utilized a step-up autotransformer (type 35C6 car ignition coil). The output impulse is produced by the secondary winding of the autotransformer, when its primary is fed by a few hundred volts impulse via power MOSFETs. In order for the pulse repetition rate to be adjustable, optical triggering was used by an external, solid state controller, which was connected by a fiber optic cable to the impulse generator. More details about the μs pulse generator and its optical controller can be found in (MacGregor et al., 1998). The impulses achieved were ~175 µs wide, and had an amplitude of ~35 kV, as shown in Figure 4-4 and Figure 4-5.

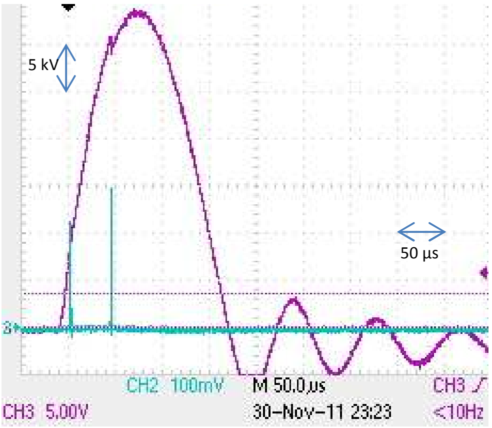

Figure 4-4: Example of an impulse applied on the first stage on the precipitator generated by the trigger impulse generator. Purple trace, voltage impulse; cyan trace, current at 100 µA/div.

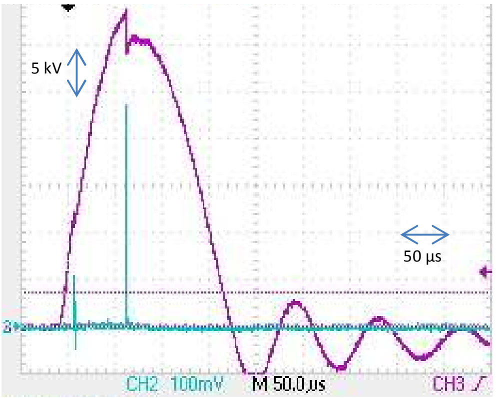

Figure 4-5: Example of an impulse applied on the first stage on the precipitator generated by the trigger impulse generator. Because of a large current impulse (cyan) a slight decrease in voltage is observed. Purple trace, voltage impulse; cyan trace, current at 100 µA/div.

In order to shape the impulse generator output, it was connected in series with a 300 kΩ resistor and a high voltage diode (6HV50K), before reaching the first stage of the reactor. This was because +35 kV was deemed too high, due to frequent breakdowns occurring. The inclusion of the diode avoided voltage collapse and polarity reversal. The voltage impulses produced, after passing through the (passive) pulse forming elements, can be seen in Figure 4-6 and Figure 4-7. The pulse repetition rate was set at 50 pps. As can be seen, the impulsive voltage amplitude was +25 kV, having full width at half-maximum impulse duration of

400 µs. In Figure 4-7 a current impulse, was produced due to a µs HV impulse, is also shown. This current impulse is a manifestation of a transient corona discharge, which is the main cause behind PM charging. This current impulse also includes the displacement current due to the capacitance of the reactor, however it is a minor fraction of it.

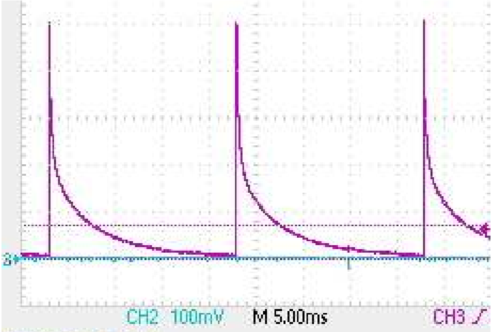

Figure 4-6: Consecutive impulses generated by the impulse generator. Impulses frequency is 50 pps. Impulsive amplitude is +25 kV applied to the corona electrode. Voltage scale is 5 kV/division, time scale is 5 ms/division.

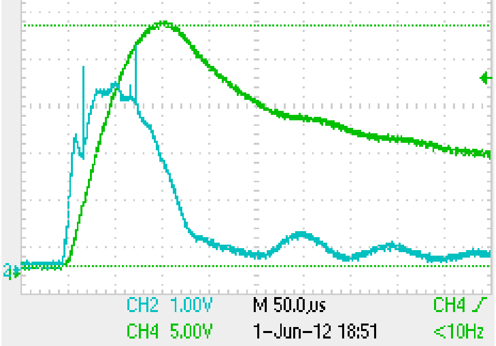

Figure 4-7: Voltage (green) and current (cyan) waveforms of individual µs impulses. Voltage scale: 5 kV/division; current scale: 1 mA/division, time scale 50 µs/division.

A 20 kV Glassmann EW series high voltage dc power supply was used to energise the 2nd (collection) stage of the reactor. In order to monitor the voltage and current waveforms, a Tektronix P6015A high voltage probe was used on the first stage, and a 1 kΩ current viewing resistor was connected between the collection electrode and the earthed busbar.

A schematic diagram of both the electrical and the pneumatic system, together with the monitoring devices and the PM measurement system, can be seen in Figure 4-8.

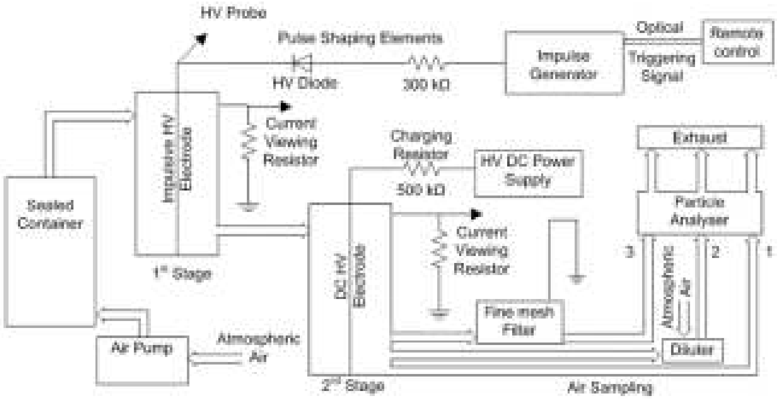

Figure 4-8: Schematic diagram of the precipitation system, adapted from (Mermigkas et al., 2013).

The different air sampling methods used in the tests are explained in Sections 4.8.1 and 4.8.3.

The same air pump, having air flow rate of 16 ℓ/min, was used for experiments with the double-stage reactor. Due to the wider cylinders used (23.88 mm radius) as particle collection electrodes, the corresponding air speed inside them was ~15 cm/s (around 1/3 that of the single stage reactor). Thus, for the pulse repetition rate of 50 pps chosen in the tests, a particle that passes straight through the reactor via the most direct path would be subject to at least 67 impulses. This number of HV impulses will produce sufficient charge on the particles for precipitation, as will be illustrated in Section 4.7. Since the time constant of a flour particle, measured to have permittivity of $\varepsilon_p = 6$ and conductivity of $\sigma_p = 10^{-10}$ S/m, is $\tau_{MW} = 71$ μs, it is expected that only a few HV impulses would be necessary for a 1 μm particle to accumulate its saturation charge by field charging. For those particles smaller than 1 μm, the diffusion charging process starts to play an important role, however the analysis of this mechanism is beyond the scope of the current research.

A coaxial reactor with a viewing window machined into its side was developed, in order to examine visually the intensity and morphology of the corona discharges produced. Thus, open shutter photographs were taken for positive dc, negative dc and positive impulsive (μs) corona. It can be seen that, at 50 pps, corona discharges can be registered by a camera operated in open shutter mode.

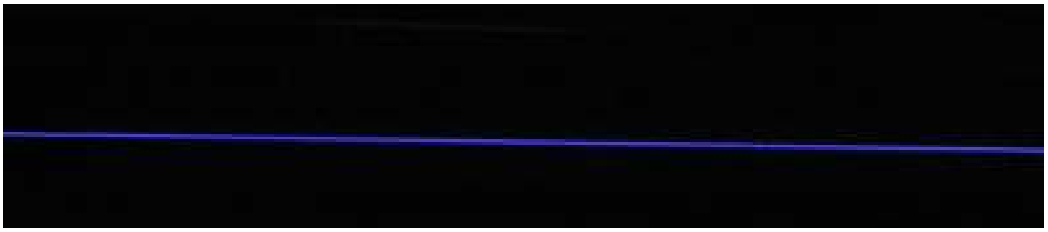

Figure 4-9: Visual appearance of corona discharge in the case of positive dc energisation.

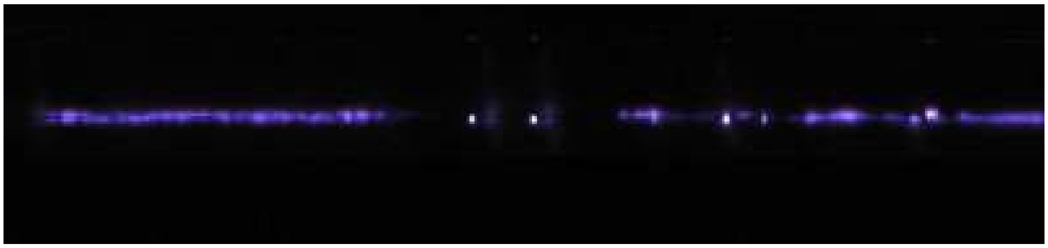

Figure 4-10: Visual appearance of corona discharge in the case of negative dc energisation.

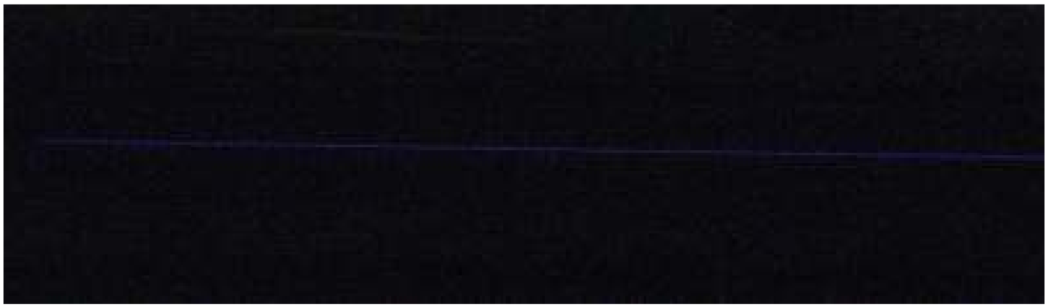

Figure 4-11: Visual appearance of corona discharge in the case of positive impulsive 25 kV (µs) energisation at 50 pps.

Despite the fact that dc corona is much more luminous, impulsive corona was also registered by the open shutter camera, using 10-15 s exposures.

4.5. ELECTRICAL PROPERTIES OF POWDERS USED IN THE TESTS

In order to analyse transient particle charging, it is important to know the electrical characteristics - conductivity and permittivity – of the particles. For measurements of electrical resistivity of powder (flour and dolomite) particles used in the present research, a test cell was designed and built based on the design provided in literature (IEEE, 1984, Yuan and Qi, 2007, Goard, 1982, Estcourt and Frisch, 1980). The test cell consists of 2 parallel metallic electrodes connected to an electrometer, and the powder is packed between these 2 electrodes. The resistivity of the powder can be calculated using equation (4.3):

$$\boldsymbol{\rho} = \frac{\boldsymbol{R} \cdot \boldsymbol{A}}{\boldsymbol{l}} \tag{4.3}$$

where R is the resistance of the test cell packed with powder, as measured by the electrometer; A is the cross-sectional area of the identical plates used as electrodes; and ℓ is the distance between the electrodes. Its resistance without any powder was calculated to be $> 10^{11}\ \Omega$, which is appropriate for measuring high resistivity powders. A picture of the resistivity measuring device can be seen in Figure 4-12.

Figure 4-12: Powder resistivity measuring device.

To calibrate the measurement system, resistors with known values were used to plot *I(V)* curves. Their slopes should provide values of actual resistance, to be compared with nominal values. The results were within the error margins (tolerance) of the resistance values of commercial resistors. The tests cell used had a 1 mm gap, guard rings, and a diameter of ~5.5 cm. Therefore, it was expected that with this test cells, high resistivity powders could be measured (limited by Keithley electrometer which cannot measure resistances >~200 GΩ) in a short amount of time. One additional advantage is that since the test cells is closed, moisture absorption that could alter resistivity is minimal.

Thus, it was decided to measure resistivity of the powders using the 1 mm gap cylindrical test cell. A Video Bridge (ESI-2160, Electro Scientific Instruments, Inc.) was also used in order to perform measurements of capacitance. The results are summarised in the Table 4-1, Figure 4-14, and Figure 4-15.

Table 4-1: Resistivities of various test cells used.

	FLOUR	DOLOMITE
R [GΩ]	5.2	3
ρ [Ωm]	$6.53 \cdot 10^9$	$3.77 \cdot 10^9$

Resistances were calculated after the powder was left for 1 hour in the test cell, in order to avoid any polarization effects. Resistances were measured with the Keithley 6514 electrometer. According to (Parker and Institution of Electrical Engineers, 2003) long (μs) impulses provide higher precipitation efficiency in the case of higher resistivity powders.

For the relative permittivity of particles, Figure 4-14 and Figure 4-15 have been made from experimental results taken from the Video Bridge. As the Video Bridge 2160 could only measure the capacitance of the test cell, the following formula was used to calculate the relative dielectric permittivity of powders.

$$\boldsymbol{C_{air} = \varepsilon_0 \varepsilon_{air} \frac{A}{d}} \tag{4.4}$$

$$\boldsymbol{C_r = \varepsilon_0 \varepsilon_r \frac{A}{d}} \tag{4.5}$$

$$\boldsymbol{C_r - C_{air} = \varepsilon_0 \varepsilon_r \frac{A}{d} - \varepsilon_0 \varepsilon_{air} \frac{A}{d}} \tag{4.6}$$

$$\boldsymbol{\varepsilon_r = \varepsilon_{air} + \frac{1}{\varepsilon_0}(C_r - C_{air})\frac{d}{A}} \tag{4.7}$$

where ε_r is the relative permittivity of the material; ε_{air} is the relative permittivity of air which can be considered ~1 for all practical applications; ε_0 is the dielectric permittivity of free space; C_r is the capacitance measured when the test cell is filled with PM that needs to be measured; C_{air} is the capacitance when there is air in-between the test cell plates; d is the distance between the plates (1 mm in this particular test cell) and A is the surface area of the plates.

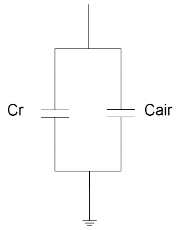

Figure 4-13: Diagram of permittivity measurement.

Firstly, capacitance of the test cell with powder was measured, C_r. Secondly, capacitance of the empty test cell was measured, C_{air}. ε_{air} is known, $\varepsilon_{air} = 1$. Therefore, ε_r can be calculated by equations (4.4) to (4.7).

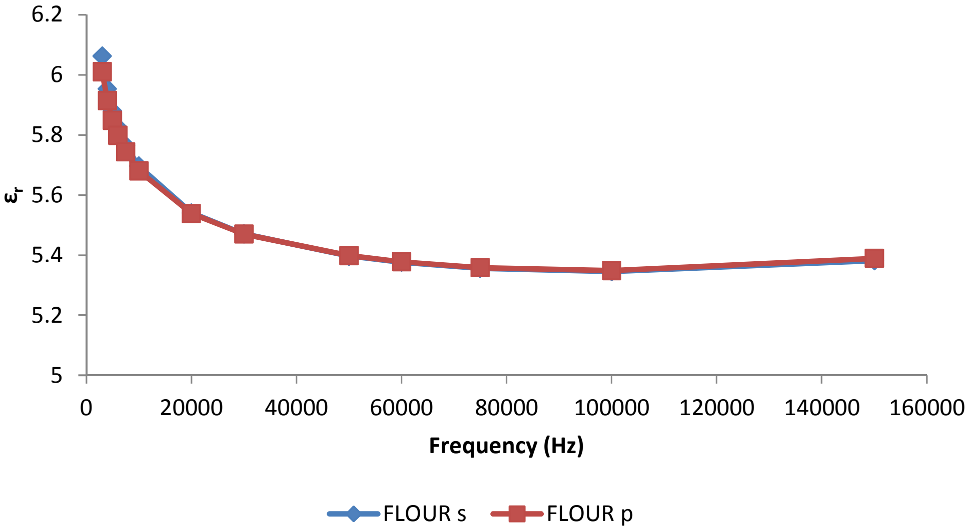

Figure 4-14: Relative permittivity, ε_r, of flour as a function of frequency.

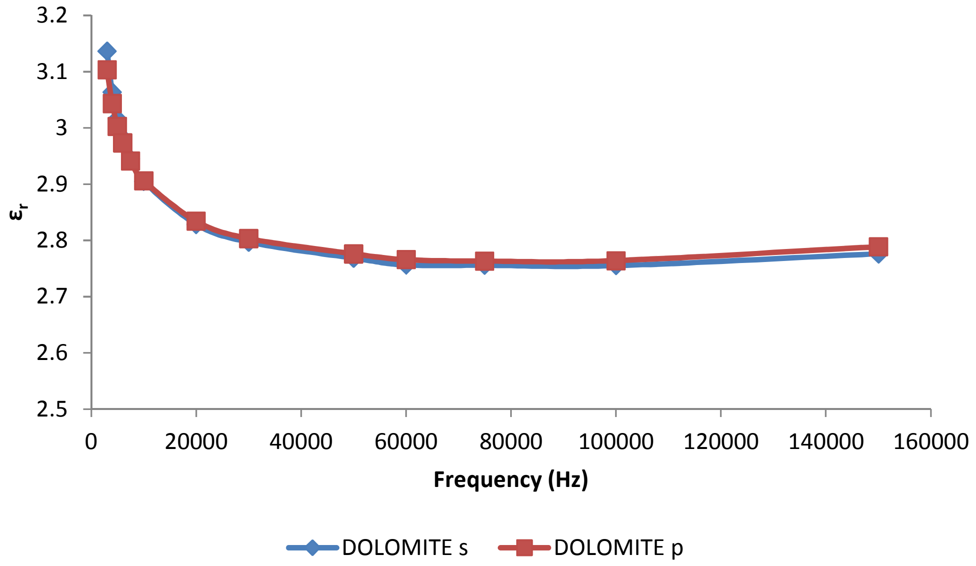

Figure 4-15: Relative permittivity of dolomite (H600) as a function of frequency.

where *s* and *p* are the series and parallel modes of measurement, respectively. As a rule of thumb, series mode is used for low impedance measurements (High *C* or low *L*) and parallel is used for high impedance measurements (Low *C* or high *L*).

In conclusion, the electrical characteristics of flour and dolomite powders are summarised in Table 4-2. Maxwell-Wagner relaxation times for both powders are also given, which were calculated by equation (4.20). Maxwell-Wagner relaxation time (τ_{MW}) is the time constant intrinsic in collection of free charges upon the surface of a particle (Jones, 2005). Despite the fact that flour and dolomite have different ε and σ, their combined effect gives very close (difference is within ~40%) Maxwell-Wagner relaxation times.

Table 4-2: Measurements of electrical characteristics of flour and dolomite (H600). $\sigma_\mu = 5.76 \cdot 10^{-7}$ S/m.

Material	Flour	Dolomite (H600)
$\varepsilon_r = f(f)$	5.3 – 7.6	2.7 – 4.1
ρ	$6.53 \cdot 10^{9}$ Ωm	$3.77 \cdot 10^{9}$ Ωm
σ	$1.53 \cdot 10^{-10}$ S/m	$2.65 \cdot 10^{-10}$ S/m
τ_{MW}	61.5 μs for $\varepsilon_r = 6$	38.4 μs for $\varepsilon_r = 3$

4.6. ELECTRICAL PARAMETERS OF THE REACTOR

In order to optimise the operational characteristics, it was necessary to characterise the electrical parameters of both stages of the reactor (applied voltage and corresponding corona current produced as well as corona ignition threshold). To this end *I-V* curves were obtained experimentally, and plotted for the first stage of the precipitator with and without air flow in Figure 4-16 and Figure 4-17, respectively. Voltage was measured with the Tektronix HV probe, while current was monitored with a viewing resistor connected between the collection cylinder and the ground point. Additionally, corona inception voltage was determined experimentally with and without air flow, and with particle laden air flow, using 1 g of dolomite powder (similar to the procedure used in the tests using the single stage reactor), for both stages of the precipitation reactor. The data are shown in Table 4-3 and Table 4-4. It was found that corona inception voltage was nearly identical with and without particles in the air flow. However, there was a slight difference in corona ignition voltage for these two cases, possibly due to the large difference in relative humidity for these tests (~25% and ~45% relative humidity (rh) for the no air flow tests and the tests with particle laden air flow, respectively). Regarding the *I-V* curves, without air flow, there is a higher current for the same voltage. Each data point in Figure 4-16 and Figure 4-17 represents the average of 3 tests; the voltage increment was 1 kV. In addition, another three individual runs were conducted with voltage step of 0.1 kV to generate *I(V)* curve with greater precision. The results are shown in Figure 4-18. Each data point represents the average of 3 tests, measured with air flow rate of 16 ℓ/min; the error bars represent the standard deviation.

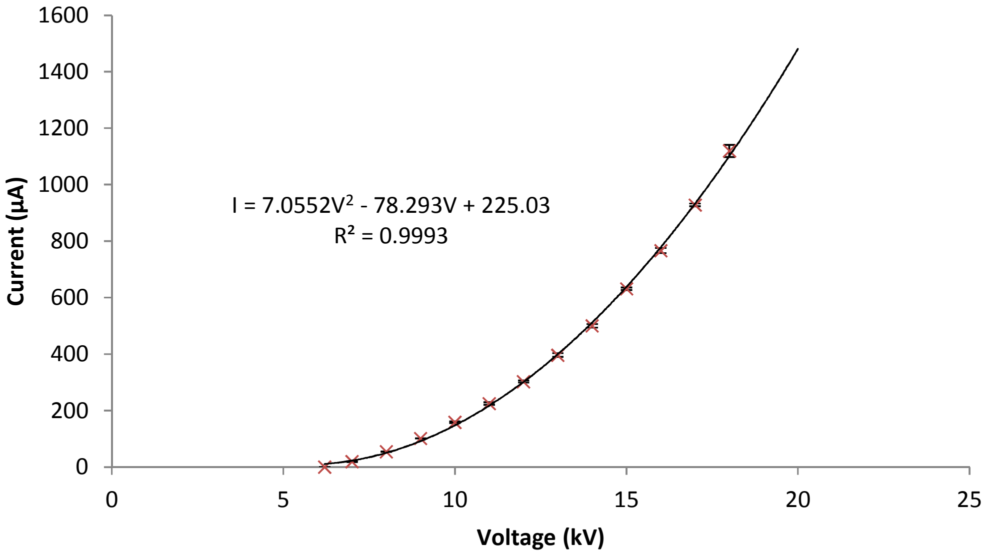

Figure 4-16: I-V curve for the first stage of the precipitator without air flow.

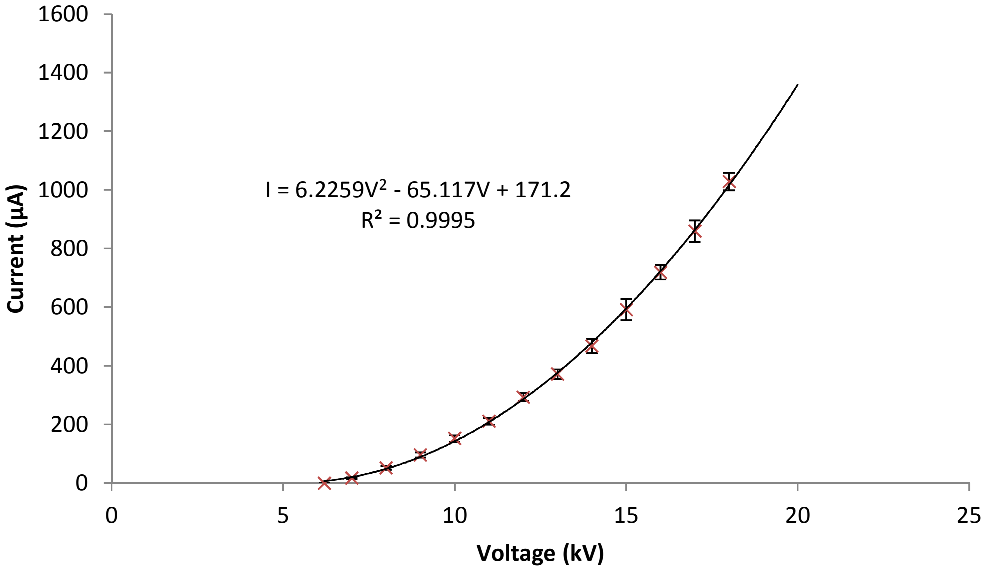

Figure 4-17: I-V curve for the first stage of the precipitator with air flow 16 ℓ/min.

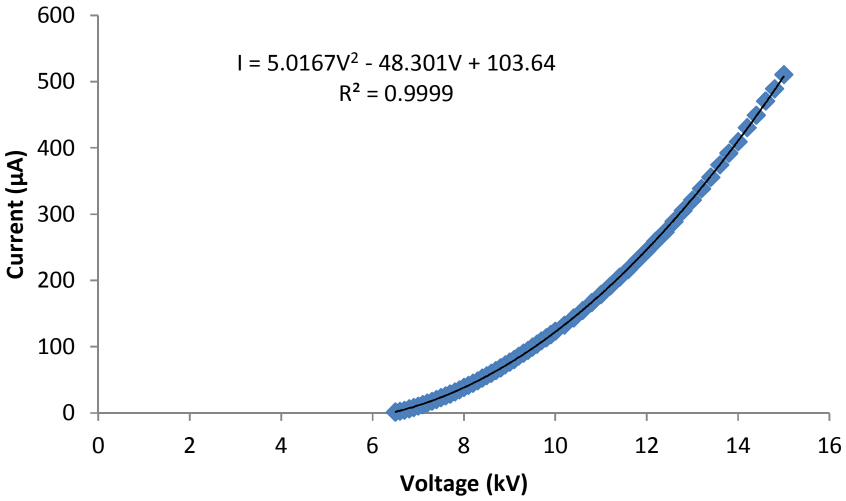

Figure 4-18: Average current in μA as a function of voltage in kV.

Table 4-3: Measured corona inception voltages for the first stage of the reactor.

Case examined	V_{inc} (kV)	σ (kV)
No Air Flow	6.07	0.09
Air Flow	6.2	0
Air Flow with 1 g dolomite powder	6.23	0.02

Table 4-4: Measured corona inception voltages for the second stage of the reactor.

Case examined	V_{inc} (kV)	σ (kV)
No Air Flow	16.8	0
Air Flow	16.6	0
Air Flow with 1 g dolomite powder	16.6	0

During the measurements shown in Table 4-4, the air temperature was 21.2 °C, relative humidity was 46.2%, which is almost the same compared to the tests shown in Table 4-3, air flow with 1 g powder case (21.8°C and 48.9% rh). There were no experimental runs for the *I(V)* curves on the second stage, as it was not intended to be operating significantly higher its corona inception voltage. However, as some tests were conducted with +17 kV dc, the dc current in the second stage for that charging level was found to be 72.8 μA.

Table 4-5: Corona current coefficients with and without air flow in the first stage of the precipitation reactor.

Coefficients	No air flow	16 /m air flow	0.1 kV step
α (A/V^2)	7.06	6.23	5.02
b (A/V)	78.3	65.12	48.3
c (A)	225.03	171.2	103.64
I_0 (A/V^2)	7.06	6.23	5.02
V_0 (V)	5.55	5.23	4.81

Frequency, pulse-width and amplitude of the corona current impulses were obtained for particle laden air flow with flour, however it was found that the amplitude of the corona impulses was less than ~30 mA in all cases. The duration of these corona impulses varied with the current amplitude. For example, impulses with magnitude of ~20 µA had a width of ~2.3 µs FWHM. For 29.8 mA current impulse magnitude, the pulse duration was 556 ns FWHM. For comparison, the current impulses produced by the µs impulse generator in the first stage of the reactor were 130 ns long FWHM. Examples can be seen in Figure 4-19 to Figure 4-20.

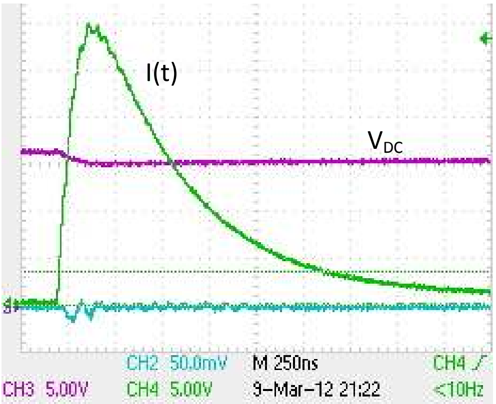

Figure 4-19: Waveform of the maximum corona current impulse observed for corona ignition voltage charging (+16.6 kV) of the second stage of the reactor. Peak amplitude is 29.8 mA. Vertical scale is 5 mA/division, horizontal scale 250 ns/division. Voltage (purple) scale is 5 kV/div.

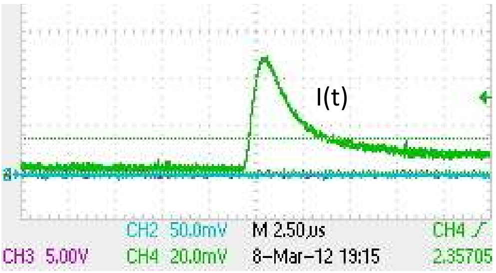

Figure 4-20: Waveform of one of the lowest corona current impulses observed for corona ignition voltage (+16.6 kV) in the second stage of the reactor. Vertical scale is 20 µA/division, horizontal scale 2.5 µs/division.

In comparison with the current impulses produced in stage one of the reactor (Figure 4-7), these impulses are shorter and the vast majority have significantly lower amplitude. The current impulses produced by the impulse generator in the first stage are longer (~100 µs compared to 2.5 µs), and their amplitude is higher compared to most of the corona current impulses at ~4 mA. Comparing the current impulses at the corona ignition level of the second stage and those produced by the impulse generator, it can be seen that those produced by the impulse generator are at least 40 times wider, with the higher the amplitude, the lower the impulse duration observed. However, the current impulses produced from the onset of dc corona voltage have variable frequency, depending on their amplitude, and the higher the amplitude the more rarely they appear. As an example, ~40 impulses appear with amplitude higher than 100 µA every 100 ms, in contrast with only ~24 higher than 2 mA every 100 ms.

The capacitance of the new reactor was calculated using topological data of the precipitator described in Section 4.3 (α = 0.213 mm, β = 47.75 mm and ℓ = 200 mm); using Equation (3.1), C ~2 pF.

4.7. ANALYTICAL INVESTIGATIONS OF TRANSIENT ELECTRIC FIELD AND TRANSIENT CHARGE ON PM

The particle charging rate is a crucial parameter that influences the total charge aquired by the particles. By gaining knowledge about this parameter, the pulse frequency and the air flow rate can be optimised, in order to maximase the induced charge. PM in the transport zone of the precipitator reactor (volume of space between the earthed collection electrode and the ionisation zone of the corona discharge) become charged at a rate that is a function of their permittivity and conductivity, as well as the conductivity of the air in the ion transport zone. The transient charging process of a spherical particle in the air flow has been analysed and modelled. Thus, the charging process of airborne PM with different conductivities and permittivities could be examined. Total charge aquired (saturation charge) and charging rates of PM have been calculated.

The electric charge induced on airborne PM inside an electrostatic precipitator is one of the major factors that influence the electrostatic precipitation efficiency. The volume of space inside the reactor can be divided into two zones: the ionisation zone and the ion transport zone. In the former, the electric field is high enough for ionisation of gas molecules to occur. The latter is the zone that the ions pass through as they drift towards the earthed electrode, under the influence of an increasingly weak electric field (Figure 4-24 shows the rate of its weakening as a function of distance from the HV rod). Figure 4-21 shows a cross section of the first stage of the precipitation reactor used (not to scale). R_{ext} is the internal radius of the earthed electrode, R is the radius of the high voltage electrode, around which corona occurs, and R_{ion} is the boundary between the ionisation and the ion transport zone.

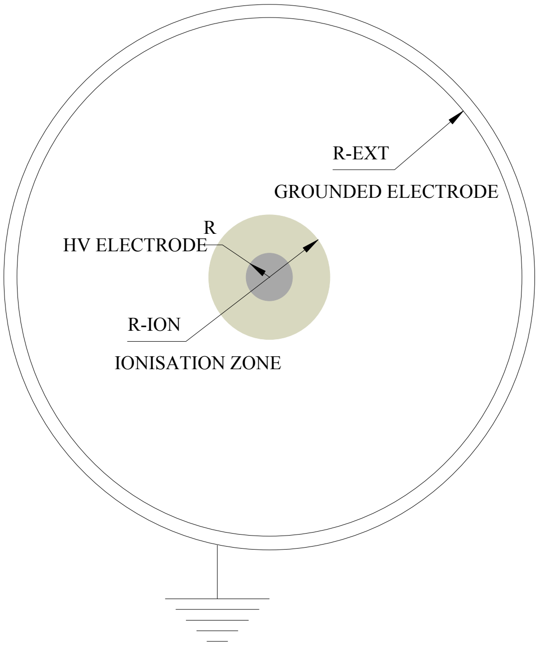

Figure 4-21: Cross-section of the coaxial electrostatic precipitator (not to scale) (Mermigkas et al., 2013).

The critical electric field for initiation of ionisation processes in atmospheric air is defined by the intersection of the ionisation and attachment coefficient curves as functions of *E/P* ($\alpha = \beta$) (Raizer, 1991). This critical field is 26 kV/cm to 31 kV/cm, depending on the calculation method. The condition $\alpha = \beta (E/P)$ gives the lowest value of E_{crit} ~26 kV/cm. Experimentally obtained values of critical field are ~30 kV/cm to ~31 kV/cm. These values have been obtained using the time of flight technique in dry gases (Raizer et al., 2012). For calculation of the radius of the ionisation zone of a corona discharge, Kaptzov's hypothesis can be used (Adamiak et al., 2005). This hypothesis states that, for voltages above the corona ignition threshold, the electric field remains the same. Thus, the ionisation zone radius for the coaxial first stage of the precipitation reactor used can be calculated by (4.8)

$$R_{ion} = \frac{E_{Peek}}{E_{crit}} R_{wire} \qquad (4.8)$$

where E_{Peek} is the corona ignition electric field obtained using the Peek equation, (4.9) for coaxial topologies with 0.01 cm < R < 1 cm for normal atmospheric conditions (Raizer, 1991). The first stage of the current coaxial reactor used is inside this range, thus, E_{Peek} can be calculated by:

$$E_{Peek} = 31 \cdot \left(1 + \frac{0.308}{\sqrt{R(cm)}}\right) \cdot 10^5 \left(V/m\right) \qquad (4.9)$$

In order to calculate the voltage drop, *V*, between the energisation and collection electrodes Poisson's and current continuity equations were solved for the coaxial topology used.

$$\nabla \vec{E} = -\frac{\rho}{\varepsilon_0 \varepsilon_r} \quad ; \qquad div \vec{J} = 0 \qquad (4.10)$$

where $\vec{J} = \mu \rho \vec{E}$, ε_r is the relative permittivity of the air flow, ε_0 is the permittivity of free space, ρ is the space charge produced in the inter-electrode space and $\vec{E}$ is the electric field, where μ is the mobility of charge carriers. Combining these equations (4.10) gives:

$$div(E)^2 + E\nabla(divE) = 0 \tag{4.11}$$

Both Poisson’s and current continuity equations, (4.10), were solved analytically for coaxial topology (cylindrical coordinates), and the derived electric field was obtained.

$$\nabla E = -\frac{1}{r}\frac{d}{dr}(rE)\hat{a}_r \qquad E^2(r) = A + \frac{B}{r^2} \tag{4.12}$$

Where $\hat{a}_r$ is the unit vector in the radial direction and A, B are constants in respect to radial coordinate r. Thus, the voltage drop in the inter-electrode space of the coaxial reactor was calculated utilising equation (4.13)

$$V = V_{ion} + \int_{R_{ion}}^{R_{ext}} E(r)\,dr \tag{4.13}$$

where V_{ion} is the voltage drop occurring across the corona ionization zone and $I = 2\pi R_{ext} lJ(R_{ext})$, where R_{ext} is the internal diameter of the grounded electrode (Figure 4-21), I is the corona current flowing between the central HV rod and the earthed outer cylinder, ℓ is the length of the coaxial topology used and $J(R_{ext})$ is the current density at the edge of the ion transport zone.

In equation (4.13), the lower integration limit is defined as R_{ion} (for the corona discharge case) and not the radius, R, of the high voltage electrode, and it is assured that outside this volume there is a unipolar space distribution (positive ions drifting through the ion transport zone for the case examined). Thus, the analytically calculated voltage drop is:

$$V = \sqrt{B}\left[\frac{\sqrt{R_{ext}^2 + B/A} - \sqrt{R_{ion}^2 + B/A}}{\sqrt{B/A}} + \ln\left\{\frac{R_{ext}}{R_{ion}}\frac{\left(R_{ion}^2 A/B + 1\right)^{1/2} + 1}{\left(R_{ext}^2 A/B + 1\right)^{1/2} + 1}\right\}\right] + V_{ion} \tag{4.14}$$

where:

$$A = \frac{I}{2\pi \ell \varepsilon_0 \varepsilon_r \mu}; \quad B = R_{ion}{}^2 \left(E_{R-ion}^2 - A\right) \tag{4.15}$$

and μ corresponds to the mobility of the charge carriers, V_{ion} is the voltage drop occurring in the corona ionisation zone and $E_{R\text{-}ion}$ is a fitting constant having a value close to the critical electric field for ionisation to occur in air (26-31 kV/cm). Therefore, mobility can be calculated by fitting an analytical curve to the experimental *I(V)* curves, assuming it is of constant value.

By using the mobility, the conductivity of the medium could be calculated, with the ultimate goal being to calculate the saturation charge (both due to conduction and polarisation) that a particle can acquire by field charging. Matlab software package was used in order to calculate a fitting curve for mobility, μ, using experimental *I(V)* curves, as shown in Figure 4-22:

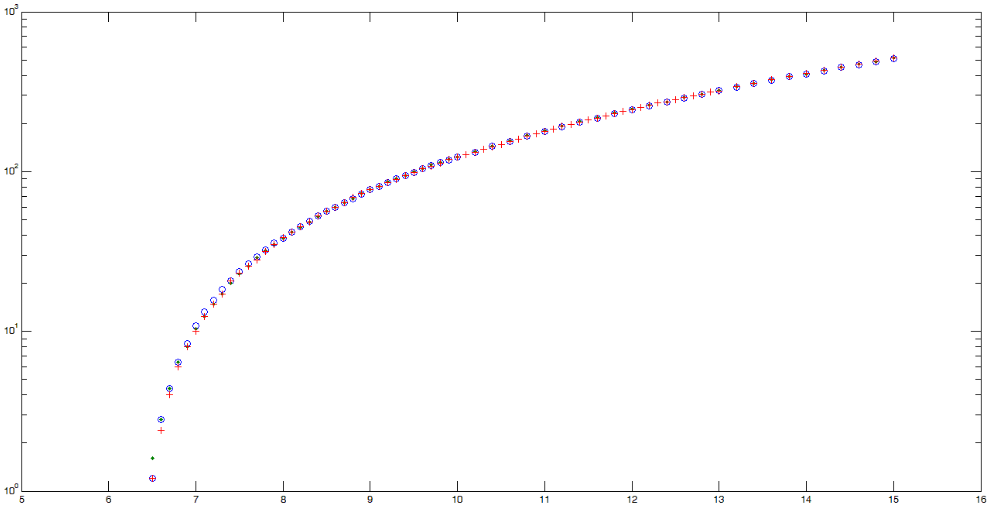

Figure 4-22: Experimental data for the 3 V(I) curves for the wire stage. X axis is in kV, Y axis is in µA.

The analytical fitting curves for an individual tests obtained by equation (4.14) is given in Figure 4-23.

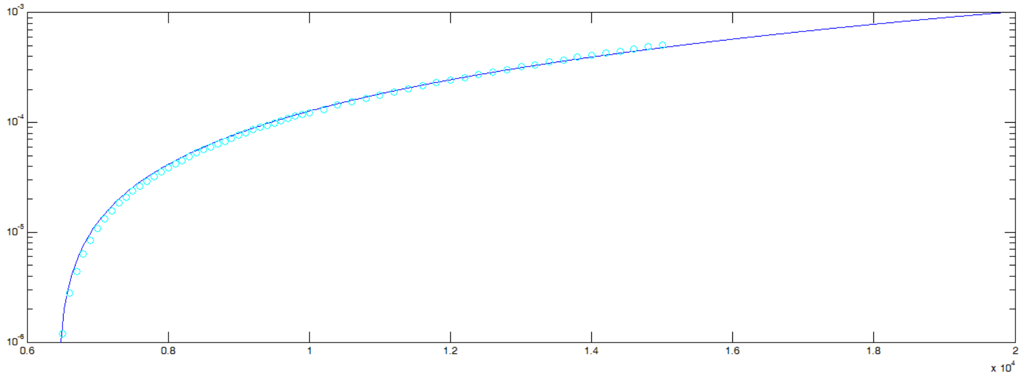

Figure 4-23: Individual I(V) datapoints, represented by cyan hollow circles, with fitting curve in blue.

As a result of this fitting, constant values of mobilities of charge carriers have been obtained, as shown in Table 4-6. The Matlab for-loop used had the following parameters: mobility, μ: from 1.7 m^2/Vs to 1.9 m^2/Vs, with 0.01 m^2/Vs step size; critical electric field for ionisation, E_{crit}: from 24 kV/cm to 32 kV/cm, with 1 kV/cm steps; V_{ion}: constant at 1.4 kV. The results of the best fit from the for-loops conducted from the 3 individual *I(V)* experimental runs can be seen in Table 4-6.

Table 4-6: Results from the 3 individual I(V) experimental runs.

	1st test	**2nd test**	**3rd test**
Mobility, μ (m^2/Vs)	$1.82 \cdot 10^{-4}$	$1.8 \cdot 10^{-4}$	$1.81 \cdot 10^{-4}$
E_{crit} (kV/cm)	29	28	28
R^2	0.9992	0.9994	0.9994
R_{ion} (mm)	0.45362	0.46982	0.46982

The theoretical limit for E_{crit} ($\alpha = \beta$) is 23.6 kV/cm, while the saturation point is ~32 kV/cm. In (Raizer, 1991) the limit is quoted as 41 V/cm·Torr which is ~31.16 kV/cm·atm. R^2 or R-squared (a.k.a. coefficient of determination) is a statistical indicator that shows how close the data are to the fit line. R^2 can take values from 0 to 1 and the closer to 1, the better the fit.

The electric field in the gap, with the positive space charge present included in the analysis (Poisson's electric field), can be seen in Figure 4-24, for the 4 mA impulsive corona current produced by the +25 kV impulses at the first stage of the reactor.

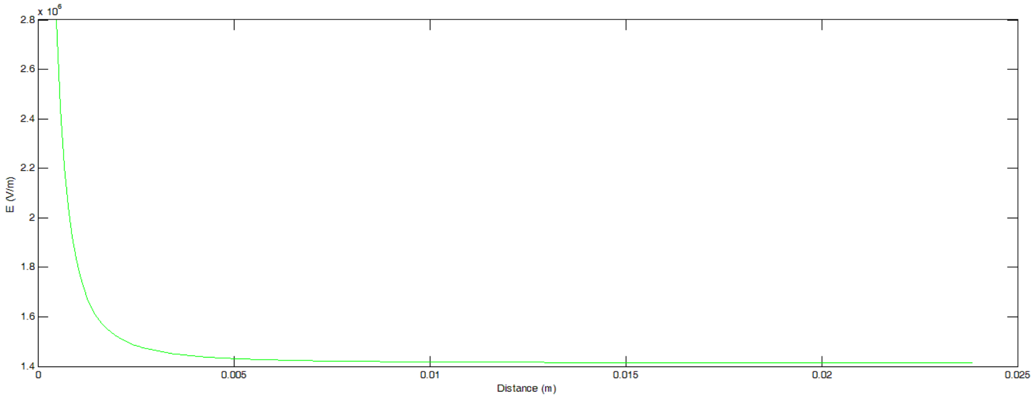

Figure 4-24: Electric field between the rod electrode and the collection electrode as a function of distance, for the time it is energised by the +25 kV impulse.

In Figure 4-25, the *I(V)* experimental data are plotted, with the analytical curve fitted, for the 1st stage of the cylindrical reactor having $R_{ext} = 2.39 \cdot 10^{-2}$ m and $R = 1.07 \cdot 10^{-4}$ m. The mobility was found to be $\mu = 1.8 \cdot 10^{-4}$ m^2/V·s. The other fitting parameters (V_{ion} and $E_{R\text{-}ion}$) were found to yield a close fit for values of $V_{ion} = 1.4$ kV and $E_{R\text{-}ion} = 29$ kV/cm, which is very close to literature data on critical fields in air. However, these two parameters affected mostly the initial part of the analytical curve, at the points close to the corona ignition voltage, and did not noticeably affect the calculation of μ, as it is influenced by the points for higher voltages (at the top right side of the curve).

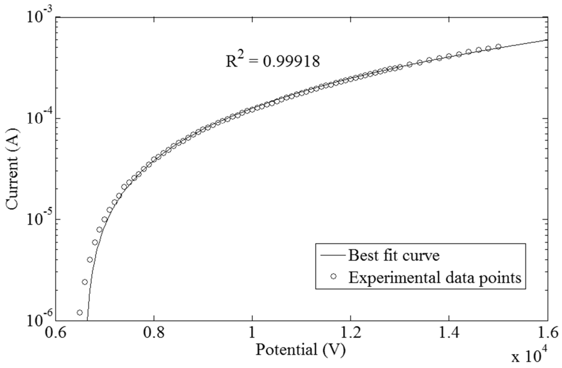

Figure 4-25: Experimental and analytical V-I curve in atmospheric air in the coaxial reactor. Open symbols, experimental points; solid line, analytical data.

From equations (4.8) and (4.9), the ionisation radius for the first stage of the reactor was calculated at ~0.5 mm radius. Therefore, almost all particles are expected to be charged in the ion transport zone, the electric field in this zone being distorted by the space charge created by the charged carriers (positive ions in the case examined). For optimisation of the precipitation process, it is important to calculate the charge that can be acquired by an individual particle passing through the reactor, as this amount of charge defines the precipitation efficiency. The charge induced on the PM by the electric field was investigated in (Pauthenier and Moreau-Hanot, 1932, White, 1951), however further analysis is required regarding the dynamics of PM charging, according to (Adamiak, 2002), who shows a numerical analysis of spherical particles being charged by a unipolar corona discharge, influenced by the space charge present. This approach is based on the current continuity equation:

$$div\ \vec{J} = -\frac{\partial \rho}{\partial t} \tag{4.16}$$

and on Poisson's equation, as for steady-state corona, (4.10). In (Adamiak, 2002), it is stated that "while an analytical solution is probably possible, it would lead to extremely complicated calculations"; it would, however, be of great advantage to acquire an analytical solution, for further optimisation of precipitation reactors.

Therefore, by solving the equations (4.12) and (4.16) an analytical solution for charging of a spherical particle, having permittivity ε_p and electrical conductivity σ_p, being placed in a volume with conductivity σ_m and permittivity ε_m, and being under the influence of a step voltage field energisation E_0 at $t = 0_+$, has been derived. Figure 4-26 shows the aforementioned spherical particle, surrounded by a medium of permittivity ε_m and conductivity σ_m. The results of this analysis are now detailed.

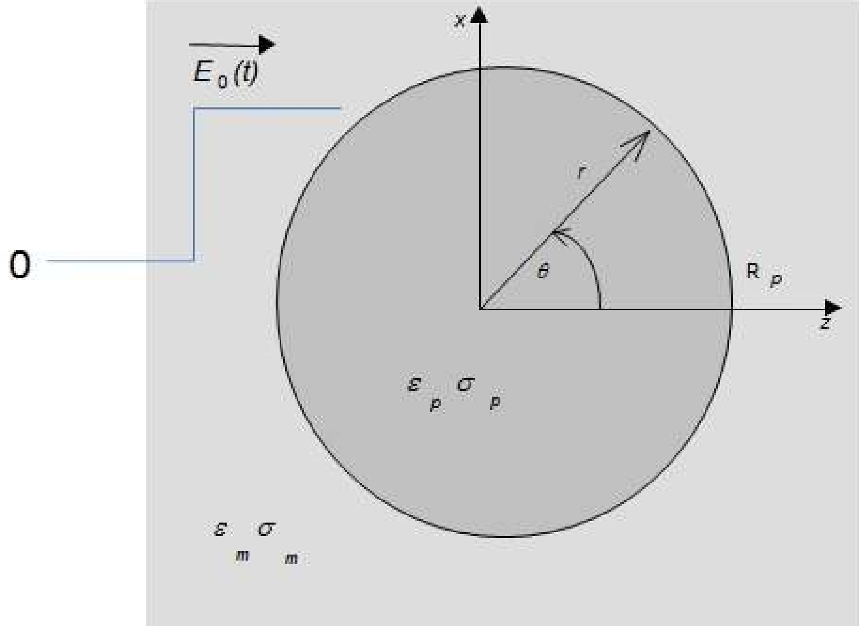

Figure 4-26: Particle suspended in the air flow, and subject to an impulsive electric field at t=0_+.

Consider a particle suspended in the air flow ($\varepsilon_m = 1$, relative permittivity of medium) at the space comprising the ion transport zone in the first stage of the reactor. The conductivity of the inter-electrode space, σ_m, was calculated using the mobility value extracted previously $1.8 \cdot 10^{-4}$ $m^2/V \cdot s$. As has been shown by (Unger et al., 2004), the concentration, *n*, of charge carriers for conditions close to the experimental conditions used in this work is ~10^{16} ions/m^3. This concentration is required for calculation of σ_m: $\sigma_m = n e \mu$, where *e* is the elementary charge (e = $1.6 \cdot 10^{-19}$ C). Thus, the conductivity of the medium in the precipitation reactor is $\sigma_m = 5.76 \cdot 10^{-7}$ S/m. The components of the electric field vertical to the particle–medium boundary can be calculated by (4.12) and (4.16). Thus, the transient density of the non-compensated surface charge at the boundary, $\rho_s(t)$, can be obtained using equation (4.17).

$$\rho_s(t) = \varepsilon_0 \varepsilon_p E_p(t) - \varepsilon_0 \varepsilon_m E_0(t) \qquad (4.17)$$

where $E_p(t)$ and $E_0(t)$ is the transient electric field created in the medium and the particle respectively, by the application of the step voltage on the reactor's HV electrode.

$$E_p(t) = E_0 \left\{ \frac{3\varepsilon_m}{2\varepsilon_m + \varepsilon_p} e^{-t/\tau_{MW}} + \frac{3\sigma_m}{2\sigma_m + \sigma_p} \left(1 - e^{-t/\tau_{MW}}\right) \right\} \cos\theta \tag{4.18}$$

$$E_0(t) = E_0 \cos\theta + 2E_0 \left\{ \frac{\varepsilon_p - \varepsilon_m}{2\varepsilon_m + \varepsilon_p} e^{-t/\tau_{MW}} + \frac{\sigma_p - \sigma_m}{2\sigma_m + \sigma_p} \left(1 - e^{-t/\tau_{MW}}\right) \right\} \cos\theta \tag{4.19}$$

These components have a dynamic behaviour subject to the Maxwell-Wagner relaxation time, which is the relaxation time associated with the accumulation of free charge at the surface of the spheres.

$$\tau_{MW} = \frac{2\varepsilon_m + \varepsilon_p}{2\sigma_m + \sigma_p} \varepsilon_0 \tag{4.20}$$

Thus, in order to obtain the sum of the non-compensated charge for the particles, an integration of $\rho_s(t)$ is needed, $Q = \oint_S \rho_s dS$, by utilizing $E_0(t)$ and $E_p(t)$. Analytical expressions of these ($E_p(t)$ and $E_0(t)$) normal field components are detailed in (Jones, 2005). The total charge calculated, $Q(t)$, is due to the combined effects of the difference of permittivities of the medium and the particle (ε_m and ε_p) and the subsequent polarisation charge developed, and the surface charge due to the difference in conductivities between again, the medium in which the PM are suspended, and the particle (σ_m and σ_p, respectively). The reason for integrating along only half of the surface is the assumption that the ion transport zone has a unipolar charged carrier population. The other (trailing) surface of the particle is assumed to be acquiring only polarisation charge (as $\varepsilon_m \neq \varepsilon_p$), and this charge ($Q_p(t)$) was calculated by defining $\sigma_m = 0$ for the trailing surface of the particle, similar to the numerical approach taken in (Adamiak, 2002), where zero current was hypothesized for the electric field's vertical components at the particle-air interface on the trailing surface of the particle. Thus, the total charge, $Q_t(t)$, is the sum of the two charges, the polarisation charge on the trailing side of the particle $Q_p(t)$, and the surface charge and polarisation charge on the leading side of the same particle $Q(t)$:

$$Q_t(t) = Q(t) + Q_p(t) \tag{4.21}$$

Polarisation and surface charge on leading side of the particle is:

$$Q(t) = 6\pi R_p^2 E_0 \varepsilon_0 \frac{\sigma_m \varepsilon_p - \varepsilon_m \sigma_p}{2\sigma_m + \sigma_p}\left(1 - e^{-t/\tau_{MW}}\right) \tag{4.22}$$

Polarisation charge on the trailing side of the particle is:

$$Q_p(t) = 6\pi R_p^2 E_0 \varepsilon_0 \varepsilon_p \left(1 - \frac{\varepsilon_p + \varepsilon_m}{\varepsilon_p + 2\varepsilon_m} e^{-t/\tau_{MW}}\right) \tag{4.23}$$

Equations (4.22) and (4.23) show that the charging process is exponential in nature, having the Maxwell-Wagner relaxation time as time constant. In Figure 4-27, the charging rate of a particle with permittivity of $\varepsilon_p = 6$ is shown, calculated by equations (4.22) and (4.23). The particle has 1 µm radius (thus its inside the PM2.5 range). This analytically obtained result was compared with the experimental data by (Hignett, 1967) for similarly sized particles, and the following values were found: $0.1\cdot10^{-15}$ C according to (Hignett, 1967) and $(0.5\text{-}2)\cdot10^{-15}$ C according to the present model. The dynamics of charging subjected to field charging of a 1 µm particle with $\varepsilon_p = 6$ and $\sigma_p = 10^{-10}$ S/m are shown in Figure 4-27. These parameters are close to the characteristics of the flour particles. The conductivity of the medium is as calculated above ($\sigma_m = 5\ 10^{-7}$ S/m). The total charge $Q(t)$ is shown as a function of normalized time, t/τ_{MW}.

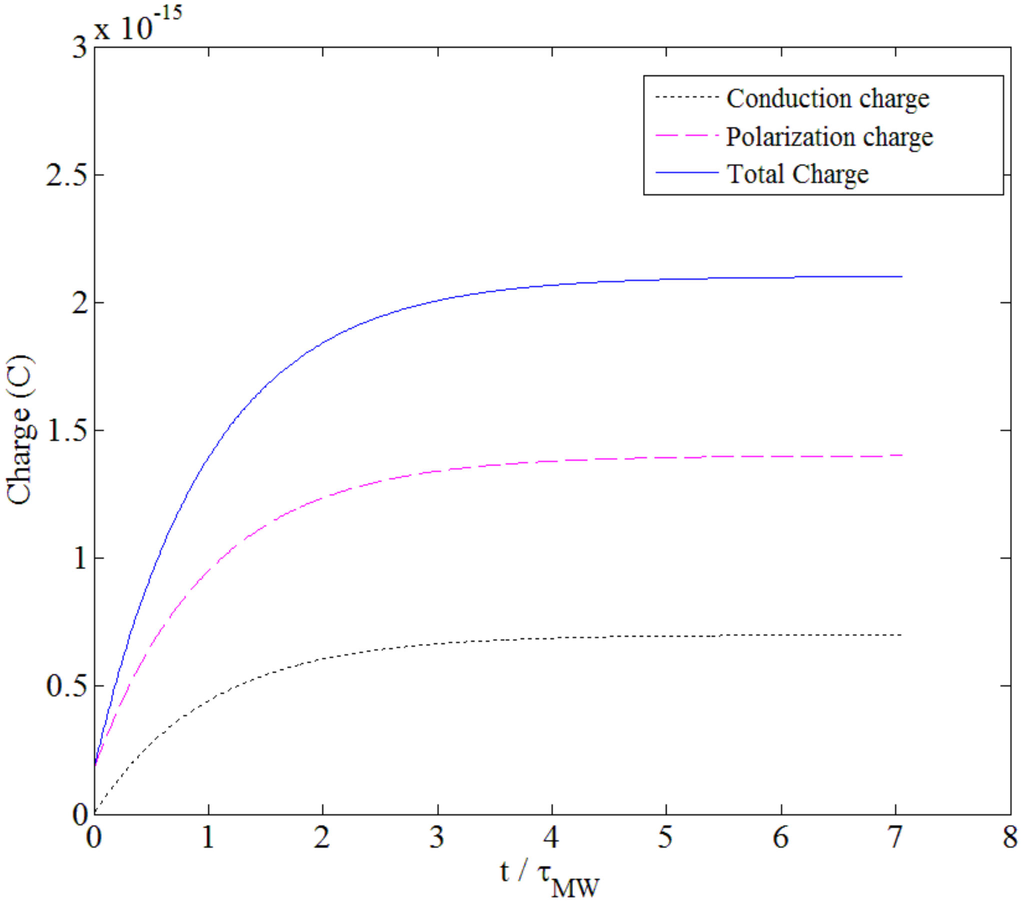

Figure 4-27: Dynamics of charging for particles with $\varepsilon_p = 6$. Conductivity medium is $5 \cdot 10^{-7}$ S/m while that of the particle is 10^{-10} S/m (Mermigkas et al., 2013).

Figure 4-27 shows that if the HV impulses used in the precipitation process are significantly longer than the Maxwell-Wagner relaxation time, then the charge acquired by the particle tends to its saturation limit. This saturation charge is plotted as a function of particle conductivity for various particle permittivities in Figure 4-28, for a 1 µm particle (in radius). The conductivity of the medium is that calculated above ($\sigma_m = 5 \cdot 10^{-7}$ S/m).

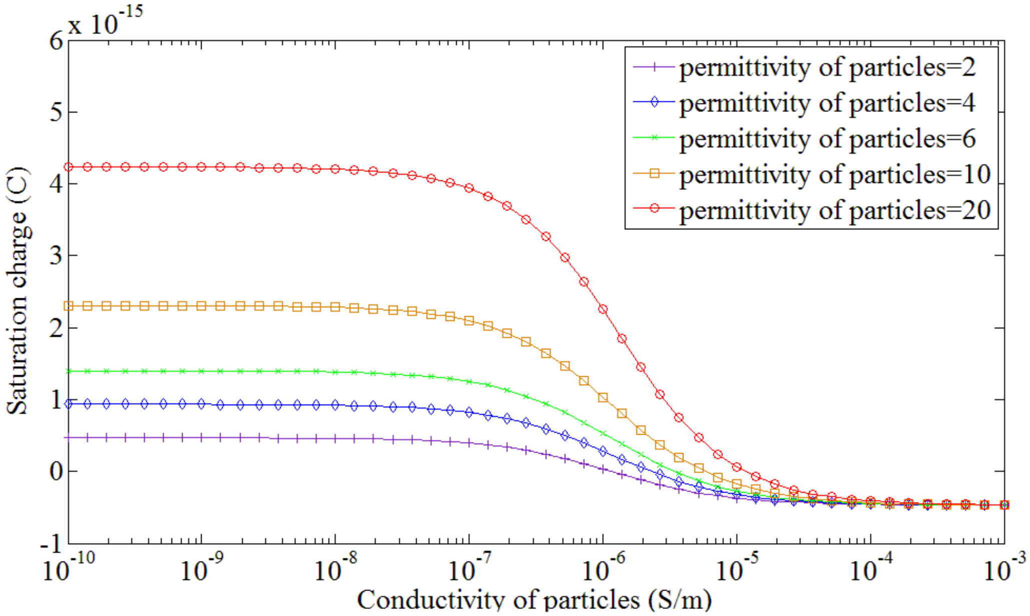

Figure 4-28: Saturation charge as a function of particle conductivity. Conductivity of medium is $5.76{\cdot}10^{-7}$ S/m.

The conclusion from this analysis, as ploted Figure 4-28, is that, depending on ε_p, there is a limit to the lower conductivity that a particle can have, in order to be able to aquire any saturation charge, that limit being between 10^{-6} and 10^{-5} S/m for the particular conditions in the reactor ($\sigma_m = 5.76\ 10^{-7}$ S/m). For higher conductivities, the particles aquire an opposite charging polarity compared to the charging voltage used, which would result in them being attracted to the HV electrode and, thus, would make high conductivity particles difficult to collect, a fact that agrees with the published literature. In Figure 4-27, the total saturation charge is shown to have almost equal contribution from the polarisation and conduction charge components.

4.8. INVESTIGATION OF PRECIPITATION EFFICIENCY OF THE DOUBLE STAGE REACTOR

Since the research conducted in this project is focused on developing reactors for small-scale, indoor, air cleaning applications, it was necessary to test the performance of the developed reactors using ambient atmospheric air in the laboratory, as this would be the expected operational conditions of the reactors.

For practical application of the developed precipitation system, it is important to investigate and optimise its performance in the case of air flows significantly contaminated with particles having their dimensions in the PM2.5 range. As a test contaminant, cigarette smoke was selected, smoke particles having their major fraction within the PM2.5 range (Chung and Dunn-Rankin, 1996).

Other types of smoke were initially considered for precipitation tests. However, the insence of joss sticks and of frankiscence (which have been tested) produced a significant amount of oily particles, which significantly contaminated the optical system and tubings of the particle analyser. Thus, these types of smoke particles were non-acceptable for the tests conducted under the framework of this project.

A diluter was introduced into the experimental system when cigarette smoke was used, to reduce the number of particles in the air flow, in order not to exceed the operational range of the particle analyser. The diluter had a 4 mm inlet, with air coming from the sampling point after the reactors second stage, and had a 12 mm outlet that was connected to the exhaust. A flow chart of the experimental system used in the tests described in this section is shown in Figure 4-8.

For both environmental air and air with smoke tests, a portable particle analyser (Grimm Aerosol GmbH portable laser aerosolspectrometer and dust monitor model 1.109) was used to sample air from the outlet and to measure the counts/ℓ of particles in 31 pre-defined size ranges (250 nm up to > 32 µm), every 6 s. The ratio of particles registered by the analyser in the case of the energised and non-energised (no high voltage applied) precipitator was used to determine the precipitation efficiency. In the case when ambient laboratory air was used in precipitation tests, the particle analyser took air samples straight from the outlet of the reactor (path 1, Figure 4-8). In the case with air flow laden with cigarette smoke, sampling was performed straight from the air diluter (path 2, Figure 4-8) to avoid saturating the particle analyser. The 1320 Nanocheck module attached to the particle spectrometer provided an opportunity to monitor ultrafine particles (25-300 nm range), including their median particle diameter, in addition to the particle concentration (number of particles per litre of air). However, because of its operational principles, the air samples had to pass through a stainless-steel mesh filter (path 3, Figure 4-8), as explained in Section 4.4.

4.8.1. PRECIPITATION TESTS USING AMBIENT AIR: METHODOLOGY

In all experiments, a strict experimental procedure was adhered to. The methodology of the ambient air tests is as follows. A laboratory air pump, having maximum air flow rate of 16 ℓ/min, was connected through 6 mm diameter flexible tubing to an air-sealed container, as shown in Figure 4-29. On top of the container, 4 similar 6 mm diameter tubes delivered the air flow uniformly to the first stage of the reactor (each tube was connected to a different quadrant at the top-inlet of the cylindrical coaxial reactor topology). Air was sampled via path 1, Figure 4-8, straight from the exhaust of the analyser. All experiments were conducted with laboratory air of ambient humidity, temperature and pressure.

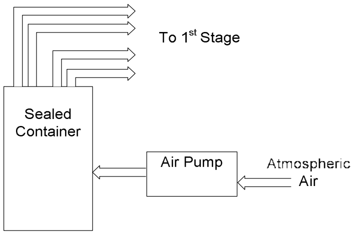

Figure 4-29: Air sealed container, used for experiments with both ambient air and beeswax candle fumes.

The experimental process was as follows. Initially, the particle analyser and its data collection software were initiated. After 30 seconds, the air pump was also turned on and was left for 4 min and 30 s, in order to achieve stable background particle concentration passing through the reactor. After the constant flow of ambient PM was achieved, the electrostatic precipitator was energised for 5 minutes. At the end of the experiment, the air pump was left running for ~15 min, in order to re-establish the ambient level of PM into the reactor, prior to commencement of the next experiment.

Efficiency levels (as a percent for each size range) were calculated by dividing the number of particles during the 5 min energisation time over the maximum level of particle concentration for the same interval.

4.8.2. PRECIPITATION EFFICIENCY FOR AMBIENT AIR

Initially, experiments with ambient laboratory air were conducted with the precipitation reactor energised only at its first stage with +25 kV impulses at various pulse repetition rates (10 pps, 25 pps, 50 pps, 75 pps, 100 pps, and 125 pps). The results of these precipitation tests are summarised in Figure 4-30. This figure gives the pass rate of particles calculated by the average of the pass rates ($1 - \eta_p$, η_p being the efficiency of precipitation) of all measurements after 1 min of HV energisation (or the average for all $N(t)/Nmax(t)$ where t is the sampling time of the particle analyser (6 s)). This is because when the HV electrode in the precipitation reactor is energised, it takes ~1 min for the majority of the PM particles to be precipitated, and thus to have a stable particle concentration at the precipitator output. This corresponds to 11 initial measurements being disregarded, as the sampling interval of the particle analyser for these tests was 6 s. Pass rate was calculated as the ratio of number of particles in each particular sampling period, over the maximum amount of particles after the reactor was energised, which occurs at the very beginning of each test, corresponding to either the first or the second particle analyser measurement. Higher penetration rate corresponds to lower efficiency, and vice versa. Penetration rate is easier to calculate, and is more intuitive when conducting experiments, as it gives a clearer indication of changes in efficiency for higher rates of efficiency even with visual inspection of instruments / data recorded (0 particles detected corresponding to 100% efficiency).

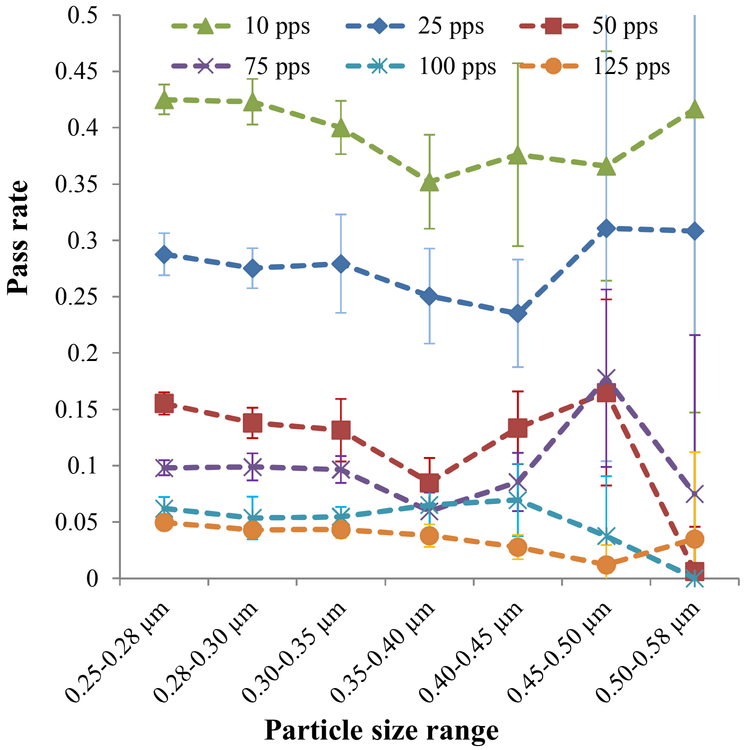

Figure 4-30: Pass rates ($1 - \eta_p$) for the different particle size ranges. Only the first stage was energized with +25 kV impulses at variable pulse repetition rates.

The precipitation experiments with only impulsive voltage showed that as the pulse repetition rate increases, so does the precipitation efficiency. At 10 pps, 40% of the ambient background particles managed to pass through the reactor. This reactor pass rate fell to ~10% at 50 pps, and as low as ~5% at 125 pps. These pass rates for various pulse repetition rates are shown in Figure 4-30. Precipitation experiments were also conducted with only dc energisation (+12 kV, 13 kV, 14 kV, 15 kV, 16 kV and +17 kV dc) at the second stage of the precipitation reactor, their results being shown in Figure 4-31. The dashed lines connecting the pass rate points in both Figure 4-30 and Figure 4-31 are for visual aid, in order to show the trend as the particle size range increases.

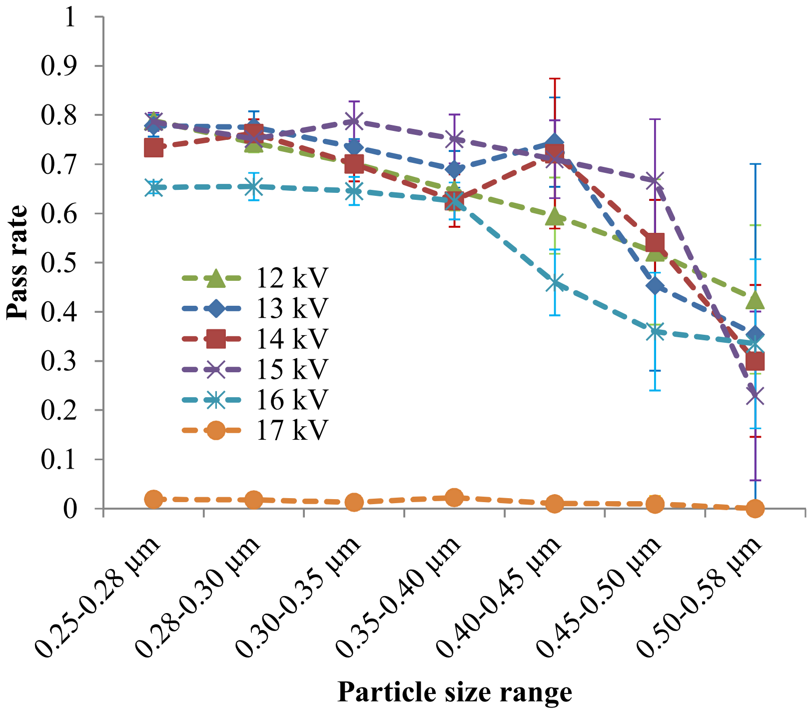

Figure 4-31: Pass rates (1 – η_p) for the different particle size ranges. Only the second stage was energised with dc voltage levels between +12 kV and +17 kV.

The corona ignition level was found to be +16.6 kV dc. It can be seen that for all levels below the corona ignition voltage (+12 kV up to +16 kV), the precipitation efficiency was low, and similar for all tested voltages. However, as soon as the applied dc voltage was above the corona ignition level, the precipitation efficiency rose sharply; at +17 kV dc energisation level, only ~1% of the ambient particles managed to pass through the reactor. The dc corona current at energisation levels above the corona ignition voltage was ~72.8 µA.

The last set of experiments was conducted with both stages of the reactor being energised, the first stage was energised with +25 kV impulses at 50 pps, and the second stage was energised with +17 kV dc voltage. This combination yields almost 100% precipitation efficiency for the double-stage reactor. The results are shown in Figure 4-34. Since Figure 4-34 is drawn on a logarithmic scale, any absence of experimental data points corresponds to zero particles detected. In addition, since there were very few particles detected larger than 0.5 µm in the ambient laboratory air, it was decided to exclude those particle size ranges from the environmental data analysis.

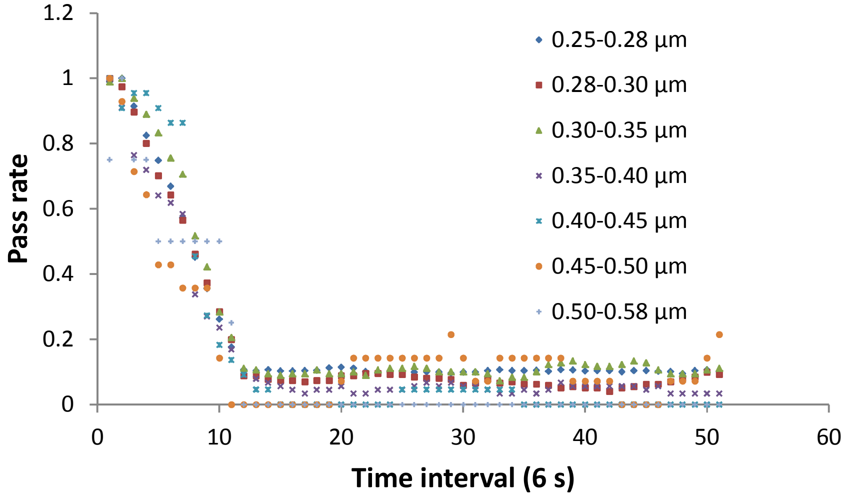

Figure 4-32: Pass rate (1 – η_p) for the energisation of only the first stage of the precipitation reactor. Voltage applied was 25 kV impulses at 50 pps (including pulse forming network).

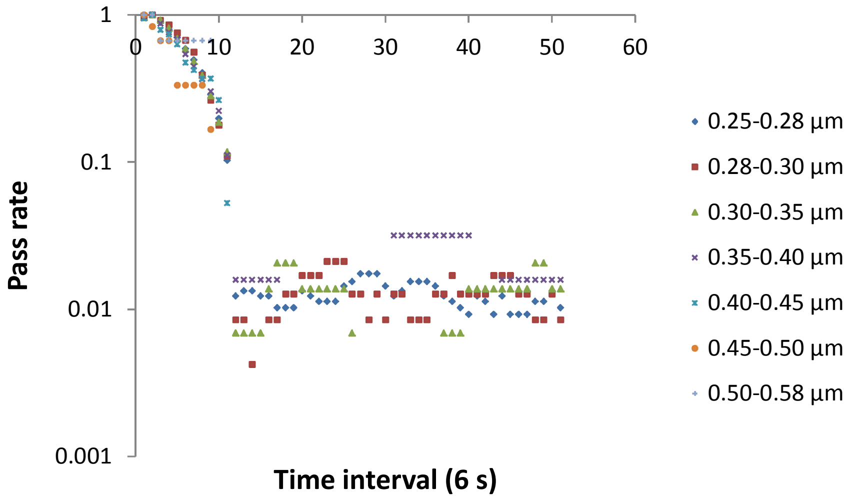

Figure 4-33: Pass rate (1 – η_p) for the energisation of only the second stage of the precipitation reactor. Voltage applied was +17 kV dc voltage corresponding to 72.8 µA corona current.

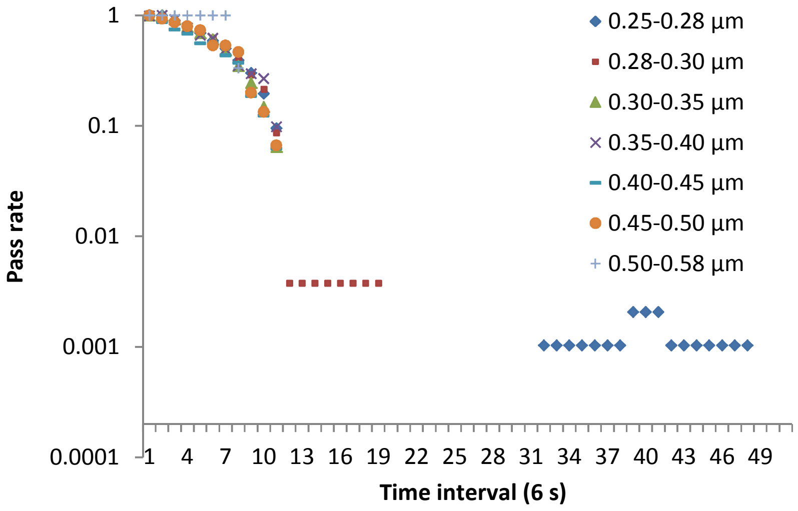

Figure 4-34: Pass rate (1 – η_p) for the simultaneous energisation of both stages of the precipitation reactor (both dc and impulsive one). 1st stage was energized with impulses of +25 kV amplitude at 50 pps. 2nd stage was stressed with +17 kV dc voltage.

Examples of the full data used to calculate the composite data points in Figure 4-30 and Figure 4-31 are shown in Figure 4-32 and , respectively. Time quantisation is evident at 6 s, as this was the time period at which the laser particle spectrometer was sampling the air. Average values and standard deviations were calculated after the 10th interval, at which point the particle concentration stabilised.

The module “Grimm Nanocheck 1320” was included in the monitoring system, thus it was possible to monitor ultra-fine particles in the range of (25–300) nm. As the Nanocheck module is very sensitive to the PM concentration, a stainless steel filter was used at its inlet (path 3, Figure 4-8), in order to avoid saturation of the module. The stainless-steel filter was made of 28 µm diameter threads, creating a fine woven mesh of 99 µm aperture. As the particle diameter is much lower than the filter aperture, mechanical filtration is negligible. The filter was grounded and its inclusion improved precipitation efficiency considerably, without any increase in the power input to the reactor. For energy consumption to be lowered, a pulse repetition rate of 50 pps was chosen for energisation of the 1st stage, while the 2nd stage was energised with dc voltage. This energisation resulted in a ~25% decrease in energy requirements compared to the experiments with the single stage reactor. In terms of precipitation efficiency, energisation of the first stage with +25 kV impulses (at 50 pps) and +17 kV dc at the second stage, increased the efficiency of precipitation to almost 100%. If only the first stage was energised with +25 kV amplitude, µs duration impulses at a pulse repetition rate of 50 pps, then the pass rate $(1-\eta_p)$ for the (250-300) nm size range was 0.1%-1%. As for larger particles, they were captured at 100% efficiency. In the "ultrafine range" (25-300 nm) made possible by the Nanocheck module, the precipitation efficiency was higher when both stages were energised, in comparison to having only the 2nd stage energised. The precipitation efficiency is displayed in Figure 4-35, having time step of 10 s instead of 6 s, corresponding to the different minimum sampling setting of the Nanocheck 1320 module.

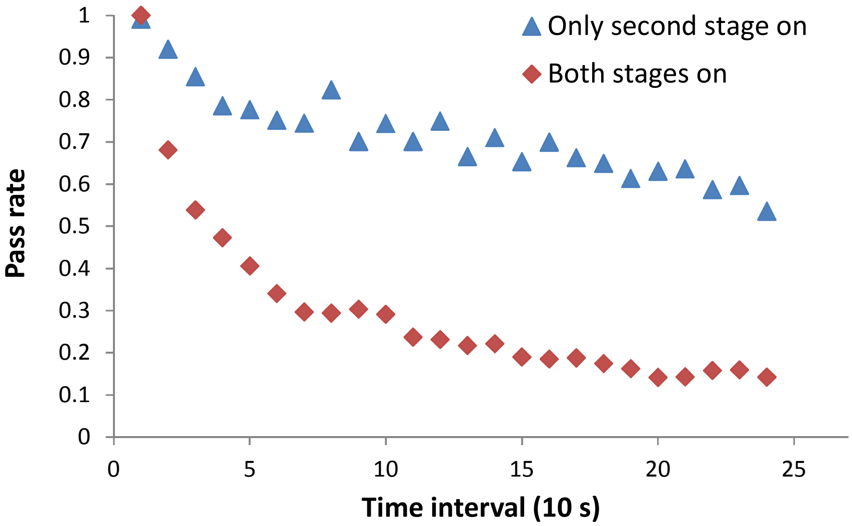

Figure 4-35: Pass rate $(1-\eta_p)$ for particles in the "ultrafine" range (25-300) nm. 1st stage was stressed with HV impulses of +25 kV at 50 pps. 2nd stage was stressed with +17 kV dc voltage.

4.8.3. PRECIPITATION TESTS USING AIR LADEN WITH CIGARETTE SMOKE: METHODOLOGY

After establishment of the precipitation efficiency of the double stage reactor using ambient laboratory air, it was necessary to demonstrate that this reactor and energisation approach could also be used for efficient removal of significantly higher concentrations of fine and ultra-fine particles in air flow. For this purpose, atmospheric air laden with cigarette smoke particles was used, as discussed in Section 4.3. Precipitation tests were performed using the same reactor and the same energisation levels for both stages as in Section 4.8.2 .However, in the tests described in the present section ambient air was contaminated with diluted cigarette smoke. As discussed in Section 4.3 the cigarette smoke had to be diluted, as even a single cigarette produced such high concentrations of PM (> 50 million particles/ℓ for all size ranges combined) that the laser particle spectrometer saturated, and was unable to produce any meaningful results. Again, the same sealed container was used as before, however in this case a lit cigarette was inserted and the airflow was used to push the air from the container to the reactor (again at 16 ℓ/min). Air was sampled either through the air diluter, connected after the end of the second stage of the reactor, or via path 2, Figure 4-8, or through the fine mesh filter (path 3, Figure 4-8) when the Nanocheck module was used.

4.8.4. PRECIPITATION EFFICIENCY FOR AIR LAID WITH CIGARETTE SMOKE

The air diluted cigarette smoke was sampled from the air diluter (path 2, Figure 4-8), and the stainless-steel mesh filter was not used in these tests. As stated in Section 4.3, 3 out of 4 of the container outlets that the smoke was generated in were connected directly to the exhaust, and completely bypassed the double stage precipitation reactor. Precipitation efficiency had the greatest drop for the (250-280) nm size range (by ~3%), compared to the precipitation efficiency conducted with ambient laboratory air using the same energisation levels. Drops in efficiency for larger size ranges were always smaller. To be more precise, the precipitation efficiency drop was 3.4% for the 17 kV dc voltage at the second stage only, and 3.2% for the case of 25 kV impulsive energisation at the first stage, in conjunction with 17 kV dc energisation at the second stage. For larger particles (> 450 nm) however, the efficiency was ~100%. Tests were also conducted by applying +18 kV dc to the second stage, and an increase in the peak magnitude of the corona current by more than 100% (to ~170 μA) was registered. The corresponding precipitation efficiency increased by only ~0.5%, and only for the (250-280) nm size range, as can be seen in Figure 4-36.

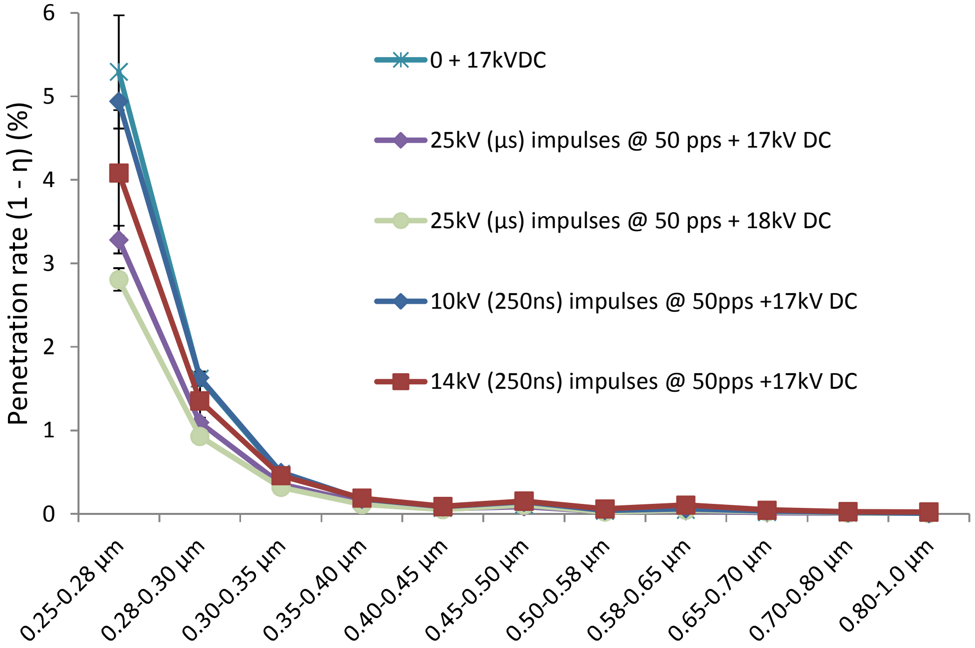

Figure 4-36: Pass rates (1 – η_p) for various energisation modes and particle size ranges for tests conducted with air-diluted cigarette smoke.

It can be concluded that the use of HV impulses in combination with dc energisation improves precipitation efficiency. The longer the impulse, the higher the efficiency was achieved. Where the HV impulses have the same length, the higher impulse magnitude produces the higher precipitation efficiency. The HV impulses produced by the Blumlein generator which have been used in the tests are shown in Figure 4-37 and Figure 4-38.

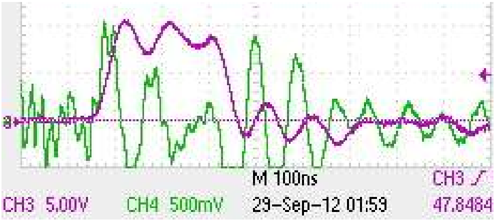

Figure 4-37: +10 kV voltage impulse applied on the first stage of the precipitation reactor. Purple: V(t) curve as measured by a Tektronix P6015A HV probe on top of the reactor, 5 kV/div; Green: I(t) curve measured by a current viewing resistor connected at the earth point of the reactor, 500 µA/div. Time scale 100 ns/div.

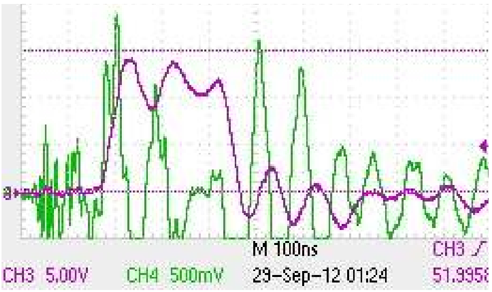

Figure 4-38: +14 kV Voltage impulse applied on the first stage of the precipitation reactor. Purple: V(t) curve as measured by a Tektronix P6015A HV probe on top of the reactor, 5 kV/div; Green: I(t) curve measured by a current viewing resistor connected at the earth point of the reactor, 500 µA/div. Time scale 100 ns/div.

In order to avoid overloading of the particle analyser, a fine mesh stainless steel filter was introduced into the experimental setup. This filter has an aperture of 99 µm, which is much higher than the size range of PM particles monitored in this work, however it increases precipitation efficiency so much that the use of the air-diluter (path 3, Figure 4-8 used) was discontinued. Still, only one of the outlets of the container was connected to the first stage of the reactor. These results can be seen in Figure 4-39. Precipitation efficiency was calculated by averaging the last 5 measurements of each test. In the (25-300) nm range, the particle analyser was saturated in all of the tests, and did not produce any meaningful results, while for particles larger than ~0.5 µm, the efficiency was 100%.

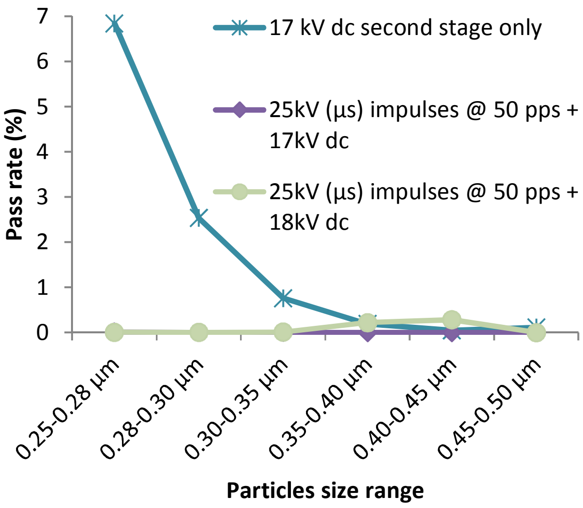

Figure 4-39: Pass rate (1 – η_p) for various energisation modes and particle size ranges of the tests with cigarette smoke and fine metallic mesh filter.

It was established that in the case of combined energisation of the reactor, the precipitation efficiency can reach almost 100%. However, as can be seen in Figure 4-39, there was negligible increase in the precipitation efficiency if the dc voltage level at the second stage was increased from +17 kV to +18 kV. Thus, the combination of impulsive and dc voltage applied to the 2 reactor stages, together with the utilisation of the stainless-steel fine mesh filter, can demonstrate ~100% efficiency (~99.99% for the (250-300) nm size ranges). The use of higher dc voltage can double the power consumption, with negligible positive effect on the precipitation efficiency.

4.9. ENERGY CONSUMPTION

The energy consumption of the precipitator was investigated. This analysis was conducted for all impulsive and dc energisation modes used in this study. In order to find the amount of air treated, which is required for calculation of energy efficiency, the air speed (based on the flow rate) was obtained for both the single and double stage reactors.

$$\boldsymbol{u} = \frac{\boldsymbol{Flow\ rate\ of\ air}}{\boldsymbol{Cross\ section\ of\ reactor}} \qquad (4.24)$$

The air flow rate was 16 ℓ/min in all experiments. While the internal diameter of the single stage reactor was 28 mm, in the double stage reactor it was expanded to 47.8 mm. Substituting these numbers into equation (4.24) gives air speeds of 0.433 m/s for the single stage reactor, and 0.15 m/s for the double stage reactor. Based on these numbers, the energy consumption was calculated as illustrated below.

For the single stage precipitator, the maximum dc energisation voltage used in experiments with flour, conducted with superimposed impulsive voltages was +16 kV dc. This is below the corona ignition level, that was found to be around +17.5 kV (corresponding to a corona current of 2.6 μA). This means that the power associated with the dc energisation is 0 Watts. In repetitive mode, the impulses had maximum peak amplitude ~30 kV at 10 pps. The charge injected is 3.52 μC/pulse, releasing energy of $1.62\cdot10^{-5}$ Wh/pulse, which corresponds to 0.6075 Wh/m^3 of treated air. Different energisation modes had lower peak impulse amplitude, thus less energy consumption is expected. For the test conducted with dc only, above corona ignition level at 18 kV dc (corresponding to 138.6 µA current), the power consumption is ~2.5 W, or 2.6 Wh/m^3 of air treated.

For the tests conducted with the single-stage precipitator and dolomite powder, the maximum dc voltage used was +16 kV, which is also below the corona ignition voltage. Thus no power consumption is expected. Superimposed impulses used were of maximum peak voltage of ~30 kV at 50 pps. The charge injected was 1.81 µC/pulse, releasing energy of 6.95 µWh/pulse, which corresponds to ~1.3 Wh/m^3 of treated air. However, this peak amplitude of ~30 kV was achieved only in single shot mode; in repetitive mode the amplitude was much lower. Hence, the calculated energy consumption is reflective of a worst-case scenario.

During the environmental tests conducted using the double stage precipitation reactor, a µs impulse generator was used, instead of the Blumlein that was used with the single stage reactor (producing impulses of 250 ns width). The maximum dc voltage used was +17 kV in the second stage, which is above the corona ignition level, and was produced a dc current of 72.8 µA, corresponding to 1.24 W, or ~1.29 Wh/m^3 of treated air. The impulses used had ~25 kV peak amplitude, and the tests were frequently conducted at 50 pps. The charge injected was 0.513 µC/pulse, releasing energy of 2.6 µWh/pulse which corresponds to 2.6 µWh/pulse x 50 pps = 0.468 J/s = ~0.47 W or ~0.49 Wh/m^3 of treated air. Thus, for the combined energisation case (second plus first stage), the total power consumption is1.71 W, or 1.78 Wh/m^3. If, however, the pulse repetition rate at the first stage was 125 pps, then the power consumed would be 0.325 mWh/s, which corresponds to 1.22 Wh/m^3. This means that if even higher pulse repetition rates were achieved, then higher efficiency with lower power consumption is expected, as the dc voltage level could be reduced in order to reach the same efficiency levels.

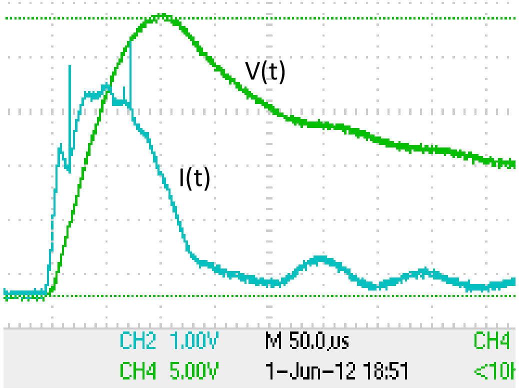

Figure 4-40: Typical example of a µs voltage pulse accompanied by a current impulse. Voltage is ~25 kV at peak while current is ~4 mA at peak. Time resolution is 50 µs/div, current is 1 mA/div and voltage is 5 kV/div.

These calculated energy consumption levels were close to, or in many case lower than, those found in published research regarding the energy consumption of electrostatic precipitators in general, as seen in Table 4-7.

Table 4-7: Comparison of my work with other papers and with industrial precipitators in general.

Cases/Papers	Wh/m^3	Air speed (m/s)	Flow rate (ℓ/min)
Flour	0.6075	0.433	16
Dolomite	1.3	0.433	16
Environmental	0.4875	0.1489	16
(Kim et al., 2010) typical	0.1–0.5	2-6	-
(Kim et al., 2010) own results	0.06–0.42	0.8	480
(Bologa et al., 2007) own results	0.44	> 15-20	min ~23k
(Liqian et al., 1996) in general	0.1	-	-

Despite the fact that the flow rate used here is low, it is safe to assume that there would be no significant decrease in precipitation efficiency with higher flow rates, as most of the particles are collected at the top part of the precipitator. This would mean that the power consumption (in Wh/m^3 of treated air) would be decreased significantly.

(Reyes and Taarning, 2008) describe a commercially available impulsive electrostatic precipitator for air treatment ("Coromax^{TM} Mrk.IV"), having similar goals to the one examined in this research. According to the patent (Reyes and Taarning, 2008) and information on the commercial website (FL Smidth, 2011), the mean dc voltage required is 60 kV, and the peak impulse magnitude is up to 80 kV, thus the total maximum voltage is 140 kV. Current flows only during the pulse voltage period, meaning that 60 kV is below the corona ignition level. It is also stated on the website that the number of pulses controls the current level. This might imply that the current pulse does not fall quickly enough to be zero after each voltage pulse for high pulse repetition rate modes. The pulse width is stated to be much less than 100 µs, while the current impulses are a few 100s of A in amplitude.

By assuming a triangular current pulse shape, with peak amplitude of 300 A and duration of 50 µs, coinciding with a voltage peak of just 100 kV, then the energy released is 750 J/pulse or 210 µWh/pulse, which is comparable to the amount of energy released per second in the current research. It is also claimed that the device can operate with (1-400) pps, meaning that the amount of energy released should be much higher compared to the double stage reactor examined in the present study. Information regarding the air flow or the air speed was not available in order to calculate the amount of energy needed per m^3 of treated air.

In the current research, since the voltage is decaying in an exponential way due to the diode used, it is not possible to calculate a duty cycle. However, since energy consumption is expected at energisation levels at which a corona current exists, the percentage of the treatment time for which the current is above the corona ignition level can be calculated. The dc corona level for the first (impulsive) stage was calculated at 6.2 kV, which corresponds to 12.5% of the time being above dc corona ignition level for the energisation regime used. However, for impulsive voltage, the corona inception voltage is higher compared to the dc case, thus the “duty cycle” is lower than 12.5%. The voltage remains above 50% of its peak amplitude for only 2.5% of the time.

4.10. CONCLUSIONS

PM2.5 are presently the center of attention due to health and environmental problems they can cause. To make matters worse, their sub-µm fraction (PM1) are the hardest to collect, showing reduced efficiencies compared to coarser or ultrafine (PM0.1) particles. In order to improve the efficiency of the ESP process in the sub-µm range, a double stage precipitator has been developed, energised with impulsive high voltage. Efficiencies of PM have been obtained for various energisation combinations, including impulsive only, dc only and combined energisation.

A double stage precipitation topology was designed based on the results obtained using the single stage reactor (Chapter 3), and accommodating for an increased air flow for practical, indoor applications. The inception voltages of corona discharges and *I(V)* curves have been obtained with and without air flow. This was done in order to find the optimal energisation regime for the double stage reactor, and in order to determine the voltage level margins for the safe and efficient use of the double-stage reactor. A trigger impulse generator was used to energise the first stage of the precipitator, producing impulses of ~175 µs duration (without the pulse forming network connected). Precipitation tests conducted with these long impulses applied to the first stage and dc voltage applied to the second stage demonstrated an improved efficiency compared to energisation with dc only.

Open shutter photographs of the corona were captured, from a specially designed, open view reactor having similar dimensions, proving that luminous corona is produced both for dc and impulsive energisation.

The resistivity of powders was measured as this parameter is of prime importance for the efficiency of precipitation and the suitability of impulsive energisation (Misaka et al., 1996, White, 1963). Measurements of the relative permittivity of various powders were conducted using a Video Bridge 2160. Samples of flour and dolomite (H600) powders used in precipitation tests were examined, and their resistivities and dielectric permittivities were obtained.

In the framework of the present research, the electric field in the inter-electrode space (space charge also taken into account) and the PM charging process inside a coaxial ESP were studied analytically (Timoshkin et al., 2012b). The mobility of charge carriers (positive ions in the case studied) was calculated from the experimental *V-I* curves, and by fitting with an analytically determined V-I curve, by utilizing the Matlab software package. The PM charging process was shown to be dependent upon the relative permittivity and the electrical conductivity of both the PM and the inter-electrode medium. Analytical expressions for both the (non-compensated) surface charge induced on the PM and for the polarisation charge were analytically obtained, as a function of time. Their sum, the total charge (due to field charging), allows for the investigations of the charging of PM with different electrical properties (σ and ε_r) to be conducted. The effects of diffusion charging were beyond the scope of the present research.

The 1320/1365 Nano Check was used to monitor particles down to 25 nm in diameter. However, it was observed that the Nanocheck module was saturated in some cases, and did not allow for the extraction of information regarding ultra-fine particles, probably due to the fact that the average size of the particulate matter reached the lower limit of 25 nm. However, the use of the Nanocheck module allowed for registration of the efficiency in the (25-300) nm size range (that includes ultra-fine PM).

In order to avoid saturation of the particle analyser, a fine mesh stainless steel filter was inserted into the air flow tube. It was found that this filter resulted in an increase of the precipitation efficiency, without any additional power delivered to the corona electrodes. It was also found that, for particles in the range (25-300) nm, the precipitation efficiency increased with the use of both stages of the reactor in the precipitation process, compared with the use of the second stage only.

The efficiency of PM removal was investigated using the double stage reactor. Three different energisation regimes were used: impulsive energisation in the first stage, dc energisation in the second stage, and a combination of the two (both stages energised). Using ambient air and cigarette smoke as test fluids, it was observed that through the combination of impulsive and dc energisation voltages, and the addition of a fine mesh filter efficiencies up to ~100% were chieved, meaning that the greatest part of PM is removed from the air flow (in the size ranges observed).

The amount of PM (in counts/ℓ) that manages to penetrate the reactor fell from ~40% at 10 pps to ~5% at 125 pps, when +25 kV μs impulses were applied to only the first stage of the precipitation reactor. Thus, as the pulse repetition rate increases, so does the efficiency of precipitation. If only the second stage is energised, precipitation occurs even below the corona ignition threshold (as was also the case with the single stage reactor). For voltages above the corona ignition threshold in the second stage, a sharp increase in the efficiency was observed, compared to that at the sub-corona energisation levels. If, however, voltage is increased to levels resulting in higher dc corona currents, the corresponding increase in efficiency is negligible, as was proven by the test summarised in Figure 4-36. To be more specific, for sub-corona ignition voltages (+(12-15) kV dc), the efficiency is ~(20-25)%, meaning that some of the particles can be removed even without corona current, as shown in Figure 4-31. At +16 kV dc energisation, the efficiency increases slightly to ~(25-30)%, due to the sub-μs corona current. The precipitation efficiency for combined energisation can be ~100% for ambient air particles, and ~97-100% for cigarette smoke particles, depending upon their size range.

In terms of energy consumption, most of this can be attributed to the dc stage. Therefore, increasing the pulse repetition rate is expected to decrease the overall power consumption, as the dc voltage level could be decreased further, while still achieving the same combined energisation levels. If the earthed, stainless-steel fine mesh filter is used as an additional precipitation tool after the reactor has collected the greatest PM amount, then the efficiency can be increased even further, without consuming any more power.

In comparison with (Podlinski et al., 2011), the efficiency achieved with the 2-stage reactor used in this work was much higher. In (Podlinski et al., 2011), the precipitation efficiency was 13%, 37% and 49% for the (250-280) nm, (500-580) nm and 37% (0.8-1) μm size ranges, respectively, using cigarette smoke, +30 kV dc voltage (energy consumption of 3.6 W) and a spike-plane configuration. In (Atten, 2008), utilizing a 2-stage parallel plate ESP charged with dc voltage (at 26 kV) and using cigarette smoke as a source of PM, the efficiency was ~83% for 300 nm particles, ~93% for 500 nm particles, ~95% for 0.7 nm particles, and ~96% for 1 μm particles respectively (for air speed of 0.4 m/s). In both cases, the efficiency was lower compared to the coaxial configuration and double stage ESP reactor used in this work.

Calculations of the power consumed by the reactors to clean the air flow have been performed, both for the cases of ambient air and air laden with smoke particles. The parameters chosen for calculation of the energy efficiency were reflective of worst-case scenarios, meaning for the highest dc and impulsive voltage levels in order to find the maximum energy consumed during the precipitation process. It was found that this maximum energy is comparable with the energy consumption reported in the literature, and with the energy consumption commonly found in industrial scale precipitators (see Table 4-7).

As the second stage of the reactor has a corona ignition voltage of 16.6 kV dc, power is consumed only at energisation levels higher than this voltage. At +17 kV dc energisation voltage, the power consumption is 1.24 W. Considering the air flow rate of 16 ℓ/min, the energy consumption for the second stage only is 1.29 Wh/m^3 of treated air. For the first stage being energised at 50 pps with the same air flow rate, the corresponding energy consumption is 0.49 Wh/m^3. Thus, the total power requirement for both stages energised is 1.78 Wh/m^3. If 125 pps is used at the first stage, then the energy consumed in the first stage rises to 1.22 Wh/m^3.

To conclude, it has been shown from the research conducted with the 2-stage reactor that by combined impulsive and dc voltage energisation, and inclusion of a (non-mechanical sieving) earthed, fine mesh filter at the outlet, the vast majority of PM2.5 can be removed efficiently from the air.

5. SCALED-UP, DOUBLE STAGE ELECTROSTATIC PRECIPITATOR

5.1. INTRODUCTION

In order to extend the potential practical application of the developed impulsive electrostatic precipitators, a larger scale, double stage precipitator was designed and developed in the present research project. This chapter is focused on an investigation of the performance of the scaled-up precipitator reactor. An impulsive electrostatic precipitation system with higher flow-rate would allow treatment of larger volumes of air to be conducted and thus, such a system could be utilised in a wider range of practical applications, including larger scale air –cleaning operations in indoor environments such as hospitals, schools, and public and private buildings.

In Sections 3 and 4 the maximum flow-rate of the developed micro-precipitation system was 16 ℓ/min. The flow-rate would be sufficient to treat ~1 m^3 of air per hour, which makes it practical to use this system in smaller scale applications, for example to treat air in rooms with volume up to a few m^3. However, in order to treat larger volumes of air, higher flow-rate is required. Thus, in order to demonstrate that the proposed impulsive precipitation system can be scaled up and potentially used for treatment of lager volumes of air, cylindrical reactors with diameters of 95 cm have been developed. In order for reactors of this diameter to reach the air speed limit of ~1 m/s at which particle re-entrainment occurs according to (McKenna et al., 2008), the flow rate could be increased up to ~42,500 ℓ/min.

As in the smaller scale precipitation system developed and investigated in Section 4, the first stage of the scaled up precipitator is intended for particle charging, and the central HV electrode of this stage was impulsively charged. The second stage of the precipitator is used for particle deflection and collection, thus it was energised with dc voltage only, close to the corona ignition level.

The high voltage electrode in the first stage was formed from 35 gauge metallic wire (0.213 mm radius), while for the second stage a smooth 5 mm rod was selected, in order to have the same electric field as in the smaller scale reactor described in Section 4.2. The central electrode of the first stage of the scaled up reactor was energised with positive HV impulses with magnitude up to 30 kV, these impulses have a FWHM duration (full-width at half-maximum) of 500 µs (instead of 25 kV and 400 µs impulses used for energisation of the original reactor in Section 4.4).

The smaller wire (HV electrode) radius in the first stage enhances the electric field, and thus lower energisation voltages are required for ionisation and particle charging processes. For the second stage, the electric field does not need to be as high as in the ionisation charging stage (voltages just above corona ignition level were used in the precipitation system developed in this project), so as to only deflect and collect the already charged PM. Therefore, the energy consumption of the whole precipitation system can be kept at low levels. In both stages, the external parts of the stainless steel cylinders were earthed, and acted as particle collection electrodes.

In this part of the research project, the study of the precipitation efficiency was focused on the PM2.5 fraction of the airborne particles. Thus, ambient laboratory air and the smoke from beeswax candles were used as samples for precipitation experiments. Further analysis is given in the subchapters that follow.

In this chapter, a numerical analysis of the PM migration velocity was also conducted, as it acts as a direct indication of the level of precipitation efficiency. This velocity depends upon the rate of charging of PM, which is ultimately a function of the dielectric permittivity and electrical conductivity of PM and the air it is suspended in, among other factors (most importantly being the PM individual particle diameter and the PM loading on the air flow). In addition to this analysis, experiments were also conducted with different energisation levels and various combinations of PM laden test fluids, like ambient laboratory air and air with 3 different concentrations of beeswax candle fumes. Particle migration velocities were obtained using the empirical formulas proposed by (Matts and Öhnfeldt, 1964, Lin et al., 2012) from the precipitation efficiency data . These experimentally obtained migration velocities were compared with analytical values, and can be used for optimisation and improvement of the ESP system.

5.2. DESIGN OF SCALED-UP REACTOR AND EXPERIMENTAL METHODOLOGY

An increase in the volume of the precipitation system was achieved by an increase in the length of the reactor, from ~20 cm to 87 cm for the first stage, and from ~20 cm to 70 cm for the second stage, and by an increase in the diameters of both stages. Thus, wider inter-electrode gaps were used in both stages. As this increase would also affect the electric field inside the reactor, and potentially the precipitation efficiency, adjustments of the energisation level and diameters of the HV electrodes were made. It was anticipated that the larger scale precipitation system would enable treatment of a greater volume of air. Longer reactor stages will also help to increase the efficiency of precipitation, as the Deutsch-Anderson equation predicts (Deutsch, 1922, Anderson, 1925, Bäck, 2013).

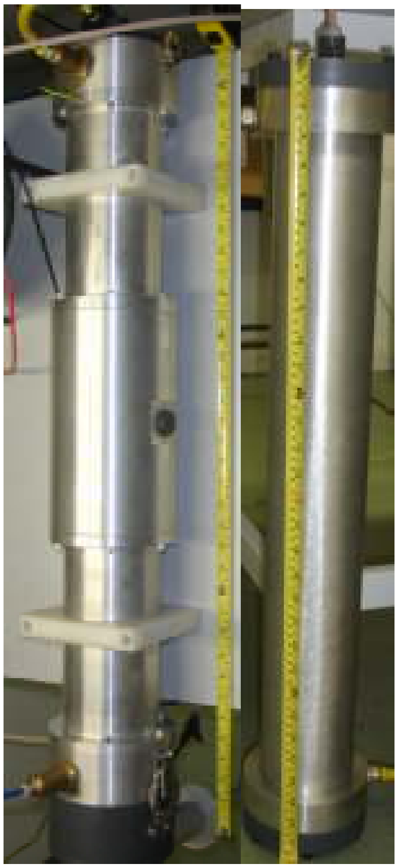

Figure 5-1: Scaled-up, double stage precipitation reactor. To the left the first (energisation) stage and to the right the second (deflection and collection of charged particles) one.

The wider inter-electrode gap in the first stage allows the use of an increased impulsive voltage, without resulting in electrical breakdown. The HV electrode was kept the same as in the previous version, as it was thin enough for a sufficiently high electric field to be created, and not so thin as to be very fragile. This, in turn, meant that the electric field would have been decreased, however since the impulsive voltage was increased, a slight increase in the electric field was achieved (from 231 kV/cm to 246 kV/cm at a distance of 0.02 cm from the center of the rod, or ~6.5% increase). The electric field close (distances up to 1 mm from its center) to the energisation electrode (35 gauge wire) is shown in Figure 5-2.

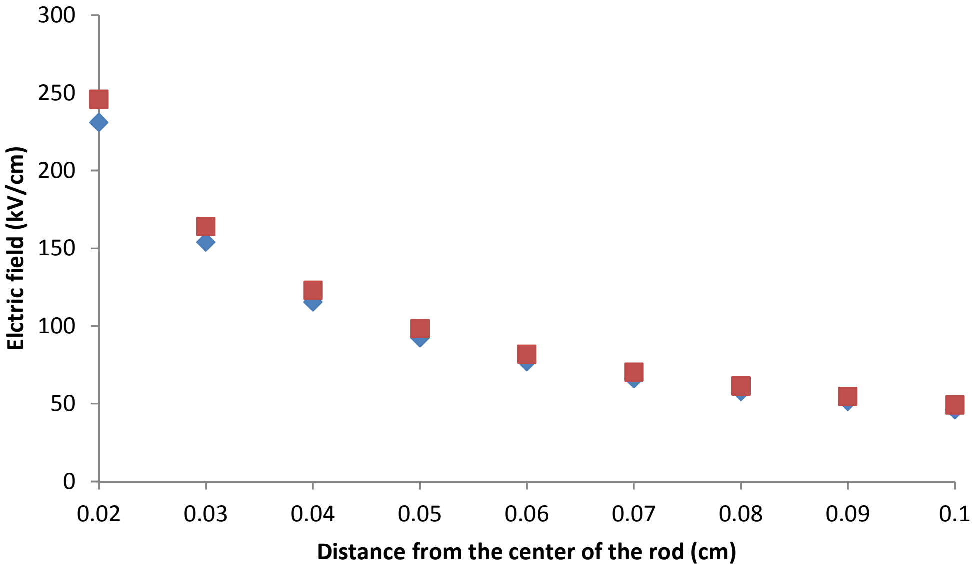

Figure 5-2: Electric field at distances 0.2 mm up to 1 mm from the centre of the high voltage electrode. Red squares: Electric field in first stage of the scaled up reactor. Blue diamonds: Electric field in the first stage of the original 2-stage rector.

The second stage of the precipitator is intended for particle collection only, therefore the field should be below the corona ignition voltage. The field in this stage was higher compared to that of the original (smaller scale) reactor described in Section 4.3, despite the fact that a new, wider (5 mm instead of 1.5 mm) smooth rod was used as the HV electrode. Numerically, for an arbitrary energisation voltage of 16 kV dc, this corresponded to a ~21% increase in electric field, at 0.26 cm from the center of the rod, compared to the field in the original reactor. If the 1.5 mm diameter smooth rod were to be placed coaxially in the wider topology, the increase in field would be 42.5% at the same distance, compared to the use of a 5 mm electrode. Figure 5-3 compares the magnitude of the electric field in the original and scaled-up coaxial reactors, with diameters of 47.75 mm and 88 mm respectively, for various electrode-configurations, (both, suggested and practical, which were used in this research), for an arbitrary charging voltage of 16 kV dc.

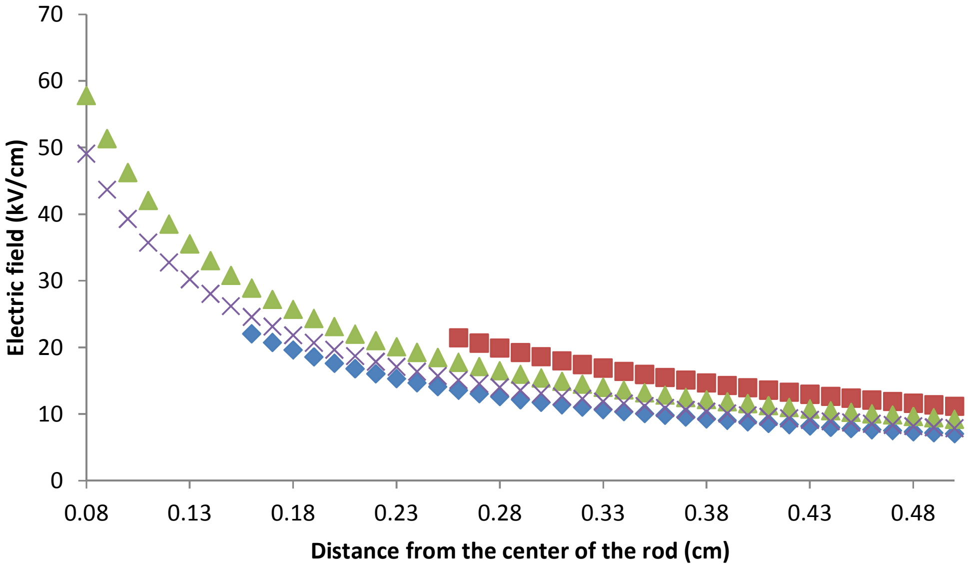

Figure 5-3: Electric field close to the energisation electrodes in the second stage of the reactors. Blue diamonds: 3 mm smooth rod, in the single stage reactor; Green triangles: 1.5 mm dia smooth rod in the 2-stage reactor; Purple crosses: 1.5 mm smooth rod placed coaxially in the wider, scaled-up, reactor; Red squares: 5 mm smooth rod placed coaxially in the wider, scaled-up reactor.

This widening of the reactor also changed the air speed inside it, the velocities are shown in Figure 5-4 for flow rates of (1-16) ℓ/min.

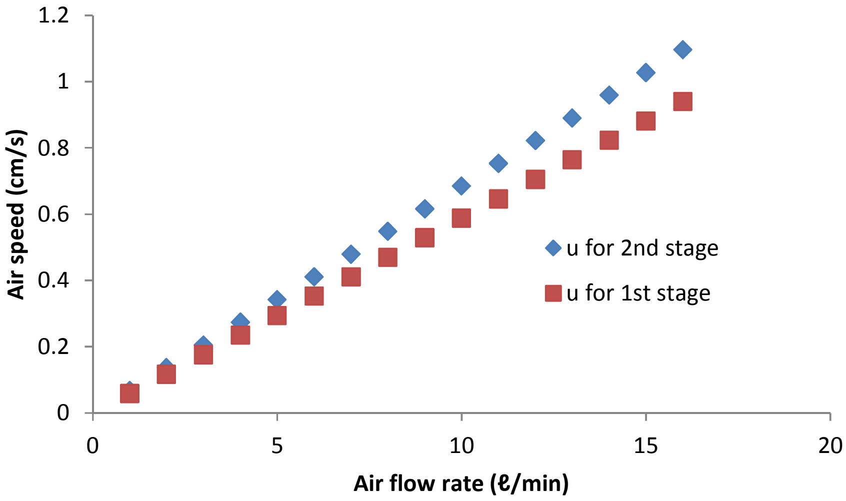

Figure 5-4: Air speed inside the reactor as a function of air flow rate for its first and the second stage. First stage of the cylindrical scaled-up reactor has 95 mm internal radius, while the second stage one has 88 mm.

The maximum flowrate that the air pump could supply, 16 ℓ/min, was again used in the tests described in the present chapter. This corresponds to air speeds ~1 cm/s, which meant that the efficiency of precipitation would be enhanced, as according to (Deutsch, 1922, Anderson, 1925, Bäck, 2013), the precipitation efficiency increases with a reduction in air speed. Low speed also introduces turbulence in the air flow, which is an important factor for the process involved in the charging of PM1 and ultrafine particles (Hinds, 1982, Li and Christofides, 2006).

Summarizing the new configuration, the electrostatic precipitator used in this part of the research is a scaled-up version of the reactor developed in Section 4. It is a two-stage reactor with a coaxial electrode configuration (earthed cylinder on the outside, HV electrode placed coaxially at its center). The first stage has a 35 gauge wire (British Standard Wire Gauge (SWG)) as HV electrode (0.213 mm diameter) and its primary purpose is to charge the PM. Its outer electrode is a stainless-steel cylinder of 87 cm length and 95 mm internal diameter. The second part of the precipitation reactor, which is connected in series (pneumatically) with the first one, consists of a 5 mm diameter smooth electrode, placed coaxially at its center and acting as an HV electrode, while an earthed cylinder of 88 mm internal diameter and 70 cm length surrounds it and acts as a particle collection electrode. Its main purpose is not to charge, but to deflect and collect the PM that have been charged in the first stage. dc electric field is used to augment the collection process, thus energisation voltage lower than corona ignition voltage is applied to the HV electrode in this stage.

5.2.1. ENERGISATION OF THE REACTOR

An impulse generator (based on a step-up autotransformer of a car ignition coil) generates impulses that are applied to the high voltage electrode (thin 35 SWG wire) of the first stage of the scaled-up, 2-stage precipitation reactor. At the second stage, a 20 kV Glassman EW series HVDC power supply is utilised to energise the coaxially located 5 mm diameter smooth rod that acts as an energisation electrode. The impulsive voltage was measured by a Tektronix P6015A high voltage probe (75 MHz bandwidth), and the current was obtained by measuring the voltage drop across a 1 kΩ current viewing resistor, connected between the collection electrode (external cylinder) and earth. A schematic diagram of the precipitation system used in these tests is shown in Figure 5-5. A detailed description of the diagnostic devices and HV energisation system has already been given in Section 4.4.

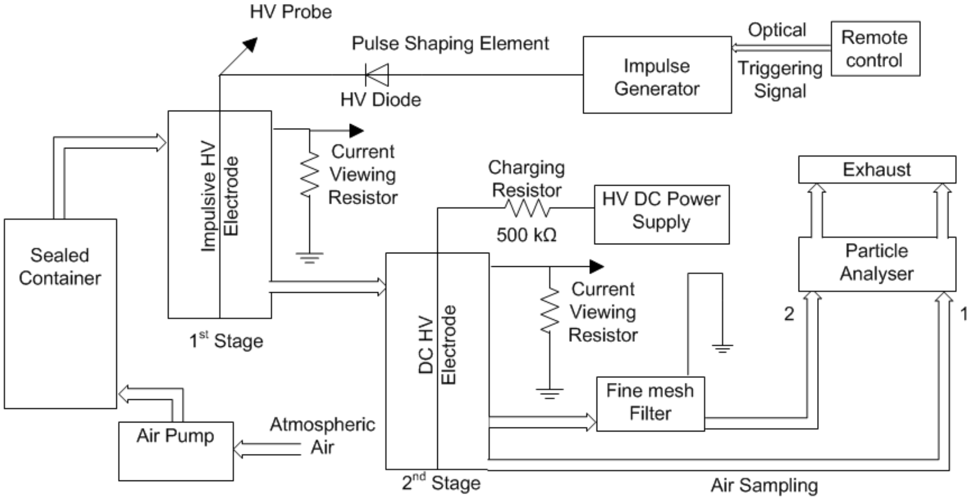

Figure 5-5: Pneumatic and electric circuitry of the scaled-up ESP system.

Figure 5-6 shows an example of a voltage and current impulse in the first stage of the reactor. HV impulses with a voltage of peak magnitude +30 kV and a FWHM duration of 500 µs (up from 400 µs in the 2-stage reactor used in Chapter 4) were applied to the HV electrode. The corresponding current impulse produced by voltage impulses of such amplitude and duration had a maximum current of ~10 mA. These current impulses are a manifestation of a transient corona discharge that charges the PM present in the inter-electrode space. Such current impulses release charge of ~1 µC in the inter-electrode space, of which only a small amount (~220 nC) is associated with the displacement current due to the capacitance of the reactor. In order to calculate the displacement current, the capacitance of the new reactor was calculated using equation (5.1):

$$\boldsymbol{\frac{C}{l} = \frac{2\pi\varepsilon_0\varepsilon_r}{ln\left(\frac{\beta}{a}\right)}} \tag{5.1}$$

For α = 0.213 mm and β = 95 mm, it was found that the capacitance, *C*, of the first stage is ~8 pF. Therefore, the displacement current can be calculated using equation (5.2):

$$\boldsymbol{i = C\frac{dv(t)}{dt}} \tag{5.2}$$

where *v(t)* is the impulsive voltage.

The displacement charge was calculated by assuming that there is a constant displacement current - calculated using equation (5.2) - for the duration of the voltage rise time from 0% to 100% of the peak amplitude (~220 nC compared to ~1 µC for the impulse). The charge injected into the inter-electrode space is the total charge minus the displacement charge calculated. The capacitance of the second stage is ~13.6 pF, for *β* = 88 mm and *α* = 5 mm.

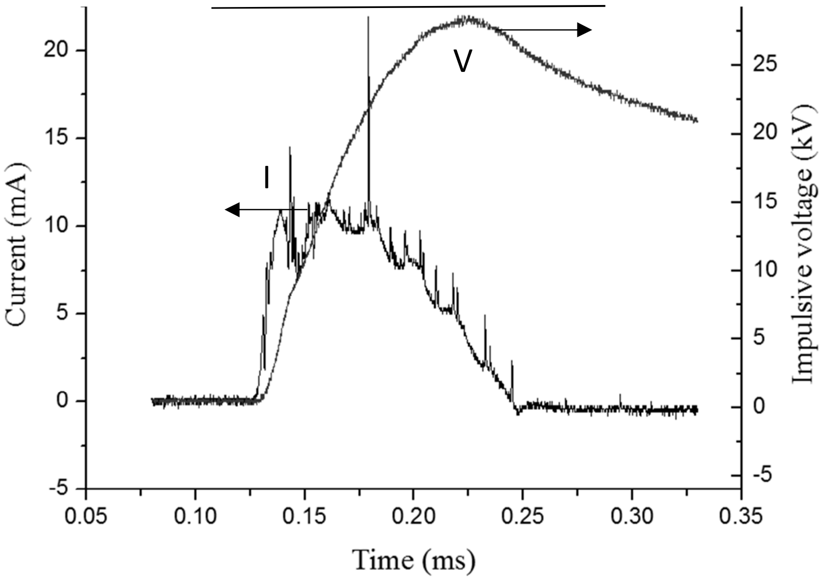

Figure 5-6: Voltage (V) and current (I) waveforms of individual impulses.

For tests with beeswax candles the air flow rate was reduced from the maximum of 16 ℓ/min to 3 ℓ/min, due to the air dilution that had to be introduced. This reduced flow rate was calculated by first measuring the air speed inside the 6 mm diameter flexible plastic tube, which supplied the particulate laden air flow to the ESP. The air velocity was found to be ~4 m/s (the air pump used does not provide air at a constant speed). Taking into account the fact that the internal diameter of the 6 mm flexible tube is 4 mm, the air flow can be calculated by equation (5.3)

$$X(m^3/s) = u(m/s) \cdot A(m^2) = 4\, m/s \cdot \pi \cdot \left(\frac{4mm}{2}\right)^2 = \frac{24}{25}\pi\, \ell/\mathrm{min} \cong 3\, \ell/\mathrm{min} \tag{5.3}$$

where *A* is the cross sectional area of the tube. This reduces the air speed inside the reactor even further compared to the environmental tests, as now it is defined by equation (5.4)

$$u_{1st\_stage} = \frac{X(m^3/s)}{\pi \cdot \left(R_{\mathrm{int}\_1st\_stage}\right)^2} = 4.25\, mm/\mathrm{min} \tag{5.4}$$

Based on the numbers presented above, the power consumption was calculated at ~1 W, reduced by ~60% (down from 1.71 W) compared to the smaller scale, double stage reactor described in Section 4.9.

5.2.2. PARTICLES SUSPENDED IN THE AIR FLOW

Initial experiments were conducted with ambient laboratory air. Subsequently, in order to have heavier particle loading of the air flow, and heavier PM2.5 loading especially, beeswax candle fumes were used. In both experiments, the portable aerosol spectrometer (Grimm 1.109) was used in order to measure PM concentration (counts/ℓ) and thus to calculate the efficiency of precipitation. As in the case of the precipitation reactor described in Section 4, the particle analyser was either sampling air directly from the exhaust of the 2nd stage of the reactor (path 1, Figure 5-5) or, in case of heavy PM loading, through a stainless-steel fine-woven mesh filter, that was earthed. This filter was made of 28 μm diameter stainless steel thread, and had an aperture of 99 μm, which is significantly larger compared to the PM examined (path 2, Figure 5-5).

5.3. MODELING OF PARTICLE CHARGING AND PRECIPITATOR EFFICIENCY

While there are many parameters that affect the electrostatic precipitation process, one of the most important, affecting the electrostatic precipitation efficiency, is the migration velocity achieved by the charged PM. To find the dynamic behavior of a particle inside the ESP reactor, the equation of motion inside the energised reactor must be solved for. Equation (5.5)) gives the forces that are applied onto a charged particle inside the reactor is subjected to:

$$\overrightarrow{\boldsymbol{P}} + \overrightarrow{\boldsymbol{F_{drag}}} + \overrightarrow{\boldsymbol{F_e}} = \overrightarrow{\boldsymbol{F_{Tot}}} \qquad (5.5)$$

where $\vec{P}$ is the particle weight, $\overrightarrow{F_{drag}}$ is a resistive force that pulls the particle in the opposite direction to its direction of movement, $\overrightarrow{F_e}$ is the electrostatic force that is exerted on the particle because of its charged state, and $\overrightarrow{F_{Tot}}$ is the vector sum of all forces that act upon the charged particle. However, since the reactors are intended to have vertical orientation, only those forces acting in the radial direction, or components of forces that act in the radial (HV to earthed electrode) direction, should be taken into account, because migration velocity is radially directed. Thus, weight, $\vec{P}$ in equation (5.5), can be disregarded and only the radially directed component of the drag force should be taken into account. In the case where the precipitation reactor is horizontally placed, the weight will be acting towards higher precipitation efficiencies, thus this vertical configuration is the worst case scenario. The sum of forces acting upon the particle in the radial direction is thus given by equation (5.6), written in scalar form as all its forces act in the same direction (meaning on the same line, could be in opposite directions):

$$\boldsymbol{F_{Tot} = m\frac{du}{dt} = F_e - F_{drag-r} = Q(E,t) \cdot E(r) - \frac{3 \cdot \pi \cdot \eta}{C_c} \cdot d \cdot u} \tag{5.6}$$

where,

Q(E,t) is the amount of charge acquired by the particle at any particular time (excluding diffusion charging),

E(r) is the electric field,

u is the speed that a particle is moving at in the radial direction,

η is the viscosity of atmospheric air,

d is the diameter of the particle under test.

C_c represents the Cunningham correction factor, which is important for calculating drag effects on PM10 and is equal to:

$$\boldsymbol{C_c = 1 + \frac{2.52 \cdot \lambda}{d}} \tag{5.7}$$

where *λ* is the mean free path and *d* is the particle diameter (Hinds, 1982). The mean free path is, in turn, equal to:

$$\boldsymbol{\lambda = \frac{1}{\sqrt{2}\cdot n\cdot \pi\cdot d_m^2}} \tag{5.8}$$

where d_m is the collision diameter, which for dry air is 3.7 Å, and n is the number of molecules inside a unit volume. For dry atmospheric air or an ideal gas (1 atm at 20°C) n is equal to $2.504\cdot 10^{25}/\mathrm{m}^3$ (Jonathan and Kenneth, 2014), (Hinds, 1982).

Based on the analytical work conducted in Section 4 and published in (Mermigkas et al., 2013), the electric field and charge acquired by the particle are given by:

$$\boldsymbol{Q(E,t) = 6\pi(d/2)^2 E_0 \epsilon_0 \frac{-\varepsilon_m\sigma_p+\sigma_m\varepsilon_p}{2\sigma_m+\sigma_p}\left(1-e^{-t/\tau_{MW}}\right)} \tag{5.9}$$

$$\boldsymbol{E(r) = \sqrt{A\cdot\left(1-\frac{R_{ion}^2}{r^2}\right)^2 + E_{rion}^2\cdot\frac{R_{ion}^2}{r^2}} = \sqrt{\frac{R_{ion}^2}{r^2}\cdot\left(E_{rion}^2 - A\right) + A}} \tag{5.10}$$

where τ_{MW} is the Maxwell-Wagner relaxation time, introduced in Section 4, and equal to:

$$\boldsymbol{\tau_{MW} = \frac{2\varepsilon_m+\varepsilon_p}{2\sigma_m+\sigma_p}\varepsilon_0} \tag{5.11}$$

Another parameter required to calculate the electric field is the radius of ionisation, R_{ion}, around the HV wire, being the limit of the ionisation zone of the coaxial corona discharge, equation (5.12). In order to calculate the radius of that zone, the Kapzov hypothesis was utilised, stating that for voltages that exceed the corona ignition threshold, the electric field inside the ionisation zone remains constant. It was also assumed that the mobility, μ, of the charge carriers is constant, in order to be able to obtain values for μ by fitting an analytical *V-I* curve to the experimental *V-I* data point curves in Subsection 4.7.

$$\boldsymbol{R_{ion} = \frac{E_{Peek}}{E_{crit}}\cdot\frac{R_{wire}}{100}} \tag{5.12}$$

where E_{Peek} is the electric field for cylindrical topology in order to have corona ignition.

$$E_{Peek} = 31 \cdot (1 + \frac{0.308}{\sqrt{R_{wire}}}) \cdot 10^5 (V/m) \qquad (5.13)$$

E_{crit}, the critical ionisation field in atmospheric air, is the field at which the ionisation (α) and attachment (β) coefficients are equal, being (26-31)·10^5 V/m for atmospheric air (Timoshkin, 2010c). Since in the Peek equation R_{wire} must be in cm, in order to calculate R_{ion}, R_{wire} is divided in (5.12) by 100 to convert it from cm to m. Constant A in Equation (5.10) is:

$$A = \frac{I_{cor}}{2\pi l \varepsilon_0 \varepsilon_r \mu} \qquad (5.14)$$

where I_{cor} is the corona current and l is the length of the first stage of the reactor. Therefore, the equation of particle motion in the radial (r) direction now becomes:

$$m\ddot{r} + C_0\dot{r} = (C_1 + \frac{C_2}{r^2}) \cdot (1 - e^{-t/C_3}) \qquad (5.15)$$

where,

C_3 the Maxwell-Wagner relaxation time (τ_{MW}) and

C_0 to C_2 are functions of the particle characteristics (size, conductivity and permittivity), of the viscosity of the air, and other parameters.

$$C_0 = \frac{3 \cdot \pi \cdot \eta \cdot d}{1 + \frac{2.52}{\sqrt{2} \cdot n \cdot \pi \cdot d_m^2 \cdot d}} = \frac{F_{drag}}{u} \qquad (5.16)$$

$$C_1 = \frac{I_{cor}}{2\pi l \varepsilon_0 \varepsilon_r \mu} \cdot 6\pi (d/2)^2 E_0 \epsilon_0 \frac{-\varepsilon_m \sigma_p + \sigma_m \varepsilon_p}{2\sigma_m + \sigma_p} = A \cdot Q_{const} \qquad (5.17)$$

where Q_{const} is the part of (5.9) that is independent of time

$$C_2 = 6\pi (\frac{d}{2})^2 E_0 \epsilon_0 \frac{-\varepsilon_m \sigma_p + \sigma_m \varepsilon_p}{2\sigma_m + \sigma_p} \cdot R_{ion}^2 \cdot \left(E_{crit}^2 - \frac{I_{cor}}{2\pi l \varepsilon_0 \varepsilon_r \mu}\right) = Q_{const} R_{ion}^2 \left(E_{crit}^2 - A\right) \qquad (5.18)$$

In equation (5.15) to (5.18)) above, the forms: $C_0\dot{r}$, C_1, and C_2/r^2 have dimensions of force. (5.15) has been solved numerically using Matlab ode45 solver, using the code in Appendix F.1. The results are shown for various cases in Figure 5-7, Figure 5-8 and Figure 5-9.

Figure 5-7 shows the migration velocity that a beeswax particle of 250 nm diameter acquires, if it is subject to a current impulse of 10 mA amplitude. Beeswax particles were chosen in the simulations due to the use of beeswax candle fumes in the precipitation tests. According to the literature (Sams and Co, 1973, Nyayate and Pendharkar, 2012), beeswax PM have relative dielectric permittivity of $\varepsilon_p = 2.4$, and conductivity in the µS range. Their density varies, however it is very close to, and less than, that of water (Bernal et al., 2005). The value of $\sigma_m = 5.76\cdot10^{-7}$ S/m was used for the conductivity of the medium, as calculated in Section 4.7.

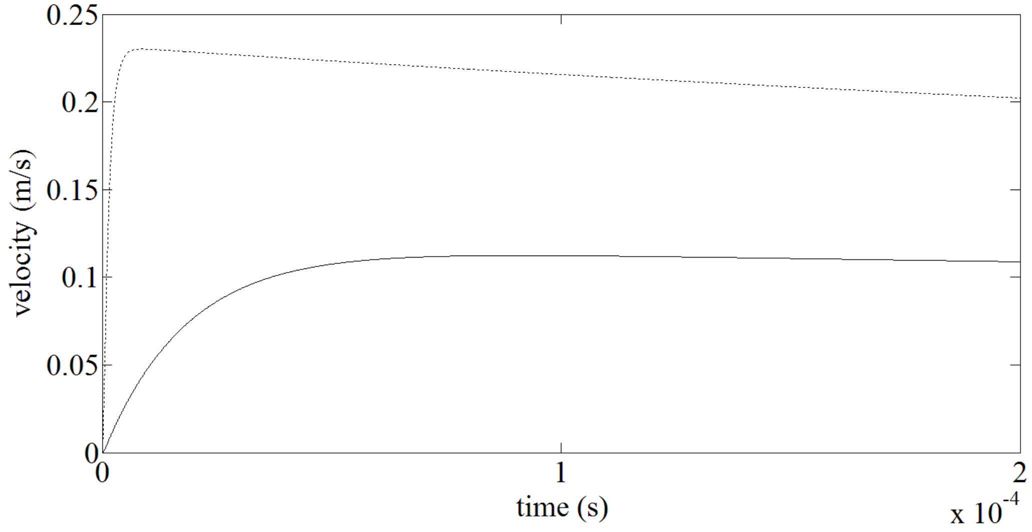

Figure 5-7: 250 nm dia beeswax particle migration velocity as a function of time. Solid line: ε_p =2.4, $\sigma_p = 10^{-6}$ S/m, $\sigma_m = 5.76\cdot10^{-7}$ S/m; dotted line: ε_p =2.4, $\sigma_p = 1.25\cdot10^{-5}$ S/m, $\sigma_m = 10^{-5}$ S/m.

According to Figure 5-7, the migration velocities of these particles reach their peak values during the first ~100 µs of the applied current impulse, which is the pulse width used in the first (charging) stage of the scaled-up precipitator. Thus, the duration of the energisation impulse applied on the first stage guarantees the maximum migration velocity achieved by the PM, which is important for maximising the efficiency of precipitation. A more clear view of this tendency with increasing particle size can be seen in Figure 5-8, which includes simulations for particle diameters of 200 nm up to 10 µm.

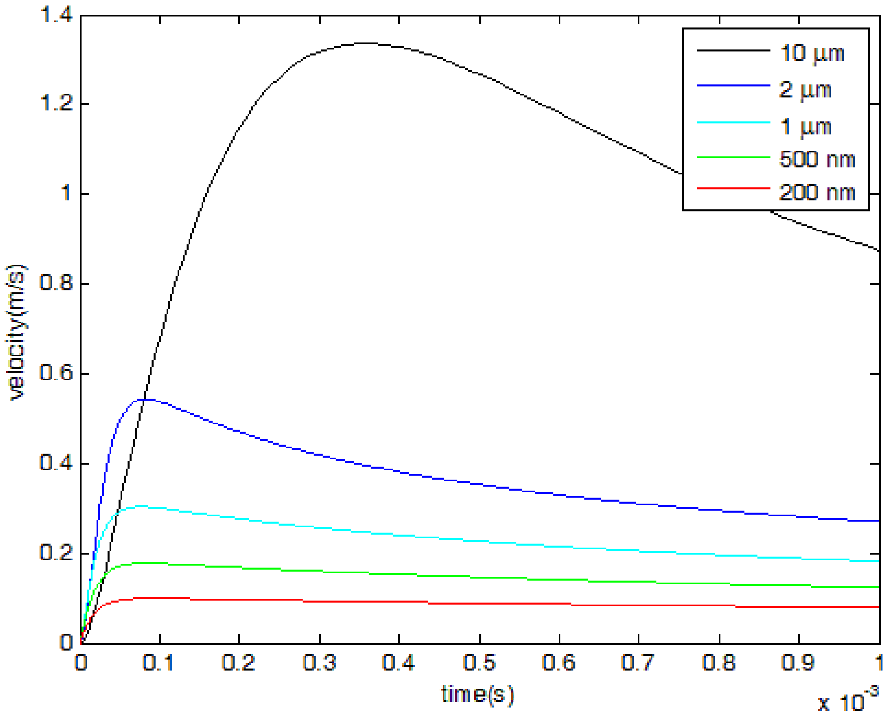

Figure 5-8: Beeswax particle migration velocity as a function of time for various particle diameters (see legend) for particles positioned at the edge of the ionisation zone, i.e. 0.0005 m from the centre of the HV electrode. ε_p =2.4, σ_p =10^{-6} S/m, σ_m =$5.76\cdot10^{-7}$ S/m.

In terms of the dependence of the initial (radial) position of a particle inside the reactor on its terminal velocity, it was found that the migration velocity acquired by a particle located at 0.5 mm from the centre of the wire of the first stage, is ~2.5 times higher than that of a particle located 0.5 mm from the surface of the collection electrode (internal part of the earthed cylinder). Additionally, particles in between these regions show little difference in their terminal migration velocities, as shown in Figure 5-9. In Figure 5-10, the same dependence is investigated, using a particle of the same diameter but of different dielectric permittivity. In this case, the difference in terminal speed is only ~22%, presupposing, of course, that the impulse width shall be long enough for PM to reach the collection electrode while the impulsive electric field is still present in the inter-electrode space. 0.5 mm was chosen as a starting point of PM movement, corresponding to the edge of the ionisation zone, as calculated by (5.12) using Matlab (code given in Appendix F.1).

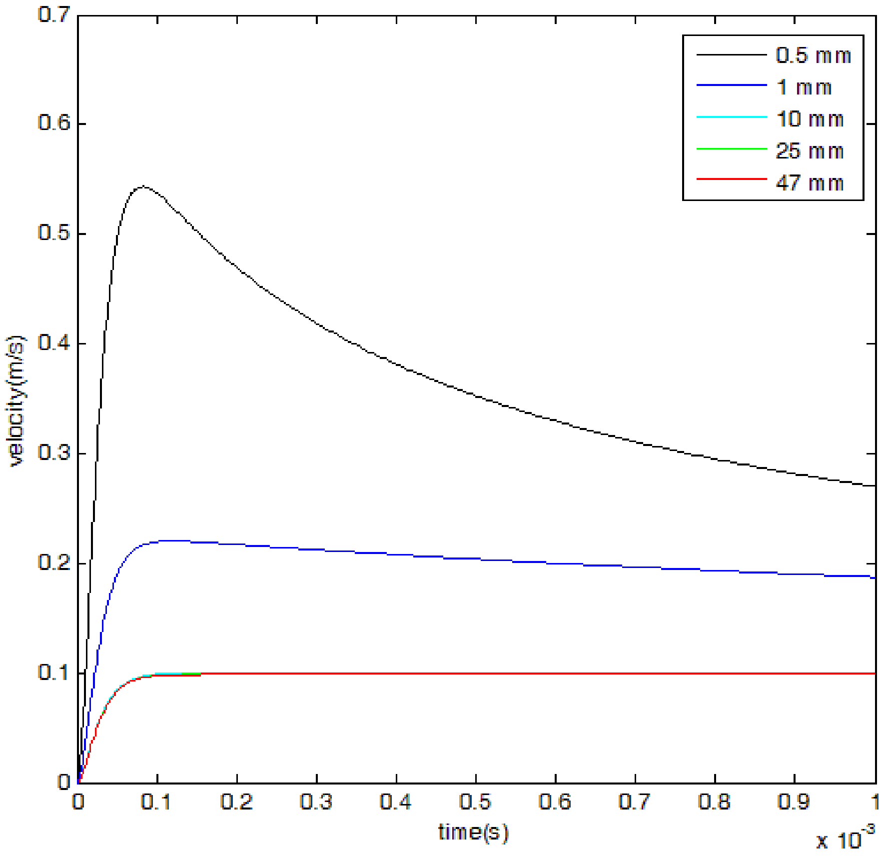

Figure 5-9: Terminal migration velocity of a 2 µm beeswax particle positioned at different distances from the first stage HV electrode (wire). ε_p **=2.4,** σ_p **=**10^{-6} **S/m,** σ_m **=**$5.76 \cdot 10^{-7}$ **S/m.**

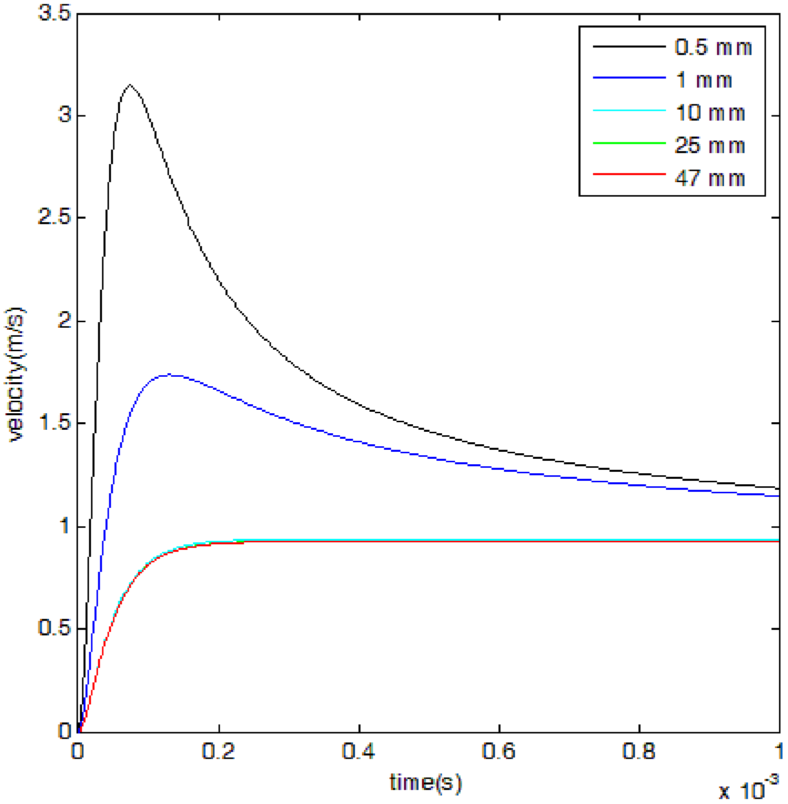

Figure 5-10: Terminal migration velocity of a 2 µm particle positioned at different distances from the first stage HV electrode (wire). ε_p =6, $\sigma_p = \sigma_m$ =5.76·10^{-7} S/m.

By changing the parameters of the equation (5.15) using the model developed in this work, the effect on migration velocity of a doubling of the corona current can be determined. The answer is that the particle migration velocity would almost double, and the difference of terminal velocity between the extreme cases of positioning of particles close to the HV electrode and close to the collection electrode would be even smaller, as can be seen in Figure 5-11 and Figure 5-12.

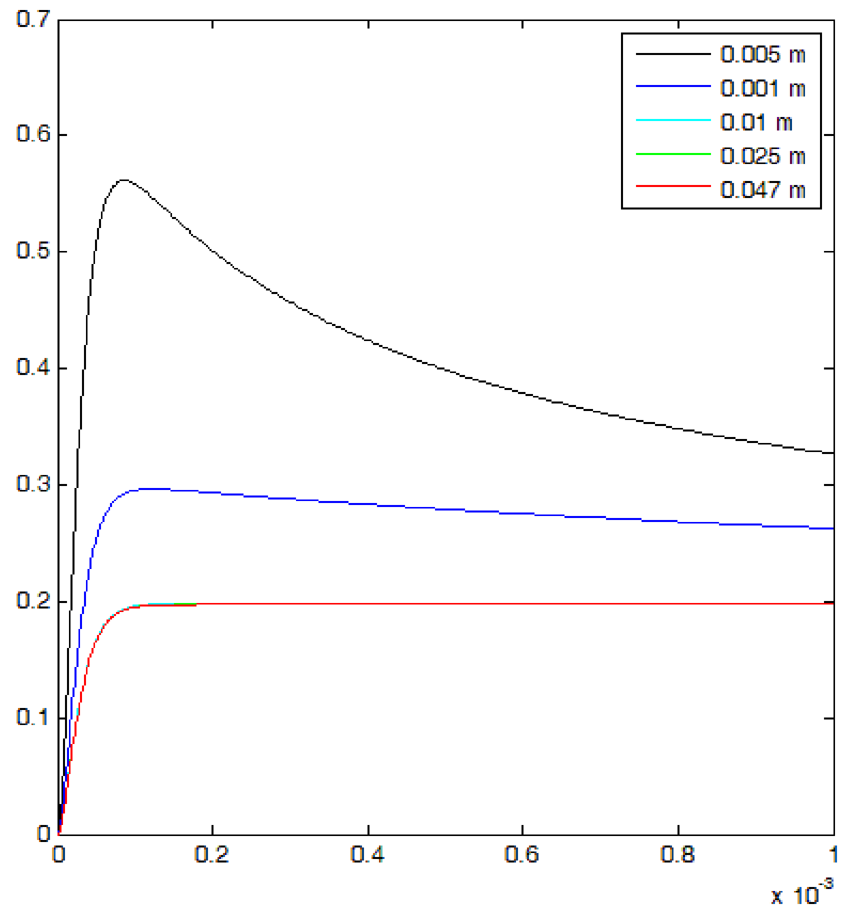

Figure 5-11: Terminal migration velocity of a 2 µm beeswax particle positioned at different distances from the first stage HV electrode (wire). ε_p =2.4, σ_p =10^{-6} S/m, σ_m =$5.76 \cdot 10^{-7}$ S/m and I_{cor} = 20 mA. Vertical axis, velocity (m/s); horizontal axis, time (s).

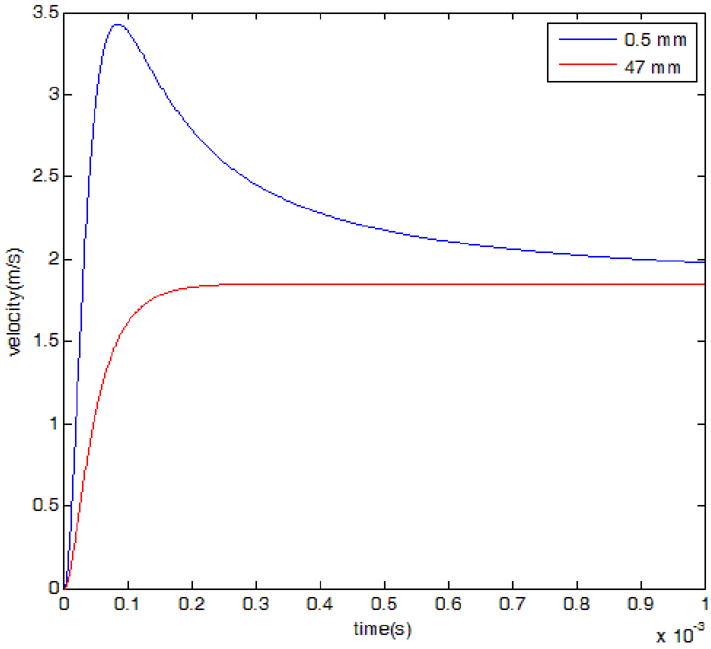

Figure 5-12: Terminal migration velocity of a 2 μm particle positioned at different distances from the first stage HV electrode (wire). ε_p =6, $\sigma_p = \sigma_m$ =5.76·10^{-7} S/m and I_{cor} = 20 mA.

Values of ε_p of 2.4 and 6 were used in these simulations, corresponding to the permittivity of beeswax particles and that of also flour particles, respectively (Section 3). Moreover, 6.1 is the permittivity of salt, that is a major pollutant for coastal localities, and thus important for consideration when developing indoor air cleaning apparatus. Therefore, this developed model, derived from the analytical work using the MATLAB software package, will aid in the optimisation of the ESP design, by maximising the probability that PM will be collected, before it can travel the full length of the reactor.

5.4. PRECIPITATION EFFICIENCY FOR ATMOSPHERIC AIR

Since the developed precipitator is targeted at air–cleaning operations in indoor environment such as hospitals, schools, and public and private buildings, it was felt critical to show how much of the PM2.5 already present in the ambient air could be precipitated. Thus, ambient laboratory air was used in the precipitator experiments.

The air pump, adjusted to its maximum setting of 16 ℓ/min with the help of an air flow meter, supplied air through a single 6 mm diameter flexible plastic tube to the sealed, 14 ℓ, container. The container was in turn, connected to the first part of the scaled-up electrostatic precipitator through four 6 mm diameter plastic tubes. At the other end of the reactor (exhaust), the portable aerosol particle spectrometer sampled air (at a rate of 1.2 ℓ/min) through path 1, Figure 5-5.

The procedure used in all atmospheric air tests (conducted using laboratory air of ambient humidity, temperature and pressure) is similar to that used for the original, 2-stage precipitation reactor described in Section 4.3. At first, the particle analyser started sampling with the air pump powered off. After 30 s, the air flow was initiated for another 4 min and 30 s in order for the background concentration of PM to stabilise, as the air in the reactor, container and tubing is enclosed, and the outside air could have quite a different amount of PM suspended in it. The electrostatic precipitator was then energised for 5 min. After that, the experiment ended, both HV supplies and the particle analyser being turned off, however the air pump was still left on for an additional ~15 min interval for the re-establishment of ambient PM levels, prior to the next test.

The efficiency of precipitation, η_p, was calculated from the ratio of the maximum number of particles, N_{max}, in the experiments time interval minus the number of particles in each 10 s interval, $N(t)$, that the particle analyser was registering data over the maximum number of particles: $(N_{max} - N(t))/N_{max}$. The efficiencies were calculated for stable, saturated, values of $N(t)$ during operation of the precipitation system and, as can be seen in Figure 5-14, efficiencies up to 1 min (5 measurements) after the maximum had to be excluded. Each particle size range had its own efficiency calculated for each test. Then, the average for the tests with the same energisation made, and their standard deviation, were calculated. The results, in the form of pass rate $(1 - \eta_p)\cdot 100\%$, are shown in Figure 5-13. The error bars represent ± one standard deviation. Each data point is the average of 3 individual tests.

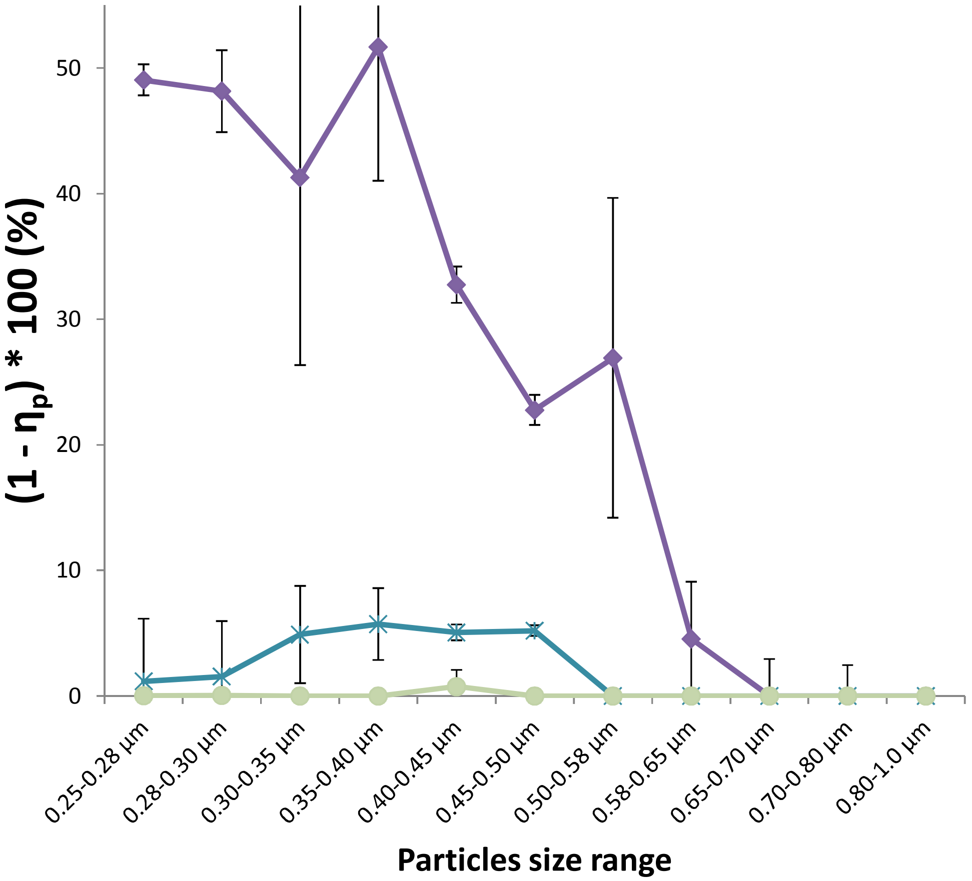

Figure 5-13: Precipitation tests in ambient air pass rate (1 - η_p) as a function of PM size range for different energisation modes. Energisation electrode (first stage) had HV impulses of +30 kV at 50 pps applied while collection stage (second stage) was energised with +17 kV dc. Blue crosses; only first stage energised, Purple diamonds; only second stage energised, Azure circles; both stages energised.

It was found that there was precipitation of PM even with the first (charging) stage off and with the second, collection, stage on at levels, below the corona ignition threshold. This occurs due to PM being charged by friction in the pneumatic delivery system (composed mainly of plastic parts). If only the charging stage was energised, the efficiency rose considerably, and if both stages were energised, the efficiency reached ~100%.

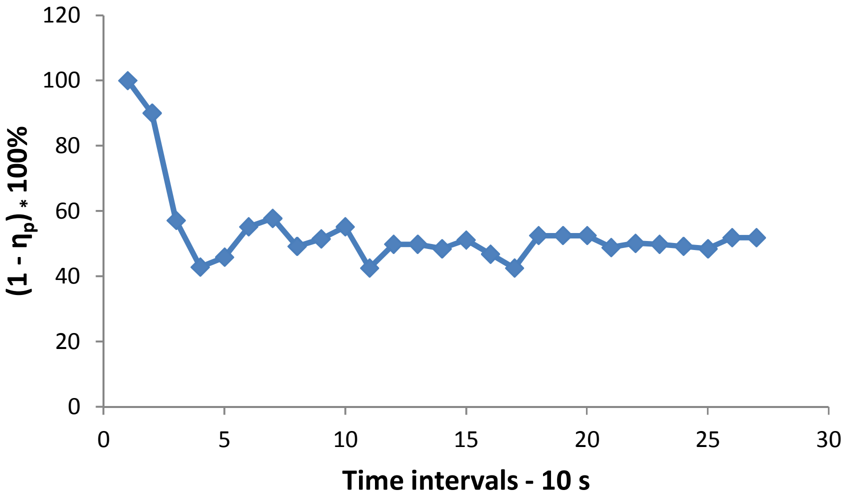

Figure 5-14: Number of particles counted per litter as a function of time, for the 250-280 nm PM size range when only the second stage is energised at +17 kV dc.

The number of particles during the tests was quite stable, as can be seen from Figure 5-14, which shows the results for the second stage only being energised at +17 kV dc, and for the (250-280) nm PM size range. This corresponds to the first purple diamond in Figure 5-13 above. This shows that experiments had a relatively stable concentration of particles at the outlet of the precipitation reactor. Thus, precipitation efficiency had low standard deviation.

5.5. PRECIPITATOR EFFICIENCY FOR BEESWAX CANDLES

Heavily laden air flow can reduce the efficiency of precipitators. Therefore, the efficiency of precipitation should be investigated with a higher concentration of PM. Fumes from beeswax candles were used as a source of additional particles. The results of this study showed almost always a reduced precipitation efficiency compared with experiments with ambient laboratory air (using the same energisation levels), peaking at ~99% when both stages were energised.

A new, direct, approach was taken for calculating the precipitation efficiency in the case of beeswax fumes. As the candles did not burn at the same rate, or could be unintentionally extinguished by the air flow, the particle analyser was turned on right at the beginning of the experiment, and turned off at the point when the candle(s) either burned out completely or were extinguished. Thus, there was no need to wait for a specific time interval prior to turning on or off the measuring equipment. The same procedure for efficiency calculation was used. The first 5 ratios of the concentration of PM to their maximum concentration, after the maximum occurred in the (250-280) nm range, were again disregarded from the calculation of the average efficiency of precipitation for any particular test.

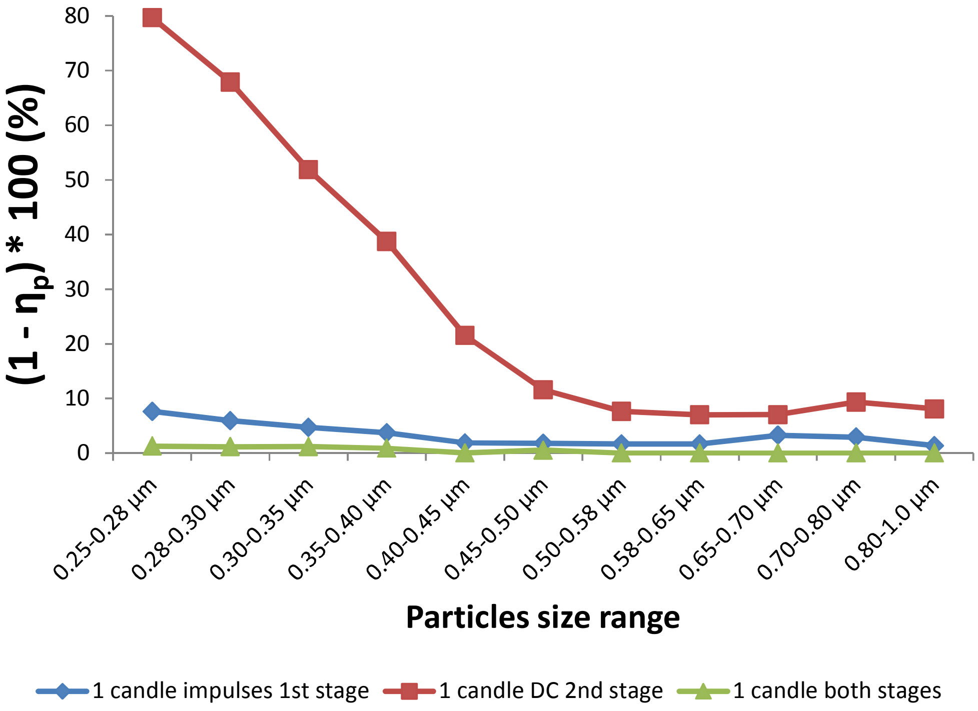

Figure 5-15: Precipitation tests with a single beeswax candle being burned inside the container. Pass rate (1 - η_p) is shown as a function of PM size range for different energisation modes. Energisation electrode (first stage) had HV impulses of +30 kV at 50 pps applied while collection stage (second stage) was energised with +17 kV dc. Blue diamonds; only first stage energised, Red squares; only second stage energised, Green triangles; both stages energised.

Figure 5-15 displays the pass rates ($1 - \eta_p$) for experiments with 1 beeswax candle, and for various energisation regimes. It was found that the highest precipitation efficiency was achieved for the combined energisation case, when HV impulses were applied to the first stage and dc voltage was applied to the second stage of the 2-stage reactor. In the tests with the original, 2-stage reactor (Chapter 4), and 1 cigarette burned, the results were similar, see Section 4.8.4 and (Mermigkas et al., 2013). To achieve an increased particulate loading, 2 and 3 candles were used for fume production. The results of tests with 2 and 3 beeswax candles are shown in Figure 5-16 and Figure 5-17, respectively.

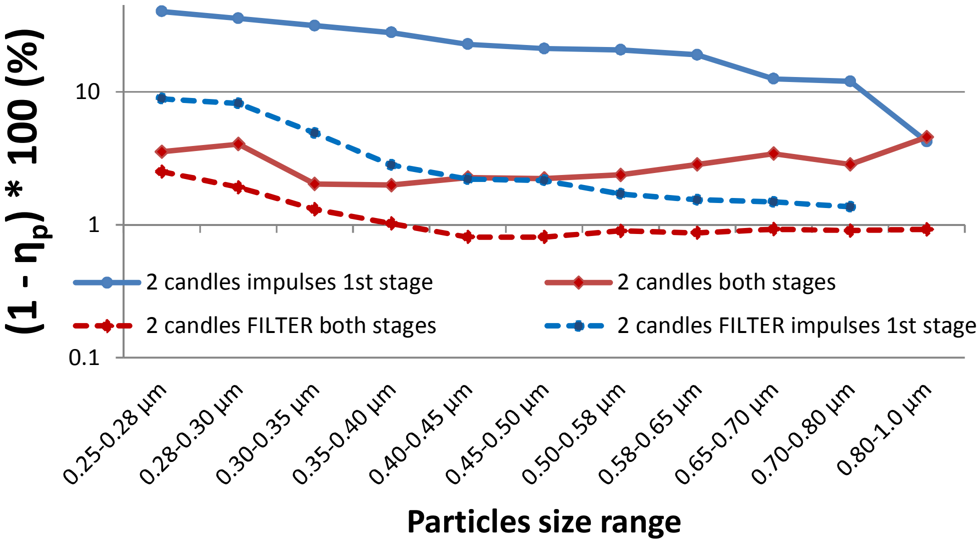

Figure 5-16: Pass rate (1 - ηp) for 2 beeswax candles burned for only the charging (first) stage energised (circles) and for all stages (diamonds) energised. Solid lines indicate that the mesh filter was not utilised, while dashed lines indicate the inclusion of the fine mesh filter. On the first stage HV impulses were applied having +30 kV amplitude at 50 pps. The second stage was energised with +17 kV dc. Blue circles, solid line; only first stage energised, no filter, Blue circles, dotted line; only first stage energised, filter inserted, Red squares, solid line; both stages energised, no filter, Red squares, dotted line; both stages energised, filter inserted.

Figure 5-16 displays that by burning 2 candles, the precipitation efficiency decreases considerably (by more than ~30% in the (250-280) nm size range) compared to burning 1 beeswax candle. By interposing the fine mesh filter between the particle analyser inlet and the 2nd stage output though, this difference is mitigated to only ~(1-1.5)% lower efficiencies compared with the 1 candle experiments (spread depends upon the particular particle size range).

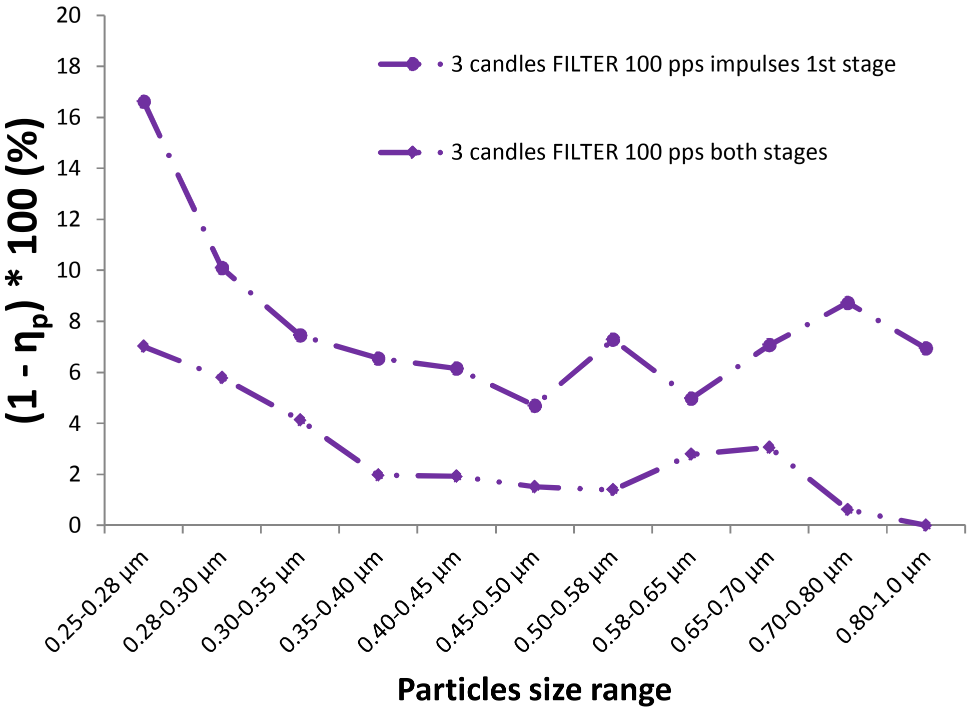

Figure 5-17: Pass rate (1 - η_p) for 3 beeswax candles burned for only the charging (first) stage energised (circles) and for all stages (diamonds) energised. The stainless steel fine mesh filter was always utilised. On the first stage HV impulses were applied having +30 kV amplitude at 100 pps. The second stage was energised with +17 kV dc. Purple circles; only first stage energised, filter inserted, Purple diamonds; both stages energised, filter inserted.

The use of burning candles in the tests made the use of the stainless-steel fine mesh filter imperative, so as to avoid the overloading of the portable laser spectrometer. The first stage of the reactor was energised at a higher pulse repetition rate of 100 pps as high (twice as high as with the experiments burning 1 or 2 candles), in order to further increase the efficiency of the PM charging process. As before (Section 5.4), it was found that the precipitation efficiency rises when all stages of the reactor are energised, compared with only the charging (first) stage being energised. A dip in efficiency due to heavy PM loading was also reported in (Beckers et al., 2013) for tests on soot.

5.6. COMPARISON WITH EMPIRICAL EFFICIENCY EQUATIONS

After completion of the precipitation experiments, it was deemed necessary to find the charged PM migration speed inside the reactor, based on the experimental results already acquired, so as to reveal important information on how to improve upon the reactor design and its precipitation efficiency.

A well-known and established empirical formula for the sizing and efficiency calculation of ESPs is the Deutsch-Anderson Equation (Deutsch, 1922, Anderson, 1925). A small correction (addition of a constant, *κ*) was subsequently made to the formula, thus deriving the widely-used Matts-Öhnfeldt empirical equation, (Matts and Öhnfeldt, 1964):

$$\boldsymbol{\eta_p = 1 - e^{-\left(\frac{A \cdot u_d}{Q}\right)^{\kappa}}} \tag{5.19}$$

where η_p is the precipitation efficiency, *Q* is the flow rate of the particle laden air, u_d is the effective migration velocity of the PM inside the reactor, *A* is the collection electrode area (or their sum if there are many), and *κ* is a constant ranging from 0.4-0.6, (Lin et al., 2012). This factor *κ* had to be added to the original Deutsch-Anderson equation, as the original equation was suggested based on ideal assumptions that are not applicable to the practical operating conditions of ESPs (Yoo et al., 1997, Kim and Lee, 1999, Park and Chun, 2002). In Section 5.4 and 5.5, the terminal velocities for various particles subjected to the long, ~100 μs, impulses, were calculated. If these values of velocities are used in (5.19), the precipitation efficiency is ~100% for practically all size ranges of PM. However, the efficiency of some particulate size ranges obtained in the experiments described in Section 5.5 is less than 100%. Thus, by using the Matts-Öhnfeldt empirical equation (5.19) together with the practical efficiencies measured, the effective migration velocities in the first stage of the reactor for different size ranges and PM loading have been obtained. These velocities are given in Table 5-1.

Table 5-1: Drift velocity (in mm/s) calculated from experimental data using the Matts-Öhnfeldt empirical equation (Matts and Öhnfeldt, 1964).

Particle diameter	ambient air	1 candle	2 candles
0.25-0.28 μm	**8.03**	**2.05**	**0.15**
0.45-0.50 μm	**2.91**	**6.32**	**0.58**
0.70-0.80 μm	*	**4.54**	**1.27**

* Denotes that η was 100% thus no terminal velocity could be calculated.

This approach indicates that an increase in the precipitation efficiency could potentially be achieved by increasing the PM terminal velocity inside the ESP reactor. This could be accomplished by increasing the impulsive pulse repetition rate. However, it was pointed out by (Lin et al., 2012) that equation (5.19), gives reduced efficiencies compared to the experimental results. Also, heavy loading of PM in the gas stream could considerably decrease the efficiency of precipitation, as shown in (Chang et al., 1998).

5.7. O_3 GENERATION AND MITIGATION

The presence of corona discharges in an ESP leads to the unavoidable production of some unwanted contaminants, one of the most important of which being ozone (O_3). Extra care should be taken to reduce the amount of ozone in the air flow when designing an ESP system, especially for indoor use. To this end, it was decided to use positive polarity for energisation of the ESP, despite the fact that negative energisation is proven in practice to yield better precipitation results, as it is also proven to produce much higher amounts of ozone and other contaminants compared to positive energisation (Asbach et al., 2005b). In addition, the second stage was energised with dc voltage below the corona ignition level, which reduces ozone production even further. The use of an Ecosensor A-21ZX ozone detector showed a level of 0.17 ppm at the outlet of the scaled-up, 2-stage, precipitation reactor. However, the use of a simple MnO_2 filter (flexible tubing filled with the catalyst in spheroid form) inserted in series at the ESP outlet, reduced the O_3 concentration to background levels (0.01-0.02 ppm).

5.8. CONCLUSIONS

A scaled-up, 2-stage ESP reactor was designed, developed and tested under impulsive, dc and combined (impulsive at the first stage, and dc at the second stage) energisation modes. The efficiency of precipitation reached ~100% for ambient laboratory air, while for heavily contaminated (with beeswax candle fumes) air, the level of precipitation was ~(99-100)%, being dependent upon the PM size range. These precipitation efficiencies are in good agreement with the ESP efficiencies obtained for cigarette smoke, achieved with the smaller scale, 2-stage ESP in Section 4. Power consumption and ozone production were minimised by the use of dc voltage below the corona threshold in the second (deflection and collection) stage of the reactor. This had the effect of reducing power consumption to ~60% compared to that of the smaller scale, 2-stage reactor described in Chapter 4 (from ~1.7 W for the smaller scale reactor to ~1 W in the scaled-up reactor), for the same precipitation efficiency.

Mathematical analysis showed that the migration velocities of PM could reach their terminal values in ~100 µs, thus the optimal pulse width applied on the first stage could be chosen. It was also established that PM terminal velocity is higher for particles with higher relative permittivity. The experimental results show that simultaneous use of impulsive energisation for charging, dc energisation at the second stage for deflection and collection, and an earthed, fine mesh filter at the output can effectively remove ~100% of PM or airborne PM from the air flow in a very energy efficient way. A similar ESP system, using higher flow rates, could be utilised in small-scale indoor air-cleaning applications. Thus, this technology could combat indoor air pollution, especially in larger cities were the problem is more prominent, and thus could passively improve people’s health and longevity.

6. CONCLUSIONS, DISCUSSION AND FUTURE WORK

There is widespread use of corona discharges in atmospheric air, utilising corona impulses for a broad range of practical applications such as destruction of noxious gases like NOx (Smulders et al., 1998, Yankelevich and Pokryvailo, 2002), disinfection of surfaces and microbiological decontamination (Timoshkin et al., 2012a, Li et al., 2013), as well as for the removal of PM from air (Mizuno, 2000, Mermigkas et al., 2013, Beckers et al., 2013). Impulsive corona discharges are produced by energising a treatment reactor with HV impulses of sufficient amplitude, and the subsequent production of transient, non-thermal plasma. The charged species produced by the corona discharge not only can charge the airborne PM, but also can destroy chemical molecules and kill any microorganisms present. The physics and chemistry behind impulsive corona discharges have been studied thoroughly, as in (Blom, 1997) and (Kim, 2004), and the findings of such research can aid in the development and optimisation of practical applications involving plasmas.

The present research work was extensively focused on the investigation and utilisation of impulsive coronas in ambient air, in order to remove PM2.5 from the air flow. The results of the current work were published in the peer-reviewed journal “IEEE Transactions on Plasma Science” (Mermigkas et al., 2012, Mermigkas et al., 2013, Mermigkas et al., 2014), and presented at IEEE international conferences.

There is growing concern regarding the dangers that PM2.5 pose to human health, as well as the environment in general, thus legislativen acts have been put into force globally, in order to mitigate their effects by reducing their emission in the first place (European Parliament and Council of the European Union, 2008, USEPA, 2013b). Thus, novel techniques should be developed in order to comply with the new legislation, and to mitigate the PM2.5 problem. This research work focused on the development of a new precipitation technology, including both single and double stage reactors of different scales. The main aim was to improve the precipitation efficiency of PM2.5, and to reduce the power consumption of the ESP process. In the case of the single stage reactor developed, nanosecond impulses were superimposed on dc voltage. In the case of the 2-stage reactors developed, their first stage was supplied with microsecond duration voltage impulses, and was intended for particle charging, while their second stage was intended for deflection and collection of the already charged PM. The narrow impulses applied enable increased electric field levels inside the reactor, without the occurrence of electrical breakdown, which results in an increase in the charge acquired by airborne PM, and thus in an increased efficiency of the precipitation process (White, 1963). An additional advantage of the shorter impulses is the reduced energy consumption in comparison with dc energisation (Dinelli et al., 1991). The dc energisation level applied in the deflection and collection stage of the 2-stage ESP was kept below the corona inception voltage, or very close to it, so as to minimise energy consumption. The obtained results show that, in the case of double-stage reactors, this approach reduced the energy requirements in comparison with the single-stage reactor in agreement with (White, 1963). In addition to the above, the selection of positive polarity for the energisation of the reactor keeps O_3 and NOx concentrations at low levels (Asbach et al., 2005a). In the case of the scaled-up reactor, O_3 levels were monitored, and the results were published in (Mermigkas et al., 2014). When a MnO_2 filter was added to the outlet of the reactor, a reduction of O_3 concentration to background levels (0.01-0.02 ppm) was observed.

An important factor determining the level of efficiency achieved in an ESP is the saturated migration velocity that the PM passing through achieves. This velocity is strongly affected by the rate of charging of PM, which is a function of the dielectric permittivity and electrical conductivity of both the PM and the air in the inter-electrode space, as well as the particle concentration in the air flow, and the diameter of individual particles. The electric field was calculated in the space charge filled inter-electrode space, and the mobility of the charged particles was calculated (in this case positive ions, assumed to be constant as *E* field changes are comparatively small to effect a change in mobility). Thus, the charge induced on the particle was calculated, through induction and polarisation (field charging case). The diffusion charging mechanism was not taken into account because of time constraints and because it is insignificant for particles above 1 μm, which constitute a major fraction of PM2.5 which are considered in this research. A numerical calculation of particle velocity and position inside the reactor was conducted, using the MATLAB software package. Experimentally, the ESP efficiency was measured under various dc and impulsive energisation combinations, with different PM matter in the air flow, ranging from ambient air, to air-blown dusts and beeswax fumes. Empirical equations which are used in industry, including the Deutsch-Anderson and the Matts-Öhnfeldt equations, were utilised in order to obtain the particle velocities, which were compared with the analytically calculated values.

6.1. SINGLE STAGE REACTOR

During the initial stages of this project, a single-stage coaxial precipitator reactor was designed and constructed, and the effect of the superimposed dc and impulsive voltages on precipitation efficiency was examined. The reactor's central electrode was composed of an M3 threaded steel rod, and was intended to charge and deflect PM towards its earthed coaxial cylinder, which acted as a collection electrode. The reactor was designed to be compact, so that it could be used in small scale indoor air-cleaning applications, or readily incorporated into existing air cleaning systems. Precipitation of both coarse (flour) and fine (dolomite) particles has been examined, using different dc and impulsive voltages energisation combinations. Efficiency was calculated using the mass of PM collected after each experiment. All experiments were conducted at ambient temperature, pressure and humidity. The electric field distribution in the coaxial test cell with threaded energising electrode was obtained and analysed. *V-I* curves, breakdown voltage and corona inception voltages were obtained for corona discharges with and without air flow for fine particles, and without air flow for coarse particles, in order to find the operational limits and to optimize the energisation regime used in the precipitation reactors.

Initial experiments showed that superimposing negative impulses on negative dc voltage increases precipitation efficiency much further compared to superimposing positive impulses on positive dc voltage, while dc only energisation had similar precipitation efficiency outcomes. However, positive energisation was used in order to avoid excessive production of ozone and NOx gases, as this technology is intended for small scale, indoor, air-cleaning applications. Therefore, all experiments were conducted with positive HV energisation. Experiments with HV and coarse PM (flour) showed that ~80% efficiency was reached. A further increase in efficiency was achieved by superimposing HV nanosecond impulses on the dc energised HV electrode. For superposition of +26 kV impulses on +11 kV dc voltage, a precipitation efficiency of ~85% was reached. By further increasing the dc voltage beyond +11 kV, no further increase in the precipitation efficiency was achieved. This counter-intuitive fact could be explained if the particles had reached their saturation charge, even at lower energisation levels, or due to the removal of collected PM at higher energisation levels, due to occasional electrical breakdowns.

Precipitation experiments using fine particles (dolomite powder) showed that HV impulses did not affect the precipitation efficiency for low levels of dc voltage, in the case of combined energisation. Experimenting with +11 kV dc voltage only, and with a combination of +24 kV impulses superimposed on the +11 kV voltage produced almost identical results, the efficiency varying from 45% to 90% depending on the size range taken into consideration. When the impulses were combined with higher dc voltages (+15 kV and +16 kV dc) though, precipitation efficiency increased considerably, from 81% to 99.6%, again depending on the size range. The size range of (0.4-0.65) μm showed a dip (with fluctuations, though), that could be expected due to the gradual change of the dominant charging mechanism (from diffusion to field) in approximately that size range (Parker and Institution of Electrical Engineers, 2003). For particles >4 μm, the combined energisation always resulted in an increased precipitation efficiency compared to only dc energisation. In terms of absolute numbers, ~100% precipitation efficiencies were achieved only for size ranges >2.5 μm. In conclusion, it was shown that for the single stage reactor developed, that sub-μs impulses superimposed on dc voltage can increase the precipitation efficiency. The results of this research work were published in (Mermigkas et al., 2012) in the IEEE Transactions on Plasma Science.

6.2. DOUBLE STAGE PRECIPITATION SYSTEM

Airborne particulate matter, in particular those particles less than 2.5 μm in diameter, are at the forefront of attention due to the potential health and environmental issues they can create. Particulate matter in the (0.1-1) μm diameter range is the hardest to collect, thus showing decreased efficiencies compared to both larger and smaller (ultrafine) PM size fractions. In order to increase the efficiency of collection of the PM1 range, a 2-stage ESP has been designed and built, utilizing HV impulses for particle charging (stage 1), and dc voltage for particle collection (stage 2). Precipitation efficiencies were obtained using different energisation regimes, namely with only the first stage energised, only the second stage energised, and with both stages energised, which correspond to impulsive only, dc only and combined energisation.

The double stage ESP design was based on that of the single stage reactor, utilising a wider outer cylinder diameter to accommodate for higher air flow rates, for possible small scale, indoor, air cleaning applications. Its operational capabilities were experimentally determined, thus corona inception voltage was measured, with and without airflow, and with particle laden air flow, while *I(V)* curves were determined in the presence and absence of air flow inside the reactor. By undertaking these tests, it was possible to know the energisation margins for the reactors safe use, and to select the energisation voltage for the subsequent experiments. An impulse generator that produced ~35 kV impulses of ~175 μs duration was connected to the first stage of the reactor through a pulse forming circuit. Experiments conducted with both stages energised showed a greater precipitation efficiency compared with the second stage only being energised (with only dc voltage).

A similar reactor to the first stage of the 2-stage one was also built, having a side opening for open shutter photographs of corona discharges to be taken. It was shown that luminous corona was present, even for the microsecond impulsive energisation (+25 kV at 50 pps).

Since particle resistivity is a critical factor in precipitation efficiency (Dinelli et al., 1991, Hall, 1990, Nelson and Salasoo, 1987), it was decided to design and build a powder resistivity measuring device, in order to characterise the resistance of various powders. It is also shown that for higher particle resistivities the increase in efficiency achieved by impulsive energisation was greater, in agreement with (Misaka et al., 1996). Therefore, a device having a 1 mm inter-electrode gap was used to measure the bulk resistivity of powders. The relative dielectric permittivity of bulk PM was measured by the use of a Video Bridge 2160.

In terms of analytical work, the electric field in the inter-electrode space (taking into account also the space charge present) and the particle charging inside the coaxial precipitation topology were studied and fitting formulas were presented. The mobilities of the positive ions drifting in the inter-electrode space were also calculated by fitting an analytically derived *V-I* curve to the experimental *V-I* datapoints, using the software package “MATLAB”. The electrical conductivities and relative dielectric permittivities of both the PM and the air in the inter-electrode space were shown to affect the particle charging process. The surface (conduction) and polarisation charge as a function of time on the surface of a particle of known diameter were analytically calculated, and fitting formulas were derived and presented. The charge acquired by a particle due to field charging is the arithmetic sum of these 2 types of charge. An investigation of PM charging and migration velocities achieved was conducted by varying the electrical properties of both the PM and the air in the inter-electrode space. Diffusion charging was not taken into account as it was beyond the scope of the current research.

Particles up to 25 nm in diameter were monitored by equipping the particle analyser with a 1320/1365 Nanocheck module. However, when the average size of the particulate matter reached the upper or lower limits, the module was mostly saturated, and did not produce meaningful results. In addition, due to its principle of operation, it tended to be overloaded by charged PM, and thus it was deemed necessary to insert an earthed, fine stainless-steel filter after the ESP's outlet. This filter resulted in much higher precipitation efficiencies without any additional power requirements. Through the utilisation of the Nanocheck module, it was also shown that the overall ESP efficiency increases when both stages are energised, compared to the case when only dc voltage is applied to the second stage.

Experimentally, with the first stage of the reactor energised by +25 kV impulses, it was demonstrated that by increasing the pulse repetition rate from 10 pps to 125 pps, the efficiency also increases, from ~60% to ~95%. When only energising the second stage with dc voltage, below the corona ignition threshold, the same tendency as with the single stage reactor was demonstrated: there were particles precipitated. When corona ignition levels were surpassed, a sharp increase in precipitation efficiency was demonstrated. From a voltage threshold however, the increase in the efficiency is very low, even for large increases in dc energisation voltage, as was shown in Figure 4-36 (17 kV and 18 kV dc). In particular, dc voltage levels from +12 kV to +15 kV, the efficiency was ~(20-25)%, which means that precipitation occurs without any corona current, as can be seen in Figure 4-31. At +16 kV dc the efficiency increases to ~(25-30)%, probably due to some sub-μs corona current present (at +16.6 kV dc, currents of a few μA were measured, and this was regarded as the corona inception voltage). When both stages were energised, the efficiency could reach ~100% for ambient air tests, and ~(97-100)% for cigarette smoke tests, depending upon the particle size range under consideration. These efficiencies were calculated for +25 kV impulses at 50 pps at the first stage, and +17 kV dc at the second stage. Between the 2-stages at such energisation voltages, the second stage exhibited higher power consumption. Thus, it is speculated that lower power consumption could be achieved via an increase in the pulse repetition rate at the first stage, since the dc voltage at the second stage could then be reduced, for the same efficiency levels to be achieved. The addition of the earthed, fine mesh stainless-steel filter after the exhaust of the reactor boosted the precipitation efficiency without increasing the reactor's power consumption.

An important consideration in the reactors design was the power consumed, thus a comparison was made with the single-stage reactor. Impulses chosen for analysis were those with the highest observed magnitudes, so as to have a worst case scenario for the energy consumption. Even so, the calculated power consumption was similar to that in industrial precipitators and other indoor air-cleaning units.

Since the second reactor stage had a corona onset level of ~16.6 kV dc, the power losses at voltages below that level are considered to be zero. When the voltage reaches +17 kV dc, then the calculated power consumption is 1.24 W. Taking into consideration the air flow rate of 16 ℓ/min, the volumetric energy consumed by the second stage is 1.29 Wh/m^3. Comparing this to the first stage at a repetition rate of 50 pulses per second, the energy per unit volume is 0.49 Wh/m^3. Combining these 2 results, the total volumetric energy consumption is 1.78 Wh/m^3. By increasing the pulse repetition rate to 125 pps, the energy consumed per unit volume in the first stage reaches 1.22 Wh/m^3.

In conclusion, experiments conducted with the double-stage reactor, with the addition of an earthed, fine mesh stainless steel filter (without any mechanical sieving occurring) after its exhaust, can capture the greatest amount of PM from the air flow. The results of this research work were published in in the IEEE Transactions on Plasma Science (Mermigkas et al., 2013).

6.3. SCALED-UP DOUBLE STAGE PRECIPITATOR SYSTEM

Experiments were conducted with a scaled-up, 2-stage reactor, when only the first (charging) stage was energised with microsecond impulses, when only the second (collection) stage was energised with dc voltage, and with both stages on (combined energisation). The ESP efficiency could reach ~100% for ambient air experiments, while for beeswax fumes the efficiency reached ~(99-100)%, depending on the particle size range under consideration. The levels of efficiency achieved agree with experiments with cigarette smoke conducted with the smaller scale, double-stage precipitator reactor in chapter 4. O_3 generation and energy consumption were kept at minimum levels by the use of positive energisation voltage, and voltages below the corona ignition threshold at the second stage. Numerically, this resulted in ~60% of the power consumed by the smaller scale, 2-stage reactor, Section 4.9, for the same efficiencies achieved (fall from ~1.71 W to ~1 W).

Analytical work on the PM migration velocity inside the first stage of the reactor showed that terminal velocity was achieved in ~100 µs, therefore optimization of the pulse width was possible. It was also found that particulate terminal migration velocity was faster the higher the particle dielectric permittivity. Experiments showed that simultaneous energisation of both stages of the precipitation reactor, the first with +30 kV peak voltage impulses with ~500 µs FWHM duration, and the second with sub corona ignition dc voltage at +17 kV dc, and the insertion of an earthed, fine mesh stainless-steel filter after the precipitation outlet could remove ~100% of airborne particles in a very energy efficient way. A similar electrostatic precipitator, working under higher air flow rates though, could be a possible solution to air-cleaning applications for small indoor spaces. Therefore, the problem of indoor air quality, especially in densely populated areas, could find a possible solution using the present technology and thus improve people's health and their life expectancy. The results of this research work were published in the IEEE Transactions on Plasma Science (Mermigkas et al., 2014).

6.4. DISCUSSIONS

Unfortunately, the air flow rate could not be increased air flow rate beyond 16 ℓ/min. Instead, by increasing the size of the precipitator (successive reactors becoming wider), the air speed inside the reactors was reduced, which corresponded to a subsequent increase in efficiency. In addition, the pulse repetition rate was increased by a factor of 10 and further, by the use of a different trigatron design, including the use of interchangeable electrodes to change the inter-electrode gap length inside the trigatron.

The energy consumed per unit volume of treated air (Wh/m^3) was comparable with industrial levels, as shown in Table 4-7. However, for the scaled-up reactor, the energy per unit volume increased due to very low air speeds. Increasing the air flow rate, and thus the air speed inside the precipitation reactor, is not expected to decrease precipitation efficiency according to the empirical Deutsch-Anderson and Matts-Öhnfeldt equations.

In terms of actual electrical power consumed (in W), this remained at very low levels in all precipitator designs. The dc and superimposed impulse regime yielded the highest output in terms of charge per pulse. Pulses applied to the double stage reactor, without any dc component, tended to have a lower charge output. For comparison, a summary of key reactor characteristics is provided in Table 6-1:

Table 6-1: Consolidated table of the various design, pneumatic energisation and energy consumption characteristics of the 3 reactor designs used in the course of this research.

Single stage		Double stage		Scaled-up double stage	
Flour	Dolomite	Atm	Cigarette	Atm	Beeswax
10 pps	50 pps	(10-125) pps	50 pps	50 pps	50 & 100 pps
16 ℓ/min	16 ℓ/min	16 ℓ/min	16 ℓ/min	16 ℓ/min	~3 ℓ/min
0.43 m/s	0.43 m/s	0.15 m/s	0.15 m/s	0.0094 m/s	0.0018 m/s
250 ns superimposed	250 ns superimposed	~400 µs just impulses	~400 µs just impulses	~500 µs just impulses	~500 µs just impulses
		12-18 kV dc	17 kV dc	17 kV dc	17 kV dc
+26; +29.3; +30.9 kV impulses	+24; +26; +32 kV impulses	+25 kV impulses	+25 kV impulses	+30 kV impulses	+30 kV impulses
0.6075 Wh/m^3	1.3 Wh/m^3		1.78 Wh/m^3	~5.3 Wh/m^3	~5.3 Wh/m^3
0.5832 W	1.251 W	~1.71 W	~1.71 W	~1 W	~1 W
3.52 µC/pulse	1.81 µC/pulse	0.513 µC/pulse	0.513 µC/pulse	~1 µC/pulse	~1 µC/pulse

6.5. FUTURE WORK

Regarding possible extensions of the current work, this could well follow different routes, including the following.

Calculation of the efficiency of precipitation as a function of powder resistivity, as impulsive energisation is shown to be better for high resistivity powders. By having the capability to measure resistivity of powders easily in the lab, identical experiments could be run with different particles, and conclusions could be drawn about efficiency as a function of powder resistivity in the reactors used. In total, five different materials were characterised, with a view to their use in future experiments. These materials were crushed charcoal powder, H600 dolomite powder, icing sugar, everyday talcum powder, and self-raising baking flour. More material, could of course, be selected.

For flour particles, the gravimetric factor (C-factor) that required by the particle analyser mass measurements (μg/m^3), was also experimentally defined. This is because the particle analyser cannot measure the powder mass and has to rely upon indirect light scattering methods. It thus assumes all particles to have a gravimetric factor of 1, leading to a systematic error in mass (in μg/m^3) measurements. In reality, this factor is dependent upon the PM density, refractive index and form, and once measured, can be applied retroactively to the stored data from the software, should further analysis, in terms of PM mass per volume, will be required in the future.

Experiments with increased flow rates, especially for the scaled-up reactor, in order to have higher air speeds inside, and also to be closer to the operational characteristics required for practical, air cleaning applications. According to (Blejan et al., 2010), high flow rates decrease precipitation efficiency and the threshold at which re-entrainment of particles increases to impractical levels should be determined. In this work, particles are blown by the air flow, and lowering the flow rate might mean that particles with different size range enter the reactor in experiments with different air flow rates.

Regarding the Scaled-up reactor, having used both ns and μs impulses to energise its first stage, it was decided that by using a pulse transformer, the impulses generated by the Blumlein could have been increased, since higher peak voltages were expected to be achieved without electrical breakdown occurring. Simulation in PSpice was successful, and results look promising, however building of the pulse transformer was above the timespan of this research project.

Another step would be to have a cleaning system for the ESP (perhaps flushing with water). For air-cleaning applications, however, this might be needed approximately every 2 weeks (Asbach et al., 2004).

Experiments with internal combustion engine (diesel) fumes would be of high importance, in order to have great amount of soot PM2.5, which constitutes a major pollutant, especially in large cities.

In terms of energisation, a pulse transformer could be utilized to multiply the Blumlein output for the scaled-up reactor (this was modelled successfully in PSpice). In terms of analytical work, the contribution to particle charging by diffusion charging could also be investigated.

However, the most important aspect to be investigated is the use of the analytical and simulation model developed to further optimise the system. By calculating the charge acquired by the PM, and depending upon the air flow, the trajectory and point of impact on the collection electrode could be estimated. This would help to optimise both the length of the reactor and the width of charging voltage impulse, depending on the efficiency that needs to be achieved and the size range of the air laden PM.

7. REFERENCES

2007. *IUPAC Glossary of Terms Used in Toxicology - Terms Starting with R* [Online]. 8600 Rockville Pike, Bethesda, MD 20894: National Institutes of Health, US Department of Health & Human Services. Available: http://sis.nlm.nih.gov/enviro/iupacglossary/glossaryr.html [Accessed 2014].

ADAMIAK, K. 2002. Rate of charging of spherical particles by monopolar ions in electric fields. *Industry Applications, IEEE Transactions on,* 38**,** 1001-1008.

ADAMIAK, K., ATRAZHEV, V. & ATTEN, P. 2005. Corona discharge in the hyperbolic point-plane configuration: direct ionization criterion versus an approximate formulations. *Dielectrics and Electrical Insulation, IEEE Transactions on,* 12**,** 1015-1024.

AIRNOW. 2014. *Today's AQI forecast* [Online]. USA: AirNow International. Available: http://www.airnow.gov/ [Accessed 25 Mar 2014].

ALLEN, N. L. 2004. 1 Mechanisms of air breakdown. *In:* HADDAD, A. & WARNE, D. F. (eds.) *Advances in High Voltage Engineering.* London, UK: Institution of Engineering and Technology.

ANANTH, K. P. & SHANNON, L. J. 1976. Evaluation of magnetics for fine particle control. Kansas City, MO.: Midwest Research Institute.

ANDERSON, E. 1925. Some factors and principles involved in the separation and collection of dust, mist, and fume from gases. *Transactions of the American Institute of Chemical Engineers,* 16**,** 69.

ANDERSON, H. R., BREMNER, S. A., ATKINSON, R. W., HARRISON, R. M. & WALTERS, S. 2001. Particulate matter and daily mortality and hospital admissions in the west midlands conurbation of the United Kingdom: associations with fine and coarse particles, black smoke and sulphate. *Occupational and Environmental Medicine,* 58**,** 504-510.

AQI. 2014. *Beijing Air Pollution: Real-time Air Quality Index (AQI)* [Online]. Beijing. Available: http://aqicn.org/city/beijing/ [Accessed].

ASBACH, C., KUHLBUSCH, T. A. J. & FISSAN, H. 2004. Development of an Electrostatic Partitioner for Highly Efficient Partitioning of Gas and Particles with Minimal Effect on the Gas Phase. *Aerosol Science and Technology,* 38**,** 322-329.

ASBACH, C., KUHLBUSCH, T. A. J. & FISSAN, H. 2005a. Effect of corona discharge on the gas composition of the sample flow in a Gas Particle Partitioner. *Journal of Environmental Monitoring,* 7**,** 877-882.

ASBACH, C., KUHLBUSCH, T. A. J. & FISSAN, H. 2005b. Investigation on the gas particle separation efficiency of the gas particle partitioner. *Atmospheric Environment,* 39**,** 7825-7835.

ATKINSON, R. W., FULLER, G. W., ANDERSON, H. R., HARRISON, R. M. & ARMSTRONG, B. 2010. Urban Ambient Particle Metrics and Health: A Time-series Analysis. *Epidemiology,* 21**,** 501-511 10.1097/EDE.0b013e3181debc88.

ATTEN, P. 2008. Collection of fine particles in electrostatic precipitators : influence of EHD induced agitation and of particles disintegration. *Proceedings Joint International Conference : "Materials for Electrical Engineering".* Bucarest, Romania.

AYRES, J. G. 2009. Long-term exposure to air pollution: effect on mortality. *COMEAP report.* COMEAP.

BÄCK, A. 2013. Some observations regarding the Matts-Öhnfeldt equation. *XIII International conference on Electrostatic Precipitation (ICESP XIII).* Bangalore, India.

BECCARIA, G. B. 1776. *Electtricismo Artificiale. English; A Treatise Upon Artificial Electricity [microform]: In which are Given Solutions of a Number of Interesting Electric Phoenomena, Hitherto Unexplained : to which is Added an Essay on the Mild and Slow Electricity which Prevails in the Atmosphere During Serene Weather*, J. Nourse.

BECKERS, F. J. C. M., HOEBEN, W. F. L. M., HUISKAMP, T., PEMEN, A. J. M. & VAN HEESCH, E. J. M. 2013. Pulsed Corona Demonstrator for Semi-Industrial Scale Air Purification. *Plasma Science, IEEE Transactions on,* 41**,** 2920-2925.

BECKETT, K. P., FREER-SMITH, P. H. & TAYLOR, G. 1998. Urban woodlands: their role in reducing the effects of particulate pollution. *Environmental Pollution,* 99**,** 347-360.

BEELEN, R., HOEK, G., VAN DEN BRANDT, P. A., GOLDBOHM, R. A., FISCHER, P., SCHOUTEN, L. J., JERRETT, M., HUGHES, E., ARMSTRONG, B. & BRUNEKREEF, B. 2008. Long-term effects of traffic-related air pollution on mortality in a Dutch cohort (NLCS-AIR study). *Environmental health perspectives,* 116**,** 196.

BEHALL, K. M., SCHOLFIELD, D. J. & HALLFRISCH, J. 1999. The Effect of Particle Size of Whole-Grain Flour on Plasma Glucose, Insulin, Glucagon and Thyroid-Stimulating Hormone in Humans. *Journal of the American College of Nutrition,* 18**,** 591-597.

BELL, M. L., EBISU, K., PENG, R. D., SAMET, J. M. & DOMINICI, F. 2009. Hospital admissions and chemical composition of fine particle air pollution. *American journal of respiratory and critical care medicine,* 179**,** 1115-1120.

BERNAL, J. L., JIMÉNEZ, J. J., DEL NOZAL, M. J., TORIBIO, L. & MARTÍN, M. T. 2005. Physico-chemical parameters for the characterization of pure beeswax and detection of adulterations. *European Journal of Lipid Science and Technology,* 107**,** 158-166.

BILLING, C. E. & WILDE, J. 1970. Handbook of Fabric Filter Technology. Volume I. Fabric Filter Systems Study. GCA Corp., Bedford, Mass. GCA Technology Div.

BISWAS, P. & WU, C. Y. 1998. Control of Toxic Metal Emissions from Combustors Using Sorbents: A Review. *Journal of the Air & Waste Management Association,* 48**,** 113-127.

BLEJAN, O., NOTINGHER, P. V., DUMITRAN, L. M., YOUNES, M., SAMUILA, A. & DASCALESCU, L. 2010. Experimental Study of the Corona Discharge in a Modified Coaxial Wire-Cylinder Electrostatic Precipitator. *Industry Applications, IEEE Transactions on,* 46**,** 3-8.

BLOM, P. P. M. 1997. *High-Power Pulsed Corona.* Doctor of Philosophy PhD Thesis, Technische Universiteit Eindhoven.

BMJ. *Pathophysiology* [Online]. Available: http://bestpractice.bmj.com/best-practice/monograph/1112/basics/pathophysiology.html [Accessed].

BÖHM, J. 1982. *Electrostatic precipitators,* Prague, Czechoslovakia, Elsevier Scientific Publishing Company.

BOLOGA, A., PAUR, H. R., SEIFERT, H. & WOLETZ, K. 2007. Novel Wet Electrostatic Precipitator for Sub-Micron Particles. *DustConf 2007.* Maastricht, The Netherlands.

BRITISH STANDARDS 1993. Workplace atmospheres. Size fraction definitions for measurement of airborne particles. *BS EN 481:1993, BS 6069-3.5:1993.* BSI.

BRITISH STANDARDS 1998. ISO general purpose metric screw threads — Selected sizes for screws, bolts and nuts. *BS ISO 262:1998.* London: BSI.

BRUNEKREEF, B., BEELEN, R., HOEK, G., SCHOUTEN, L., BAUSCH-GOLDBOHM, S., FISCHER, P., ARMSTRONG, B., HUGHES, E., JERRETT, M. & VAN DEN BRANDT, P. 2009. Effects of long-term exposure to traffic-related air pollution on respiratory and cardiovascular mortality in the Netherlands: the NLCS-AIR study. *Research report (Health Effects Institute)***,** 5-71; discussion 73-89.

BRUNEKREEF, B. & FORSBERG, B. 2005. Epidemiological evidence of effects of coarse airborne particles on health. *European Respiratory Journal,* 26**,** 309-318.

BUCK, J. & HAYT, W. 2001. *Engineering Electromagnetics*, McGraw-Hill International Edition.

BURNETT, R. T., BROOK, J., DANN, T., DELOCLA, C., PHILIPS, O., CAKMAK, S., VINCENT, R., GOLDBERG, M. S. & KREWSKI, D. 2000. ASSOCIATION BETWEEN PARTICULATE- AND GAS-PHASE COMPONENTS OF URBAN AIR POLLUTION AND DAILY MORTALITY IN EIGHT CANADIAN CITIES. *Inhalation Toxicology,* 12**,** 15-39.

CA.GOV. 2008. *Hazardous Ozone-Generating "Air Purifiers"* [Online]. CA, USA. Available: http://www.arb.ca.gov/research/indoor/ozone.htm [Accessed].

CALDERÓN-GARCIDUEÑAS, L., REED, W., MARONPOT, R. R., HENRIQUEZ-ROLDÁN, C., DELGADO-CHAVEZ, R., CALDERÓN-GARCIDUEÑAS, A., DRAGUSTINOVIS, I., FRANCO-LIRA, M., ARAGÓN-FLORES, M. & SOLT, A. C. 2004. Brain inflammation and Alzheimer's-like pathology in individuals exposed to severe air pollution. *Toxicologic Pathology,* 32**,** 650-658.

CALDERÓN-GARCIDUEÑAS, L., SOLT, A. C., HENRÍQUEZ-ROLDÁN, C., TORRES-JARDÓN, R., NUSE, B., HERRITT, L., VILLARREAL-CALDERÓN, R., OSNAYA, N., STONE, I. & GARCÍA, R. 2008. Long-term air pollution exposure is associated with neuroinflammation, an altered innate immune response, disruption of the blood-brain barrier, ultrafine particulate deposition, and accumulation of amyloid β-42 and α-synuclein in children and young adults. *Toxicologic Pathology,* 36**,** 289-310.

CHANG, J. S., LAWLESS, P. A. & YAMAMOTO, T. 1991. Corona discharge processes. *Plasma Science, IEEE Transactions on,* 19**,** 1152-1166.

CHANG, J. S., LOOY, P. C. & WEBSTER, C. 1998. The effects of dust loadings on the collections of fine particles by an electrostatic precipitator with DC or pulse energized prechargers. *Journal of Aerosol Science,* 29, Supplement 2**,** S1127-S1128.

CHEN, L. C. & LIPPMANN, M. 2009. Effects of Metals within Ambient Air Particulate Matter (PM) on Human Health. *Inhalation Toxicology,* 21**,** 1-31.

CHOWDHURI, P., MISHRA, A. K. & MCCONNELL, B. W. 1997. Volt-time characteristics of short air gaps under nonstandard lightning voltage waves. *Power Delivery, IEEE Transactions on,* 12**,** 470-476.

CHUNG, I. P. & DUNN-RANKIN, D. 1996. In Situ Light Scattering Measurements of Mainstream and Sidestream Cigarette Smoke. *Aerosol Science and Technology,* 24**,** 85-101.

CITEAIR. 2014. *Air Quality in Europe* [Online]. Available: http://www.airqualitynow.eu/ [Accessed].

CLACK, H. L. 2006. Mass Transfer within Electrostatic Precipitators:□ In-Flight Adsorption of Mercury by Charged Suspended Particulates. *Environmental Science & Technology,* 40**,** 3617-3622.

CLANCY, L., GOODMAN, P., SINCLAIR, H. & DOCKERY, D. W. 2002. Effect of air-pollution control on death rates in Dublin, Ireland: an intervention study. *The Lancet,* 360**,** 1210-1214.

COMMISSION OF THE EUROPEAN COMMUNITIES 2005. Thematic Strategy on air pollution. Brussels.

COORAY, V. 2014. *The Lightning Flash*, Institution of Engineering and Technology.

COTTRELL, F. G. 1911. The Electrical Precipitation of Suspended Particles. *Journal of Industrial & Engineering Chemistry,* 3**,** 542-550.

COULOMB, C. 1785a. Premier Mémoire sur l. *Électricité et le Magnétisme'Mém. Acad. R. Sci,* 88**,** 569-577.

COULOMB, C. A. 1785b. First memoir on electricity and magnetism. *A Source Book in Physics***,** 408-413.

COUNCIL OF THE EUROPEAN UNION 1996. Council Directive 96/62/EC of 27 September 1996 on ambient air quality assessment and management *Official J. Eur. Union,* L 296**,** 55-63.

COUNCIL OF THE EUROPEAN UNION 1997. 97/101/EC: Council Decision of 27 January 1997 establishing a reciprocal exchange of information and data from networks and individual stations measuring ambient air pollution within the Member States *Official J. Eur. Union,* L 35**,** 14-22.

COUNCIL OF THE EUROPEAN UNION 1999. Council Directive 1999/30/EC of 22 April 1999 relating to limit values for sulphur dioxide, nitrogen dioxide and oxides of nitrogen, particulate matter and lead in ambient air *Official J. Eur. Union,* L 163**,** 41-60.

CROWN. *Silicosis* [Online]. Available: http://www.hse.gov.uk/lung-disease/silicosis.htm [Accessed 2014].

CROWN 2011. *Controlling Airborne Contaminants at Work: A Guide to Local Exhaust Ventilation (LEV)*, Health and Safety Executive Books.

CROWN. 2014. *Protecting and enhancing our urban and natural environment to improve public health and wellbeing* [Online]. Gov.uk. Available: https://www.gov.uk/government/policies/protecting-and-enhancing-our-urban-and-natural-environment-to-improve-public-health-and-wellbeing/supporting-pages/international-european-and-national-standards-for-air-quality [Accessed].

DAVIS, W. T. 2000. *Air pollution engineering manual,* New York, John Wiley & Sons Inc.

DE LEEUW, F. & HORÁLEK, J. 2009. Assessment of the health impacts of exposure to PM2.5 at a European level. *In:* MITIGATION, E. T. C. O. A. P. A. C. C. (ed.). Bilthoven, The Netherlands: The European Topic Centre on Air and Climate Change (ETC/ACC)

DEFRA 2007. The air quality strategy for England, Scotland, Wales and Northern Ireland. London: Department for Environment, Food & Rural Affairs.

DEFRA 2010. Valuing the Overall Impacts of Air Pollution. London: Department for Environment, Food & Rural Affairs.

DEFRA. 2013. *What is the Daily Air Quality Index?* [Online]. Available: https://uk-air.defra.gov.uk/air-pollution/daqi?view=more-info [Accessed].

DEFRA. 2014a. *Industrial Emissions Directive* [Online]. Department for Environment, Food & Rural affairs. Available: http://www.defra.gov.uk/industrial-emissions/eu-international/industrial-emissions-directive/ [Accessed].

DEFRA. 2014b. *UK-AIR: Air Information Resource* [Online]. Available: http://uk-air.defra.gov.uk/ [Accessed].

DENAT, A. 2006. High field conduction and prebreakdown phenomena in dielectric liquids. *Dielectrics and Electrical Insulation, IEEE Transactions on,* 13**,** 518-525.

DEUTSCH, W. 1922. Bewegung und Ladung der Elektrizitätsträger im Zylinderkondensator. *Annalen der Physik,* 373**,** 335-344.

DIETZ, P. W. & PETERS, P. H. 1986. *Method and apparatus for ramped pulsed burst powering of electrostatic precipitators*. US 06/681,170.

DINELLI, G., BOGANI, V. & REA, M. 1991. Enhanced precipitation efficiency of electrostatic precipitators by means of impulse energization. *Industry Applications, IEEE Transactions on,* 27**,** 323-330.

DONALDSON, K., MILLS, N., MACNEE, W., ROBINSON, S. & NEWBY, D. 2005. Role of inflammation in cardiopulmonary health effects of PM. *Toxicology and Applied Pharmacology,* 207**,** 483-488.

DOONAN, P. & REYNOLDS, J. 2007. SO3 Control and Wet ESP Technology. *100th Annual Conference and Exhibition of the Air and Waste Management Association 2007* Pittsburgh, Pennsylvania: Curran Associates, Inc. .

ELDER, A. C. P., GELEIN, R., FINKELSTEIN, J. N., COX, C. & OBERDÖRSTER, G. 2000. Pulmonary Inflammatory Response To Inhaled Ultrafine Particles Is Modified By Age, Ozone Exposure, And Bacterial Toxin. *Inhalation Toxicology,* 12**,** 227-246.

EPA, U. S. 2004. Air Quality Criteria for Particulate Matter (Final Report, Oct 2004). Washington, DC: U.S. Environmental Protection Agency.

EPA, U. S. 2009. Integrated Science Assessment for Particulate Matter (Final Report). Washington, DC: U.S. Environmental Protection Agency.

ESTCOURT, V. F. & FRISCH, N. W. 1980. Measuring and Reporting Fly Ash Resistivity. *Power Apparatus and Systems, IEEE Transactions on,* PAS-99**,** 573-581.

EUROPA.EU. 2013a. *Euro VI - emissions from heavy duty vehicles* [Online]. European Commission. Available: http://ec.europa.eu/enterprise/sectors/automotive/environment/eurovi/ [Accessed].

EUROPA.EU. 2013b. *Smoke-free environments* [Online]. Available: http://ec.europa.eu/health/tobacco/smoke-free_environments/index_en.htm [Accessed].

EUROPA.EU. 2014a. *Air Quality Standards* [Online]. European commission. Available: European commission [Accessed].

EUROPA.EU. 2014b. *Regulations, Directives and other acts* [Online]. European Union. Available: http://europa.eu/eu-law/decision-making/legal-acts/index_en.htm [Accessed].

EUROPEAN COMMISION 2013. EXECUTIVE SUMMARY OF THE IMPACT ASSESSMENT. Brussels.

EUROPEAN COMMISION. 2014. *Environment-Air* [Online]. Available: http://ec.europa.eu/environment/air/index_en.htm [Accessed].

EUROPEAN COMMISSION 2013. ANNEXES to the Proposal for a DIRECTIVE OF THE EUROPEAN PARLIAMENT AND OF THE COUNCIL on the reduction of national emissions of certain atmospheric pollutants and amending Directive 2003/35/EC. Brussels.

EUROPEAN PARLIAMENT & COUNCIL OF THE EUROPEAN UNION 2000. Directive 2000/69/EC of the European Parliament and of the Council of 16 November 2000 relating to limit values for benzene and carbon monoxide in ambient air *Official J. Eur. Union,* L 313**,** 12-21.

EUROPEAN PARLIAMENT & COUNCIL OF THE EUROPEAN UNION 2002a. DECISION No 1600/2002/EC OF THE EUROPEAN PARLIAMENT AND OF THE COUNCIL of 22 July 2002 laying down the Sixth Community Environment Action Programme. *Official Journal of the European Communities,* L 242**,** 1-15.

EUROPEAN PARLIAMENT & COUNCIL OF THE EUROPEAN UNION 2002b. Decision No 1600/2002/EC of the European Parliament and of the Council of 22 July 2002 laying down the Sixth Community Environment Action Programme *Official J. Eur. Union,* L 242**,** 1-15.

EUROPEAN PARLIAMENT & COUNCIL OF THE EUROPEAN UNION 2002c. Directive 2002/3/EC of the European Parliament and of the Council of 12 February 2002 relating to ozone in ambient air. *Official J. Eur. Union,* L 67**,** 14-30.

EUROPEAN PARLIAMENT & COUNCIL OF THE EUROPEAN UNION 2004. Directive 2004/107/EC of the European Parliament and of the Council of 15 December 2004 relating to arsenic, cadmium, mercury, nickel and polycyclic aromatic hydrocarbons in ambient air *Official J. Eur. Union,* L 23**,** 3-16.

EUROPEAN PARLIAMENT & COUNCIL OF THE EUROPEAN UNION 2008. Directive 2008/50/EC of the European parliament and of the council of 21 May 2008 on ambient air quality and cleaner air for Europe. *Official J. Eur. Union,* vol. L 152**,** 1-44.

EUROPEAN PARLIAMENT & COUNCIL OF THE EUROPEAN UNION 2009. Regulation (EC) No 595/2009 of the European Parliament and of the Council of 18 June 2009 on type-approval of motor vehicles and engines with respect to emissions from heavy duty vehicles (Euro VI) and on access to vehicle repair and maintenance information and amending Regulation (EC) No 715/2007 and Directive 2007/46/EC and repealing Directives 80/1269/EEC, 2005/55/EC and 2005/78/EC. *Official J. Eur. Union,* L 188**,** 1-13.

EUROPEAN PARLIAMENT & COUNCIL OF THE EUROPEAN UNION 2010. DIRECTIVE 2010/75/EU OF THE EUROPEAN PARLIAMENT AND OF THE COUNCIL of 24 November 2010 on industrial emissions (integrated pollution prevention and control) (Recast). *Official J. Eur. Union,* L 334**,** 17-119.

FEI, X., ZHONGYANG, L., BO, W., LINA, W., XIANG, G., MENGXIANG, F. & KEFA, C. 2008. Electrostatic Capture of PM2.5 Emitted from Coal-fired Power Plant by Pulsed Corona Discharge Combined with DC Agglomeration. *XI International conference on Electrostatic Precipitation (ICESP XI).* Hangzhou, China.

FL SMIDTH. 2011. *Coromax™ mrk. IV* [Online]. Valby: FL Smidth. Available: http://www.flsmidth.com/en-US/Products/Product+Index/All+Products/Air+Pollution+Control/Electrostatic+Precipitator/Coromax [Accessed 21 October 2013].

FREDERICK, E. R. 1978. Electrostatic effects in fabric filtration: Triboelectric measurements and bag performance (annotated data). Research Triangle Park, N.C Springfield, Va.

FRIDMAN, A. 2008. *Plasma Chemistry,* New York, Cambridge University Press.

FRIDMAN, A., CHIROKOV, A. & GUTSOL, A. 2005. Non-thermal atmospheric pressure discharges. *Journal of Physics D: Applied Physics,* 38**,** R1.

GAVETT, S. H., MADISON, S. L., DREHER, K. L., WINSETT, D. W., MCGEE, J. K. & COSTA, D. L. 1997. Metal and Sulfate Composition of

Residual Oil Fly Ash Determines Airway Hyperreactivity and Lung Injury in Rats. *Environmental Research,* 72**,** 162-172.

GERLOFS-NIJLAND, M. E., DORMANS, J. A. M. A., BLOEMEN, H. J. T., LESEMAN, D. L. A. C., BOERE, A. J. F., KELLY, F. J., MUDWAY, I. S., JIMENEZ, A. A., DONALDSON, K., GUASTADISEGNI, C., JANSSEN, N. A. H., BRUNEKREEF, B., SANDSTRÖM, T., VAN BREE, L. & CASSEE, F. R. 2007. Toxicity of Coarse and Fine Particulate Matter from Sites with Contrasting Traffic Profiles. *Inhalation Toxicology,* 19**,** 1055-1069.

GILBERT, W. 1900. De Magnete (London, 1600). *Translation: Chiswick Press, London,* English edition prepared by Sylvanus P. Thomson.

GIVEN, M. J., TIMOSHKIN, I. V., WILSON, M. P., MACGREGOR, S. J. & LEHR, J. M. 2011. A novel design for a multistage corona stabilized closing switch. *Dielectrics and Electrical Insulation, IEEE Transactions on,* 18**,** 983-989.

GOARD, P. R. C. 1982. A probe technique for determining the electrical potentials in an ionized corona field for the measurement of resistivity of electrostatically precipitated deposits. *Journal of Applied Physics,* 53**,** 1437-1444.

GOLDBERG, M. S., BURNETT, R. T., BAILAR III, J. C., BROOK, J., BONVALOT, Y., TAMBLYN, R., SINGH, R., VALOIS, M.-F. & VINCENT, R. 2001. The association between daily mortality and ambient air particle pollution in Montreal, Quebec: 2. Cause-Specific Mortality. *Environmental Research,* 86**,** 26-36.

GOREE, J. 1994. Charging of particles in a plasma. *Plasma Sources Science and Technology,* 3**,** 400.

GRAEDEL, T. E. & FRANEY, J. P. 1975. Field measurements of submicron aerosol washout by snow. *Geophysical Research Letters,* 2**,** 325-328.

GRAHAME, T. & SCHLESINGER, R. 2010. Cardiovascular health and particulate vehicular emissions: a critical evaluation of the evidence. *Air Quality, Atmosphere & Health,* 3**,** 3-27.

GRAHAME, T. J. & SCHLESINGER, R. B. 2005. Evaluating the Health Risk from Secondary Sulfates in Eastern North American Regional Ambient Air Particulate Matter. *Inhalation Toxicology,* 17**,** 15-27.

GRAHAME, T. J. & SCHLESINGER, R. B. 2007. Health Effects of Airborne Particulate Matter: Do We Know Enough to Consider Regulating Specific Particle Types or Sources? *Inhalation Toxicology,* 19**,** 457-481.

GREENFIELD, S. M. 1957. RAIN SCAVENGING OF RADIOACTIVE PARTICULATE MATTER FROM THE ATMOSPHERE. *Journal of Meteorology,* 14**,** 115-125.

GRIMM AEROSOL TECHNIK GMBH & CO. KG. 2010. *Aerosol spectrometer and dust monitor, series 1.108 and 1.109* [Online]. D-83404 Ainring, Germany: GRIMM Aerosol Technik. Available: http://cires1.colorado.edu/jimenez-group/Manuals/Grimm_OPC_Manual.pdf [Accessed].

GUITARD, C. F. 1850. Condensation by Electricity. *The Mechanics' Magazine,* 53**,** 346.

HALL, H. J. 1990. History of pulse energization in electrostatic precipitation. *Journal of Electrostatics,* 25**,** 1-22.

HAPPO, M. S., HIRVONEN, M.-R., HÄLINEN, A. I., JALAVA, P. I., PENNANEN, A. S., SILLANPÄÄ, M., HILLAMO, R. & SALONEN, R. O. 2008. Chemical Compositions Responsible for Inflammation and Tissue Damage in the Mouse Lung by Coarse and Fine Particulate Samples from Contrasting Air Pollution in Europe. *Inhalation Toxicology,* 20**,** 1215-1231.

HARRISON, R. M., SMITH, D. J. T. & KIBBLE, A. J. 2004. What is responsible for the carcinogenicity of PM2.5? *Occupational and Environmental Medicine,* 61**,** 799-805.

HAUTANEN, J., KILPELÄINEN, M., KAUPPINEN, E. I., LEHTINEN, K. & JOKINIEMI, J. 1995. Electrical Agglomeration of Aerosol Particles in an Alternating Electric Field. *Aerosol Science and Technology,* 22**,** 181-189.

HEERING, P. 1992. On Coulomb's inverse square law. *American Journal of Physics,* 60**,** 988-994.

HIGNETT, E. T. 1967. Particle-charge magnitudes in electrostatic precipitation. *Electrical Engineers, Proceedings of the Institution of,* 114**,** 1325-1328.

HINDS, W. C. 1982. *Aerosol Technology: Properties, Behavior, and Measurement of Airborne Particles*, John Wiley & Sons.

HOHLFELD, M. 1824. Das niederschlagen des rauches durch elektricität. *Kastner Archiv. für die gesammte Naturlehlre,* 2**,** 205-206.

HOLLAND, M., WATKISS, P., PYE, S., DE OLIVEIRA, A. & VAN REGEMORTER, D. 2005. Cost-Benefit Analysis of the Thematic Strategy on Air Pollution Didcot, OX11 0QR, United Kingdom: AEA Technology Environment.

HORI, T. 1953. *Studies on fogs in relation to fog-preventing forest,* Institute of Low Temperature Science, Hokkaido University.

HOUSE OF COMMONS - ENVIRONMENTAL AUDIT COMMITTEE 2010. Air Quality - Fifth Report of Session 2009–10. London.

HOWARD, W. H. 1914. Electrical fume precipitation at Garfield. *Transactions of the American Institute of Mining Engineers,* 49**,** 540-560.

HOWATSON, A. M. 1976. *An Introduction to Gas Discharges,* Oxford : Robert Maxwell, M.C., Pergamon Press.

HUGHES, J. F. 1997. *Electrostatic particle charging: industrial and health care applications*, Research Studies Press.

IEEE 1984. IEEE Standard Criteria and Guidelines for the Laboratory Measurement and Reporting of Fly Ash Resistivity. *IEEE Std 548-1984.*

IRANI, R. R. & FONG, W. S. 1961. MEASUREMENTS OF PARTICLE SIZE DISTRIBUTION OF FLOUR. *Cereal Chemistry,* 38**,** 67-75.

JANTUNEN, M., FERNANDES, E. O., CARRER, P. & KEPHALOPOULOS, S. 2011. *Promoting Actions for Healthy Indoor Air (IAIAQ),* Luxembourg, European Commission Directorate General for Health and Consumers.

JARIYASOPIT, N., MCINTOSH, M., ZIMMERMANN, K., AREY, J., ATKINSON, R., CHEONG, P. H.-Y., CARTER, R. G., YU, T.-W., DASHWOOD, R. H. & MASSEY SIMONICH, S. L. 2013. Novel Nitro-PAH Formation from Heterogeneous Reactions of PAHs with NO2, NO3/N2O5, and OH Radicals: Prediction, Laboratory Studies, and Mutagenicity. *Environmental Science & Technology,* 48**,** 412-419.

JAWOREK, A., KRUPA, A. & CZECH, T. 2007. Modern electrostatic devices and methods for exhaust gas cleaning: A brief review. *Journal of Electrostatics,* 65**,** 133-155.

JONATHAN, S. G. & KENNETH, H. Y. 2014. Systematic Application of Background Oriented Schlieren for Shock-Boundary Layer Interaction Study. *52nd Aerospace Sciences Meeting.* National Harbor, Maryland, USA: American Institute of Aeronautics and Astronautics.

JONES, T. B. 2005. *Electromechanics of Particles*, Cambridge University Press.

KABATA-PENDIAS, A. 2011. *Trace Elements in Soils and Plants*, CRC Press.

KAGOSHIMA PREFECTURAL ADVISORS. 2013. *Air Pollution* [Online]. Kagoshima, Japan. Available: https://kagoshimajet.com/living/health/air-pollution/ [Accessed 2016].

KANAZAWA, S., OHKUBO, T., NOMOTO, Y. & ADACHI, T. 1993. Submicron particle agglomeration and precipitation by using a bipolar charging method. *Journal of Electrostatics,* 29**,** 193-209.

KARVOSENOJA, N., TAINIO, M., KUPIAINEN, K., TUOMISTO, J. T., KUKKONEN, J. & JOHANSSON, M. 2008. Evaluation of the emissions and uncertainties of PM 2.5 originated from vehicular traffic and domestic wood combustion in Finland. *Boreal environment research,* 13.

KENTECH INSTRUMENTS LTD. Blumlein. Available: http://www.kentech.co.uk/PDF/Blumlein_paper.pdf [Accessed 3rd July 2011].

KETCHUK, M. M., WALSH, A. & FORTUNE, O. F. 1984. Fundamental strategies for cleaning reverse-air baghouses. *Proceedings, Fourth Symposium on the Transfer and Utilization of Particulate Control Technology.* U.S. Environmental Protection Agency, Research Triangle Park, NC.

KHALIFA, M. 1990. *High-voltage engineering: theory and practice*, Marcel Dekker, Inc.

KIM, H.-H. 2004. Nonthermal Plasma Processing for Air-Pollution Control: A Historical Review, Current Issues, and Future Prospects. *Plasma Processes and Polymers,* 1**,** 91-110.

KIM, J.-H., LEE, H.-S., KIM, H.-H. & OGATA, A. 2010. Electrospray with electrostatic precipitator enhances fine particles collection efficiency. *Journal of Electrostatics,* 68**,** 305-310.

KIM, S. H. & LEE, K. W. 1999. Experimental study of electrostatic precipitator performance and comparison with existing theoretical prediction models. *Journal of Electrostatics,* 48**,** 3-25.

KO, F. W. S., TAM, W., WONG, T. W., LAI, C. K. W., WONG, G. W. K., LEUNG, T. F., NG, S. S. S. & HUI, D. S. C. 2007. Effects of air pollution on asthma hospitalization rates in different age groups in Hong Kong. *Clinical & Experimental Allergy,* 37**,** 1312-1319.

KOIZUMI, Y., KAWAMURA, M., TOCHIKUBO, F. & WATANABE, T. 2000. Estimation of the agglomeration coefficient of bipolar-charged aerosol particles. *Journal of Electrostatics,* 48**,** 93-101.

KOLMOGOROV, A. N. 1941. On the logarithmically normal law of distribution of the size of particles under pulverisation. *Doklady Akademii Nauk SSSR,* 31**,** 99-101.

KRÄMER, U., HERDER, C., SUGIRI, D., STRASSBURGER, K., SCHIKOWSKI, T., RANFT, U. & RATHMANN, W. 2010. Traffic-related air pollution and incident type 2 diabetes: results from the SALIA cohort study. *Environmental health perspectives,* 118**,** 1273-1279.

KUFFEL, E., ZAENGL, W. S. & KUFFEL, J. 2000. *High Voltage Engineering: Fundamentals*, Newnes.

KUMAR, K. & MANSOUR, A. 2002. Wet ESP for controlling sulfuric acid plume following an SCR system. *Presented at the ICAC Forum.* Houston, TX.

LADEN, F., NEAS, L. M., DOCKERY, D. W. & SCHWARTZ, J. 2000. Association of fine particulate matter from different sources with daily mortality in six US cities. *Environmental health perspectives,* 108**,** 941-947.

LADEN, F., SCHWARTZ, J., SPEIZER, F. E. & DOCKERY, D. W. 2006. Reduction in fine particulate air pollution and mortality: extended follow-up of the Harvard Six Cities study. *American journal of respiratory and critical care medicine,* 173**,** 667-672.

LAXEN, D., MOORCROFT, S., MARNER, B., LAXEN, K., BOULTER, P., BARLOW, T., HARRISON, R. & HEAL, M. 2010. PM2.5 in the UK. *Scoping study: PM2.5 concentrations, sources, and regulatory impacts of new policy framework.* Edinburgh: Sniffer.

LEGENDRE, M., BARTOLI, J., SHMAKOVA, L., JEUDY, S., LABADIE, K., ADRAIT, A., LESCOT, M., POIROT, O., BERTAUX, L., BRULEY, C., COUTÉ, Y., RIVKINA, E., ABERGEL, C. & CLAVERIE, J.-M. 2014. Thirty-thousand-year-old distant relative of giant icosahedral DNA viruses with a pandoravirus morphology. *Proceedings of the National Academy of Sciences,* 111**,** 4274-4279.

LERNER, B. J. 1995. Particulate Wet Scrubbing: The Efficiency Scam. *AIR AND WASTE MANAGEMENT ASSOCIATION International specialty conference, Particulate matter: health and regulatory issues* Pittsburgh, Pennsylvania: AIR AND WASTE MANAGEMENT ASSOCIATION - PUBLICATIONS.

LI, M. & CHRISTOFIDES, P. D. 2006. Collection efficiency of nanosize particles in a two-stage electrostatic precipitator. *Industrial & engineering chemistry research,* 45**,** 8484-8491.

LI, S., TIMOSHKIN, I. V., MACLEAN, M., MACGREGOR, S. J., WILSON, M. P., GIVEN, M. J., ANDERSON, J. G. & TAO, W. 2013. Steady-State Corona Discharges in Atmospheric Air for Cleaning and Decontamination. *Plasma Science, IEEE Transactions on,* 41**,** 2871-2878.

LIN, G.-Y., CHEN, T.-M. & TSAI, C.-J. 2012. A Modified Deutsch-Anderson Equation for Predicting the Nanoparticle Collection Efficiency of Electrostatic Precipitators. *Aerosol and Air Quality Research,* 12**,** 697-706.

LIQIAN, W., JINING, W., WEIMIN, Z., JIANRONG, F. & LISHENG, J. 1996. An Energy Management System for Electrostatic Precipitator. *VI*

International conference on Electrostatic Precipitation (ICESP VI). Budapest, Hungary.

LIU, Y., TIMOSHKIN, I., WILSON, M., GIVEN, M. & MACGREGOR, S. Charging and dynamics of fine air-borne particles in impulsive electric fields. 2014 IEEE International Power Modulator and High Voltage Conference (IPMHVC), 1-5 June 2014 2014. 435-438.

LIU, Y., TIMOSHKIN, I. V., MACGREGOR, S. J., WILSON, M. P., GIVEN, M. J. & WANG, T. Analysis of influences of dielectric and electrical properties on particle charging. 2013 19th IEEE Pulsed Power Conference (PPC), 16-21 June 2013 2013. 1-6.

LLORENS, J. F., FERNÁNDEZ-TURIEL, J. L. & QUEROL, X. 2001. The fate of trace elements in a large coal-fired power plant. *Environmental Geology,* 40**,** 409-416.

LODGE, S. O. J. 1886. The Electrical Deposition of Dust and Smoke: With Special Reference to the Collection of Metallic Fume, and to a Possible Purification of the Atmosphere. *J. Soc. Chem. Ind.,* 5**,** 572.

LOEB, L. B. 1955. *Basic processes of gaseous electronics,* Berkeley, CA, Univ of California Press.

LOEB, L. B. 1965. *Electrical Coronas, Their Basic Physical Mechanisms*, University of California Press.

LOHMANN, U. & MENSAH, A. A. 2013. Aerosol Particles. *In:* CHANGE, I. F. A. A. C. (ed.) *Atmosphärenphysik.* Zürich: ETH Zürich.

LOHR, V. I. & PEARSON-MIMS, C. H. 1996. Particulate matter accumulation on horizontal surfaces in interiors: Influence of foliage plants. *Atmospheric Environment,* 30**,** 2565-2568.

LOWKE, J. J. & D'ALESSANDRO, F. 2003. Onset corona fields and electrical breakdown criteria. *Journal of Physics D: Applied Physics,* 36**,** 2673.

MACGREGOR, S. J., KOUTSOUBIS, J. M. & TURNBULL, S. M. 1998. The design and operation of a compact high-voltage, high pulse repetition frequency trigger generator. *Measurement Science and Technology,* 9**,** 1899.

MACGREGOR, S. J., TURNBULL, S. M., TUEMA, F. A. & FARISH, O. The application of corona stabilised breakdown to repetitive switching. Pulsed Power '96, IEE Colloquium on, 13 Mar 1996 1996. 21/1-21/3.

MADDEN, M. C., RICHARDS, J. H., DAILEY, L. A., HATCH, G. E. & GHIO, A. J. 2000. Effect of Ozone on Diesel Exhaust Particle Toxicity in Rat Lung. *Toxicology and Applied Pharmacology,* 168**,** 140-148.

MARTIN, G. 1928. Chemical engineering applied to the flow of industrial gases, steam, water and liquid chemicals, including the pneumatic transport of powders and granulated materials. *Crosby, Lockwood & Son, London*.

MASTROPIETRO, R. A. 1997. The use of Treatment Time and Emissions Instead of SCA and Efficiency for Sizing Electrostatic Precipitators. *EPRI-DOE-EPA mega-symposium.* Washington DC, USA.

MATTS, S. & ÖHNFELDT, P. O. 1964. Efficient gas cleaning with SF electrostatic precipitators. *AB Svenska Fläktfabriken Review,* 6-7**,** 91-110.

MCDONNELL, W. F., NISHINO-ISHIKAWA, N., PETERSEN, F. F., CHEN, L. H. & ABBEY, D. E. 2000. Relationships of mortality with the fine and coarse fractions of long-term ambient PM10 concentrations in nonsmokers. *Journal of exposure analysis and environmental epidemiology,* 10**,** 427-436.

MCKENNA, J. D., TURNER, J. H. & MCKENNA, J. P. 2008. *Fine Particle (2.5 microns) Emissions: Regulations, Measurement, and Control*, Wiley.

MCPHERSON, E. G., NOWAK, D. J. & ROWNTREE, R. A. 1994. Chicago's urban forest ecosystem: results of the Chicago Urban Forest Climate Project. Radnor, PA: U. S. Department of Agriculture, Forest Service, Northeastern Forest Experiment Station.

MEDLEY, A. J., WONG, C.-M., THACH, T. Q., MA, S., LAM, T.-H. & ANDERSON, H. R. 2002. Cardiorespiratory and all-cause mortality after restrictions on sulphur content of fuel in Hong Kong: an intervention study. *The Lancet,* 360**,** 1646-1652.

MEEK, J. M. & CRAGGS, J. D. 1954. *Electrical breakdown of gases*, Clarendon Press.

MERMIGKAS, A. C., TIMOSHKIN, I. V., MACGREGOR, S. J., GIVEN, M. J., WILSON, M. P. & WANG, T. 2012. Superposition of DC Voltage and

Submicrosecond Impulses for Energization of Electrostatic Precipitators. *Plasma Science, IEEE Transactions on,* 40**,** 2388 - 2394.

MERMIGKAS, A. C., TIMOSHKIN, I. V., MACGREGOR, S. J., GIVEN, M. J., WILSON, M. P. & WANG, T. 2013. Removal of Fine and Ultrafine Particles From Air by Microelectrostatic Precipitation. *Plasma Science, IEEE Transactions on,* 41**,** 2842-2850.

MERMIGKAS, A. C., TIMOSHKIN, I. V., MACGREGOR, S. J., GIVEN, M. J., WILSON, M. P. & WANG, T. 2014. Impulsive Corona Discharges for Fine Particles Precipitation in a Coaxial Topology. *Plasma Science, IEEE Transactions on,* 42**,** 3089-3094.

MILLS, N. L., DONALDSON, K., HADOKE, P. W., BOON, N. A., MACNEE, W., CASSEE, F. R., SANDSTROM, T., BLOMBERG, A. & NEWBY, D. E. 2009. Adverse cardiovascular effects of air pollution. *Nat Clin Pract Cardiovasc Med,* 6**,** 36-44.

MILLS, N. L., TÖRNQVIST, H., ROBINSON, S. D., GONZALEZ, M., DARNLEY, K., MACNEE, W., BOON, N. A., DONALDSON, K., BLOMBERG, A. & SANDSTROM, T. 2005. Diesel exhaust inhalation causes vascular dysfunction and impaired endogenous fibrinolysis. *Circulation,* 112**,** 3930-3936.

MISAKA, T., AKASANA, A., OURA, T., HIRANO, M. & ASANO, H. 1996. Electrostatic Precipitator Combined Pulse Charging Section with Moving Electrode Section for High Resistivity Dust. *VI International conference on Electrostatic Precipitation (ICESP VI).* Budapest, Hungary.

MITTERMAYER, C. & STEININGER, A. 1999. On the determination of dynamic errors for rise time measurement with an oscilloscope. *Instrumentation and Measurement, IEEE Transactions on,* 48**,** 1103-1107.

MIZUNO, A. 2000. Electrostatic precipitation. *Dielectrics and Electrical Insulation, IEEE Transactions on,* 7**,** 615-624.

MÖLLER, C. 1884. *Gas- und Dampffilter, röhrenförmiges*. Kupferhammer bei Brackwede, Deutschland patent application.

MORABIA, A., AMSTISLAVSKI, P. N., MIRER, F. E., AMSTISLAVSKI, T. M., EISL, H., WOLFF, M. S. & MARKOWITZ, S. B. 2009. Air Pollution and Activity During Transportation by Car, Subway, and Walking. *American Journal of Preventive Medicine,* 37**,** 72-77.

MORROW, R. 1997. The theory of positive glow corona. *Journal of Physics D: Applied Physics,* 30**,** 3099.

NAHRWOLD, R. 1878. Über die Luftelectricität. *Annalen der Physik,* 241**,** 460-499.

NASA. 2012. *SCIENCE FOCUS: DUST TO DUST* [Online]. Available: http://disc.sci.gsfc.nasa.gov/education-and-outreach/additional/science-focus/ocean-color/sahara_dust.shtml [Accessed].

NATIONAL RESEARCH COUNCIL 2004. *Damp Indoor Spaces and Health,* Washington DC, The National Academies Press.

NELSON, J. K. & SALASOO, L. 1987. The Impact of Pulse Energization on Electrostatic Precipitation Peformance. *Electrical Insulation, IEEE Transactions on,* EI-22**,** 657-675.

NONHEBEL, G., COLVIN, J., PATTERSON, H. S. & WHYTLAW-GRAY, R. 1927. The coagulation of smokes and the theory of Smoluchowski. *Proceedings of the Royal Society of London. Series A,* 116**,** 540-553.

NORDBERG, M., DUFFUS, J. & TEMPLETON, D. M. 2004. Glossary of terms used in toxicokinetics (IUPAC Recommendations 2003). *Pure Appl. Chem.,* 76**,** 1033-1082.

NOWAK, D. J., CRANE, D. E. & STEVENS, J. C. 2006. Air pollution removal by urban trees and shrubs in the United States. *Urban Forestry & Urban Greening,* 4**,** 115-123.

NYAYATE, M. & PENDHARKAR, J. 2012. Measurement of Dielectric constant of unprocessed Indian Bee Wax, using IC 555 timer and measurement of change in its resistivity with Temperature. *Golden research thoughts,* 1**,** 1-4.

OBERDÖRSTER, G., CELEIN, R. M., FERIN, J. & WEISS, B. 1995. Association of Particulate Air Pollution and Acute Mortality: Involvement of Ultrafine Particles? *Inhalation Toxicology,* 7**,** 111-124.

OHLIGER, T. 2013. AIR AND NOISE POLLUTION. European Parliament.

OMYA UK LTD. 2005. *MICRODOL H600 product information* [Online]. Derby, UK: Omya Northern Europe. Available: http://www.bentleychemicals.co.uk/files/dat_microdol_h600-info.pdf [Accessed].

ONDOV, J. M. & WEXLER, A. S. 1998. Where Do Particulate Toxins Reside? An Improved Paradigm for the Structure and Dynamics of the Urban Mid-Atlantic Aerosol. *Environmental Science & Technology,* 32**,** 2547-2555.

OSTRO, B., BROADWIN, R., GREEN, S., FENG, W.-Y. & LIPSETT, M. 2006. Fine particulate air pollution and mortality in nine California counties: results from CALFINE. *Environmental health perspectives,* 114**,** 29-33.

PARK, J.-H. & CHUN, C.-H. 2002. An improved modelling for prediction of grade efficiency of electrostatic precipitators with negative corona. *Journal of Aerosol Science,* 33**,** 673-694.

PARKER, K. & INSTITUTION OF ELECTRICAL ENGINEERS 2003. *Electrical Operation of Electrostatic Precipitators*, Institution of Engineering and Technology (IET).

PARKER, K. R. 1997. *Applied Electrostatic Precipitation*, Springer.

PARKINSON, G. A. 1989. A hot and dirty future for baghouses. *Chemical engineering,* 96**,** 30-35.

PATTERSON, H. S., WHYTLAW-GRAY, R. & CAWOOD, W. 1929a. The Process of Coagulation in Smokes. *Proceedings of the Royal Society of London. Series A,* 124**,** 502-522.

PATTERSON, H. S., WHYTLAW-GRAY, R. & CAWOOD, W. 1929b. The structure and electrification of smoke particles. *Proceedings of the Royal Society of London. Series A,* 124**,** 523-532.

PAULING, L. 1932. THE NATURE OF THE CHEMICAL BOND. IV. THE ENERGY OF SINGLE BONDS AND THE RELATIVE ELECTRONEGATIVITY OF ATOMS. *Journal of the American Chemical Society,* 54**,** 3570-3582.

PAUTHENIER, M. & MOREAU-HANOT, M. 1932. La charge des particules sphériques dans un champ ionisé. *J. Phys. Radium,* 3**,** 590-613.

PEARSON ELECTRONICS INC. 2012. *Pearson current monitor model 6585* [Online]. Palo Alto, CA: Pearson Electronics, Inc. Available: http://www.pearsonelectronics.com/pdf/6585.pdf [Accessed 2011].

PEEK, F. W. 1915. *Dielectric phenomena in high voltage engineering,* New York [etc.], McGraw-Hill Book Company, Inc.

PENG, R. D., BELL, M. L., GEYH, A. S., MCDERMOTT, A., ZEGER, S. L., SAMET, J. M. & DOMINICI, F. 2009. Emergency admissions for cardiovascular and respiratory diseases and the chemical composition of fine particle air pollution. *Environmental health perspectives,* 117**,** 957.

PENNEY, G. W. 1937. A New Electrostatic Precipitator. *American Institute of Electrical Engineers, Transactions of the,* 56**,** 159-128.

PODLINSKI, J., NIEWULIS, A., SHAPOVAL, V. & MIZERACZYK, J. 2011. Electrohydrodynamic secondary flow and particle collection efficiency in a one-sided spike-plate type electrostatic precipitator. *Dielectrics and Electrical Insulation, IEEE Transactions on,* 18**,** 1401-1407.

POPE, C. A. 2007. Mortality Effects of Longer Term Exposures to Fine Particulate Air Pollution: Review of Recent Epidemiological Evidence. *Inhalation Toxicology,* 19**,** 33-38.

POPE, C. A., EZZATI, M. & DOCKERY, D. W. 2009. Fine-Particulate Air Pollution and Life Expectancy in the United States. *New England Journal of Medicine,* 360**,** 376-386.

POPE III, C. A., BURNETT, R. T., THUN, M. J., CALLE, E. E., KREWSKI, D., ITO, K. & THURSTON, G. D. 2002. Lung cancer, cardiopulmonary mortality, and long-term exposure to fine particulate air pollution. *Jama,* 287**,** 1132-1141.

RADKE, L. F., HOBBS, P. V. & ELTGROTH, M. W. 1980. Scavenging of Aerosol Particles by Precipitation. *Journal of Applied Meteorology,* 19**,** 715-722.

RAETHER, H. 1964. *Electron avalanches and breakdown in gases*, Butterworths London.

RAIZER, Y. P. 1991. *Gas discharge physics*, Springer-Verlag.

RAIZER, Y. P., ALLEN, J. E. & KISIN, V. I. 2012. *Gas Discharge Physics*, Springer.

RAJAN, R. & PANDIT, A. B. 2001. Correlations to predict droplet size in ultrasonic atomisation. *Ultrasonics,* 39**,** 235-255.

RÄSÄNEN, J. V., YLI-PIRILÄ, P., HOLOPAINEN, T., JOUTSENSAARI, J. & PASANEN, P. 2012. Soil drought increases atmospheric fine particle capture efficiency of norway spruce. *Boreal environment research,* 17.

REISS, R., ANDERSON, E. L., CROSS, C. E., HIDY, G., HOEL, D., MCCLELLAN, R. & MOOLGAVKAR, S. 2007. Evidence of Health Impacts of Sulfate-and Nitrate-Containing Particles in Ambient Air. *Inhalation Toxicology,* 19**,** 419-449.

RESOURCES, T. N. M. B. O. G. M. 2014. *Fly Ash from New Mexico Coals* [Online]. Socorro, NM. Available: http://geoinfo.nmt.edu/geoscience/projects/horizon_flyash.html [Accessed].

REYES, V. & TAARNING, C. 2008. *Pulse Generating System for Electrostatic Precipitator*. PCT/DK2005/000686.

RIEHLE, C. & LÖFFLER, F. 1993. Reflections on similarity laws concerning particle transport in electrical precipitators. *Powder Technology,* 77**,** 201-208.

ROHMANN, H. 1923. Methode zur Messung der Größe von Schwebeteilchen. *Zeitschrift für Physik,* 17**,** 253-265.

SAMS, H. W. & CO 1973. *Handbook of electronic tables & formulas*, Sams.

SARNAT, J. A., MARMUR, A., KLEIN, M., KIM, E., RUSSELL, A. G., SARNAT, S. E., MULHOLLAND, J. A., HOPKE, P. K. & TOLBERT, P. E. 2008. Fine particle sources and cardiorespiratory morbidity: an application of chemical mass balance and factor analytical source-apportionment methods. *Environmental health perspectives,* 116**,** 459-466.

SCHLESINGER, R. B. 2007. The Health Impact of Common Inorganic Components of Fine Particulate Matter (PM2.5) in Ambient Air: A Critical Review. *Inhalation Toxicology,* 19**,** 811-832.

SCHMIDT, W. A. & ANDERSON, E. 1938. Electrical precipitation. *Electrical Engineering,* 57**,** 332-338.

SEATON, A., GODDEN, D., MACNEE, W. & DONALDSON, K. 1995. Particulate air pollution and acute health effects. *The Lancet,* 345**,** 176-178.

SEINFELD, J. H. & PANDIS, S. N. 1998. *Atmospheric chemistry and physics: from air pollution to climate change*, Wiley.

SEPPÄLÄ, T. & SKROCH, R. Ion blast precipitator. XII International conference on Electrostatic Precipitation (ICESP XII), 2011 Nürnberg, Germany.

SHAW, G. 1986. Size distribution of atmospheric aerosols at Ross Island. *Antarct. JUS,* 21**,** 241-242.

SIGMOND, R. S. 1982. Simple approximate treatment of unipolar space□charge□dominated coronas: The Warburg law and the saturation current. *Journal of Applied Physics,* 53**,** 891-898.

SMIC 1971. Inadvertent Climate Modification, Report of the Study of Man's Impact on Climate (SMIC). Cambridge, MA: MIT Press.

SMULDERS, E. H. W. M., VAN HEESCH, B. E. J. M. & VAN PAASEN, S. S. V. B. 1998. Pulsed power corona discharges for air pollution control. *Plasma Science, IEEE Transactions on,* 26**,** 1476-1484.

SRIVASTAVA, R. K., JOZEWICZ, W. & SINGER, C. 2001. SO2 scrubbing technologies: A review. *Environmental Progress,* 20**,** 219-228.

STIER, P., FEICHTER, J., KINNE, S., KLOSTER, S., VIGNATI, E., WILSON, J., GANZEVELD, L., TEGEN, I., WERNER, M., BALKANSKI, Y., SCHULZ, M., BOUCHER, O., MINIKIN, A. & PETZOLD, A. 2005. The aerosol-climate model ECHAM5-HAM. *Atmos. Chem. Phys.,* 5**,** 1125-1156.

TAINIO, M., TUOMISTO, J. T., PEKKANEN, J., KARVOSENOJA, N., KUPIAINEN, K., PORVARI, P., SOFIEV, M., KARPPINEN, A., KANGAS, L. & KUKKONEN, J. 2010. Uncertainty in health risks due to anthropogenic primary fine particulate matter from different source types in Finland. *Atmospheric Environment,* 44**,** 2125-2132.

TESLA, N. 1888. A new system of alternate current motors and transformers. *AIEE Transactions,* 5**,** 305-327.

THOMPSON, J. R., MUELLER, P. W., FLÜCKIGER, W. & RUTTER, A. J. 1984. The effect of dust on photosynthesis and its significance for roadside plants. *Environmental Pollution Series A, Ecological and Biological,* 34**,** 171-190.

THOMSON, E. 1922. The nature of tribo-electricity or electricity of friction and other kindred matters. *American Institute of Electrical Engineers, Journal of the,* 41**,** 342-345.

TIMOSHKIN, I. V. 2010a. Part 1. Breakdown in Gases - Lecture 7. *Lecture notes for High Voltage Technology EE920.* Glasgow, UK: The University of Strathclyde.

TIMOSHKIN, I. V. 2010b. Part 1. Breakdown in Gases - Lectures 3,4. *Lecture notes for High Voltage Technology EE920.* Glasgow, UK: The University of Strathclyde.

TIMOSHKIN, I. V. 2010c. Part 1. Breakdown in Gases - Lectures 5,6. *Lecture notes on High Voltage Technology EE920.* Glasgow, UK: The University of Strathclyde.

TIMOSHKIN, I. V. 2010d. Tutorial 1. *Lecture notes on High Voltage Technology EE920.* Glasgow, UK: The University of Strathclyde.

TIMOSHKIN, I. V., MACLEAN, M., WILSON, M. P., GIVEN, M. J., MACGREGOR, S. J., TAO, W. & ANDERSON, J. G. 2012a. Bactericidal Effect of Corona Discharges in Atmospheric Air. *Plasma Science, IEEE Transactions on,* 40**,** 2322-2333.

TIMOSHKIN, I. V., MERMIGKAS, A. C., MACGREGOR, S. J., GIVEN, M. J., WILSON, M. P. & WANG, T. Analysis of particle charging mechanism for optimisation of precipitation efficiency. Power Modulator and High Voltage Conference (IPMHVC), 2012 IEEE International, 3-7 June 2012 2012b. 114-117.

TINSLEY, B. A., ROHRBAUGH, R. P., HEI, M. & BEARD, K. V. 2000. Effects of Image Charges on the Scavenging of Aerosol Particles by Cloud Droplets and on Droplet Charging and Possible Ice Nucleation Processes. *Journal of the Atmospheric Sciences,* 57**,** 2118-2134.

TRICHEL, G. W. 1938. The Mechanism of the Negative Point to Plane Corona Near Onset. *Physical Review,* 54**,** 1078-1084.

TSAI, F. C., APTE, M. G. & DAISEY, J. M. 2000. An exploratory analysis of the relationship between mortality and the chemical composition of airborne particulate matter. *Inhalation Toxicology,* 12**,** 121-136.

UNGER, L., BOULAUD, D. & BORRA, J. P. 2004. Unipolar field charging of particles by electrical discharge: effect of particle shape. *Journal of Aerosol Science,* 35**,** 965-979.

USEPA. 2012. *National Ambient Air Quality Standards (NAAQS)* [Online]. US-Environmental Protection Agency. Available: http://www.epa.gov/air/criteria.html [Accessed].

USEPA 2013a. *Electrostatic Precipitator (ESP) Training Manual*, BiblioGov.

USEPA. 2013b. *History of the National Ambient Air Quality Standards for Particulate Matter During the Period 1971-2012* [Online]. Available: http://www.epa.gov/ttn/naaqs/standards/pm/s_pm_history.html [Accessed].

VESILIND, P. A., PEIRCE, J. J. & WEINER, R. F. 1988. *Environmental engineering*, Butterworths.

VINTHER, F. A. H. & NIELSEN, O. J. 1984. A literature review on wet deposition. Roskilde: Risø National Laboratory.

WESSELS, A., BIRMILI, W., ALBRECHT, C., HELLACK, B., JERMANN, E., WICK, G., HARRISON, R. M. & SCHINS, R. P. F. 2010. Oxidant Generation and Toxicity of Size-Fractionated Ambient Particles in Human Lung Epithelial Cells. *Environmental Science & Technology,* 44**,** 3539-3545.

WHITBY, K. T. 1978. The physical characteristics of sulfur aerosols. *Atmospheric Environment (1967),* 12**,** 135-159.

WHITE, H. J. 1951. Particle Charging in Electrostatic Precipitation. *American Institute of Electrical Engineers, Transactions of the,* 70**,** 1186-1191.

WHITE, H. J. 1963. *Industrial Electrostatic Precipitation*, Addison-Wesley Publishing company, INC.

WHITE, H. J. 1977. Electrostatic precipitation of fly ash. *Journal of the Air Pollution Control Association,* 27**,** 15-22.

WHITE, H. J. & COLE, W. H. 1960. Design And Performance Characteristics of High-Velocity, High-Efficiency Air Cleaning Precipitators. *Journal of the Air Pollution Control Association,* 10, 239-245.

WHO 2003. Health aspects of air pollution with particulate matter, ozone and nitrogen dioxide: Report on a WHO Working Group. Bonn, Germany: World Health Organization, WHO, Regional Office for Europe.

WICHMANN, H.-E. & PETERS, A. 2000. Epidemiological evidence of the effects of ultrafine particle exposure. *Philosophical Transactions of the Royal Society of London. Series A: Mathematical, Physical and Engineering Sciences,* 358, 2751-2769.

WILSON, M. P. 2011. *Impulse breakdown of liquid-solid interfaces.* PhD, University of Strathclyde.

WILSON, W. E. & SUH, H. H. 1997. Fine Particles and Coarse Particles: Concentration Relationships Relevant to Epidemiologic Studies. *Journal of the Air & Waste Management Association,* 47, 1238-1249.

WOLFF, S. P. 1992. Correlation between car ownership and leukaemia: Is non-occupational exposure to benzene from petrol and motor vehicle exhaust a causative factor in leukaemia and lymphoma? *Experientia,* 48, 301-304.

YANKELEVICH, Y. & POKRYVAILO, A. 2002. High-power short-pulsed corona: investigation of electrical performance, SO₂ removal, and ozone generation. *Plasma Science, IEEE Transactions on,* 30, 1975-1981.

YOO, K. H., LEE, J. S. & OH, M. D. 1997. Charging and Collection of Submicron Particles in Two-Stage Parallel-Plate Electrostatic Precipitators. *Aerosol Science and Technology,* 27, 308-323.

YUAN, Y. & QI, L. Study and Apply on Field Test Instrument for Specific Resistivity of Fly Ash Burned Coal. Electronic Measurement and Instruments, 2007. ICEMI '07. 8th International Conference on, Aug. 16 2007-July 18 2007 2007. 4-382-4-386.

ZHANG, J. P., DU, Y. Y., WU, H., LIU, Y., REN, J. X. & JI, D. M. 2011. A Numerical Simulation of Diffusion Charging Effect on Collection Efficiency in Wire-Plate Electrostatic Precipitators. *IEEE Transactions on Plasma Science,* 39**,** 1823-1828.

ZUKERAN, A., LOOY, P. C., CHAKRABARTI, A., BEREZIN, A. A., JAYARAM, S., CROSS, J. D., ITO, T. & CHANG, J.-S. 1999. Collection efficiency of ultrafine particles by an electrostatic precipitator under DC and pulse operating modes. *Industry Applications, IEEE Transactions on,* 35**,** 1184-1191.

8. LIST OF PUBLICATIONS

8.1. JOURNAL PUBLICATIONS

1. A. C. Mermigkas, I. V. Timoshkin, S. J. MacGregor, M. J. Given, M. P. Wilson, and T. Wang, "Superposition of DC Voltage and Submicrosecond Impulses for Energization of Electrostatic Precipitators," Plasma Science, IEEE Transactions on, vol. 40, no. 10, pp. 2388 - 2394, 2012. 10.1109/TPS.2014.2301039
2. A. C. Mermigkas, I. V. Timoshkin, S. J. MacGregor, M. J. Given, M. P. Wilson, and T. Wang, "Removal of Fine and Ultrafine Particles from Air by Microelectrostatic Precipitation," Plasma Science, IEEE Transactions on, vol. 41, no. 10, pp. 2842-2850, 2013. 10.1109/TPS.2013.2253133
3. A. C. Mermigkas, I. V. Timoshkin, S. J. MacGregor, M. J. Given, M. P. Wilson, and T. Wang, "Impulsive Corona Discharges for Fine Particles Precipitation in a Coaxial Topology," Plasma Science, IEEE Transactions on, vol. 42, no. 10, pp. 3089-3094, 2014. 10.1109/TPS.2012.2186467

8.2. CONFERENCE PRESENTATIONS AND PUBLICATIONS

A. **A. C. Mermigkas**, I. V. Timoshkin, S. J. MacGregor, M. P. Wilson, M. J. Given, T. Wang, "The Use of Impulsive Corona Discharges for the Removal of Fine Particles in a Novel Coaxial Electrostatic Precipitator", 19th IEEE International Pulsed Power Conference (PPC) and 40th IEEE International Conference on Plasma Science (ICOPS) (PPPS 2013), San Francisco CA, USA, 16-21 June 2013. 10.1109/PLASMA.2013.6633200

B. I. V. Timoshkin, S. J. MacGregor, **A. C. Mermigkas**, M. MacLean, S. Li, J. G. Anderson, M. P. Wilson, M. J. Given, T. Wang, "Environmental Applications of Non-Thermal Impulsive Plasmas", Joint Seminar of Environmental and Disaster Mitigation Research (JSED2013), Muroran Institute of technology, Muroran, Japan, 8 March 2013.

C. **A. C. Mermigkas**, I. V. Timoshkin, S. J. MacGregor, M. P. Wilson, M. J. Given, T. Wang, “Micro-electrostatic precipitation process for removal of fine particles from air”, 4th Euro-Asian Pulsed Power Conference and 19th International Conference of High-Power Particle Beams, KIT, Karlsruhe, Germany, 30 September – 4 October 2012.

D. **A. C. Mermigkas**, I. V. Timoshkin, S. J. MacGregor, “Micro Electrostatic Precipitation for Air Treatment“, 6th Environmental and Clean Technology Conference, Glasgow, UK, June 2012.

E. I. V. Timoshkin, **A. C. Mermigkas**, M. J. Given, T. Wang, M. P. Wilson, S. J. MacGregor, “Analysis of Particle Charging Mechanism for Optimisation of Precipitation Efficiency”, 2012 IEEE International Power Modulation and High Voltage Conference, San Diego CA, USA, June 2012. 10.1109/IPMHVC.2012.6518693

F. **A. C. Mermigkas**, I. V. Timoshkin, S. J. MacGregor, “Micro Electrostatic Precipitation for Air Treatment”, Research Presentation Day 2012, University of Strathclyde, Glasgow UK, May 2012.

G. **A. C. Mermigkas**, I. V. Timoshkin, S. J. MacGregor, M. J. Given, M. P. Wilson, T. Wang, “Sub-Microsecond Impulsive Corona Discharges for Electrostatic Precipitation Applications”, 18th International Pulsed Power conference, Chicago IL, USA, June 2011. 10.1109/PPC.2011.6191582

H. **A. C. Mermigkas**, I. V. Timoshkin, S. J. MacGregor, M. J. Given, M. P. Wilson, T. Wang, “Investigation of impulsive corona discharges for energisation of electrostatic precipitation systems”, 4th UHVnet colloquium, Winchester UK, January 2011.

I. **A. C. Mermigkas**, I. V. Timoshkin, S. J. MacGregor, “Investigation of Efficiency of Micro Electrostatic Precipitation (micro-ESP)”, Research Presentation Day 2011, University of Strathclyde, Glasgow UK, January 2011.

J. **A. C. Mermigkas**, I. V. Timoshkin, S. J. MacGregor, T. Wang, M. P. Wilson, M. J. Given, “DC and sub-microsecond impulse energisation of electrodes in electrostatic precipitation”, 8th Technological plasma workshop, Bristol UK, January 2011.

K. **A. C. Mermigkas**, I. V. Timoshkin, M. J. Given, S. J. MacGregor, M. P. Wilson, “Effect of corona stabilisation in atmospheric air in DC and impulse conditions”, 8th Technological plasma workshop, Bristol UK, January 2011.

APPENDIX A BAG FILTER MATERIAL AND CLEANING PROCESSES

One of the most widely used methods of cleaning in bag filtration applications is the mechanical shaker one; this method has proven to be simple as well as effective. The bag is shaken usually in a direction perpendicular to the air flow, which forces the cake to be detached from the bag. The air flow should be stopped when the filter is cleaned as even small positive flows can have detrimental effects in the bag cleaning process. Reverse air flow can also be applied during cleaning. It is also desirable to have some amount of the cake remaining into the bag, so as not to start particle accumulation from scratch and thus retain higher collection efficiency. The only limitation of this method is that the PM collected should be easily detached from the bag. Failure to do so can be addressed by increasing the shaking intensity, which in turn will increase the bag degradation rate.

Reverse air method was invented and applied for sensitive bag fabrics, so as not to damage them by excessive shaking. It works by having the air flow inverted while cleaning leading to a simultaneous collapse of the bag from the inside leading to a cracking of the cake. Cleaning is further augmented by the piston-like process that occurs, as the cake is dislodged down the bag towards the hopper (Ketchuk et al., 1984). The low gas velocity that is applied in the opposite direction for cleaning does not force the bag filter to violent movements, which further preserves them. While it is a much gentler process than mechanical shaking, it is less effective too. It is also not effective for felted fabrics, as they retain PM in a greater level compared to woven fabrics due to their structure, which makes them much harder to clean.

Pulse-jet method is fairly new (employed since the late 50s) and it gains popularity as it can handle heavily PM laden gas flows at higher gas flow rates, the flow design itself is more compact and possesses few moving parts. Other important advantages is that the cleaning time is very short, pulses last only for 0.03 – 1 s, and that the air flow does not need to stop when cleaning pulses are applied. In terms of functionality, it is similar to the previous cleaning method with the difference that a reverse pulse air blow is used in high pressure (4-8 atm), that causes the bag to inflate abruptly and the corresponding inertial forces detach the cake from the bag filter. It should be noted that the bag filter in this case is used the opposite way, the cake is attached from the outside and clean air flows inside the bag. Thus, PM is accumulated on the outside of the bag, and when the pulse shock wave arrives, the detached cake then falls into the hoppers below it. As this process occurs often, less cake can be accumulated between the cleaning cycles. Therefore, felted fabrics are used as they rely less on filter cake thickness in order to have high efficiency. Woven fabrics on the other hand would have been problematic for the same reason. Additionally, in order to achieve maximum inertial forces for the cake removal, the filter material should be as lightweight and inelastic as possible.

One method that is used when high collection efficiency is required even for fine PM is the reverse-jet one. It is employed mainly when precious or toxic gases should be collected however PM loading should be low. It collects dust from the internal part of the bag, having a ring around it on the external side. When cleaning is required, the ring forces jets of moderate pressurized air towards the filter as it moves along the bag, which forces the dust cake to be extracted from the inside. This method is however used less and less nowadays.

Vibrational cleaning is used when fine PM collection is not considered. It theory, it bears many similarities with the mechanical cleaning, however this method employs high frequency vibration of the bags. This is usually enough to detach most coarse particles that exhibit weaker adhesive forces however it is ineffective for the fine PM.

One of the other methods employs the use of sonic waves, produced by horns. Although this method is not fully investigated, it is clear from practice that the sonic waves produce enough acceleration to detach the accumulated dust from the fabric. Other alluring characteristics this method has are its simple design and low cost. This method is also used to augment other bag cleaning methods, as the sonic wave causes a different, less adhesive, layer upon the filter cake, causing it to be more easily detached during cleaned. This of course causes less of the filter cake to be present after each cleaning application; however the use of the horns could be adjusted to counteract this theoretical fall in efficiency. It has been shown that this method reduces the residual cake width 76% on average (Davis, 2000). A study should take place in each system though regarding the sound frequency used, the sound wave pressure levels, and the periodic intervals that it should be used so as to maximize its effect and efficiency. As a general rule, lower frequencies seem to have the best results though (Parkinson, 1989).

Finally, there are the cartridge collectors. These collectors have the advantage of being very compact while at the same time keeping filtration efficiency at high levels. These can be single use, or used again after washing or being subject to pulse cleaning. It is also much easier to replace a cartridge than a bag as in the previous cases. The only disadvantages they have is that they are cannot cope with high gas flow rates and are not suited for high temperature gas streams.

Fabric material: Depending on the condition under which to be used e.g. temperature and on the chemical properties of the dust to be collected, like whether it is acidic or alkaline, there is a plethora of fabric to choose form. To name a few, bags can be made from Polyester, polypropylene, Teflon, Nomex, Cotton or even fiberglass. Each one has its own advantages and disadvantages, for example Teflon can be used for acidic or Alkaline Dusts, Nomex is resistant to fluoride, while Fiberglass can withstand high temperatures and high tensile forces, being very easily damaged though by flex forces. Even the way it is woven plays a major role under which operating conditions it can be used. It is also important for the fabric to be able to release the dust cake easily during cleaning. It has been found that this ability relates to the electrical resistance of the fibers (Frederick, 1978). Usually it is not clear what the best option for a bag filter in a specific installation is, thus various compartments could be equipped with different media as a testbed for future orders.

APPENDIX B PM AND HUMAN HEALTH

Appendix B.1 HUMAN RESPIRATORY SYSTEM

The respiratory system of humans is a very complicated system in terms of geometry and aerodynamic behavior as the air needs to be filtrated before it reaches the gas exchange surfaces while at the same time the flow rate is transient (a function of time) and even inverts its direction with breathing. Its geometry resembles fractals, its shape is like an inverted tree, and the volume it handles is 10 to 20 m^3 per day and up to 20 ℓ per minute. This causes the air as it enters to increase its speed up until the air reaches the air lobar bronchi. From that point on, as the cross-section increases ~250 fold due to the large number of small airways, it causes a similar decrease in the air speed. This causes the air to travel up until the alveolar duct, making the gas exchange process a strictly diffusion one. In Figure B-8-1 it is shown that the respiratory system could be divided into three parts, the nasopharyngeal which consist of the nose and mouth up to the larynx, the tracheobronchial which begins at the larynx extends through the trachea branching into the bronchi, the bronchioles and extending up to the terminal bronchioles, while the third part that the gas exchange takes place is the pulmonary which starts at the respiratory bronchioles, through the alveolar ducts and reaching the alveoli.

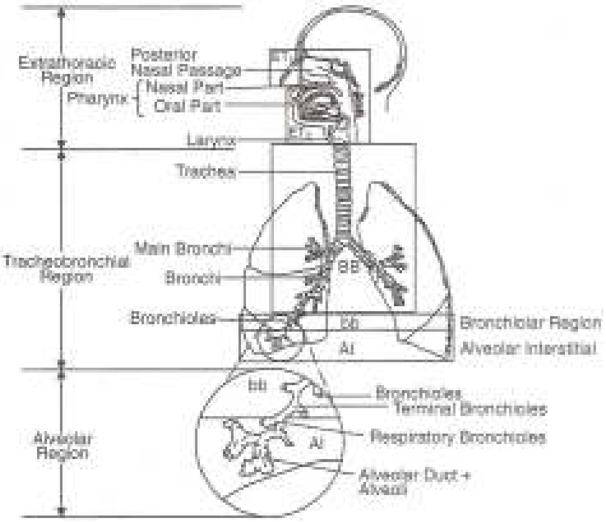

Figure B-8-1: Human respiratory system, adapted from (McKenna et al., 2008).

The major ways that the inhaled particles are removed from the air flow as it moves through the respiratory system is through inertial impaction, sedimentation and Brownian motion. Electrostatic deposition and inception, though they take place, play only a minor role in the deposition of suspended particles in the respiratory system. Inertial impaction, which is prevalent among the largest diameter fraction of the particles, happens because suspended particles in the air flow are reluctant to change their direction fast enough when they encounter forks or various obstacles, because of their inertia. This makes this method particularly useful as the respiratory system is composed of airways that get separated into smaller and smaller ones. And since the largest particles have largest inertia, this method is helpful in removing the largest part of the mass fraction of the inhaled particulate matter. Sedimentation happens mostly in the narrower air ducts of the alveolar duct in which air speed is extremely small (few mm/sec) (Hinds, 1982). It is augmented by the fact that some of these airways are horizontal and saturated with water vapor. This causes hydroscopic particles to expand and therefore be removed easier by sedimentation or impaction. Brownian motion helps submicrometer particles deposit in air ducts of the respiratory system. This happens at a much higher rate in the pulmonary part of the respiratory system in which very narrow airways and long residence times (due to extremely low speed) help submicrometer particles diffusion. Information on the velocity and residence time in various parts of the lungs are shown in Figure B-8-2:

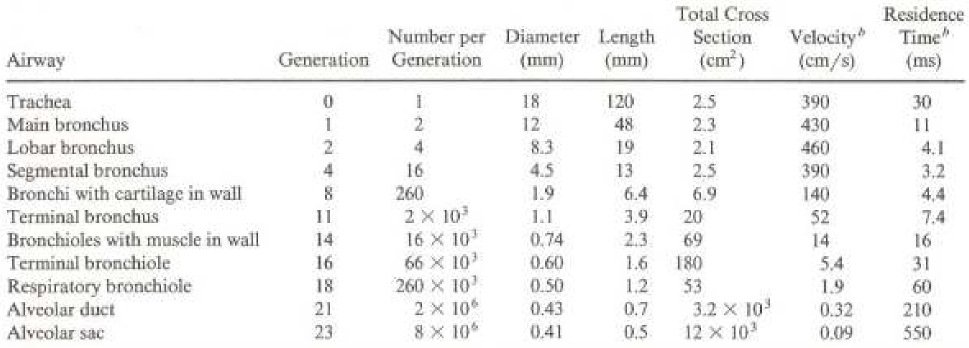

Airway	Generation	Number per Generation	Diameter (mm)	Length (mm)	Total Cross Section (cm^2)	Velocity[b] (cm/s)	Residence Time[b] (ms)
Trachea	0	1	18	120	2.5	390	30
Main bronchus	1	2	12	48	2.3	430	11
Lobar bronchus	2	4	8.3	19	2.1	460	4.1
Segmental bronchus	4	16	4.5	13	2.5	390	3.2
Bronchi with cartilage in wall	8	260	1.9	6.4	6.9	140	4.4
Terminal bronchus	11	2×10^3	1.1	3.9	20	52	7.4
Bronchioles with muscle in wall	14	16×10^3	0.74	2.3	69	14	16
Terminal bronchiole	16	66×10^3	0.60	1.6	180	5.4	31
Respiratory bronchiole	18	260×10^3	0.50	1.2	53	1.9	60
Alveolar duct	21	2×10^6	0.43	0.7	3.2×10^3	0.32	210
Alveolar sac	23	8×10^6	0.41	0.5	12×10^3	0.09	550

Figure B-8-2: PM velocity and residence time in various parts of the lungs (Hinds, 1982).

In terms of deposition of particles in each part of the respiratory system, Figure B-8-3, in a simplified manner it is acceptable to say that the first and second part acts as a defense for the third one which is responsible for the all-important gas exchange process. In the first part (head region till larynx), one of the most important factors is being whether air is inhaled by the mouth or nose. Air taken through the nose gets filtered in greater extent compared to air inhaled from the mouth (Hinds, 1982). This is because in the former case air has to pass through nasal hair and turns in the air path that favor deposition by impaction, while in the latter case airways are more direct and hair is missing. An additional advantage is that when air gets through the turbinates in the nasal passage it gets both warmer and humidified something that helps especially in the case of hydroscopic particles as has been discussed before. Sedimentation is also a factor in particle removal in the first part of the respiratory system.

Impaction is also the major deposition mechanism in the second part of the respiratory system from the coarse fraction of particles that manage to pass through, while sedimentation is more prevalent for the finer particles. However, the vast majority of the fine particles manage to pass through and reach the alveolar region. The ultrafine particles though tend to be mostly deposited in this stage due to their rapid Brownian motion, in the narrow paths that lead to the third part of the respiratory system.

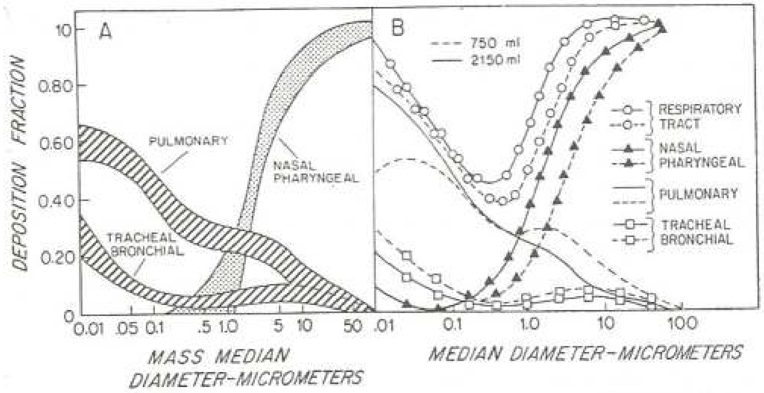

Figure B-8-3: Fraction of PM deposition as a function of its diameter (Hinds, 1982).

The first two stages have a very elaborate mechanism of self-cleaning. This consists of the mucociliary escalator, which comprises of a layer on mucus upon the airways that is left propelled through ciliary action. The deposited particles are thus driven to the pharynx where they enter the peptic system, with the whole process taking a couple of hours. However, this is a way to mitigate the problem as the particles might still find a way into the body through the digestive tract. While this is less efficient than entering straight into the blood flow through the gas exchange membranes in the lungs, it is still a cause of concern especially for the more toxic particles.

Deposition in the alveolar region, Figure B-8-4, in much harder, not only due to the filtering mechanisms of the two previous regions, but also because of the alveolar gas exchange mechanism itself. The mechanism relies on gas diffusion of O_2 and CO_2 molecules in the last mm before the gas exchange membranes. In this volume the air inhaled stops progressing and only reserve air from previous breathing is in contact with the alveoli. O_2 and CO_2 diffuse very fast, while even sub-micrometer particles are too slow to deposit by diffusion, and sedimentation in this particle size range is low. There can be sedimentation though of particles suspended into the reserve air close to the alveoli, but the deposition rate of the (0.1-1) µm fraction is low, ~20% (Hinds, 1982). Even these few and small particles can be a problem however, as there is no mucociliary escalator as in the previous regions and soluble particulate matter can easily pass into the blood stream. Insoluble matter can be either be dissolved by phagocytic cells, or be moved to the mucociliary escalator, both slow processes that might take months.

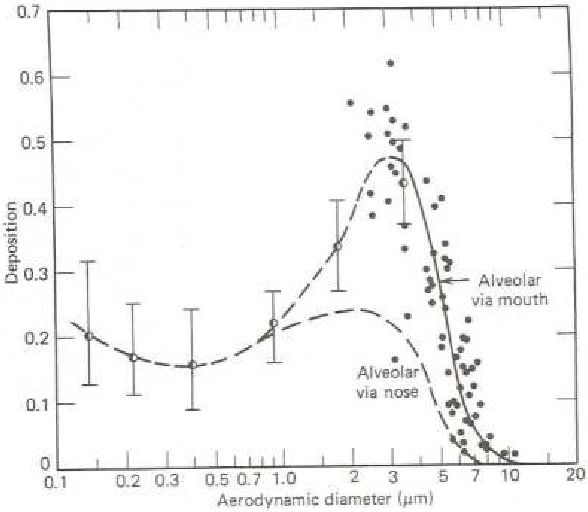

Figure B-8-4: PM deposition in the alveolar region (Hinds, 1982).

Another important category of inhaled PM that can be detrimental to health is microscopic fibers. Fibers are defines as "any particle having a length greater than 5 µm and an aspect ratio of 3:1 or greater" (Hinds, 1982). As high strength materials get milled, relatively long fibers can be created, which have the ability to circumvent the filter mechanisms of the respiratory system, as they align themselves with the airways and can even manage their way to the alveoli. Once deposited there, these large particles are too difficult to be transported back to the mucociliary escalator, are too large in comparison to the macrophage to be engulfed by them or be dissolved by lung fluids. The very enzymes that the macrophage cells used to dissolve them can cause fibrosis, or in the case of asbestos fibers, asbestosis. They can even cause bronchial carcinoma. Therefore, the upper limit for Chysolite asbestos is only 2 fibers/cm^3 US according to the occupational health exposure standard (Hinds, 1982).

Silicosis can cause fibrosis of the alveolar region (Hinds, 1982) and a corresponding loss of functionality for the particular alveoli affected (Crown). This is caused not by fibers but by respiratory crystalline silica (RCS) (Crown), which is small crystalline silica particles, able to reach the pulmonary region. This is because silica particles not only cause the macrophage that try to engulf them to secrete fibrogenic proteins, but also kill them in the process, called Cytolisis (BMJ). Silicosis is incurable and can also continue to develop even after there is no exposure to RCS. Thus, it comes as no surprise that the workplace exposure limit (8-hour time weighted average) for RCS is only 100 μg/m^3 (Crown). Similar problem with silica in terms of lethal interaction with macrophages can even be caused by coal, in particular freshly pulverized or high rank one (like anthracite) as it contains many free radicals (Crown).

Another important conclusion derived from the respiratory systems filtering mechanisms and used in hazardous particles regulations is that mass concentration of suspended particulate matter does not correlate with disease. This is because particles larger than 10 μm that contain around 60% of the mass of an average mine dust are considered non-respirable, while 98% of the total number of particles can penetrate as deep as the pulmonary region of the lungs. Due to that fact, for hazardous particles consideration, the number concentration is used instead of the mass one (Hinds, 1982).

Appendix B.2 POSSIBLE HEALTH EFFECTS

Based on the analysis of the human respiratory system, it is important to approximate the portion of particles reaching each stage of the respiratory system, despite its complexity. This is important for evaluation of the hazards of inhaled PM as it depends not only on their chemical composition, but also on the area of the respiratory system on which they are deposited (Hinds, 1982). To make matters worse, because of the size-selective behavior of the respiratory system shown above, the particles that ultimately deposit anywhere on the lungs of ducts of the respiratory network, may have different size distribution and chemical characteristics from the originally inhaled volume. As a general rule, the first 2 stages of the respiratory system tend to protect the third one, namely the alveoli and their all-important gas exchange membranes from harmful particle deposition (Hinds, 1982). To these ends EN 481 standard was made which defines the mass fractions of particles inhaled, reaching the larynx and finally the mass fraction that reaches the unciliated airways (meaning alveolar region). These are called inhalable, thoracic and respirable conventions respectively. They are defined as a “target specification for sampling instruments when the inhalable, thoracic or respirable is the fraction of interest” respectively and they correspond to the inhalable, thoracic and respirable fraction of particles entering the various stages of the respiratory system. Inhalable are the “mass fraction of the total airborne particles which is inhaled through the nose and mouth”. This corresponds to a very wide mass fraction, essentially the particles that pass through a size-selective inlet with a 50% efficiency cut-off at 100 μm. It is essentially all the particles that can be inhaled through the nose or mouth, however since no experimental data exist for larger particles than 0.1 mm, the convention is not valid for particles of greater aerodynamic diameter. The Thoracic fraction is defined as the “mass fraction of inhaled particles penetrating beyond the larynx”. This corresponds to the PM10 fraction of the particles that was discussed in a previous subchapter. Lastly, the respirable fraction is the “mass fraction of the inhaled particles penetrating to the unciliated airways” which corresponds to PM4, with standard deviation of 1.5 μm (Nordberg et al., 2004), (2007). However, in practice the PM2.5 fraction is often used (Laxen et al., 2010). It should be noted though that this approach leads to an overestimation of the of the potential health hazard as particulate matter needs to be deposited to affect the organism. One of the most striking cases is that of the respirable particles, because a part of these particles is exhaled by breathing and thus is not attached to the lungs (British Standards, 1993). Plot of the Inhalable, thoracic and respirable conventions as a percentage of the sum of the PM can be seen in Figure B-8-5:

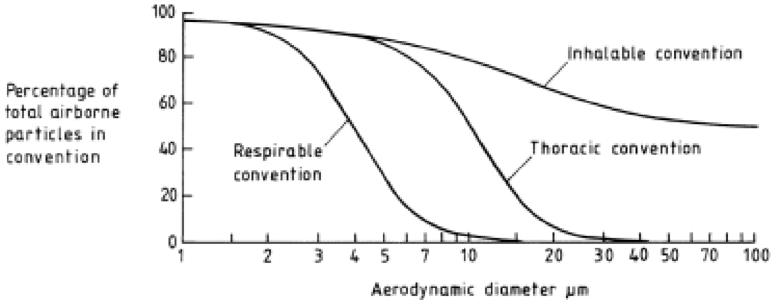

Figure B-8-5: Inhalable, thoracic and respirable definitions according to (British Standards, 1993).

Generally increased levels of PM2.5 lead statistically to a greater number of admissions in hospitals on those days and on the ones immediately after these PM2.5 peaks. In addition to the above, a higher number of deaths from respiratory and cardiovascular diseases are manifested on the same days. A much greater number of people are affected by having increased asthma symptoms or simply feeling less active. In the long term, PM2.5 is linked to a reduced life expectancy, with some research for the UK even pointing to 6 months per person by being exposed to 2008 man-made PM2.5 levels of ~10 µg/m^3 (for the rest of their lives, and born in 2008) (Laxen et al., 2010), (DEFRA, 2010). The gain from eliminating this exposure would have an equal effect with having no more road accidents and having no one being subject to passive smoking (Laxen et al., 2010), (House of Commons - Environmental Audit Committee, 2010).

Regarding the particular background level of particulate matter that starts to be detrimental to human health, the consensus among scientists is that such level most probably does not exist as the research done shows a linear relationship between PM2.5 concentration and health risks. In addition to the above, there is a dependence on the time length that a particular population was exposed to Particulate matter. While short term exposure can be related mostly to respiratory and cardiovascular problems, long term ones can have a cumulative function including appearance of, or development of, lung cancer (Laxen et al., 2010), (Pope, 2007), type 2 diabetes (Laxen et al., 2010), (Krämer et al., 2010) or even effects on cognitive function (Laxen et al., 2010), (Calderón-Garcidueñas et al., 2004), (Calderón-Garcidueñas et al., 2008). However, not all people show the same susceptibility to PM pollution. It has been shown that people with health problems (Laxen et al., 2010), the youngest (Laxen et al., 2010), (Ko et al., 2007) and the eldest (Laxen et al., 2010), (Goldberg et al., 2001), (Ostro et al., 2006) population age groups seem to be more affected by PM exposure. On the long run, men and people that are in the least educated subgroup seem to have the highest effect from airborne particulate pollution (Laxen et al., 2010), (Pope III et al., 2002).

In terms of Particular fraction of PM that cause the most problems, it seems that the PM2.5 fraction of the PM10 particles seem to be more toxic, as it has been shown that larger particulate fractions, like PM10 and PM15, have less impact upon mortality than PM2.5 (Laxen et al., 2010), (Pope III et al., 2002). However, there have not been many studies that take into account both PM2.5 and PM10 fractions (Laxen et al., 2010). At this point an interesting question might arise, regarding the toxicity of the coarse fraction, aka the PM2.5-10 fraction. In the short term, it has been shown that coarse particles are connected to an increased level of hospital admissions (morbidity) (Laxen et al., 2010), (Brunekreef and Forsberg, 2005), rather than mortality (Laxen et al., 2010), (EPA, 2009). In the long term, research failed to associate a change in mortality with the coarse fraction of the particles (Laxen et al., 2010), (Pope III et al., 2002), which seems to be best explained by the PM2.5 fraction (Laxen et al., 2010), (McDonnell et al., 2000). A problem with the aforementioned work, is that the coarse particles do not show the same spatial and temporal uniformity in the atmosphere as their PM2.5 counterparts which leads to underestimation of their effects on human health (Laxen et al., 2010), (Wilson and Suh, 1997). This fact might have affected the aforementioned studies too (Laxen et al., 2010).

It has also been claimed by many studies that PM2.5 has different toxicity depending on its source. To be more precise PM2.5 from traffic or oil combustion sources seems to have the highest toxicity (Laxen et al., 2010, Laden et al., 2000, Sarnat et al., 2008, Peng et al., 2009, Tsai et al., 2000, Burnett et al., 2000, Anderson et al., 2001, Bell et al., 2009, Happo et al., 2008, Wessels et al., 2010), together with the ultrafine fraction of its mass (PM0.1) that is a mostly diesel engine combustion derivative too (Laxen et al., 2010, Atkinson et al., 2010). A research has also pointed out the different effects that these particles have as PM2.5 from combustion processes seem to have the greatest effect in respiratory cases (effects being mostly immediate) while the ultrafine PM are mostly related to cardiovascular malfunctions and have a time lag of one or a couple of days after the surge of the ultrafine particles (Laxen et al., 2010, Anderson et al., 2001, Wichmann and Peters, 2000). There has also been shown, despite the limited research being conducted, that nitrate (secondary emission) has no, or very limited, health effects in its current concentration in the atmosphere, the same being for crustal fraction of PM2.5, which shows chemically no negative biological health effects (Laxen et al., 2010, Schlesinger, 2007). The reason that these particular sources of PM have such negative health effects can be attributed to their oxidizing and inflammatory effect they have in the part of the lung the get deposited upon (Laxen et al., 2010, Donaldson et al., 2005). In the case of respiratory problems, the effect is seen as shortening of the airways, thus augmenting the effects of asthma or other conditions (Laxen et al., 2010). In the case of cardiovascular malfunctions, the causes can be harder to find, but the case is that ultrafine particles have a negative effect when deposited on the pulmonary interstitium of the alveoli or enter the blood flow, which can lead ultimately to a cardiac event (Laxen et al., 2010, Seaton et al., 1995). Lastly, since PM0.1 are usually diesel combustion byproducts, they can harbor reactive organic and transition metals which have deleterious, or even mutagenic (Jariyasopit et al., 2013), effects by themselves (Laxen et al., 2010, Mills et al., 2009). This is usually the case with fly ash particles, which can have sulphate molecules or metals attached to them which can cause lung injuries (Laxen et al., 2010, Gavett et al., 1997, Ondov and Wexler, 1998, Clack, 2006). In the long term, PM2.5 seems to be responsible for lung cancer even in people that do not smokers (Laxen et al., 2010, Harrison et al., 2004).

This can lead us into a very important finding, as road traffic particles not only seem to be more toxic than particles from other sources (Laxen et al., 2010, Gerlofs-Nijland et al., 2007), but also contribute more towards the overall PM2.5 fraction (Laxen et al., 2010). In a recent research, it has been testified that instead of controlling the total PM emissions, it would be more beneficial to limit the road traffic in terms of the public health perspective (Laxen et al., 2010, Grahame and Schlesinger, 2007). Supporting this, another research from the same authors pointed out the fact that there were higher health risks for people living closer to highways compared to the ones residing further away (Laxen et al., 2010, Grahame and Schlesinger, 2010). If we want to analyse it in more detail it would seem that the diesel exhaust particles are particularly noxious based on recent research (Laxen et al., 2010, Beelen et al., 2008, Brunekreef et al., 2009, McKenna et al., 2008), which and can even be associated to myocardial infraction and atherothrombosis (Laxen et al., 2010, Mills et al., 2005). Apart from diesel, petrol has been associated with the cause of Leukemia (Wolff, 1992).

Another important finding is that even secondary particles produced through combustion can be much more toxic compared to their ‘pure’ form (Laxen et al., 2010). An example is sulphate which forms from sulphur dioxide, usually a coal and oil combustion product. While studies of it have indicated the health risk associated to it to be small (Laxen et al., 2010, Grahame and Schlesinger, 2005), if it is formed by coal (Laden et al., 2000) or oil burning, the trace metals, like Ni and V, attached to the particles can have significant health effects (Chen and Lippmann, 2009). Nitrate, as has been discussed above, it is not considered to be highly toxic (Laxen et al., 2010). In summary, despite the gaps in the literature (Ayres, 2009), sulphate and especially nitrate cannot be easily identified as a cause of health risks (Laxen et al., 2010, Reiss et al., 2007).

In the announcements regarding air quality, PM2.5 levels are not announced by themselves, but usually together in combination with the ozone levels (Airnow, 2014, AQI, 2014, DEFRA, 2014b, CITEAIR, 2014). This is because there is evidence of combined detrimental effects of ozone in conjunction with PM2.5 (Laxen et al., 2010, Madden et al., 2000) and even of ozone and PM0.1, which is part of the PM2.5 fraction (Laxen et al., 2010, Oberdörster et al., 1995, Elder et al., 2000). However, the opposite could also happen, as there is speculation that exposure to sulphur dioxide (noxious gas and precursor of sulphate secondary particles) over a long period of time could augment mucous secretions thus improving the cleaning mechanism of PM deposited in the lungs (Laxen et al., 2010, WHO, 2003).

For the population the health benefits resulting from improved air quality conditions after a possible reduction of the atmospheric aerosol concentrations can be huge. According to theoretical calculations for the UK, after the implementation of the CAFE directive control measures in 2020, ~(6.4-12.2) million life years would have been saved in the form of increased life expectancy and reduced mortality (Laxen et al., 2010). This can be speculated also from tangible results, based on sporadic bans of specific emissions around the world. Examples are plenty, one being the recent law forbidding coal sales in Dublin. This resulted in a steep decrease of mortality from respiratory and cardiovascular origins (Laxen et al., 2010, Clancy et al., 2002). Another example comes from Hong-Kong, after a reduction of the percentage of sulphur in the oil used as a fuel, the life expectancy increased some tens of days per year, with the most pronounced effect (double the gain) on men's life expectance (Laxen et al., 2010, Medley et al., 2002). A decreased mortality rate was also found during an 8-year period in six large cities in Europe, which have managed to reduce their PM2.5 mean levels during the same period (Laxen et al., 2010, Laden et al., 2006). On the other side of the Atlantic, there was also a rise in life expectancy associated with reduction of PM2.5 levels in 51 major US metropolitan areas. It was stated that a reduction of 10 μg/m^3 in PM2.5 levels was statistically significant in a 0.61 rears rise in the population life expectancy, as the data was normalized to account for the increase in the life expectancy during the same period (Laxen et al., 2010, Pope et al., 2009). In terms of monetary costs of exposure to PM2.5 pollution, a very conservative research has pointed on ~£8.5-20.2 billion per year for the UK (Laxen et al., 2010, DEFRA, 2007), without taking into account the NHS costs due to the higher morbidity (Laxen et al., 2010, House of Commons - Environmental Audit Committee, 2010). Another piece of research showed that while the costs of implementing the CAFE directive would be €776 million per year (in 2020), the gain expected from the abatement of the health conditions associated with increased PM2.5 exposure (mainly respiratory and cardiovascular conditions) would be €15.9-16.8 billion, a profit ratio of ~7.6-21.7 (Laxen et al., 2010, Holland et al., 2005). In comparison, it is estimated that health costs in the EU because of poor air quality reach a staggering €(330-940) billion which corresponds to 3%-9% of EU GDP (European Commision, 2014, European Commision, 2013).

There are two main ways in trying to control PM2.5 emissions. One is to impose limit values on the production of PM2.5 at certain cites (called hot-spots) and the other is to try to reduce the overall population exposure by imposing small reductions in particulate levels over wide areas (e.g. across countries). The recent CAFE directive includes both ways and it has been shown scientifically that, provided all CAFE targets are met, the exposure reduction way provides the greatest benefits in term of gains by improved population health levels (de Leeuw and Horálek, 2009). If however, the toxicity of various types of PM is taken into account, then the greatest benefits would arise from a reduction of PM2.5 from road traffic (Laxen et al., 2010, Tainio et al., 2010).

In general, the negative health effects of PM2.5 on humans is not fully investigated yet and there is not a safe level of PM2.5 established, however there is an agreement that it leads to a reduced life expectancy and to the contrary, if PM2.5 levels are reduced, there is evidence that mortality is decreased. Another fact that makes the problem more complicated is that depending on its source, PM2.5 can have variation in its toxicity effects for example traffic PM2.5 particles tend to be more toxic compared to other PM2.5 particles (Laxen et al., 2010).

APPENDIX C LEGISLATIVE INITIATIVES

To address the adverse health effects of PM and other noxious airborne substances, initiatives have been taken and air pollution legislation has been introduced in the EU and also by individual countries. An extensive literature review has been conducted covering main aspects of the European Union policy on air pollution. This includes the Thematic Strategy on Air Pollution of 2005 (COMMISSION OF THE EUROPEAN COMMUNITIES, 2005), the Ambient Air Quality Directives (AAQDs) (European Parliament and Council of the European Union, 2008) and (European Parliament and Council of the European Union, 2004), the National Emission Ceilings Directive (NECD: 2001/81/EC), and a wide range of legislation regarding limiting pollution directly at its sources (European Commision, 2013).

From Appendix B it is clearly shown that there is a need for cleaner air, especially in large urban centers and near industrial areas. Therefore, attempts have been, and continue to be made, in an international, EU and national level. In terms of PM2.5 is concerned, measures to reduce SO_2, NOx, VOCs and NH_3 are important because, as it has been discussed in previous subchapters, they act as precursors for secondary particle formation. In addition to the above, any measures that address the reduction of total PM, also reduce PM2.5 as they are a major fraction of total PM concentration (Laxen et al., 2010).

Appendix C.1 INTERNATIONAL LEGISLATION

In the international level, there has been an attempt to tackle various environmental problems like eutrophication of rivers and lakes, acid rain and ground level ozone, by agreeing on a protocol which assigns emission ceilings to each country for various, organic and inorganic, precursor emissions. This protocol, named multi-effect or Gothenburg protocol was signed in 1999 and aims in reducing SO_2, NOx, VOCs and NH_3 emissions. PM2.5 has not been addressed directly however, the reduction of precursor substances reduces secondary PM pollution. PM2.5 ceilings are expected to be introduced in a future revision of the protocol (Laxen et al., 2010). In the EU this protocol has been incorporated by the National Emissions Ceilings directive (NECD – 2001/81/EC) and has also been ratified by the UK in the National Emissions Ceilings regulations 2002 (Crown, 2014).

Another international agreed protocol, the Aarhus protocol, sets emissions limits for various heavy metals, namely the Cd, Pb, Hg. This protocol also proposes best available techniques (BAT) which can be used in the industrial sector, like scrubbers and filters. These methods indirectly help in combating PM2.5 as they are effective in combating particulate pollution (Laxen et al., 2010).

There have been also international conventions (Laxen et al., 2010), in trying to reduce emissions from the shipping and aircraft sector. These are aimed in the reduction of S from fuel, thus avoiding SO_2, and in the reduction of NOx from diesel engines. This helps in reducing 2 important precursor gases for secondary PM creation. Special emission standards are also produced for aircraft engines.

Appendix C.2 EU LEGISLATION

The EU has, since the early 70s, tried to improve air quality and preserve the natural environment though implementing policies and enforcing legislations and directives. These were aimed in many directions like emissions control of various pollutants, reducing sulfur and eliminating lead from fuel and imposing environmental protection schemes into the industrial, transport, energy and waste management sector (European Commision, 2014).

The EU have adopted in May 2001, the clean air for Europe program. Its purpose is to collect the various parts of the air quality policy within the 6th Environmental Action program (EAP), covering the years 2002-2012 (European Parliament and Council of the European Union, 2002a), so that the various environmental measures taken can be coordinated effectively. Apart from the NEC directive discussed above, which imposes national emission ceilings for various pollutants, there are many other directives addressing the pollution from sources like industrial installations, large combustion plants, waste and even from paints. Most of these directives have been recast into a single industrial emissions directive effective from 6th January 2011, which had to be transposed into national law by the member states by the 7th January 2013 (DEFRA, 2014a, European Parliament and Council of the European Union, 2010) .

In terms of control of emissions from the transport sector, there are standards from the EU regarding light duty vehicles, heavy duty vehicles (Euro VI standard concerning NOx and PM emissions (Europa.eu, 2013a, European Parliament and Council of the European Union, 2009)) and two-wheel vehicles. There has been also a legislative move towards regulations instead of directives in this sector in the recent years. This means that the EU addresses this sector in a direct way, rather than setting goals and leaving the individual member states the freedom to decide how to achieve them (Europa.eu, 2014b). These regulations and directives impose not only exhaust emission tests but also incentives for scrapping old vehicles which pollute more. Interestingly enough, there are no PM emission limits for two-wheel vehicles in the legislation (Laxen et al., 2010). Apart from that there is a directive (96/96/EC) for in service inspection of vehicles, which in the UK is implemented as the annual roadworthiness inspection (MoT). However, there are no provisions for NOx and PM emissions in the MoT tests (Laxen et al., 2010). Additionally, there has been legislation both in the EU and in the UK, regarding the sulphur content of the fuel. Due to that, it has been reduced substantially to max 10 ppm S effective from 1/1/2009 (Laxen et al., 2010).

Regarding non-road mobile machinery (NRMM), there is the directive 97/68/EC regarding gas and particulate emissions from internal combustion engines installed upon NRMM. This is also implemented in the UK law in the “Non-Road Mobile Machinery (Emissions of Gaseous and Particulate Pollutants) Regulations 1999” (Laxen et al., 2010). Regarding trains, the latest international standards from the International Union of Railway (UIC) for diesel engines upon trains (UIC stage III) are harmonized with the non-road engines standards of the EU (stage IIIA) (Laxen et al., 2010).

EU formulated the 2005 Thematic Strategy on Air Pollution, calling its member states to major reductions in the levels of PM2.5, O_3 and to the level of acidification and eutrophication occurring by the year 2020. To achieve this, it required among others the steep reduction of precursor gases emissions of up to 82% compared to the 2000 levels as in the case of SO_2. If implemented these measures could have improved environmental and living conditions as well as helping the avoidance of 1.71 million life years lost and the 2200 excess deaths due to increased ozone concentration compared to the year 2000 (COMMISSION OF THE EUROPEAN COMMUNITIES, 2005). However this strategy had only a suggestive role and member states were not obliged to the target specified (Ohliger, 2013). Details of the reductions in this strategy can be seen in Table C-1:

Table C-1: Reduction targets set by the EU, to be achieved by 2020.

<table>
<tr><th colspan="2">Environmental & health objectives (reductions by 2020)</th></tr>
<tr><td>Eutrophication & acidification</td><td>55%</td></tr>
<tr><td>O_3</td><td>60%</td></tr>
<tr><td>PM2.5</td><td>75%</td></tr>
<tr><th colspan="2">Reduction targets in order to achieve the aforementioned objectives (compared to 2000 levels)</th></tr>
<tr><td>SO_2</td><td>82%</td></tr>
<tr><td>NOx</td><td>60%</td></tr>
<tr><td>VOCs</td><td>51%</td></tr>
<tr><td>NH_3</td><td>27%</td></tr>
<tr><td>PM2.5</td><td>59%</td></tr>
</table>

The strategy also includes decisions for cooperation between EU and USA and EU and China for the control of air pollution.

In order to enforce the reduction of the negative environmental and health effects that particulate pollution causes, the EU published a new directive in 2008. This directive moves in the same direction as the previous one (Council of the European Union, 1996, Council of the European Union, 1999, European Parliament and Council of the European Union, 2000, European Parliament and Council of the European Union, 2002c, Council of the European Union, 1997) that it encompasses, amends and expands, and also adds some important measures for the reduction of PM2.5 in the EU. It also discusses the possible merging of a sixth one (2004/107/EC) (European Parliament and Council of the European Union, 2004) having to do with emissions of As, Cd, Hg, Ni and polycyclic aromatic hydrocarbons (PAHs) in order to encompass air pollutants in a great extent (European Parliament and Council of the European Union, 2002b). Moreover, O_3 objectives, sampling points and precursor molecules were extensively covered in the directive as it has been shown that it can act in combination with PM2.5 augmenting the ill health effects especially for sensitive groups. In addition to the above aims, the directive also aims, among others, in co-operation between member states in terms of cross border pollution migration, use common methodology in checking air quality and have information about air pollution easily and readily available to the public (European Parliament and Council of the European Union, 2008), or even draw-up plans for the protection of sensitive population groups when alert thresholds are reached (European Parliament and Council of the European Union, 2008) article 24. In the end the directive asks for the member states to pass the decisions of the directive into state law before the 11th June 2010 and inform the commission accordingly (European Parliament and Council of the European Union, 2008) article 33.

To these ends a dual approach has been attempted. As usual, limit values have been imposed on hotspots, meaning industrial or other areas having huge PM2.5 emissions, in order to curb their particulate matter contribution. In addition to that, in order to reduce the impact of PM2.5 for as large a number of people as possible, a new scheme was created intending to reduce the overall exposure to PM2.5. These measures strive to increase the ambient air quality for as large the population percentage as possible, without having the member states go to extreme ends or sacrifice sustainable development (European Parliament and Council of the European Union, 2008) articles 12 and 15. Additionally, any proven natural contributions towards the limit values, or even contributions from sanding and salting of roads for the winter, are to be excluded by the commission (European Parliament and Council of the European Union, 2008) articles 20 and 21.

According to this scheme, each EU member state will have to divide its land area into zones and install sampling points in large urban centers (one per 100k people), in increasing numbers for larger number of inhabitants in order to have representative data for the exposure of the population. Zones can also be created in co-operation between neighboring countries for the border areas, and should be at least one per country. Based on the mean of the annual averages of all sampling stations in one country, the average exposure indicator (AEI) is calculated for that country. It is the running average of the annual means of all zones of that country for three years and it is used as an indicator of the population exposure to PM2.5 for that particular country.

This AEI should be maximum 20 μg/m^3 by 2015 (called exposure concentration obligation) and to fall by a particular percent (exposure reduction target – Table C-2) in 2020 compared and depending on the AEI of 2010. This 3-year average was decided in order to avoid particular years with extremes in PM2.5 pollution. The number three is for practical reasons as it goes without saying that the more years are taken into account the less the effect one “extreme” year would have upon the average (Laxen et al., 2010). The EU countries are obliged to meet the directives decisions by bringing them into state laws and also by keeping sufficient sampling points for the calculation of AEI (European Parliament and Council of the European Union, 2008) article 33.

Table C-2: Exposure reduction target of AEI 2020 compared to AEI 2010 (European Parliament and Council of the European Union, 2008) annex XIV.

AEI in 2010 (μg/m^3)	Reduction target (%)
≤ 8.5	0
8.5-13	10
13-18	15
18-22	20
≥ 22	Reduce to 18 μg/m^3

In terms of PM2.5 average over calendar years, there is a target value of 25 μg/m^3 for 1st January 2010, and further limit values of 25 and 20 μg/m^3 for the 1st January 2015 and 2020 respectively (European Parliament and Council of the European Union, 2008) annex XIV. Further information regarding other atmospheric pollutants can be found in the official air quality standards website of the EU (Europa.eu, 2014a).

In terms of PM10, both intended for protecting population health levels, 24vh and annual levels of exposure had already been in effect from the 1st January 2005 (European Parliament and Council of the European Union, 2008) annex XI because of a previous directive council directive 1999/30/EC of 22 April 1999 (Council of the European Union, 1999), that the CAFÉ directive replaces. The daily limit is 50 μg/m^3, not to go beyond that value more than 35 times per annum, while the limit value for the calendar year is 40 μg/m^3 (European Parliament and Council of the European Union, 2008) annex XI. This is because it is anticipated that the objectives for PM2.5 will be met if the 24-hour limits for PM10 are kept, as a reduction of PM10 will cause a consequent decrease of its smaller fraction, PM2.5.

This directive was subject to review in 2013, with the aim of implementing a mandatory national exposure reduction instead of a target AEI value, with reevaluating the population exposure concentrations based on new data available, with the adoption of a more stringent limit for the PM2.5 exposure and with the adoption of new prototype way of PM2.5 and PM10 measurements based on technological progress in the meantime. New ambitious reduction targets for various pollutants, including precursor gases to PM, and PM2.5, for the years up to 2030 and beyond, have been included in the Clean Air Policy package which was adopted on the 18th December 2013 (EUROPEAN COMMISSION, 2013). In a nutshell the current limits for various pollutants can be summarized in the Table C-3:

Table C-3: Limits on emissions of various pollutants according to (Europa.eu, 2014a).

Pollutant	*Concentration*	*Averaging period*	*Legal nature*	*Permitted exceedances each year*
Fine particles (PM2.5)	25 µg/m^3	1 year	Target value entered into force 1.1.2010 Limit value enters into force 1.1.2015	n/a
Sulphur dioxide (SO_2)	350 µg/m^3	1 hour	Limit value entered into force 1.1.2005	24
	125 µg/m^3	24 hours	Limit value entered into force 1.1.2005	3
Nitrogen dioxide (NO_2)	200 µg/m^3	1 hour	Limit value entered into force 1.1.2010	18
	40 µg/m^3	1 year	Limit value entered into force 1.1.2010*	n/a
PM10	50 µg/m^3	24 hours	Limit value entered into force 1.1.2005**	35
	40 µg/m^3	1 year	Limit value entered into force 1.1.2005**	n/a
Lead (Pb)	0.5 µg/m^3	1 year	Limit value entered into force 1.1.2005 (or 1.1.2010 in the immediate vicinity of specific, notified industrial sources; and a 1.0 µg/m^3 limit value applied from 1.1.2005 to 31.12.2009)	n/a
Carbon monoxide (CO)	10 mg/m^3	Maximum daily 8 hour mean	Limit value entered into force 1.1.2005	n/a
Benzene	5 µg/m^3	1 year	Limit value entered into force 1.1.2010**	n/a
Ozone	120 µg/m^3	Maximum daily 8 hour mean	Target value entered into force 1.1.2010	25 days averaged over 3 years
Arsenic (As)	6 ng/m^3	1 year	Target value enters into force 31.12.2012	n/a
Cadmium (Cd)	5 ng/m^3	1 year	Target value enters into force 31.12.2012	n/a
Nickel (Ni)	20 ng/m^3	1 year	Target value enters into force 31.12.2012	n/a
Polycyclic Aromatic Hydrocarbons	1 ng/m^3 (expressed as concentration of Benzo(a)pyrene)	1 year	Target value enters into force 31.12.2012	n/a

Appendix C.3 UK LEGISLATION

The UK had passed its own decisions into law, in the “Air quality strategy for England, Scotland, Wales and Northern Ireland” (Laxen et al., 2010, DEFRA, 2007). This law sets almost similar targets, obligations and limits for the UK, however the Scottish government decided to set more challenging targets. These can be seen and compared in the Table C-4:

Table C-4: Comparison of Scottish, UK and EU particulate matter objectives, obligations, targets and limits (Laxen et al., 2010).

	Scotland	UK	EU
PM2.5 Annual mean	12 µg/m^3 by 2020	25 µg/m^3 by 2020	Target of 25 µg/m^3 by 2010
			Limit of 25 µg/m^3 by 2015
			Limit of 20 µg/m^3 by 2020
AEI	15% reduction of AEI 2010 by 2020	15% reduction of AEI 2010 by 2020	Exposure concentration obligation of 20 µg/m^3 by 2015
			0-20% reduction of AEI 2010 by 2020 or 18 µg/m3 if AEI 2010 $\geq$ 22 µg/m^3
PM10 24h-mean	Objective of 50 µg/m^3 not to be surpassed 7 times a year by 2005	Objective of 50 µg/m^3 not to be surpassed 35 times a year by 2005	Objective of 50 µg/m^3 not to be surpassed 35 times a year by 2004
PM10 Annual mean	18 µg/m^3 by 2005	40 µg/m^3 by 2005	40 µg/m^3 by 2004

The UK has however passed the decisions of the CAFE directive into national law according to article 33 of the directive (European Parliament and Council of the European Union, 2008). This law is the "Air quality (standards) regulations 2010" which imposes on a national (English) level the decisions of directive 2008/50/EC on ambient air quality and directive 2004/107/EC related to emissions of As, Cd, Hg, Ni and polycyclic aromatic hydrocarbons (PAHs), while similar laws were also made in Scotland, Wales and Northern Ireland (Crown, 2014).

Appendix C.4 US LEGISLATION

At the last amendment of the Clean Air Act, that took place in 1990, it was decided to introduce the National Ambient Air Quality Standards (NAAQS). These standards aim at the reductions of pollutants harmful to both human health and the environment. By default, the Clean air act divides its standards in two categories, the primary and the secondary ones. The former are for the protection of sensitive human groups like the young, the elderly, and people suffering from chronic respiratory problems, while the latter aim for the conservation of the welfare of society, and avoidance of low visibility and of damage to structures and vegetation among others. Both standards for PM2.5 can be summarized in the Table C-5:

Table C-5: PM pollution standards in the US as of 14 Dec 2012 (USEPA, 2012).

Primary annual PM2.5	12 μg/m^3 annual average of 3-year mean
Secondary annual PM2.5	15 μg/m^3 annual average of 3-year mean
Primary and Secondary daily PM2.5 limit	35 μg/m^3 98th % of a 3-year mean
Primary and Secondary daily PM10 limit	150 μg/m^3 not to be surpassed more than once on average over 3 years

It is clear that a similar approach with the EU has been taken, by having both emission ceilings for the daily values and a reducing exposure approach for the annual PM2.5 levels. For the latter in particular, the approach is identical to the AEI used in EU (USEPA, 2012).

APPENDIX D AGGLOMERATION OF PM

As it has been discussed in the previous subchapters, small particles tend to coagulate in air and form bigger agglomerates. This is prevalent for ultrafine particles, however as the agglomerates enter the fine spectrum, this process gets significantly decelerated (Hinds, 1982). This phenomenon is based mainly on the Brownian motion, meaning the impact of gas molecules on the particle, thus the more pronounced it is, the larger the coagulation rate. It is of no wonder then that attempts have been made to promote this phenomenon in ESPs so as to increase its efficiency for the problematic (0.1-1) μm size range. While the process of agglomeration of smoke and other ultrafine matter has been studied early on (Nonhebel et al., 1927, Patterson et al., 1929a, Patterson et al., 1929b), its industrial applications are still limited (Jaworek et al., 2007). They can be used in modular configuration together with ESPs (Koizumi et al., 2000).

While sonic and water vapor condensation agglomeration is mostly utilized to coagulate PM in order to be collected more effectively by an ESP or other collection device (Kanazawa et al., 1993), it has been shown these are very energy demanding processes that cannot be used for large industrial applications. Another way to try to coagulate PM, especially the sub-micrometer one, is by using an AC field and thus have particles charged with opposite polarity, thus promoting attractive forces and in the end coagulation of opposite charged particles. However, this method while using electrostatic forces to agglomerate the opposite charged PM, the net result is a larger particle which cannot contribute to extra agglomeration due to its low to non-existed remaining charge. In addition, while with an increasing mass concentration of PM the agglomeration efficiency increases, the opposite is true for PM number concentration of above $5 \cdot 10^{12}$ particles/m^3. (Jaworek et al., 2007). In the case of the 2-stage reactors used in the current work, the second stage that receives the charged particles from the first stage, can act as an agglomeration stage, much like in (Fei et al., 2008); however it was not designed for that purpose.

It has been shown that it is practically impossible to achieve agglomeration of particles using magnetic fields. This is because the dipole forces created, that are expected to enhance agglomeration of fine PM, are appreciable only for ferromagnetic dusts in addition to the elevated magnetic fields needed (Ananth and Shannon, 1976).

APPENDIX E STEP-BY-STEP PROCESS FOR PRECIPITATION EXPERIMENTS USING THE SINGLE STAGE REACTOR AND FINE PM

1. When the experiments start, wait 30 s (or until fifth measurement if 6 s interval is used) so as to have an indication of the background particles level.
2. Right after the 5th measurement (30 s interval) turn on the air pump and the HV and run the system for 5 minutes.
3. After experiment finished, empty the leftovers of the container into a special resealable bag. When this gets full, it should be disposed of and not have its contents emptied into the bin.
4. Then wash the container (under the tap) and dry it with paper.
5. Use wet paper in order to clean the reactor and the top part of the container, and then dry it with dry paper.
6. Wait 5-10 min in order to be sure that they are dry, in order not to introduce humidity that might affect the system.
7. Fill the pressure pump with air (~6-7 bar)
8. Reassemble the system and let all this pressure through in order to blow away all leftover particles that might be in the tubes or anywhere else. At first the particle analyser inlet must remain open so as to clean the 4 mm tube that connects it, and when pressure reaches about 20 lb/in^2 block it and let the rest of the air discharge through the reactor only. When the pressure is ~10 lb/in^2, then stop the air flow towards the reactor and let pressure build up only in trigatron. This will lead in a ~20 lb/in^2 in the trigatron which is approximately the operating pressure needed in the experiments conducted so far. I might have to do this step 2 times.
9. Then disassemble the system again and open the container in order to see if there are some droplets remaining due to depressurisation. If there are then clean it with dry paper and wait for an additional ~5 min. If not put the new powder sample and continue with the next experiment.
10. When putting the powder in the container It must applied uniformly to the entire bottom area by shaking and spinning gently the container, and not just leave it where it fell. This helps in making more particles take off by the air flow. Use powder only from the 25 kg bag (packed well) and not use the container at all (in loose form)!

APPENDIX F SOFTWARE CODE USED

Programming has been used not only for simulation purposes, but also to vastly accelerate data handling and visualization. Simulation work was conducted using MATLAB software package, while for the raw data from the Grimm 1.109 particle analyser, Microsoft Excel was used in conjunction with visual basic script that greatly accelerated the process.

Appendix F.1 MATLAB CODE

The following code was used in software package MATLAB. It has examples of various parameter values. These can be changed with values in the comments (% sections) or with parametric functions.

```
function rk=g(t,x)
% m=4.19*10^-15;

pdensity=1000;
diam=2*10^-6;
V=(pi*4*(diam/2)^3)/3;

m=V*pdensity;

% a=3.452*10^-10;

visc=1.983*10^-5;
molpervol=0.02504*10^27;
colldiam=3.7*10^-10;
```

```
a=3*pi*visc*diam/(1+(2.52/(sqrt(2)*molpervol*pi*colldiam^2*diam)));
% below 10nm Cc(denominator) has a different form!


% d=4.1*10^-5;


e0=8.854*10^-12;
em=1;
ep=6;
n=2*10^16;
e=1.6*10^-19;
mob=1.8*10^-4;
sm=n*e*mob;
sp=10^-10;


% b=5.373*10^-10;
% c=3.48*10^-16;


Icor=10*10^-3;
l=0.87;
A=Icor/(2*pi*l*e0*em*mob);


Ecrit=28*10^5;
Erion=Ecrit;


Rwire=0.213/2;
Epeek=31*(1+0.308/sqrt(Rwire/10))*10^5;
```

```
Rion=(Epeek*Rwire)/(Ecrit*1000);


Qconst=6*pi*(diam/2)^2*e0*((-em*sp+sm*ep)/(2*sm+sp));
b=A*Qconst;
c=Qconst*Rion^2*(Erion^2-A);


d=((2*em+ep)/(2*sm+sp))*e0;
rk=[x(2); ((b+(c/x(1).^2))*(1-exp(-t/d))-a*x(2))/m];
```

In order for the above simulation to run, the following codes had to be types on MATLAB’s command prompt:

In order to calculate particle position:

```
clear all
timerange=[0 0.001]; %seconds
initialvalues=[0.0005 0];
    nv=700;
    set(0,'recursionlimit',nv);
    options=odeset('RelTol',1e-6,'Stats','on');
[t,x]=ode45(@g,timerange,initialvalues,options);
plot(t,x(:,1));
hold on
ylabel('position from wire(m)')
xlabel('time(s)')
```

In order to calculate particle speed:

```
clear all
timerange=[0 0.001]; %seconds
initialvalues=[0.0005 0];
    nv=700;
    set(0,'recursionlimit',nv);
    options=odeset('RelTol',1e-6,'Stats','on');
[t,x]=ode45(@g,timerange,initialvalues,options);
Test=plot(t,x(:,2))
hold on
ylabel('velocity(m/s)')
xlabel('time(s)')
xD = get(Test,'XData');
yD = get(Test,'YData');
```

and then yD(last value) gives the final PM speed.

The following for-loop code was used to produce the plots as a function of particle distance from the electrode in Subchapter 5.3.

```
clear all
timerange=[0 0.001]; %seconds
for ab=[0.0005 0.001 0.01 0.025 0.047]
initialvalues=[ab 0];
    nv=700;
    set(0,'recursionlimit',nv);
    options=odeset('RelTol',1e-6,'Stats','on');
[t,x]=ode45(@g,timerange,initialvalues,options);
Test=plot(t,x(:,2))
```

```
hold on
end
ylabel('velocity(m/s)')
xlabel('time(s)')
```

Appendix F.2 VISUAL BASIC SCRIPT USED IN MS EXCEL

The following code was used in order to gather the data collected by the particle analyser and automatically calculate efficiency of all PM size ranges as well as visualizing the efficiency data in plots.

```
Sub MACRO_SUB()

Const Rowno = 1 'row me ta onomata twn columns
Const Colno = 1 'h prwth kolona

Dim wb As Workbook
Dim i As Integer
Set wb = ActiveWorkbook
Dim j As Integer ' just to have only one sub

' diagram types
' 1 noHV 1g
' 2 DC 1g
' 3 HV 1g
' 4 Average
```

```
Dim chartHeights(1 To 4) As Long
    chartHeights(1) = 325
    chartHeights(2) = 325
    chartHeights(3) = 325
    chartHeights(4) = 325
Dim chartWidths(1 To 4) As Long
    chartWidths(1) = 500
    chartWidths(2) = 500
    chartWidths(3) = 500
    chartWidths(4) = 500
Dim chartTops(1 To 4) As Long
    chartTops(1) = 100
    chartTops(2) = 100
    chartTops(3) = 100
    chartTops(4) = 600
Dim chartLefts(1 To 4) As Long
    chartLefts(1) = 100
    chartLefts(2) = 700
    chartLefts(3) = 1500
    chartLefts(4) = 300
Dim chartFirstColumn(1 To 4) As Integer
    chartFirstColumn(1) = 1
    chartFirstColumn(2) = 11
    chartFirstColumn(3) = 21
Dim chartLastColumn(1 To 4) As Integer
    chartLastColumn(1) = 9
    chartLastColumn(2) = 19
    chartLastColumn(3) = 29
```

```
Dim chartName(1 To 4) As String
    chartName(1) = "noHV 1g"
    chartName(2) = "HV 1g"
    chartName(3) = "DC 1g"
    chartName(4) = "Average"



    Dim ws As Worksheet
    For Each ws In ActiveWorkbook.Worksheets
    j = deleteCharts(ws)
    j = addChart(wb, ws, chartHeights(1), chartWidths(1), chartTops(1), chartLefts(1),
chartName(1), "Range", chartFirstColumn(1), chartLastColumn(1))
    j = addChart(wb, ws, chartHeights(2), chartWidths(2), chartTops(2), chartLefts(2),
chartName(2), "Range", chartFirstColumn(2), chartLastColumn(2))
    j = addChart(wb, ws, chartHeights(3), chartWidths(3), chartTops(3), chartLefts(3),
chartName(3), "Range", chartFirstColumn(3), chartLastColumn(3))
    j = addChart(wb, ws, chartHeights(4), chartWidths(4), chartTops(4), chartLefts(4),
chartName(4), "List", 10, 20, 30)


    Next ws



End Sub
```

```
Function addChart(wb As Workbook, ws As Worksheet, height As Long, width As Long, top As Long, left As Long, chartName As String, sourceType As String, ParamArray params() As Variant) As Integer
Dim hasMeasures As Integer

  wb.Charts.Add

Dim ch As Chart

  ActiveChart.ChartType = xlLine   'typos grafhmatos
  ActiveChart.Location Where:=xlLocationAsObject, Name:=ws.Name 'se poio sheet
  Set ch = ActiveChart

  Do Until ActiveChart.SeriesCollection.Count = 0
    ActiveChart.SeriesCollection(1).Delete
  Loop

  If sourceType = "Range" Then
    hasMeasures = seriesCollectionFromRange(wb, ws, ch, (params(0)), (params(1)))
  End If
  If sourceType = "List" Then
    Dim tmpArr As Variant
    tmpArr = params()
    hasMeasures = seriesCollectionFromList(wb, ws, ch, tmpArr)
  End If
  If hasMeasures > 0 Then

    Set ch = ActiveChart
```

```
        ch.HasLegend = True

        ch.Legend.Select

        Selection.Position = xlRight

        ch.ChartArea.Select

        ch.HasTitle = True

        ch.ChartTitle.Characters.Text = chartName & " " & ws.Name

        With ch.Parent

            .height = height

            .width = width

            .top = top

            .left = left

        End With

    Else

        ch.ChartArea.Select

        Selection.Parent.Parent.Delete

    End If


End Function


Function deleteCharts(ws As Worksheet) As Integer

    For Each chtObj In ws.ChartObjects

        chtObj.Delete

    Next

End Function


Function seriesCollectionFromRange(wb As Workbook, ws As Worksheet, ByRef ac As Chart, firstCol As Integer, lastCol As Integer) As Integer

Dim m As Integer
```

```
Dim hasMeasures As Integer
hasMeasures = 0

  For i = firstCol To lastCol 'range for measures diagram

    m = Application.WorksheetFunction.CountA(ws.Columns(i))

    If m > 2 Then
      hasMeasures = hasMeasures + 1
      wb.Names.Add Name:="cellStart", _
        RefersToR1C1:=ws.Cells(1, i)
      wb.Names.Add Name:="DynamicRange", RefersTo:= _
        "=OFFSET(cellStart,0,0," & m & ",1)"



      ActiveChart.SeriesCollection.NewSeries
      ActiveChart.SeriesCollection(hasMeasures).Values = Range("DynamicRange")
      ActiveChart.SeriesCollection(hasMeasures).Name = ws.Cells(1, i)

    End If
  Next i

  seriesCollectionFromRange = hasMeasures
End Function

Function seriesCollectionFromList(wb As Workbook, ws As Worksheet, ByRef ac As Chart,
params As Variant) As Integer
Dim m As Integer
```

```
Dim hasMeasures As Integer
hasMeasures = 0

  For i = 0 To UBound(params) - LBound(params)  'list for measures diagram

    m = Application.WorksheetFunction.CountA(ws.Columns((params(i))))
    If m > 2 Then
      hasMeasures = hasMeasures + 1
      wb.Names.Add Name:="cellStart", _
        RefersToR1C1:=ws.Cells(1, (params(i)))
      wb.Names.Add Name:="DynamicRange", RefersTo:= _
        "=OFFSET(cellStart,0,0," & m & ",1)"

      ActiveChart.SeriesCollection.NewSeries
      ActiveChart.SeriesCollection(hasMeasures).Values = Range("DynamicRange")
      ActiveChart.SeriesCollection(hasMeasures).Name = ws.Cells(1, (params(i)))

    End If

  Next i
  seriesCollectionFromList = hasMeasures
End Function
```